A Numerical Investigation of the Array Effects of Wave Energy Converters with a Realistic Power Take-Off System Utilizing a Coupled Model Suite

Philip Balitsky

Promotoren: prof. dr. ir. P. Troch, dr. ir. V. Stratigaki
Proefschrift ingediend tot het behalen van de graad van
Doctor in de ingenieurswetenschappen: bouwkunde

UNIVERSITEIT
GENT

Vakgroep Civiele Techniek
Voorzitter: prof. dr. ir. P. Troch
Faculteit Ingenieurswetenschappen en Architectuur
Academiejaar 2018 - 2019

ISBN 978-94-6355-262-2
NUR 956
Wettelijk depot: D/2019/10.500/70

Examination board

Supervisors:

prof. Peter Troch

dr. Vasiliki Stratigaki

Coastal Engineering Research Group
Department of Civil Engineering
Faculty of Engineering and Architecture
Ghent University
Technologiepark 60
B-9052 Ghent, Belgium

Voting members:

prof. Patrick De Baets	Ghent University, Belgium	chairman
prof. Kurt Stockman	Ghent University, Belgium	secretary
em. prof. Marc Vantorre	Ghent University, Belgium	
prof. Joris Degroote	Ghent University, Belgium	
dr. Maxim Candries	Ghent University, Belgium	
prof. Jens Peter Kofoed	Aalborg University, Denmark	
dr. George Lavidas	Delft University of Technology, Netherlands	
dr. Irina Temiz	Uppsala University, Sweden	

Internal defence (Ghent University): 28/05/2019
Public defence (Ghent University): 02/07/2019

"Pain is inevitable...the struggle is not."

- Haruki Murakami -

Acknowledgements

Finishing a PhD is a marathon, not a sprint. Although I am no long-distance runner, somehow I am here at the last meters, exhausted, but holding my head up proudly. And as I cross the finish line I look back on the course behind me I cannot but think of those who have helped me get here.

Firstly, thank you to my two supervisors who took a chance on me and believed that I could do it. To Peter Troch, thanks for your flexibility which although I have stretched at times, has allowed me to follow my research instincts. As well as set-up my work and my time off the way I saw fit. The slack has allowed me to stick through the hard stretches where I normally would break. Thank you to Vicky Stratigaki. You has helped me make my work more presentable. And readable. Even though I did not always follow your advice. To my detriment.

Moitas grazas to Gael. Although a PhD project is on paper a solo pursuit, en nuestro caso es cosa de dos. It is good knowing you had my back in the good and the bad. Especially those times when the barge got stuck in the mud and would not budge. Yet even more thank you for being a kind a generous friend from day one. To Max, vielen Dank for those day trips exploring the 'wild side' of Belgium and for being a great listened for my philosophical rants. Hartelijk bedankt to Nicolas for your enthusiasm in taking up my somewhat vague idea and having the motivation to seeing it to completion in the form of a Masters thesis. Then for sticking around to continue the work in your PhD. Without your input I would have not have been able to produce work of such high quality.

Thanks to Brecht for showing that a PhD can be completed on time, and for setting the bar for personal organization, and to Tim that you can keep your sanity and have a life while doing it! All the while sharing your wonderful skills with us. And a big thanks for showing us that the Pythonic way is the right way! Gracias to David for throwing that movie party which led me to find a decent place to live upon arriving here - in your flat! Evxaristou to Panagiotis for being a cheerful company in a crowded office and putting up with my sun worship. Zhixíe to Minghao for his willingness to listen to my wave energy talks which inadvertently turned to a commentary on the state of the world.

Dank je wel to Lien and Ellen who have helped deal with the sea of paperwork that

can drown anyone coming to work in Belgium and for explaining me intricacies of Flemish when I needed to figure it out. Thanks to Tom your help in getting the right workhorse without which the simulations would have never been done and for and to Dave and Herman for your friendly chats and helping with getting random parts to fix my constantly in-need-of-fixing bike. Thank you to my examination committee members. Your thorough reviews and criticism, although challenging, helped make my dissertation stronger.

Большое спасибо моим родителям, брату и бабушке и дедушке. Без вашей любви и поддержки вряд ли я бы выдержал эту нагрузку. Ваша вера в мою победу помогла мне через трудные отрезки в пути когда я сомневался что могу это осуществить. Благодарю всех родственников, дальних и не очень, а так же друзей, кто всегда меня толкал вперед своим энтузиазмом к моему делу.

This thesis is dedicated to my late grandmother, Evgenia Ospivona Balitskaia (1928-2018), who, as a life-long academic, mathematician, and hydrodynamicist, followed my journey until her last days. She always believed I could achieve this and I am sure somewhere out there she is smiling.

Philip Balitsky
Zwijnaarde, Juin 2019

Contents

Nomenclature

Acronyms

BEM Boundary Element Method

BVP Boundary Value Problem

CAPEX CApital EXpenditrue of a WEC array project

CFD ComputationalFluid Dynamics

CMA Covariance Matrix Algorithm

DoF Degree of Freedom

EMEC European Marine Energy Centre

FP (European Union) Framework Programme

GA Genetic Algorithm

GPU Grapthical Processing Unit

GSO Glowworm Swarm Optimization

IPCC Intergovernmental Panel on Climate Change

IRENA International Renewable ENergy Agenc

JONSWAP Joint North Sea Wave Observation Project

l.h.s. left hand side

LCOE Levelized Cost of Energy

MPC Model Predictive Control

NWT Numerical Wave Tank for a CFD simulation

ORE Ocean Renewable Energy

OWC Osciallting Water Column

PTO Power Take-off

r.h.s. right hand side

RANS Reynolds Averaged Navier-Stokes

RANS Reynolds-Average Navier Stokes

SGA Search Group Algorithm

SPH Smoothed Particle Hydrodynamics

VOF Volume of Fluid

W2W Wave-to-Wire

WSI Wave-Structure Interaction solver

Definitions

capture width - A measure of WEC efficiency based on the energy captured by the WEC given as the equivalent energy in the incoming wave front [m]

far-field referring to the area away from the immediate location of a WEC array

inter-array - referrring to the variables relating WEC arrays in a WEC farm

intra-array - referrring to the variables relating individual WECs in a WEC array

near-field referring to the area in between or in the immediate vicinity of the WECs in a WEC array

point absorber - A WEC with dimensions much less than the incident wave with a response primarily in heave

WEC array effects changes in the incident wave field brought on by the radiated and diffracted waves in the presence of multiple WECs in an array

Boundary Element Method - a numerical computational method of solving linear partial differential equations which have been formulated in boundary integral form.

Model Predictive Control a real-time control strategy approximating optimal complex conjugate control

Potential Flow Theory - also referred to a Linear Wave theory or Airy Wave theory. A idealized non-rotational mathematical representation of gravity waves

PowerTake-off or PTO system - a mechanism for converting mechanical to electrical power.

Reynolds Averaged Navier-Stokes - non-linear equations solved via a Volume of Fluid method

Smoothed Particle Hydrodynamics - A mesh-less Lagrangian method for solving non-linear fluid motion

Wave-to-Wire - a suite of numerical models that simulates the joint hydrodynamic, mechanical, and electrical systems of wave energy conversion.

Subscripts

$array$ referring to WEC array

D diffracted

$farm$ referring to WEC farm

h hydraluic

I incident

i wave angluar frequency

irr irregular

j osciallation mode

k DoF

l linear

n n_{th} spectral moment

R radiated

r regular

r resonance

s sponge layer

t total

Symbols

α, σ, ω_p JONSWAP spectral distribution constants [-]

β angle of incidence of the incoming wave to the x-axis [°]

ϵ_0 spectral bandwidth parameter [-]

η_1 *capture width [m]*

γ peakedness factor of the JONSWAP spectral distribution [-]

Γ_m wetted surface of body [m^2]

$\hat{\phi_D}$ complex diffracted velocity potential [$-$]

$\hat{\phi_I}$ complex incident velocity potential [$-$]

$\hat{\phi_I}$ complex radiation impedance [-]

$\hat{\phi_R}$ complex radiated velocity potential [$-$]

$\hat{\varphi_k}$ proportionality coefficient of the complex radiated velocity potential [$-$]

$\hat{\varphi}$ phase angle of the complex body motion [rad^{-1}]

λ wave length [m]

$\mathbf{P}_{array}$ total power output of an isolated WEC array [kW]

$\mathbf{P}_{farm}$ total power output of an WEC farm composed of multiple WEC arrays [kW]

$\mathcal{A}, \mathcal{B}$ Mild-slope equation discretization coefficients [-]

$\mathcal{M}$ number of bodies in the WEC array [-]

$\mathcal{N}$ number of WEC arrays in a WEC farm

$\mathcal{T}_{PTO,h}$ PTO-torque for hydraulic PTO system [$N \cdot m$]

$\mathcal{T}_{PTO,l}$ PTO-torque for linear PTO system [$N \cdot m$]

ν coefficient of kinematic viscosity [m^2/s]

Ω The fluid domain in the Boundary Value Problem

ω angular wave frequency [rad/s]

ϕ fluid velocity potential [m^2/s]

ρ density of seawater [kg/m^3]

ρ water densitty [kg/m^3)]

τ time integration variable in the Cummins equation [s]

Θ complex amplitude of pitch angular displacement [-]

$\theta(t)$ pitch angular displacement in time-domain [rad]

Υ a given point in the fluid domain

φ phase angle of the complex free surface elevation [rad^{-1}]

ζ wave amplitude [m]

$A(\omega)$ added mass [kg] or added moment of inertia [N $\cdot m^2$]

b distance from outside boundary of the sponge layer

$B(\omega)$ hydrodynamic damping [kg/s^2]

B_s length of the sponge layer

$B_{PTO,h}$ power-take-off hydraulic damping equivalent coefficient[kg/s^2]

$B_{PTO,l}$ power-take-off linear damping coefficient [kg/s^2]

C hydrodynamic stiffness [N/m]

C_g wave group velocity [m/s]

C_{PTO} PTO system spring

CWR Capture Width Ratio [-]

D *intra-array* separation distance [m]

d *inter-array* separation distance [m]

$D(\theta)$ directional spectral distribution [$m^2 \cdot s$]

D_m variable motor displacement [rev/s]

d_x, d_y inter-array separation distances in the x and y direction [m]

F_e, k wave excitation force for DoF k [N]

F_e, k wave excitation force for DoF k [N]

F_r, j, k wave radiation force for DoF k for oscialltion mode j [N]

$f_{PTO,h}$ PTO system force for hydraulic PTO system [N]

$f_{PTO,l}$ PTO system force for linear PTO system [N]

g acceleration due to gravity [m/s^2]

$G(\Upsilon)$ Greens function for source Υ

h water depth [m]

H_I wave height at the wave generation boundary (m)

h_z WEC draft

H_{m0} significant wave height [m]

H_t Total wave height at a point in the simulation domain (m)

k wave number [m^{-1}]

K_d The disturbance coefficient [-]

K_{PTO} power take-off linear stiffness coefficient [$\frac{N}{m}$]

m_n n_{th} wave spectral moment $[m^2]$

M_{PTO} PTO system supplementary mass $[kg]$

N number of frequency compoentns in irregular sea state spectral representation $[-]$

n unit normal on body surface [-]

n_z normal component in heave direction [-]

$p(x, y, z, t)$ fluid pressure $[kg/(m \cdot s^2)]$

$P_(\omega, \beta)$ power for a single WEC for a given angular wave frequency for a given direction [kW]

P_h mechanical power produced by the WEC with a hydraulic PTO system [kW]

P_l mechanical power produced by the WEC with a linear PTO system [kW]

$q - value$ - a measure of the magnitude of WEC array and/or WEC farm effects [-]

r WEC radius

r_d radial distance away from body (WEC) centre [m]

$S(\omega)$ non-directional (omni-directional) spectral density function for a sea state distribution $[m^2 \cdot s]$

s_c piston area $[m^2]$

S_{JS} JONSWAP spectral sea state distribution $[m^2 \cdot s]$

S_{PM} Pierson-Moskowitz spectral sea state distribution $[m^2 \cdot s]$

T_p wave peak period $[s]$

T_r resonance or natural period of an oscillating body [s]

u general body velocity moving in a fluid $[m/s]$

W charactersitic dimension of a WEC array or a WEC farm $[m]$

X_m complex excitation force for a single body $[m]$

Z complex amplitude of heave displacement [-]

$z(t)$ heave displacement in time-domain [m]

$Z_{j,k}$ radiation impedance in direction j for osicalltion mode k $[\Omega]$

dS integration surface for calculating hydrodynamic forces [-]

Summary

Ocean Wave Energy has the potential to make a significant contribution to the de-carbonization of the world's energy supply, which is one of the preconditions for avoiding catastrophic warming of the planet beyond 1.5°. However, in order for wave energy to contribute in the mitigation of climate change, it must follow the path of offshore wind and become a commercially viable power source. For this outcome to occur, significant cost reductions must be implemented. Because of physical limitations of operating in a highly energetic environment, individual Wave Energy Converters (WECs) will have to be deployed in large numbers in close proximity in order to benefit from the same economies of scale such as those currently seen in the offshore wind industry. Moreover, such close spacing increases the economic profitability of a project by limiting the spatial extent of a wave energy project which may cause potential ocean space conflicts. Such dense clusters of WECs are commonly termed 'WEC arrays', where the number of units is less than 10 and 'WEC farms' for projects matching the power output of offshore wind farms, consisting of many tens and hundreds of WECs.

Determining the economic profitability or environmental impacts of a WEC array project is no trivial matter because both facets are determined by complex hydrodynamic processes that link the individual WECs through the wave field. The 'WEC array problem' arises then from the fact that the power output and the wave field impacts that determine the two aforementioned aspects are not the simple sum of the respective wave field and power outputs of individual WECs. Unlike the case of wind farms where close positioning of individual turbines exhibit only a detrimental effect on the farm power output, the interactions in WEC arrays due to these 'array effects' can be both beneficial and deleterious. Due to the lack of operational and experimental data on WEC farm modelling which is costly and time consuming to obtain, numerical models are the primary tools of wave energy developers in assessing the economics and environmental impacts of a WEC array. Such models must account for all the variables influencing a WEC farm or array such as the wave climate, bathymetry, WEC farm layout and the changes in motion due to the presence of a Power Take-off (PTO system), yet modelling them in parallel leads to significant demands on computational power, and often prompts unclear conclusions. A trade-off must therefore be made between the accuracy of the numerical model and practical considerations such as speed of simulations and CPU usage.

At the core of this thesis is a coupling strategy that enables a linearly accurate

and fast calculation of array effects in both the near-field and far-field regions of a WEC array. The 'near-field' here refers to the area immediately surrounding the individual WECs, while the 'far-field' refers to the external effects of the WEC farm on the surrounding sea and coastal area. While not mutually exclusive , the near-field wave field is the primary determinant of the economic viability of the WEC array because it directly influences the WEC array power output, while the far-field free surface elevation is a proxy for the majority of environmental effects, namely those relating to the modification of the wave field in the adjoined coastal area. The coupling strategy consists of simulating individual WECs in an array in a high resolution Wave-Structure Interaction (WSI) solver in the near-field domain, and propagating the resulting information to a lower resolution but faster wave propagation model in the far-field domain. The resulting coupled model balances the trade-off between accuracy in modelling and expediency of simulation time. Furthermore, the coupled model is enhanced by a separate module which simulates the PTO system of the WECs in the array. The PTO simulation is performed in the time-domain in the Matlab Simulink® environment, and the resulting linearised coefficients are coupled to the hydrodynamic coefficients calculated with the WSI. The three pieces together constitute a prototype wave-to-wire (W2W) model suite with the double objective of quantifying the power output and the far-field environmental impacts of a WEC array. The distinguishing characteristic of a WEC is the PTO system that extracts the mechanical energy of a wave and converts it to usable mechanical or electrical energy. By modifying the motion of the device the PTO system changes the hydrodynamics of a WEC and by extension of the WEC array, therefore necessitating the inclusion of the PTO module in the W2W model.

In this thesis, various facets of the WEC array problem are explored firstly using the individual components of the W2W model, and then in the final chapter, with the entire model suite. Firstly, various permutations of the WSI-wave propagation model coupling strategy were investigated with the goal of determining the fastest and most accurate method of passing the information from the near-field to the far-field domain model. It was found that coupling the perturbed wave field, *i.e.* the sum of the radiated and diffracted wave fields, directly into the far-field model resulted in a better model performance than individual coupling the respective wave fields. Next, various array configurations were investigated to study the influence of environmental parameters such as the incident wave conditions, the type of WECs modelled, and the site bathymetry. It was found that the 'array effects' for arrays consisting of heaving cylindrical WECs are less likely to produce strong wave field modifications than bottom-fixed Oscillating Surge Wave Energy Converters (OSWECs). Furthermore, the influence of the wave period was found to much more strongly affect both the power output and the strength and extent of the wave field for a heaving cylindrical WEC than for an OSWEC in parallel wave conditions. Finally, the difference of the behaviour of a WEC array between regular waves and irregular waves was inspected for similar WEC array configurations.

In addition to the numerical coupling model procedure, an iterative analytical method was developed to simplify the calculation of a wave field in a WEC farm. Building on the ideas of the superposition principle and the multiple scattering method, the iterative procedure introduced in this work enables a simplified calcu-

lation of the wave field resulting from WEC arrays in a WEC farm by sorting the interaction effects by order and summing the successive orders to an arbitrary precision. Furthermore, the motion of 'hydrodynamic independence' of WEC arrays in a WEC farm was introduced, where the mutual influence of 'independent' arrays in a WEC farm is less than 5% of the total perturbed wave field. In the analysis of a WEC farm consisting of two closely-spaced WEC arrays of heaving cylindrical WECs, it was found that for wave incidence angles away from the WEC farm axis and for wave periods distant from the WEC resonance period, all WEC array configurations simulated were below the determined 'hydrodynamic independence' threshold.

Next, the time-domain PTO module was introduced into the coupled model suite to study the near-field effects and the WEC array power output. Two types of PTO systems were compared for two types of WECs: a linear and a hydraulic PTO for a heaving cylindrical WEC and an OSWEC. Because the PTO model affects the 'near-field' interactions of a WEC array, it is essential to understand the differences between a WEC array with realistic PTOs versus one modelled with simplified linear description of a PTO. The simulations were performed for both single isolated WECs and densely packed arrays of 5 WECs. It was found that the difference between the power output between the two PTO systems was greater for the heaving cylindrical WECs but that the discrepancy in the near-field effects was greater for the array of OSWECs. Finally, the W2W consisting of the three modules was run for a proposed near-shore WEC array project consisting of a 50-WEC farm with 2 rows of 5 arrays of 5 staggered OSWECs for a real wave climate and site bathymetry. The modelled location was chosen based on a proposed WEC array project with a commercially promising OSWEC technology and the bathymetry and wave climate were determined from site data. It was found that the interaction of the 'array effects' with the near-shore bathymetry under the site wave regime produced significant effects on the WEC array proposal and on the far-field. The results showed a significant reduction in the lee of the WEC array with power output of the back row of the WEC farm significantly reduced. An increase in the wave incidence angle from the WEC farm axis mitigated the detrimental effects. While at the same time the overall extent of the so called 'wake zone' of reduced wave heights in the lee of the WEC farm increased.

Samenvatting

Dutch summary

Oceaangolfenergie heeft het potentieel om een belangrijke bijdrage te leveren aan de ontkoling van de wereldwijde energievoorziening, wat een van de voorwaarden is om een catastrofale opwarming van de planeet boven de 1.5° te voorkomen. Om bij te dragen aan de matiging van de klimaatverandering, moet golfenergie de weg van de offshore wind volgen en een commercieel haalbare energiebron worden. Om dit resultaat te bereiken, moeten er aanzienlijke kostenreducties worden doorgevoerd. Vanwege de fysieke beperkingen van het werken in een zeer energieke omgeving zullen individuele golfenergieconvertoren (GECs) in grote aantallen in elkaars nabijheid moeten worden ingezet om te profiteren van dezelfde schaalvoordelen zoals die momenteel in de offshore windindustrie worden waargenomen. Bovendien verhoogt een dergelijke nauwe afstand de economische rendabiliteit van een project door het beperken van de ruimtelijke omvang van een golfslagenergieproject dat potentiële conflicten in de oceaanruimte kan veroorzaken. Zulke dichte clusters van GECs worden gewoonlijk 'GEC-reeksen' genoemd, waarbij het aantal eenheden minder dan 10 is en 'GEC-parken' voor projecten die passen bij de energieproductie van offshore windmolenparken, bestaande uit vele tientallen en honderden GECs.

Het bepalen van de economische rendabiliteit of economische effecten van een GEC-reeks project is geen triviale zaak, omdat beide facetten worden bepaald door complexe hydrodynamische processen die de afzonderlijke GECs en het golfveld met elkaar linken. Het 'GEC-reeks-probleem' ontstaat dan uit het feit dat het vermogen en de golfveldbelasting die de twee bovengenoemde aspecten bepalen, niet de eenvoudige som zijn van het respectieve golfveld en het vermogen van de afzonderlijke GECs. De GEC-reeks-problematiek is een probleem dat zich voordoet in het geval van de twee bovengenoemde aspecten. In tegenstelling tot windparken, waar de nauwe positionering van individuele turbines slechts een nadelig effect heeft op het vermogen van het park, kunnen de interacties in GEc-reeksen als gevolg van deze 'reeks-effecten' zowel gunstig als schadelijk zijn. Door het gebrek aan operationele en experimentele gegevens over GEC-parkmodellering, die kostbaar en tijdrovend zijn om te verkrijgen, zijn numerieke modellen de belangrijkste instrumenten van golfenergie-ontwikkelaars om de economische en milieu-impact van een GEC-reeks te beoordelen. Zulke modellen moeten rekening houden met alle variabelen die een GEC-park of -reeks beïnvloeden, zoals het golfklimaat, de bathymetrie, de GEC-schikking en de veranderingen in beweging als gevolg van de aanwezigheid van een Power Take-off (PTO-systeem). Echter, het parallel modelleren van deze

variabelen leidt tot aanzienlijke eisen aan het rekenvermogen, en leidt vaak tot onduidelijke conclusies. Er moet daarom een afweging worden gemaakt tussen de nauwkeurigheid van het numerieke model en praktische overwegingen zoals de snelheid van de simulaties en het gebruik van de CPU.

De kern van dit proefschrift is een koppelingsstrategie die een lineair nauwkeurige en snelle berekening van reeks-effecten in zowel de nabije als verre golfvelden van een GEC-reeks mogelijk maakt. Het nabije-golfveld verwijst hier naar het gebied direct rond de individuele GECs, terwijl het verre-golfveld verwijst naar de externe effecten van het GEC-park op de omliggende zee en kustgebieden. Het nabije-golfveld is de belangrijkste determinant van de economische levensvatbaarheid van de GEC-reeks, omdat het rechtstreeks van invloed is op het vermogen van de GEC-reeks, terwijl de hoogte van het verre-golfveld een proxy is voor het merendeel van de milieueffecten, namelijk die welke betrekking hebben op de aanpassing van het golfveld in het aangrenzende kustgebied. De koppelingsstrategie bestaat uit het simuleren van individuele GECs in een reeks in een hoge-resolutie golfstructuur-interactie (GSI) solver in het nabije-veld domein, en het doorgeven van de resulterende informatie naar een lagere resolutie, echter sneller golfpropagatiemodel in het verre-golfveld domein. Het resulterende gekoppelde model balanceert de afweging tussen nauwkeurigheid in de modellering en opportuniteit van de simulatietijd. Verder is het gekoppelde model uitgebreid met een aparte module die het PTO-systeem van de GECs in de reeks simuleert. De PTO-simulatie wordt uitgevoerd in het tijdsdomein in de Matlab-Simulink®-omgeving, en de resulterende gelineariseerde coëfficiënten worden gekoppeld aan de hydrodynamische coëfficiënten berekend met de GSI solver. De drie stukken vormen samen een prototype wave-to-wire (W2W) modelsuite met als dubbel doel het vermogen en de milieueffecten van een GEC-array in het verre-golfveld te kwantificeren. Het onderscheidende kenmerk van een GEC is het PTO-systeem dat de mechanische energie van een golf onttrekt en omzet in bruikbare mechanische of elektrische energie. Door de beweging van het toestel te wijzigen verandert het PTO-systeem de hydrodynamica van een GEC, en met uitbreiding van de GEC-reeks, waardoor de PTO-module in het W2W-model moet worden opgenomen.

In dit proefschrift worden verschillende facetten van het GEC-reeks-probleem eerst aan de hand van de afzonderlijke componenten van het W2W-model, en vervolgens in het laatste hoofdstuk met de gehele modelsuite, onderzocht. Eerst werden verschillende permutaties van de koppelingsstrategie van het GSI-golfpropagatie model onderzocht met als doel de snelle en meest nauwkeurige methode te bepalen om de informatie van het nabije-golfveld naar het verre-golfveld domein model door te geven. Het koppelen van het verstoorde golfveld, d.w.z. de som van het geradieerde en gediffracteerde golfvelden, direct in het verre-golfveld model resulteerde in een betere modelprestatie dan het individueel koppelen van de respectievelijke golfvelden. Vervolgens werden verschillende reeksconfiguraties onderzocht om de invloed van omgevingsparameters, zoals de omstandigheden van de invallende golven, het type GECs gemodelleerd en de bathymetrie van de locatie te bestuderen. Het bleek dat de 'reeks-effecten' voor reeksen bestaande uit dompende cilindrische GECs minder waarschijnlijk sterke golfveldmodificaties produceren dan bodem-gemonteeerde oscillerende schrikkende (surging) golfenergiecon-

vertoren (OSGECs). Bovendien bleek de invloed van de golfperiode veel sterker te zijn op zowel het vermogen als de sterkte en de omvang van het golfveld voor een dompende cilindrische GEC dan voor een OSGEC in parallelle golfcondities. Ten slotte werd het verschil in gedrag van een GEC-reeks tussen regelmatige golven en onregelmatige golven geïnspecteerd op vergelijkbare GEC-reeks-configuraties.

Naast de procedure van het numerieke koppelingsmodel werd een iteratieve analysemethode ontwikkeld om de berekening van een GEC-golfveld in een GEC-bedrijf te vereenvoudigen. Voortbouwend op de ideeën van het superpositieprincipe en de meervoudige verstrooiingsmethode, maakt de iteratieve procedure die in dit werk wordt geïntroduceerd een vereenvoudigde berekening mogelijk van het golfveld dat het resultaat is van een GEC-reeks in een GEC-park door de interactie-effecten op volgorde te sorteren en de opeenvolgende orders op te tellen tot een willekeurige precisie. Verder werd de beweging van 'hydrodynamische onafhankelijkheid' van GEC-reeksen in een GEC-park geïntroduceerd, waarbij de wederzijdse invloed van 'onafhankelijke' reeksen in een GEC-park minder dan 5% van het totale verstoorde golfveld bedraagt. In de analyse van een GEC-park bestaande uit twee dicht bij elkaar liggende GEC-reeksen van dompende cilindrische GECs, werd vastgesteld dat voor golfincidentiehoeken ver van de GEC-park-as en voor golfperioden ver van de GEC-resonantieperiode alle gesimuleerde GEC-reeks-configuraties onder de bepaalde 'hydrodynamische onafhankelijkheidsdrempel' lagen.

Vervolgens werd de tijddomein PTO-module geïntroduceerd in de gekoppelde modelsuite om de nabije-golfveld effecten en het GEC-reeks vermogen te bestuderen. Twee typen aftakassystemen (PTO) werden vergeleken voor twee typen GECs: een lineaire en een hydraulische aftakas voor een dompende cilindrische GEC en een OSGEC. Omdat het PTO-model de 'nabije-golfveld' interacties van een GEC-reeks beïnvloedt, is het essentieel om de verschillen te begrijpen tussen een GEC-reeks met realistische PTOs versus een GEC-reeks met een vereenvoudigde lineaire beschrijving van een PTO. De simulaties werden uitgevoerd voor zowel enkelvoudig geïsoleerde GECs als dicht opeengepakte reeksen van vijf GECs. Er werd vastgesteld dat het verschil tussen het vermogen tussen de twee PTO-systemen groter was voor de dompende cilindrische GECs, maar dat de discrepantie in de nabije-golfveld effecten groter was voor de reeks van OSGECs.

Ten slotte werd het W2W model bestaande uit de drie modules uitgevoerd voor een voorgesteld GEC-reeks project, bestaande uit een 50 GEC-park, twee rijen van vijf reeksen van vijf OSWECs voor een echt golfklimaat en bathymetrie op de site. De gemodelleerde locatie werd gekozen op basis van een voorgesteld GEC-reeks project met een commercieel veelbelovende OSWEC-technologie en de bathymetrie en het golfklimaat werden bepaald op basis van de locatiegegevens. Het bleek dat de interactie van de 'reeks effecten' met de near-shore bathymetrie onder de site golfcondities significante effecten had op het WEC-reeks voorstel en op het verre veld. De resultaten toonden een significante vermindering in het zog van de WEC-reeks aan, waarbij het vermogen van de achterste rij van het WEC-park aanzienlijk verminderde. Tegelijkertijd werd door een toename van de golfincidentiehoek vanaf de WEC-park-as de schadelijke effecten beperkt, terwijl tegelijkertijd de totale omvang van de zogenaamde 'wake-zone met verminderde golfhoogten in het zog van het WEC-park werd vergroot.

Chapter 1

Introduction

1.1 Background

As we move further into uncharted territory of increasing CO_2 concentrations in the Earth's atmosphere, the race to de-carbonize the world's energy supply is taking on increasing stakes. It is pointed out in the 2018 Intergovernmental Panel on Climate Change (IPCC) Special Report on Global Warming of 1.5°C, that "Climate-related risks to health, livelihoods, food security, water supply, human security, and economic growth are projected to increase with global warming of 1.5°C and increase further with 2.0°C (Rogelj et al., 2018). In order to mitigate the effects of disastrous climate change and avoid a catastrophic destabilization of the world's livelihood and ecosystems, the IPCC forecasts that renewable will need to supply anywhere from 70–85% of electricity in 2050 (Rogelj et al., 2018). An overwhelming majority of the world's large industrial powers committed to taking decisive steps to ramp up their renewable energy production. The EU has a recently updated 40% goal for 2030 and China at 35% of the total energy consumption by the same date.

Given the high stakes and a short time frame for implementation, an 'all of the above' energy strategy needs to be pursued by the world's major industrial powers and developing nations, where all viable renewable energy sources must be given due consideration. With a global resource estimated between 18 500 Twh/yr and 29 500 Twh/yr, even a conservative estimate of capturing 5% of the exploitable wave energy resource yields 925 Twh/yr to 1475 Twh/yr of energy. This can satisfy near 5% of the world's electricity consumption, estimated to be around 22 000 Tw in the year 2017 (Mork et al., 2010; Gunn and Stock-Williams, 2012; Enerdata, 2018). The ORE Catapult, the UK's leading technology innovation and research centre for offshore wind, identified that for every kWh of power generated by a tidal stream or wave device, 394g of CO2 is saved compared to the same power generated from a Combined Cycle Gas Turbine (CCGT) power plant (Scottish Renewables, 2019). With respect to Europe, the industry body Ocean Energy Europe predicts that installing 100GW of wave energy capacity could provide nearly 10% of European Energy needs by the year 2050 (Ocean Energy Systems, 2018). Outside of the potential for climate change mitigation, the economic benefits of developing the

marine renewable energy are enormous. The UK government enterprise Scottish Renewables estimates that ocean energy will be worth €90 billion by 2050 (Scottish Renewables, 2019). If we look at a map of the world wave energy resource Fig. 1.1,

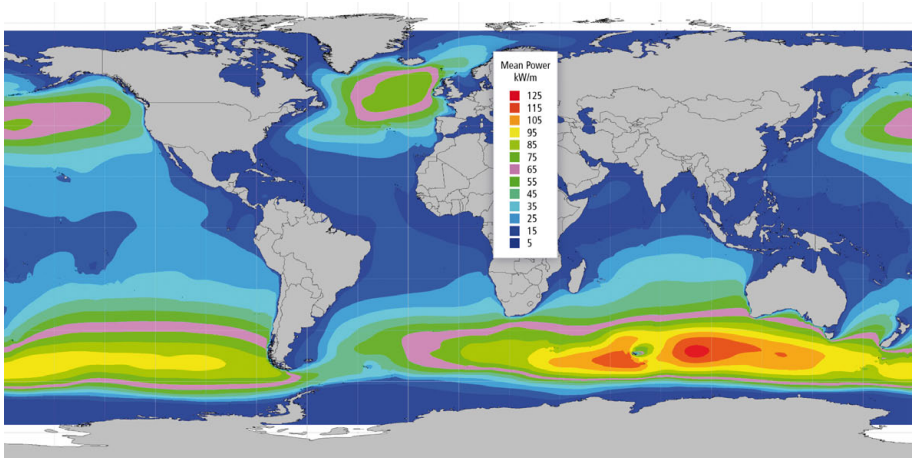

Figure 1.1: Global offshore annual wave power level distribution (Lewis et al., 2011)

we see that areas like the west coast of North America, Europe, South America as well as the south and west coasts of Australia are in particularly favourable locations for wave energy extraction. According to the UN, 44 % of the world's population currently resides within 150 km of the coastline and this number is only projected to increase in the future (Food and Agriculture Organization (FAO) of the United Nations, 2012).

Furthermore, wave energy has the benefit of being a much less intermittent source of energy than either solar or wind power, the dominant sources of renewable energy today. Wave energy is predictable up to several days in advance and unlike solar is available both night and day. It potentially decreases the need for grid storage that is at present the biggest roadblock in the path to a 100% renewable energy generation scenario.

However, wave energy suffers some distinct disadvantages that need to be overcome should it play a significant role in the global electricity supply:

- Wave energy has a very high ratio of peak to average power, necessitating costly structural components;
- Wave Energy Converters (WECs) need to be deployed in areas of climatologically high sea states, therefore deployment, maintenance and decommissioning is an issue;
- There is no established paradigm for the operation of a WEC: wildly different concepts are put forth by developers making it hard to develop a uniform supply chain;

- The Power Take-off (PTO) system of a WEC needs to convert high power low frequency oscillations to lower power high frequency electricity suitable for a grid connection;
- Unlike wind and solar power and to a lesser extent tidal energy, the wave energy industry does not have a good track record of success and cost reductions, necessary to attract commercial-grade investors for large projects.

In spite of these challenges and given the enormous potential of wave energy, research institutions, government agencies and private enterprises around the world are currently pursuing the challenge of making wave energy conversion profitable.

1.2 Motivation

As identified by numerous international and national organizations, including the IPCC (Lewis et al., 2011), IRENA (Kempener and Neumann, 2014), the UK Carbon Trust (Carbon Trust, 2011), CSIRO in Australia (CSIRO, 2012), the Irish Government (RPS and REMTec Consulting, 2018), and the Scottish Government Scottish Renewables (2019), the only way for wave energy to play a significant role in the clean energy sector and reach its theoretical potential is by aggressive cost reduction. As we observe in Fig. 1.2 the Levelised Cost of Energy (LCOE) for wave energy is the highest amongst all listed sources yet also has the biggest margin for cost reduction as indicated by the shaded bars. Although the figure is several years old and the costs of wave energy have come down somewhat, so have the costs of other renewable like offshore wind and solar photovoltaic. Therefore the wave energy sector still needs to explore multiple avenues for significant cost reduction. Such a path is not unforeseen; this is the situation that both wind and solar energy have overcome as we can see in Fig. 1.3 where the exponential decline in the cost of both renewable energies is seen. Recently, offshore wind, the technology most similnar in its technical challenges vis-a-vis wave energy, has been a shining example of significant LCOE reactions (Lazard, 2018). The broad scientific consensus is that the aforementioned cost reduction will be unattainable without deploying multiple WECs in close geographic proximity, whether joined by a superstructure or moored independently to the sea bottom, the primary reason for it being the physical limitations on the sizes of individual WECs. These agglomerations of WECs, referred to alternatively as 'WEC or wave farms', 'WEC arrays' or 'wave parks', will allow the benefits of scale to be applied to wave energy technologies. They also enable additional cost reductions through the sharing of common infrastructure such as electrical cables and mooring systems.

However, the placement of WECs in farms or arrays itself presents a set of challenges, namely that the WECs interact with each other through a mutual influence on the surrounding wave field. These interactions, known as the 'farm effects' or 'array effects', can both increase or decrease the expected power output of a WEC farm, and also influence the survivability of the WECs in extreme conditions. In looking at 'array-effects' one can split the problem into two constituents: the *near-field* and the *far-field*. Both are consequences of the modification of the incoming

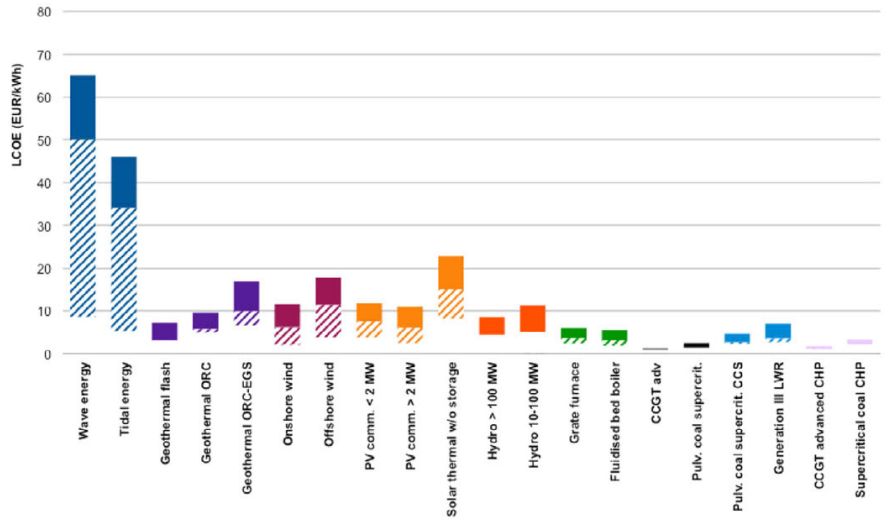

Figure 1.2: LCOE for alternative and conventional energy technologies. Solid bars indicate current cost ranges, while shaded bars indicate expected future cost reductions. (Magagna and Uihlein, 2015)

wave in the presence of the array. Yet shall refer to the *near-field* when discussing the power output and the geometric layout of an array of WECs, because the *near-field* wave field is the chief determinant of the economic viability of a WEC array project via the aforementioned parameters. When referring to the *far-field*, we refer to the modification of the wave field away from a given WEC array and to the effects on the surroundings of the immediate project area. As an example, the *far-field* effects of WEC arrays could potentially modify the sediment transport and beach profile of the surrounding coastline by modifying the strength, direction, and spectral distribution of the incoming wave energy. These consequences can be both beneficial, such as reducing the erosion rates along a section of a coastline. They can also be deleterious by creating unforeseen changes in the long-shore sediment transport. They can also be used for benefit in reducing the wave energy in offshore wind farms and coastal infrastructure which improves the economic operation of the two.

As a result of the monetary and temporal expense of setting up an experimental investigation into WEC array effects, the primary tools in simulating WEC farm effects are numerical models. Still, given the numerous variables influencing the hydrodynamic interactions in a WEC array, the numerical modelling of the 'array effects' is no trivial matter. A balance must therefore be struck between the accuracy of modelling a given phenomena with the speed and computational power of the calculation.

In this thesis, this balance is achieved via 'coupling', that is incorporating information from a high-resolution, computationally intensive model utilized in the near-field into a lower resolution but faster model that is applicable to a larger

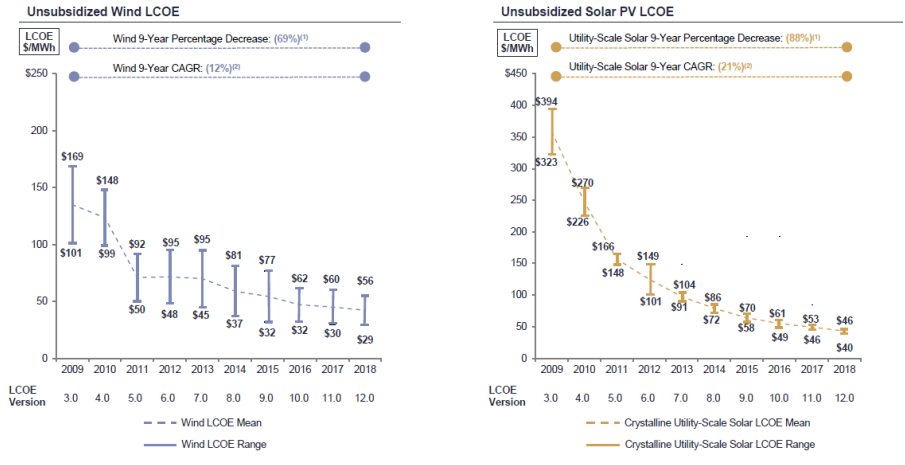

Figure 1.3: Exponential Reductions in the LCOE of wind (left) and solar (right) electricity generation (Lazard, 2018)

domain in the far-field. Such a hybrid model can therefore be used as part of an economic and environmental assessment of a 'WEC array' that is a technical requirement for setting up a commercial wave energy project. Note, however, that an assessment of the WEC array of farm operating in high sea states in what would be considered 'survival mode' is outside the scope of this thesis. Therefore, the chosen modelled sea states reflect this restriction. Consequently, phenomena that tends to occur in high sea states such as overtopping or vortex shedding is not given consideration here.

A note on the WEC array configurations utilized in this thesis. Since an optimization of a WEC array is not one of the objectives of the present thesis, it was deemed appropriate to choose one array configuration and apply it to the various scenarios of the chapters. The rationale for the modelling of a smaller 5 m radius heaving cylindrical WEC in Chapter 4 and Chapter 5 while selecting a larger 10 m radius heaving cylindrical WEC in Chapter 6 was motivated by the need to directly compare the heaving cylindrical WEC to an OSWEC. Since the target OSWEC chosen for this thesis has a specific width of 20 m based on a promising commercial prototype (AW-Energy Oy, 2019), it was deemed appropriate to select a heaving cylindrical WEC of similar dimensions, especially in light of the fact that this WEC also corresponds to a pre-commercial design Carengie Clean Energy (2018).

1.3 Objectives

The main target of the work introduced in this thesis is to address the knowledge gap in the numerical modelling of WEC arrays used to resolve the related economical and environmental impacts in a cost-effective manner. The secondary target is the development of a suite of models to fill the above knowledge gap that are

able to perform the task in a timely and computationally efficient manner with the inclusion of a PTO system model. It is the hope that the knowledge presented in this thesis will contribute to the reduction in the cost of electricity derived from waves. This has been achieved via an improved siting and arrangement of WECs in farms. This also enables the reduction of uncertainties in environmental planning due to potential spatial conflicts of interest.

1. One-way coupling between a Boundary Element Method (BEM) Wave Structure Interaction (WSI) solver and a wave propagation model;
   A linear coupling methodology between the WSI solver NEMOH and the wave propagation model MILDwave was developed. This allows the user to model linear wave-structure interactions of WECs and WEC arrays in the near-field and propagate the resulting wave transformations in a large domain with variable bathymetry in the far-field.

2. Introduction of an iterative additive scheme for calculating the perturbed wave fields in a WEC array;
   A sequential, arbitrary-order precise method is developed for calculating the perturbed, *i.e.* radiated and diffracted, wave fields in a WEC array.

3. Development of a time-domain model for the PTO system to calculate the WEC motions and power output in a WEC array;
   A time-domain mechanical model of the PTO system is developed in the dynamical solver WEC-Sim for an efficient model of a hydraulic PTO system.

4. Coupling of the time-domain PTO solver into the WSI solver - wave propagation Wave-to Wire (W2W) coupled model suite;
   A time-domain PTO system model is coupled into the WSI-wave propagation model suite to enable the simulation of the 'near-field' and 'far-field' effects of a WEC array with a realistic hydraulic PTO system.

   To achieve objectives 1-4, an updated version of the wave propagation model MILDwave was developed integrating the one-way coupling into the graphical user interface (GUI)-enabled and the command line (CLI) MILDwave software packages. Furthermore an extensive set of operational and data manipulation scripts were written in the Python scientific computing language.

1.4 Layout of Thesis

The remainder of the thesis is structured as follows:

Chapter 2 is a comprehensive state-of-the-art review on numerical and experimental modelling of WEC farms or arrays. The fundamentals behind wave energy conversion under the auspice of linear potential flow are presented in Chapter 3. The focus of Chapter 4 is on introducing the coupling methodology that is utilized in achieving the results in the subsequent chapters of the thesis. Chapter 5 explores the various facets influencing the WEC farm power output and WEC farm wave field using the coupling methodology of Chapter 4. Chapter 6 details the development of a realistic time-domain PTO system module and its application to WEC

farm modelling via its coupling to the WSI solver. In Chapter 7, the advancements of the previous chapters are joined in the complete W2W model. The model is then used to simulate a real WEC array project utilizing wave data and bathymetric profiles from an actual project site off the coast of Bretagne in France. Finally, a summary of the work related in this thesis and vectors for future research are given in Chapter 8.

Chapter 2

A Review of Hydrodynamic Modelling of WEC Arrays

Abstract

As a result of the large number of interdependent variables and a computational time that rapidly increases with the number of interacting WECs modelled, simulating the hydrodynamics of WEC arrays or farms puts forth a unique set of challenges to both the numerical modeller and experimenter. In this chapter a comprehensive review is presented of the different techniques to resolve hydrodynamic interactions in an array of WECs is given. The review begins with a historical perspective that traces the development of analytical and numerical techniques in tandem with improving computational power. Four analytical approximations that have shaped the development of WEC array research are highlighted. The increasing sophistication of numerical methods starting with grossly simplified linear models to a more and more realistic scenarios is traced. Finally the move towards non-linear approaches which are becoming commonplace in WEC hydrodynamic modelling is examined. The complementary topics of WEC array geometry optimization and WEC array control are commented. Following that a review the multitude of studies devoted to measuring the coastal impacts of WEC arrays and extra-hydrodynamic parameters related to WEC array deployment is performed. The review is terminated with a look at major European funding efforts in accelerating WEC array research and development and the major takeaways from the review are given in the conclusion.

2.1 Introduction

The first pre-commercial Wave Energy converter (WEC) arrays have been deployed and several commercial WEC array projects are in project development stages. Therefore, the topic of WEC arrays is getting increasing attention from funding agencies and numerous research groups in the UK, Europe and the US (Greaves and Iglesias, 2019). However, even though many aspects of the complicated problem of quantifying the power capture in an array of WECs have recently been looked at; there are still many urgent questions that need to be answered. In this chapter, an extensive review of the state-of-the-art on WEC array modelling is presented. The focus on the evolution of numerical modelling as computer technologies have improved and enabled the transition away from purely linear modelling. The first part of the chapter is devoted to presenting the analytical, numerical, and experimental approaches to WEC array modelling. The second part of the chapter hones in on the applications of the aforementioned modelling techniques, with a specific focus on array layout optimization studies and investigations into the coastal impacts of WEC arrays. Section 2.2, gives a brief historical overview of WEC array modelling, Section 2.3 details analytic methods in solving WEC array hydrodynamics, and Section 2.5 and 2.6 look at the numerical and experimental approaches to the WEC array hydrodynamic problem. Section 2.7 highlights those investigations focusing on array layout and optimization, and Section 2.8 explores the related WEC array control problem and recent work therein. In Section 2.9, those investigations measuring the coastal impacts of WEC arrays including those on offshore wind farms are examined. The research in moorings, grid connection issues and power smoothing of WEC arrays is summarized in Section 2.10, and the societal perceptions of WEC array projects in Section 2.11. Finally Section 2.13, remarks on the arc of research and makes some general conclusions about the key findings of WEC array research and identify key gaps yet to be filled.

2.2 Brief Historical Overview

Even though the idea for wave energy conversion has existed since the late 18th century, it was not until the 1973 oil crisis that a rigorous research programme was undertaken to study the emerging discipline of wave energy conversion. In 1974 Stephen Salter from the University of Edinburgh introduced the *Salter's duck* which was shown to absorb 100% of the incoming wave energy in a series of experiments.

In 1975 Johannes Falnes and colleague Kjell Budal introduced the concept of a *Point Absorber i.e.* a heaving WEC with a scale much smaller than the incoming wave; they also introduced the concept of *capture width* as a proxy for efficiency (Budal and Falnes, 1975). A year later, at the Massachusetts Institute of Technology in the US, J.N. Newman and C.C. Mei independently published theoretical results which linked ship hydrodynamics to the principle of wave energy conversion (Mei, 1976; Newman, 1977). The same was done by Evans (1976) at Bristol University in the UK. Their publications were the first to apply the equations of Linear Potential Flow Theory to a Wave Energy Converter (WEC). While much

more detail has been gleaned on the various aspects of wave energy conversion, the fundamental principles and equations put forth by Budal and Falnes (1975); Mei (1976); Newman (1977); Evans (1976) are still the foundations of the theory of wave energy conversion more than 40 years later. The history of WEC arrays, *i.e.* a wave energy plant consisting of multiple WECs deployed in a geographic area, also began in late 1970s. While Salter conceptualized an array of *Salter Ducks* in a *Nature* article (Salter, 1974), the first attempt to describe the hydrodynamics of a fully interactive WEC array was done by Budal (1977). He was also the first to introduce the array interaction factor $q - value$ as a benchmark measurement for array power capture. In simplest terms the $q - value$ is the ratio between the power produced by an array to the power produced by the same number of WECs operating in isolation or:

$$\text{q-value} = \frac{\text{Power converted by array}}{\text{Power converted by the same number isolated WECs}} \tag{2.1}$$

Budal, however, made the invalid assumption that all WECs must oscillate with equal amplitudes. This assumption was proven inadequate by Falnes (1980) while Evans (1979) independently arrived at the same result as Falnes. A few years later both Falnes and Budal (1982) and Thomas and Evans (1981) showed that an array configuration can significantly increase power capture over that of isolated WECs. A few commercial array projects were proposed by Budal et al. (1982) in Norway and by Salter in 1983 (Thorpe, 1999). However, because of the oil glut of the 1980s and a strong concurrent push for nuclear power in the UK, these projects were cancelled and funding for research into arrays and into wave energy in general was severely curtailed with a nadir occurring around 1990 (Babarit, 2017). The majority of research carried out in the next 15 years on arrays of floating bodies was on structures other than WECs, still, some of the results were applied to the problem of WEC arrays, *e.g.* (Kagemoto and Yue, 1986; Mavrakos and Koumoutsakos, 1987; McIver, 1994). By the early 2000s, with increasing oil prices and the threat of climate change renewing an interest in all forms of alternative energy, wave energy conversion, and by extension WEC array research was put back on the funding agenda of government agencies around the world (see Section 2.12 for details on a subset). Coupled with a rapid increase in computing power that enabled complicated hydrodynamics to be accurately resolved, an increasing body of research began to be published in the topic, especially toward the start of the current decade. For example, the number of papers submitted to the bi-annual European Wave and Tidal Energy conference, the pre-eminent forum in the field more than doubled from 2005 to 2019 (European Wave and Tidal Energy Conference, 2019).

2.3 Analytical Approaches to Solving WEC Array Hydrodynamic Interactions

The problem of calculating the power absorption of an array of WECs in a realistic deployment scenario requires not only the complete knowledge of the hydrodynamics of each individual WEC, but also knowledge of the scattering and radiation

effects between all WECs in the array as well as interactions with mooring systems and bathymetry. Therefore, except for a few special cases such as a truncated cylinder and a sphere, the power absorption equation cannot be fully solved analytically without making simplifying assumptions about the shape of the bodies and the hydrodynamic and mechanical forces in play. Even with the availability of powerful computers, a solution without gross simplifications is only tractable for arrays with a maximum of a few WECs. As the number of WECs increases, the equations become fundamentally more difficult to solve. Thus the numerical complexity necessitates analytical simplifications even when applying numerical methods (Newman, 2001). Thus, historically, resolving WEC array hydrodynamics was done with analytic simplifications, the most commonly used ones of which are detailed in Sections 2.3.1 to 2.3.4. A number of these methods continue to be used today to elucidate parts of the problem that are not readily clarified by numerical means. Also, a hybrid approach described as *semi-analytic*, one that solves part of the WEC array hydrodynamic equations numerically and part analytically, is a more recent concept that builds on the analytical approaches outlined below in Sections 2.3.1 to 2.3.3. Semi-analytic methods are reviewed in Section 2.4.

2.3.1 The Point Absorber Method

The first analytical method to be introduced chronologically is the *point-absorber* approximation, introduced by Budal (1977). Its main assumption is that the scattered or diffracted waves are negligible, which occurs when the wavelength is much longer than the WEC dimensions. This assumption was used to test the basic framework of the theory in the first wave of papers on the subject, in the late 1970s and early 1980s, mainly for simplified examples of linear arrays of heaving cylindrical WECs. The approximation is capable of calculating the optimal power absorption of an array regardless of individual WEC geometry, but is not capable of doing so with the motions within the limits of linear wave theory. This results in solutions with unrealistic WEC displacements, as shown in Thomas and Evans (1981). To tackle this problem, an analytical method of placing restrictions on body motion was developed by Evans (1981) and extended by Pizer (1993). However the *point absorber* formulation requires knowledge of the hydrodynamic properties of the bodies in order to calculate radiation and absorption, which cannot be calculated analytically except for a few special cases. Still, as a number of WECs under development today fit the criteria for the validity of the theory, point-absorber approximation is a useful tool for WEC array analysis. For example, it has recently been used in the optimization of array geometry in Fitzgerald and Thomas (2007) and to optimize the positions of WECs in an array in irregular waves (Folley and Whittaker, 2009b). In a study on array layout configuration, Ricci et al. (2007) compared the point-absorber approximation with a numerical method, obtaining favourable agreement for a range of sea states.

2.3.2 The Plane Wave Method

Introduced by Simon (1982) and expanded by McIver and Evans (1984), the *plane wave* method assumes that the diverging wave scattered from a cylinder is a plane wave of appropriate amplitude in the vicinity of another cylinder in the WEC array. In contrast to the point absorber approximation the plane wave method assumes wide spacing between the WECs in the array, *i.e.* of the order of several wavelengths. Also, unlike the point-absorber method, the plane wave approximation takes scattering into account. It has particular validity for large WECs where the size of the structure naturally creates outgoing waves more closely resembling a plane wave than for a small WEC. In this respect the plane wave method is applicable in situations where the Point Absorber method is not, and vice-versa. A sensitivity analysis for the application of the plane wave method was performed by McIver (1994).

2.3.3 The Multiple Scattering Method

The *multiple-scattering* method is another analytical procedure first used to calculate the scattering and radiation of surface waves on floating structures in Okhusu (1974). The method considers interaction as a series of scattering events for which the amplitude of the scattered wave decreases with each iteration, enabling a truncation to be made at a desired accuracy. Using this approach, Mavrakos and Koumoutsakos (1987) solved the scattering problem, and Mavrakos (1991) solved the radiation problem. The method was applied in the context of WEC arrays by McIver et al. (1996) and Mavrakos and McIver (1997); both groups compared the multiple-scattering method to the plane wave and point absorber approximations. A big benefit of the method is that it enables a considerable reduction of both computing time and storage requirements. This is due to the fact that the formulation enables the successive satisfaction of the imposed boundary conditions on each body of the arrangement (Mavrakos, 1991). The *multiple scattering* method is in principle accurate to an arbitrary precision, depending on where the series representation is truncated. Nonetheless, it has an important drawback in the need for single-body hydrodynamic characteristics that can only be calculated for a simplified system without resorting to a numerical method, because the individual body hydrodynamics must be known.

The point absorber, plane wave and multiple scattering methods were compared for a linear array of 5 vertical cylinders by Mavrakos and McIver (1997). As expected, the authors found that the point absorber approximation brakes down for large values of kd where k is the wave number and d is the magnitude of the intra-array spacing. By contrast, they observed that the plane wave approximation, in addition to the wide-spacing regime, also works for closely-spaced configurations. These in fact violate the original assumptions behind the theory, calculating the hydrodynamic forces down to a dimensionless wave number $kd = 0.4$ within 5% of the more accurate multiple scattering method. The authors conclude that for most circumstances of practical interest the hydrodynamic forces can be calculated using the plane wave approximation. However, they caution that the errors might

be amplified for a greater number of cylinders than the five considered in their study (Mavrakos and McIver, 1997).

2.3.4 The Direct Matrix method

A procedure similar to the multiple scattering method, often termed the *direct matrix* method, was presented by Kagemoto and Yue (1986). This is an exact algebraic method within the framework of linear theory, subject to truncation of an infinite sum. The interaction of the bodies is accounted for by taking the scattered wave of each body to be the incident wave upon all other bodies in addition to the ambient incident wave (Kagemoto and Yue, 1986). Doing this for all bodies the authors were able to solve for the coefficients of the scattered wave fields of all bodies simultaneously. The authors extended the approach to radiation in (Kagemoto and Yue, 1993). A solution for a truncated cylinder, one of the most common WEC shapes, was provided by Yilmaz and Incecik (1998). This result along with a model for the power take-off (PTO) was used in Eriksson et al. (2005) to resolve a cylinder connected to a linear generator and this result was incorporated into the approach of Child and Venugopal (2007, 2008) where the authors analysed several configurations of arrays of floating cylinders. A drawback of this particular approach is the need for solutions to the diffraction transfer matrix of the particular body considered, again necessitating resorting to a numerical method for all but the simplest body shapes.

2.4 Semi-Analytic Methods

A limitation of the methods presented in Section 2.3 is that a complete analytical solution is possible only in the case of the simplest geometrical shape such as a truncated cylinder or a sphere moving in only one degree of freedom. Most real WEC concepts however, consist of one or more bodies of more complex geometry. Moreover, the simulation of a realistic PTO, mooring forces or any motion restrictions necessarily introduced non-linearities into the system which cannot be solved with pure analytics. However, having an analytical framework clarifies the underlying physics of the problem which is not always possible with a purely numerical solution. It also speeds up the numerical calculations even in the cases where a fully analytic solution is not possible. The logical step therefore is a combination of numerical and analytical methods in what are often termed *semi-analytic* methods or approaches. Most of the work builds on the direct matrix described in Section 2.3.4 where the hydrodynamics of the individual WECs in the array are solved numerically. Such an approach was undertaken by Child and Venugopal (2010); Child et al. (2011), who investigated the optimal configurations of a 5-WEC array of cylinders. A semi-analytic method has also been tackled in Wolgamot et al. (2012) to investigate the directional sensitivity of a 3-cylinder WEC array and in Wolgamot et al. (2016) to investigate WEC array second order effects. A new method based on the direct matrix approach was introduced by McNatt et al. (2013) that calculated the cylindrical field around WECs to investigate WEC array interactions. The

concept of a diffraction transfer matrix was introduced in (McNatt et al., 2015) to enable the calculation of interactions for large arrays of WECs without recourse to Boundary Element Methods (BEM), described in the next section. A recent investigation compared two different semi-analytic approaches utilizing the direct matrix method in Flavià et al. (2018). In contrast, Singh and Babarit (2013), coupled a BEM solver with the plane-wave approximation introduced in Section 2.3.2. Wolgamot et al. (2016) utilized a semi-analytic method to investigate second-order effects in an array of 4 cylindrical heaving WECs, becoming one of the first research groups to do so.

Finally, the multiple scattering method introduced in Section 2.3.3 was utilized by Göteman et al. (2018) as part of a semi-analytic approach of large arrays of point absorber WECs in short-crested waves. Outside of the canonical heaving cylindrical WEC, the only other common WEC type amenable to a semi-analytic solution is the Oscillating Surging WEC (OSWEC). An analytical model for a single OSWEC in a channel was developed in Renzi and Dias (2012) and extended to an array of 3 WECs in Renzi and Dias (2013) via a numerical solution of the potential equation. Similar work was performed by Sammarco et al. (2013); Michele et al. (2015) which analysed a OSWEC-type WEC array consisting of multiple surging flaps arranged in multiple rows for the optimal wave energy production.

2.5 Numerical Methods

As mentioned in Section 2.3, analytical methods have a limited applicability for realistic WEC array investigations. As we will witness in Section 2.6, experimental methods are generally too costly and time consuming. Consequently, since the time of the earliest computer programmes capable of solving systems of differential equations in a timely manner, numerical models have been the WEC array researcher's workhorse since roughly the 1990s.

The vast majority of WEC array investigations to date have been performed using numerical approaches. While numerical tools enable the calculation of a large number of WEC array scenarios and moreover are making stunning progress in terms of the difficulty of the numerical problems they can resolve, it is important to be aware of the limitation of the scope and application of each model. It is with this view that we we will explore the development of numerical methods for calculating the hydrodynamics of WEC arrays and the associated systems.

2.5.1 Frequency-domain Methods

While numerical methods have been used in marine hydrodynamics since the earliest days of numerical computation, only relatively recently have advances in computer technology made possible the direct numerical simulations of arrays of WECs. Since the earliest numerical investigations of WEC array hydrodynamics in the 1990s, linear models have been the simulation tool of an overwhelming number of publications, with the balance only recently tilting toward non-linear modelling approaches. Of all linear methods, the *Boundary Element Method* abbreviated

as BEM, an algorithm based on solving Green's functions on a discretised wetted body surfaces, is the still the most widely used numerical method (for the present application see Section 4.2.1). The application of BEM to the radiation-diffraction problem essentially requires a mesh of only the boundary of the domain, and the determination of the boundary condition on the wetted surface(s). Results produced by BEM are calculated in the frequency-domain and thus are time invariant. For a comprehensive overview of the BEM method and its application see (Lee and Newman, 2005). A number of commercial software packages exist for applying the BEM to wave-structure interaction like WAMIT®, originally developed by the Massachusetts Institute of Technology (WAMIT inc., 2019), ANSYS Aqwa (ANSYS inc., 2019) and Dynaflow 3DynaFS-BEM (Dynaflow, inc., 2019). A number of software packages have also been developed by research institutions, particularly AQUADYN and AQUAPLUS at the École Centrale de Nantes in France (Delhommeau, 1993), which formed the basis of the most commonly used open source BEM tool NEMOH (École Centrale de Nantes, 2019).

The full gamut of studies that utilise BEM in WEC array modelling is too numerous to list here. It is safe to say that the large majority of existing results on the topics explored in this thesis have been obtained via BEM. As we shall be using the open-source BEM code NEMOH in the body of the thesis, it is prudent to mention here the studies which have utilized NEMOH in gathering the results of WEC array hydrodynamics, namely (Verbrugghe et al., 2016, 2017b; Ruiz et al., 2017b; Balitsky et al., 2017a; Verao Fernandez et al., 2017; Balitsky et al., 2018b,a; Tomey-Bozo et al., 2016, 2019; Flavià et al., 2018).

Although BEM methods are computationally intensive for large WEC arrays (those containing 10s to 100s of individual WECs), there have been several attempts in recent years to rectify the issue. One line of research is an improvement in the way that the equations resolved by the BEM are calculated to better take advantage of computer processors. This development has been investigated in (Taghipour et al., 2008; Borgarino et al., 2011a). The second way of solving the WEC array problem has been described in Section 2.4, where BEM is combined with an analytic method to optimize calculation.

2.5.2 Time-domain Methods

For tractability of calculations, all the analytic methods of Section 2.3 and a plurality of the BEM methods of Section 2.5.1 utilize a frequency-domain formulation for the calculation of hydrodynamic effects. While this is a useful tool, especially with regards to mapping overall trends in WEC array behaviour, this method precludes modelling a time-variant system as well as a non-linear one. Therefore, despite the increased complexity, a number of papers utilizing linear or quasi-linear time-domain calculations in the area of WEC array modelling have been published in the past two decades. It is important to note that one of the processes *i.e.* not correctly resolved in the frequency-domain implementation is non-linear control. As we shall see in Section 2.8, a majority of existing WEC technologies use non-linear control to improve WEC performance. As a consequence the greatest need for WEC array time-domain models is to correctly simulate the effect of such

control schemes on WEC arrays. In addition to the aforementioned benefits, the time-domain formulation enables the modelling of non-linear forces such as viscous damping and inertia, PTO friction forces, as well as mooring forces.

The most common way of resolving WEC array equations in the time-domain is based on the integro-differential Cummins equation method (Cummins, 1962), where the steady state responses are calculated *a priori* in a BEM solver. Some of the investigations utilizing this method in investigating WEC arrays are (Vicente et al., 2010; Bacelli et al., 2013; Balitsky et al., 2014; Garcia Rosa et al., 2015). A recent extension to the method incorporating non-linear Froude-Krylov forces has been developed in (Merigaud et al., 2012; Peñalba Retes et al., 2015). It can be noted that the increase in computational time is well justified by the improved calculation of motion for large sea states, which in turn enables a more accurate estimate of power production (Merigaud et al., 2012).

2.5.3 CFD Methods

As computer power escalates, more realistic and complex modelling scenarios are starting to be resolved within a reasonable time frame. In the field of hydrodynamics, this means a gradual movement away from a purely linear computer modelling with its set of limitations as mentioned in Section 3.8.4 in Chapter 3. Interest is turned to modelling non-linear hydrodynamics which more closely approximate the full Navier-Stokes equations of fluid motion. The most common method of modelling non-linear WEC hydrodynamics is Computational Fluid Dynamics abbreviated as CFD. Broadly speaking it is a class of solvers that resolve the Navier-Stokes equations over a domain which is discretised or meshed via different methods.

The accuracy of the solution depends on the refinement of the mesh and the approximations that are made to enable closure of the problem. One of the common issues with CFD modelling is that of accurately simulating turbulent effects. Recent progress has been made by Devolder et al. (2018b) with regards to a turbulence closing scheme for breaking wave simulations, a subject pertinent to studying WECs in extreme conditions. While an ever-larger number of investigations have been looking at single WEC hydrodynamics via CFD modelling, only a few have looked at the behaviour of WEC arrays, given the formidable complexity of the multi-body non-linear problem. One of the first was by Agamloh et al. (2008), who presented results from a 2-WEC array in a numerical test tank. McCallum (2017) investigated a linear array of 5 WECs of the point absorber type for viscosity and non-linear effects due to the body shape. A similar approach was taken in Devolder et al. (2017, 2018a) where a 5-WEC array configuration was examined in the open-source CFD package OpenFOAM and compared to experimental results from (Stratigaki et al., 2014; Stratigaki, 2014). The aforementioned investigations use the open-source CFD solver called OpenFOAM which solve Reynolds Averaged Navier-Stokes (RANS) equations for two incompressible, isothermal, immiscible fluids using a Volume Of Fluid (VOF)-based interface. Recently, results were published in (Bharath, 2018) which studied the non-linearities in a 2-WEC and a 4-WEC array of submerged cylindrical spheres in a CFD-based numerical

tank. The author finds that for the WEC array configurations investigated, the benefits to power output of the linearly-optimized WEC array configuration are not mirrored in the CFD results. A comprehensive review of CFD-based non-linear methods in WEC analysis was published in Windt et al. (2018).

2.5.4 Lagrangian methods

Lagrangian methods are a class of numerical schemes which are particle-following. That is unlike running the calculations over a fixed or malleable mesh as is done in CFD methods. A Lagrangian solver calculates the trajectory of each particle in a fluid at every time step Δt. Given that the number of particles in a realistic simulation of one floating moving body is on the order of one million, only recently has computer power, specifically in the form of fast GPU (Graphical Processing Units), allowed the simulation of WEC hydrodynamics using Lagrangian Methods. The most commonly used Lagrangian solver is the Smoothed Particle Hydrodynamics (SPH) method DualSPHyics (Crespo et al., 2015), which has been used to model WECs such as the multi-buoy Wavestar (Canelas et al., 2018), an Oscillating Surge WEC (OSWEC) (Brito et al., 2016), and an Oscillating Water Column (OWC) (Crespo et al., 2018). Although as of the writing of this thesis, no results have been published on modelling arrays of WECs with DualSPHysics, a recent investigation proposed coupling DualSPHysics with a wave propagation model in order to simulate WEC arrays (Verbrugghe et al., 2017a, 2018).

2.5.5 Phase-averaged wave propagation models

On the other end of the model precision spectrum from non-linear particle following models are spectral models that are usually used to study coastal effects. These models are deployed in medium size basins on the order of tens of kilometres spectral model assume that the dynamics can be separated into a set of orthogonal frequency components. As a consequence, they are phase-averaged wave propagation models. The basis of spectral models is the conservation of energy, thus all wave interaction effects in an array must be formulated so that a net loss or gain of energy is represented. SWAN (Simulating WAves Nearshore), an open-source code originally developed at TU Delft is by far the most used model in studies of WEC array hydrodynamics (Booij et al., 1999). SWAN has been used to simulate WEC array dynamics, specifically the impacts of arrays on the near-shore wave field in an extensive number of investigations (Millar et al., 2007; Venugopal and Smith, 2007; Smith et al., 2007; Alexandre et al., 2009; Smith et al., 2012; Oskamp and Ozkan-Haller, 2010; O'Dea et al., 2018; Stokes and Conley, 2018). The commercial spectral model MIKE21SW was utilized in analysing the wave energy potential off the north-west coast of Sardinia, Italy in Vicinanza et al. (2013). Significant limitations of spectral models vis-a-vis WEC arrays is their coarse resolution, phase independence, and the modelling of a WEC as an absorber at every frequency in the spectrum. The latter limitation has been in part rectified via a frequency dependent absorption coefficient in (Smith et al., 2012) and (Ruehl et al., 2013). Other spectral models such as TOMAWAC and Delft3D-WAVE exist but have less

presence in the WEC array literature (Folley et al., 2012). The biggest advantage of spectral models is the computational efficiency when compared with potential flow methods, their usefulness in modelling very large WEC arrays (hundreds of elements), and the coupling of array effects into models that represent coastal processes (Folley and Whittaker, 2010). Spectral models have recently been used to model the effects of interactions in arrays of WECs for a linear array of WECs (Alexandre et al., 2009) as well as staggered configurations (Oskamp and Ozkan-Haller, 2010).

2.5.6 Phase-resolving wave propagation models

An important class of numerical models used in simulating WEC arrays are phase-resolving models. Generally these models solve a simplified version of the Navier-Stokes equations making certain assumptions about the physics of the hydrodynamical problem. The first class of models are known as mild-slope because of the assumption of a slowly changing bathymetry in the governing equations. The mild-slope equation model MILDwave, developed at Ghent University over the past 20 years (see Section 4.2.2 in Chapter 4), has been used for the last 15 years in a number of studies on WEC arrays, their environmental impacts and economic performance. In (Beels et al., 2010), a modified 'sponge layer' technique was developed which enabled MILDwave to model frequency-dependent obstacles that mimic WECs or compact WEC array. This work was extended in Beels et al. (2011) to add a cost function to model the economic performance of a WEC array of overtopping WECs. This line of work was continued in Stratigaki (2014, 2019) where the semi-permeable obstacle technique of Beels et al. (2010) was compared to the result of coupling MILDwave with the BEM solver WAMIT. Moreover, Stratigaki et al. (2011) investigated the effect of wind re-generation behind WEC arrays by adding a wind energy addition term in MILDwave. A summary of the intrinsic modelling of WECs and WEC arrays in MILDwave is provided in Troch and Stratigaki (2016). A novel coupling technique with the BEM solver NEMOH was introduced in (Balitsky et al., 2017b) and applied to a study of the array effects of heaving Point Absorbers and OSWECs in Verao Fernandez et al. (2017); Balitsky et al. (2017a). The coupling technique was combined with an iterative approach to calculate the power output of a WEC array in Balitsky et al. (2017a, 2018b) and compared to experimental results for a WEC array in Verao Fernandez et al. (2018) for the *far-field* effects. Further studies on the impact of arrays of OSWECs utilizing an alternate coupling methodology were conducted in Tomey-Bozo et al. (2016, 2019). An alternative mild-slope model REFDIF was used to study the impact of a WEC array of the terminator type on the Portuguese coast in Palha et al. (2010). The limitations of the particular model only allowed for bulk absorption coefficients and for simulating regular waves.

The open-source SWASH model, developed by TU Delft in the Netherlands, is another class of coastal wave propagation models which solve the non-linear non-hydrostatic shallow water equations This model has been recently utilized for investigating the impact of a WEC array consisting of submerged cylindrical WECs in (Rijnsdorp et al., 2017, 2018). The 3-D fully integrated wave propagation

model OceanWave3D has been used via a coupling methodology with NEMOH in a number of recent publications (Verbrugghe et al., 2016, 2017b) to model an array of cylindrical WECs. A validation with experimental data of Stratigaki et al. (2013, 2014) was performed in (Verbrugghe et al., 2017a).

Another class of non-linear wave propagation models called Boussinesq models, based on their canonical equations has been used to model the effects of an array of WECs in (Venugopal and Smith, 2007). Two studies were conducted using the Boussinesq model MIKE21BW to model an array of small floating barge WECs (Angelelli et al., 2012; Angelelli and Zanuttigh, 2012) and compared with experimental data. The authors found that the model provided a much more faithful representation of transmission coefficients, with a less than 3.5% difference whilst a significant difference in the reflection coefficients of 16 to 34 %. In addition, recently the performance of a Boussinesq model in reproducing array effects was compared to that of a spectral model in (Greenwood et al., 2016). A review of mild-slope and Boussinesq models for wave energy conversion studies is given in Folley et al. (2012).

2.6 WEC Array Experimental Methods

One of the biggest research gaps in the wave energy literature is a lack of experimental data of multiple WECs,*i.e.* WEC array experiments. Because of the substantial resources and large dimensions of the basin required to host such an experiment, there exist only a few experimental databases of experimental analysis of WEC array effects. Apart from several small scale (1:70) experiments performed at Manchester University in the UK, involving a line row of 5 heaving WECs (Bellew and Stallard, 2010) and a rectangular configuration of 12 heaving WECs (Weller et al., 2010), there were no publicly available experimental WEC array datasets available until the 2010s.

Two large (1:20 and 1:25 scale experiments, respectively) WEC array tests designed specifically to experimentally measure the WEC array effects, took place in the early part of the decade. The first experiment, named PerAWaT, was conducted at the large basin of Queens University Belfast in Portaferry, Northern Ireland (Folley and Whittaker, 2013). It involved 22-24 heaving cylindrical WECs arranged in 3 different staggered configurations; the design of the WEC was similar to the one utilized in the WECwakes experiment. The second experiment, entitled WECwakes, performed at the DHI large basin, modelled up to 25 heaving buoys arranged in various configurations (Stratigaki et al., 2014, 2015). The WECwakes buoy was constrained to move in heave by a rigid shaft and the PTO mechanism was modelled as a friction brake (Stratigaki et al., 2013). The change in the wave field was measured by a network of wave gauges and compared with numerical predictions in (Stratigaki, 2014). The WECwakes data are publicly available based on the funding agency protocol. A further WEC array test at Portaferry involved an experimental investigation utilizing a 1:25 scale fixed OWC arranged in 4 different reconfigurations (O'Boyle et al., 2017). A similar experiment involving 5 scaled OWC models is in the active phase at the O.S. Hinsdale large wave basin at

Oregon State University in the USA. Finally, in the year 2020, upon the completion of the Coastal and Ocean Basin in Oostende, Belgium (Troch et al., 2018), Ghent University will conduct a set of WEC Array experiments with a 1:20 scale heaving WEC with an adjustable PTO designed to mimic successful commercial WEC designs Vervaet et al. (2019).

2.7 WEC Array Configuration and Optimization

For a given wave energy project, the most important variable in determining its economic validity is the WEC array power output. Because of hydrodynamic interactions between the WEC array units, one of the key factors influencing the power output is the array geometrical layout or configuration. The positioning of individual elements in an array has been acknowledged by many authors to have a significant effect on power production. In the 1980s and early 1990s, Falnes (1980), Budal et al. (1982), and Thomas and Evans (1981) showed the geometric layout to have a significant impact on the $q - value$, Eq. (2.1), acknowledging that the layout created phase differences in the radiated and scattered waves that lead to this phenomena. However, their investigations were limited by the technological constraints of the time to analytical models. Consequently the researchers were only able to consider equally spaced linear arrays of heaving point absorbers in regular waves that limited their applicability to realistic WEC array scenarios.

2.7.1 WEC array layout configuration studies

With improvement in modelling techniques, more recent investigations have considered different WEC shapes, modes of motions, irregular array geometries and finally true algorithmic optimizations with the algorithm selecting from a 2-D grid. In the first category, McIver (1994) compared a linear array of five heaving cylinders, with equal and unequal spacing between the WECs, noting that the latter offers performance benefits by smoothing out large differences in power output. Stansby et al. (2015) also investigated a line configuration of a 3-WEC array, but with bodies of different shapes and thus resonance bands. The study found that such a hydrodynamically complex system indicates high overall capture widths in irregular waves across a range of peak periods without damping optimisation. Ricci et al. (2006) investigated three different configurations of heaving cylinders for regular and irregular sea, acknowledging the role of layout, but concluding that without a directional spectra for the exciting waves their results have a limited application. The study of Ricci et al. (2007) followed up the previous investigation with a look at the performance of two 5-WEC arrays of heaving cylinders in a spectral wave climate off the Portuguese west coast. The investigators established the sensitivity of the configurations to wave spreading as well as concluding that the effects on array performance with intra-array spacing d larger than 4 WEC diameters can be neglected. More recent investigations by Wolgamot et al. (2011, 2012), also considered a 3-WEC array, but with four different configurations. As well as looking at axisymmetric heaving WECs, the authors looked at surge and sway motion as

well as at arbitrarily shaped bodies. They determined that matching the width of a peak in the $q-value$ curve to the range of expected incident wave directions would be a valuable consideration for a new array. At the same time they acknowledged that the results need to be shown for cases other than the regular sea input that they considered.

Babarit (2010) studied the influence of the array inter-WEC spacing on the power output of a 2-WEC array of heaving cylinders and surging barges. Investigating a range of distances from 110m up to 20km, for a number of wave incidence angles β, he concluded that at close distances the interaction is significant for both types of WECs and for all simulated angles of incidence. However, at long distances, *i.e.* up to 2 km, only the array of surging WECs aligned parallel to the incident waves exhibit significant modification of power output, with the other cases all converging within 1% of unity at a 500m distance. The author also derives an important general result which shows that for a two-WEC array, in a regular monochromatic wave, the influence of interaction on the power output decays as a function of the square root of the distance d between the WECs (Babarit, 2010). The paper by Borgarino et al. (2012), extended the approach in Babarit (2010) to two dimensions and multiple bodies, by varying d between WECs in an array first jointly, in what they term square-based arrays, and then letting both the x and y separating distance vary independently. For arrays of 9, 16, and 25 WECs, they find a general area of constructive interference *i.e.* a function of both the x and y separating distance, with a similar shape for the heading cylinder and surging barge array. Because the dependence is not the same as x and y change for the case of the 10-cylinder array, the authors note a benefit to letting both separation distances vary independently.

The same group of authors further investigated the shadowing effects in an array by first looking at a 20-WEC densely packed cluster, then by splitting the cluster into 2 clusters of ten WECs, separated by increasing distances Borgarino et al. (2012). They investigated the power output of one 10-body cluster placed in various locations behind a fixed cluster, looking at a range of sea states. In the first part of the paper, the authors concluded that there is a net benefit in splitting the clusters into two parts because as the number of rows (WECs one behind another) increases in densely placed arrays, the overall performance of the array suffers. In the second part, the authors noted a significant reduction in the wave energy immediately behind a dense cluster, indicating that separated clusters should preferably not be placed in a row, but preferably off the wave incidence axis. They note however, that the shadowing effect diminishes when directional spreading is included in the incident wave forcing.

A number of recent investigations focused on the connection between WEC array control (see Section 2.8) and layout optimization. In Garcia Rosa et al. (2015); Balitsky et al. (2014), researchers found that depending on the control strategy chosen for a given array, the optimal configurations from the point of view of power production will turn out to be quite different.

2.7.2 WEC array layout optimization studies

One of the first studies to conduct an optimization of array layout based on the objective of maximizing power production was published by Fitzgerald and Thomas (2007). The authors applied a sequential quadratic programming algorithm to arrays of three and five point absorbers in regular incident waves with a fixed wave number. They found a substantial increase in the $q-value$ for some array geometries. Indeed, by varying the angle of wave incidence, for an optimal symmetric and non-symmetric layout, they obtained a maximum $q-value$ of 2.777 and 2.746, respectively. Fitzgerald and Thomas (2007), in figure 8, where the $q-value$ is plotted for a range of incident wave directions for three array configurations (marked S for symmetrical and N for non-symmetrical), one can see a very large peak for a specific incidence angle β around 1.5π and values of $q-value$ close to unity away from that peak. The increases are impressive, showing an almost three-fold improvement in WEC power output versus an identical number of independent WECs. Yet, the authors qualify that these increases, based on unrestricted WEC motions and regular seas, would be much less dramatic if more realistic operating assumptions were made. Nonetheless the study offers valuable insight into the possibilities of using optimization and a grid-free layout for arrays of WECs. The authors also present an important consistency condition stating that in varying the angle of incidence of the incoming waves β, with regard to the array axis, a net benefit at one angle will be offset by a decrease in performance in another:

$$\frac{1}{2\pi}\int_0^{2\pi} q(\beta)d\beta = 1. \tag{2.2}$$

In effect, this states an intuitive result that an array cannot be simultaneously optimized to all incident wave directions and thus forms a natural limit for any power-maximizing algorithm. Since all wave climates have a predominant direction from which the majority of the incident energy arrives, this results points to the benefits of aligning an array to the wave direction to maximize constructive interference. This consistency condition of Eq. (2.2) was further confirmed in Wolgamot et al. (2012), where the authors investigated an array of 3 WECs for regular waves for various wave incidence angles β.

In the past decade, developments in machine learning led to the development of robust free-form optimization algorithms where the solution is formed iteratively through prior algorithmic learning and without necessarily allowing an analytic closed form of the solution. One such class of algorithms is called a Genetic Algorithm, GA for short, which is based on evolutionary principles GA algorithms are an established method that has been previously used in array applications such as the design of acoustic lenses, electromagnetic antennae and communication transmitter networks (Child and Venugopal, 2010).

The work of Child and Venugopal (2010) was one of the first to use GA to optimize a WEC array layout for power maximization. This investigation verified the consistency condition, Eq. (2.2), under less restrictive assumptions than those in Fitzgerald and Thomas (2007), and found it to hold true for a range of array configurations.

Child et al. (2011), extended the work in Child and Venugopal (2010), optimized in regular seas only, to the case of irregular seas. Implementing a GA optimization for a 5-WEC array of heaving cylinders for the same tasks as mentioned in the previous paragraph, he utilized a JONSWAP spectrum with directional spreading as the input sea state. The results, as expected, show much less increase in power production compared with the regular wave case, with a $q - value$-max of only 1.044 for real-tuned WECs and 1.176 for reactively-tuned ones. Although optimization in this case offers a net benefit, it is not very significant. It does however point to the need to explore this line of investigation further, particularly by looking at optimization with real sea climates. In addition, the investigators studied an alternative, first principles based approach which they termed a Parabolic Intersection (PI) method and compared the two approaches. They found *i.e.* given appropriative constraint, the GA and PI method give similar *q*-value with the GA having a slight edge.

A similar approach was followed in Giassi and Göteman (2018), where a GA is used together with a semi-analytic method to find the optimal configurations of an array of several heaving cylindrical WECs. In addition to including the layout in the objective function, the researchers vary the individual WEC size and the number of WECs in the array. The conclusions they make are very similar to the ones put forth in Child and Venugopal (2010), showing that a GA layout optimization tool is effective in finding WEC array layouts that avoid destructive interactions and to obtain a *q*-value slightly above unity for real sea states.

Another recent series of papers, (Sharp and DuPont, 2015, 2016, 2018) also used a GA based array layout optimization for an array of heaving cylindrical WECs, together with a semi-analytical approach to calculate the array hydrodynamics. In addition to the hydrodynamic model, a minimum-distance sensitivity analysis was performed in Sharp and DuPont (2015) and an economic model developed in Sharp and DuPont (2016) were both analysed in Sharp and DuPont (2018).

The authors reached similar conclusions to the rest of the investigations presented in this section, where they indicated the usefulness of a GA based layout optimization approach to avoid areas of destructive interference and achieve *q*-values slightly greater than unity for real seas. The performance of a GA-based optimization for WEC array layouts was compared to two other algorithms, namely the covariance matrix adaptation evolution strategy (CMA), and the glowworm swarm optimisation (GSO) algorithm in Ruiz et al. (2017b). The investigators found that on the one hand, the results of the GA and the GSO is very similar and slightly higher than that of the CMA, while on the other hand, the CMA led to a significantly lower computational cost than the GA and the GSO. They suggested further investigation into a CMA-based array optimization though cautioned that the results of any layout optimization are very sensitive to the initial and boundary conditions. Finally, a search group algorithm (SGA) based layout optimization, adapted from studies on optimal wind farm configuration, was put forth in Bossuyt et al. (2017). For an array of 5 heaving cylindrical WECs, the authors find optimal *q*-values slightly higher than those found in Child and Venugopal (2010) and Sharp and DuPont (2016) whilst at the same time reaching the results with less iterations and therefore less computational time (Bossuyt et al., 2017).

2.8 Control of Arrays of WECs

Dynamic control of WEC implies changing the dynamics of a WEC to enable it to extract more energy from the wave, *i.e.*, power-maximizing control, and/or to enable the WEC to survive extreme sea states in what can be termed survivability control. Control can also be implemented to smooth the WEC power output to the grid (Molinas et al., 2007). While the spring or stiffness, damping and inertia of a WEC system can be changed, in practise by far the most common of modifying the motion of a WEC is done by changing only the damping in the PTO mechanism in what is termed *passive control* and less commonly *real control*.

Less used in practise but often presented in theoretical studies is *reactive control*, *i.e.* the changing of both the spring or stiffness of the PTO during WEC operation. We note here that in the context of wave energy the term *control* has a meaning different from that used in control engineering. It is an energy optimization problem, as opposed to *closed loop control* where the difference between the desired state and measurements of an actual state are used to determine the controlled inputs.

The need for dynamic control of individual WECs was established in the mid 1970s, only a few years after the initial investigations into the possibility of converting wave energy into electricity for the electric grid (Cruz, 2008). The primary need for control arises between the mismatch of most WECs' frequency response and the predominant frequency of incident waves in the ocean. For a vast majority of WECs maximization of power output necessitates a match between the motion of the wave and the motion of the WEC. To achieve this, the phases of the WEC oscillation and the wave oscillation must match (see 3.8 in Chapter 3 for details). For WECs, and in particular heaving buoys, to achieve phase matching in average ocean frequencies without dynamic control to modify their oscillations, their physical dimensions must be much greater than what is economically feasible (Gilloteaux and Ringwood, 2010).

Control of WEC arrays differs from that of individual WECs because the motion of controlled WECs results in a different radiated wave field that in turn influences the optimal performance parameters of the other WECs in the array (Bacelli et al., 2013). Because realistic control of a number of WECs requires large computer resources, only in the past decade has WEC array control become an active area of research. The chief reason for the need for large and fast computing power is that a majority of control schemes are inherently non-linear; furthermore active control, if it is to be deployed in practise, needs to calculate the control parameters on the order of a wave period, *i.e.* in a few seconds of model run time.

To achieve optimal control, *i.e.* to extract the greatest possible power from the array, both the mass and damping of all WECs need to be modified to cancel the impedance of the incoming wave force (Falnes, 2001). No WECs currently in development offer this possibility, so this value serves more as a benchmark against which real WEC performance can be measured. We can consider two main classes of arrays of WECs, those generally known as closely-spaced arrays attached to a fixed structure and those that are sparsely spaced and individually moored. For the former, both the mass and the damping can be modified in operation while for the

latter the modification of the floater mass is not feasible and therefore any form of control will only optimize the PTO damping.

For a regular wave input, Bellew and Stallard (2010) varied the supplementary mass and damping for a linear array of 5 WECs with inter-WEC spacing $d = 4r$ where r is the WEC radius. They found that over most of the operating frequency range a diagonalised optimal damping matrix provides the best power output, noting however that close to the resonance frequency of an isolated WEC an iterative approach to finding the damping matrices for the WECs is better. They note however, that this increase is mitigated when a restriction is placed on the possible values of the damping (Bellew and Stallard, 2010).

De Backer et al. (2010) investigated two rectangular arrays of 12 and 21 buoys with roughly one diameter inter-WEC spacing varying both the supplementary mass M_{PTO} and damping B_{PTO}. The authors considered three control strategies: the first strategy applies the optimal control parameters for a single body to all WECs in an array, the second optimizes the power for an array and applies the resulting M_{PTO} and B_{PTO} to each WEC, and the final method determines separate values of M_{PTO} and B_{PTO} for each WEC. Running the simulation for a range of simulated real sea states, the investigators noted a significant increase in performance for the individually optimized WECs versus the other two methods, while noting that in the unconstrained case the individual optimisation converged to an unrealistic solution. In practical operating conditions with multiple constraints on the motions and forces on the WECs, individual control provides the best solution, with a $q - value$ of 0.79 compared to 0.70 for the diagonal and single-WEC optimal cases.

The paper by Child and Venugopal (2008) looked at the difference in performance between reactively tuned WECs and real tuned ones, for a two-body array with separation distance of $8r$. They observed a large peak in the $q - value$ for a reactively-tuned WEC noting however that despite the higher power produced in this case, the motion required to achieve it may not be achievable in deployment (Child and Venugopal, 2008).

The investigation of Folley and Whittaker (2009b) studied two floating hemispheres of 10 m radius for heave and surge motion for two scenarios of suboptimal control. In the first, the reactive control force applied to the system differs from the optimum control tuned to a particular frequency, and in the second case only passive tuning is considered. There is a significant reduction in power compared to the optimally tuned case because in both cases the resulting array is not able to take advantage of the beneficial phase relationships between the indecent and radiated waves that leads to positive $q - value$s (Folley and Whittaker, 2009b). In addition, the authors studied the $q - value$ for a real spectral wave climate, finding that for reactively controlled WECs the optimal average $q - value$ for arrays of 2, 3 and 5 WECs was 1.16, 1.15, and 1.19 in a when they allowed the distance between the WECs to vary up to 300 meters (Folley and Whittaker, 2009b). Cruz et al. (2010) investigated the effect of tuning a rectangular array of 4 heaving cylindrical WECs with WEC separation equal to $4r$ in irregular sea states. They tuned each WEC independently by iterating on a linear damping coefficient, achieving $q - value$s between 0.88 and 0.97 for a range of sea states and heading angles. Similarly, Antonutti and Hearn (2011) studied a configuration of semi-submerged

heaving hemispheres of radius 1.2 m and separation distance $4r$. They compared the annual power yield from an array of 2, 3 and 4 WECs for a site-specific wave climate, finding a significant decrease in array performance for both sea state specific tuning and scatter diagram based tuning of B_{PTO} (Antonutti and Hearn, 2011). Finally Annuar et al. (2012) investigated an array of six WECs in regular seas with real and reactive control, in addition modelling the PTO and generator system, finding a more than two-fold increase in power output with reactive control. In the research by Bacelli et al. (2013), it was determined that a centralized control strategy for a small array of heaving cylindrical WECs, which the author termed Global Control, outperformed an independent control strategy where one WEC is aware of the motions of the other WECs in the array. The authors also investigated the effect of inter-array distance on the effectiveness of the proposed control scheme and performed a sensitivity analysis regarding the WEC positions In a similar vein, Li and Belmont (2014), used a centralized model predictive control (MPC) strategy to increase the power of a closely-spaced array of heaving cylindrical WECs. The authors noted that the optimized power output is an increasing function of degree of intra-array interdependence. They observed that increases in power of up to 20% were achieved using realistic ranges of parameters with respect to the independent case. A more recent investigation by O'Sullivan et al. (2018) explored the intra-array separation distance d at where a centralized MPC control strategy can bring a benefit to a WEC array power output. The also showed that the introduction of power constraints, either locally at each WEC or globally for the entire array, improved the quality of the power exported to the grid. A comprehensive overview of energy-maximizing control including the application to WEC arrays is given in Ringwood et al. (2014).

2.9 WEC Array Coastal Impact Studies

While the goal of any renewable energy project is to obtain the maximum amount of clean energy for the end users, the environmental effects of any such endeavour must not be overlooked. Like any other renewable energy generating facilities, wave farms will have both positive and negative effects on the surrounding area external to their primary purpose. A specific concern with WEC arrays is the potential impact of the uptake and redistribution of wave energy on coastal processes and the surrounding environment.

The potential impact of WEC arrays on the coast has been studied since the late 2000s with a number of publications which raised concerns about the potential impacts (Millar et al., 2007; Smith et al., 2007; Venugopal and Smith, 2007; Vidal et al., 2007). These studies used spectral models and employed semi-porous grid cells in the space occupied by the WECs to model WEC arrays. As was seen in Section 2.5.5, due to the inherent limitations of spectral modelling, a significant impact was shown with a reduction of up to 30% in the lee of a WEC farm in a number of these publications (Smith et al., 2007; Millar et al., 2007). A second wave of studies sought to refine the methodology by introducing frequency-dependent obstacles mimicking the physics of a real WEC in a spectral model

(Smith et al., 2012; Carballo and Iglesias, 2013) or in a phase-resolving model (Beels et al., 2010; Beels, 2009; Beels et al., 2011). All of these investigations showed significant impacts, on the order of a 10% reduction in the wave energy behind a WEC array. Stratigaki et al. (2011) indicated that some of the reduction is mitigated when wind generation is added into the wave propagation model. It can be noted that all of the aforementioned investigations dealt with large scale WECs on the order of several tens of meters of effective wave front such that their impact would be magnified in contrast to a WEC array of sparsely-spaced small scale point absorbers. A limitation of these investigations is that no radiation was modelled and the WECs were simulated as fixed objects. An extension of the SWAN model introduced in Ruehl et al. (2013) was recently utilized by Contardo et al. (2018) to model a submerged cylindrical buoy. The study found a reduction of up to 20% in the wind seas behind a small array of WECs that quickly recovered to a decrease of only 12% in the wave height 800 m away.

Recent studies sought to allay the problem presented by the course resolution of wave propagation models by simulating WEC arrays in a finer-resolution model and then propagating the results via a coarser model to a wider area. Such an approach is taken in Verbrugghe et al. (2017b); Verao Fernandez et al. (2017, 2018); Balitsky et al. (2018b) where the WEC farm is modelled in a BEM wave-structure solver and coupled into the wave propagation models OceanWave3D and MILDwave, respectively. The results of these investigations, performed for heaving point-absorber like WECs, show a minimal impact on the far-field zones pointing to a much lower impact on the coastline than that predicted by the coarse resolution spectral models. The investigations of Tomey-Bozo et al. (2016, 2019) using a similar coupling methodology for OSWECs in shallow coastal areas also show a significant but lesser impact of the WEC arrays on the coast than those predicted by the earlier studies using spectral models.

A number of studies looked at various facets of WEC array impacts. The investigation by Abanades et al. (2014) coupled a spectral model to a morphodynamic model which showed a potential impact on the sediment transport, while Mendoza et al. (2014); Abanades et al. (2018) specifically investigated the coastal defence potential of a WEC array. Rodriguez-Delgado et al. (2018) applied the idea of looking at the sediment transport in conjunction with a spectral model to assess the impact of WEC arrays of different configurations on a gravel coast. Realizing the benefit of a reduction in the wave energy for the growing offshore wind industry, recent investigations by Perez Collazo et al. (2014); Astariz et al. (2015); Astariz and Iglesias (2016a,b) explore the potential of co-locating offshore wind farms and wave energy arrays for mutual economic benefit. In Astariz and Iglesias (2016a), a Co-Location Feasibility Index was developed via an environmental and economic analysis as a metric of the mutual benefit of co-location wind and wave farms *i.e.* WEC arrays. The follow-up investigation found that the energy yield per unit area with the combined wave-wind farm increases by a factor of 3.4 relative to a standalone wind farm, the downtime periods decreases by 58%, and the power output variability reduces by 12.5%.

2.10 Moorings, Grid Integration and Connection Issues

Two important facets of a commercial WEC array project that are often ignored in the layout and coastal impact studies outlined in Section 2.7 and Section 2.9, respectively are moorings and electrical connections to the grid. Both parameters contribute a significant proportion to the CAPEX (CAPital EXpenditure) of a wave energy project and thus will play an important role in the eventual layout, control strategy, number of WECs etc. of a commercial WEC array project.

Recognizing its importance on the performance and survivability of WECs, the issue of mooring systems for WEC arrays has been investigated in depth over the past 15 years. Early publications on the subject, Johanning et al. (2004, 2005); Fitzgerald and Bergdahl (2008), argued for the inclusion of moorings in the design and simulation of WECs and presented dynamical models for doing so. As with control presented in Section 2.8, mooring dynamics are an inherently non-linear modelling problem, consequently, the time-domain approach is the most accurate one.

One of the first articles to explicitly look at mooring systems for WEC arrays was that of Gao and Moan (2009) which looked at the mooring configuration of an array of 9 heaving WECs in a grid arrangement. Vicente et al. (2009) investigated a triangular array of 3 point absorbers including the mooring lines and a PTO system using a linear frequency-domain approach. The work was updated to the time-domain and extended to a more complex triangular gird array in (Vicente et al., 2010). Konispoliatis and Mavrakos (2014) studied the impact of mooring forces on an array of OWC coupled to a floating wind turbine in a 3-WEC configuration. Ringsberg et al. (2018) analysed the impacts of various mooring configurations on the cost of wave energy produced by an array of heaving WECs via a direct search optimization of various mooring configurations Yang et al. (2018) compared the two lowest-cost mooring designs from Ringsberg et al. (2018) for an array of 10 heaving WECs with various array layouts and performed a fatigue analysis study. A review of the various approaches to moored WECs was recently published in Davidson and Ringwood (2017).

Since the aim of WEC array projects is to provide electrical power to the grid, the issue of electrical connections and grid compatibility is of chief importance. To this end, several studies have looked into integration of WEC arrays into the electrical grid. Tedeschi et al. (2011) investigated different scenarios of a hypothetical 20MW power plant from the point of view of the electrical supply variability. O'Sullivan and Dalton (2009); Kiprakis et al. (2009) studied the specific challenges of integrating a WEC array project in an area of weak electrical grids. Molinas et al. (2007); Tissandier et al. (2008); Sjolte et al. (2013) looked at the power smoothing effect of placing WECs in an array as opposed to a single connected WEC. All of the mentioned references indicated the benefits of connecting WECs in an array, thus reducing the need for costly electrical subsystems. From the standpoint of grid connection and existing grid infrastructure, O'Sullivan and Dalton (2009) and Sharkey et al. (2011) honed in on the specifics of integrating a small WEC array off the west coast of Ireland, and Blavette et al. (2012, 2014) looked at the effects

of a medium size WEC array at various European locations. Finally, Parkinson et al. (2015) studied the impacts of large scale wave energy deployment off the Northwest Pacific coast of the US.

2.11 Public Perception and Societal Impacts

In addition to technical and environmental issues, we, as wave energy researchers, developers and decision makers, must be cognizant of societal concerns about WEC array production facilities which may provide or preclude the political will often necessary to obtain such complex and costly projects off the ground. There are various social and environmental concerns of wave energy utilization that apply specifically to the specific case of WEC arrays, for example ocean territory management, fishing right-of-ways, visual impacts, spatial planning issues, and the effect of WEC arrays on the near-shore sediment transport that might impact coastal communities. Several studies into the public perspective of wave energy have been conducted in conjunction with the launch of the Wave Hub testing facility in the UK (West et al., 2009; Bailey et al., 2011; Stokes et al., 2014). The findings suggest general public support for wave energy as an economically beneficial method of power generation with few adverse side-effects. However, the public perception was strongly influenced by the WEC array size and distance from shore, with off-shore WEC installations having less perceived negative impact. Another paper focused on both the social and environmental impacts of wave energy extractions and made recommendations including making provisions for public input in WEC array design (Bonar et al., 2015). Finally, a comprehensiveness review of the interaction between marine renewable energies and public perception and various stakeholders was performed in a recent paper by Ruano-Chamorro et al. (2018).

2.12 European Research and Commercial WEC Array Projects

In this brief overview, a selection of European wave energy projects related specifically to the numerical, experimental, and commercial WEC Array development is presented. The European Union (EU) is at the forefront of ocean energy technology development, and currently hosts more than 50% of tidal energy and about 45% of wave energy developers (Magagna and Uihlein, 2015). To date, the majority of ocean energy infrastructure such as ocean energy test centres and deployment sites are also located in European waters. The premier example of this is EMEC, the European Marine Energy Centre in the Orkney Islands in Scotland, UK. In addition hosting the world's first successful pre-commercial WEC and WEC array deployments, EMEC is a centre of research and expertise *i.e.* a partner in past and ongoing research efforts (European Marine Energy Centre Ltd., 2019). Over the past decade, as the need for costs savings via scaling for wave energy technologies was recognized on the national and European policy level, several initiatives were launched and successfully completed that specifically targeted WEC array research

gaps.

One of the first was the €10m Performance assessment of Wave and Tidal Array Systems (PerAWaT) project launched in 2009 that produced validated software tools capable of significantly reducing the levels of uncertainty associated with predicting the energy yield of major wave and tidal stream energy arrays (Energy Technologies Institute, 2019). The collaboration between several academic institutions and the consulting firm DNV-GL produced a series of software tools to aid WEC array planning and development.

The Streamlining of Ocean Wave Farms Impact assessment (SOWFIA) project, funded by EU Intelligent Energy Europe (IEE) and led by the University of Plymouth (UK), focused on studying the impacts of the large-scale developments of WEC arrays in the social, economic, and environmental realms. The result of the project was the development of a Geographical Information System (GIS) tool for the monitoring of wave energy projects in the EU (Greaves et al., 2013).

The FlanSea project was led by Ghent University with the goal of developing a Flemish wave energy converter adapted to moderate wave climates. As a starting point, a test buoy, the Wave Pioneer, was developed in order to validate the simulation models, to understand the economics behind wave energy, and to experience the challenges (e.g. efficiency of the drive train, the forces on the components) (Ghent University, 2019). Ghent University was also involved in the EU FP6 (6th Framework Programme) project SEEWEC (Sustainable Economically Efficient Wave Energy Converter) (Rouck and Meirschaert, 2009). The consortium included industrial players such as Fred Olsen and Bosch-Rexroth but also the local SME Spiromatic. The project developed an actual wave energy converter.

The 'WECwakes' project, also coordinated by Ghent University, funded by the EU FP7 HYDRALAB IV programme, resulted in the world's largest WEC array experiment, performed for up to 25 WECs at the Shallow Water Wave Basin of the DHI (Hørsholm, Denmark). The project not only served to validate existing numerical models resulting in a large number of research publications on intra-array interaction, but also created a publicly accessible database which continues to serve as a benchmark for validating WEC array numerical models (Stratigaki et al., 2014).

Another project resulting in a significant amount of research on WEC array placement was the DTOcean project (DT Ocean Developers, 2019). DTOcean was a European collaborative project funded by the European Commission under the (FP7) for Research and Development. DTOcean aimed at accelerating the industrial development of ocean energy power generation knowledge, and providing design tools for deploying the first generation of wave and tidal energy converter arrays.

At the time of publication of this document, the European Cooperation in Science and Technology (COST) is funding the WECANet Action, the first pan-European Network on an interdisciplinary marine wave energy approach that will contribute to large-scale WEC Array deployment by dealing with the current bottlenecks (Stratigaki, 2019; COST European Cooperation in Science & Technology, 2019). One of the innovations of the new project is a focus on the support of WECs for niche markets, a sector that has been overlooked in many past European

efforts but that shows promise of being an early adapter of wave energy technology.

While there have been many efforts to launch commercial WEC arrays in the European Union over the past decade, some of which have resulted in extended deployment, the only ongoing long-term WEC array project which is in continuous operation is the Seabased Lysekill wave power project in Sweden. The project, consisting of 10-20 point absorber type WECs connected to a bottom-fixed linear generator, has resulted in numerous learnings related to every facet of wave energy conversion and has resulted in a large number of publications in collaboration with Uppsala University (Sjökvist et al., 2017; Wang and Isberg, 2015; Engström et al., 2013; Sjolte et al., 2013), to cite a few from a very long list.

Finally, mention must be made of the SURGE (Simple Underwater Renewable Generation of Electricity) and SURGE projects undertaken by AW-Energy Oy from Finland with funding by the European Investment Bank for a demonstration OSWEC array project off the coast of Peniche, Portugal (AW-Energy Oy, 2019; EIB, The European Investment Bank, 2016). The first demonstration project, undertaken in 2010-2014 involved the successful deployment of 3 WaveRoller® OSWECs. The second project of the initiative, SURGE2, with committed funding of €10 m, will see the installation of up to 10 units of the next generation of Wave Rollers® in the same location. As of the time of writing the project is undergoing testing prior to deployment *i.e.* scheduled to be deployed later in 2019. A similar WEC array project with the Wave Roller® OSWEC technology, entitled WATTMOR Kasanen (2015), is to be located in the baie d'Audierne in Bretagne in France, is currently in the development stage with confirmed funding from the regional council and several industrial partners (Région Bretagne, 2019) with the same proposed timeline as the SURGE project.

2.13 Conclusions

With the swell in publications into the WEC array problem, we finally can cautiously make conclusions about the best placement of WECs in an array and the magnitude of their impacts on the coastline. In spite of enormous progress achieved in a relatively short time, the are still many unanswered questions. Of a particular concern is the lack of experimental and operational data for WEC arrays that would serve to validate numerical models. Moreover, given the lack of commercial WEC array in operation, the uncertainty in the economic parameters in technoeconomic array models are often an order of magnitude greater than in the hydrodynamic modelling. Therefore one must always be cautious in extrapolating the results of an 'ideal' modelling scenario to the often harsh economic reality of WEC array operations.

Furthermore, there are still areas of investigation with sparse research coverage such as non-linear inter-array interactions in an WEC array, the effects of realistic uneven bathymetry, extreme wave effects on WEC arrays, interactions of arrays with currents and/or tides, and the effects of marine organisms in the water in the form of biofouling. All of these issues may become important for array projects located near-shore in water depth of less than 30 meters, which, because of the

costs of electrical and mooring infrastructure, is currently the most economically sensible location for placement of WEC arrays.

One fact has however become clear, even though in theory arrays can be used to increase power output through constructive interference, for realistic operating conditions, it will be hard to achieve a WEC array power output much greater than that of sum of individual WECs. These conditions can be multi-directional spectral seas, PTO force motion restrictions, plus friction in the mechanical systems Indeed, a more approachable goal, stated as far back as the mid 1990s in McIver (1994), will be to use knowledge of hydrodynamics to minimize destructive interference. This is still a worthwhile goal, and a 5 - 10 % difference in the $q-value$ can mean the difference between economic success and failure of a project.

Chapter 3

Background Theory

Abstract

This chapter outlines the theory underlying the methodologies and results presented in this thesis. The fundamental tenets of linear Potential Flow Theory which forms the entirety of the theoretical basis of the thesis are introduced. To start the chapter a brief look at the sources of waves in the ocean, segues into a succession on wave modelling before moving into the fundamental equations and assumption of linear wave theory. The bulk of the chapter is devoted to deriving the hydrodynamic expressions of forces, motions, and the power output of a forced oscillating body, namely a WEC. The theory is extended to multiple bodies whence it can be applied to WEC arrays. We discuss the theory of optimal motions and power capture and present in brief the limitations imposed by Linear Potential Flow Theory on the WEC modeller are presented in brief. Finally, a short conclusion summarizes the suitability of linear wave theory in application to deriving the research results exhibited in this thesis.

In this chapter the theoretical background for the results presented in the thesis is introduced. The conventions and assumptions of Linear Potential Flow Theory, which forms the basis of the results herein presented, are introduced in Section 3.3. This is a brief overview of the subject; a much more thorough analysis can be found in the following essential references (Newman, 1977; Falnes, 2001; Mei et al., 2005; Goda, 2000). The fundamental equations of Linear Potential Flow Theory are introduced in Section 3.3.1. The interaction of a floating body with waves, wave-structure interaction under the auspices of linear wave theory is detailed in Section 3.4.

The frequency-domain approached is explained in Section 3.5 while the equations of the time-domain linear method are outlined in Section 3.6. We define the linear superposition assumption that allows us to model irregular sea states. Then we give attention to the power output of a WEC and a WEC array system in Section 3.8. First by looking at the available power in a given sea state in Section 3.8.1, we define the theoretical limits for the power absorption of an array of WECs in Section 3.8.2 and the realistic power output expected of the type of WEC modelled in this thesis in Section 3.8.3. After an analysis of the limitations of Linear Potential Flow Theory, we summarize the motivations of the chapter in Section 3.8.5.

3.1 Source of Ocean Waves

It is common knowledge that the source of waves in the ocean is the wind. However the actual range of all disturbances in the ocean is much wider, with what we commonly term waves actually constituting a small part of the spectrum as shown in Fig. 3.2. As we observe in the figure, virtually all the energy of the spectrum is contained in two of the period ranges: ordinary gravity waves, and ordinary tides. These are the ones that can be perceived with the naked eye, and the ones which can be harnessed for useful energy. The focus in this thesis and this chapter will be gravity waves, also called wind-generated waves, that are indeed caused by the wind which in turn is generated by uneven solar heating of the earth. Thus we can state that wave energy is a transformed kind of solar energy.

Wave generation by wind starts as small ripples which increase in size due to the sustained force input from the wind. The waves continue to grow until a limit is reached where the continuous input of energy from the wind is balanced by the steady loss to white-capping and turbulent losses. This is the case where the waves are considered to be fully developed.

Whether a sea is fully developed or not will also depend on the distance over which the wind can blow over open water, called the fetch. Over large fetches, when the wind stops blowing; the waves will continue to exist and can travel for very large distances with essentially no loss of energy. In this case they are called swell waves because the wind responsible for their generation is no longer present. A simplified representation of these processes is seen in Fig. 3.1. The cut-off point between wind and swell waves is somewhat arbitrary, it is commonly determined from the ratio of the celerity (velocity) of the waves and the velocity of the blowing

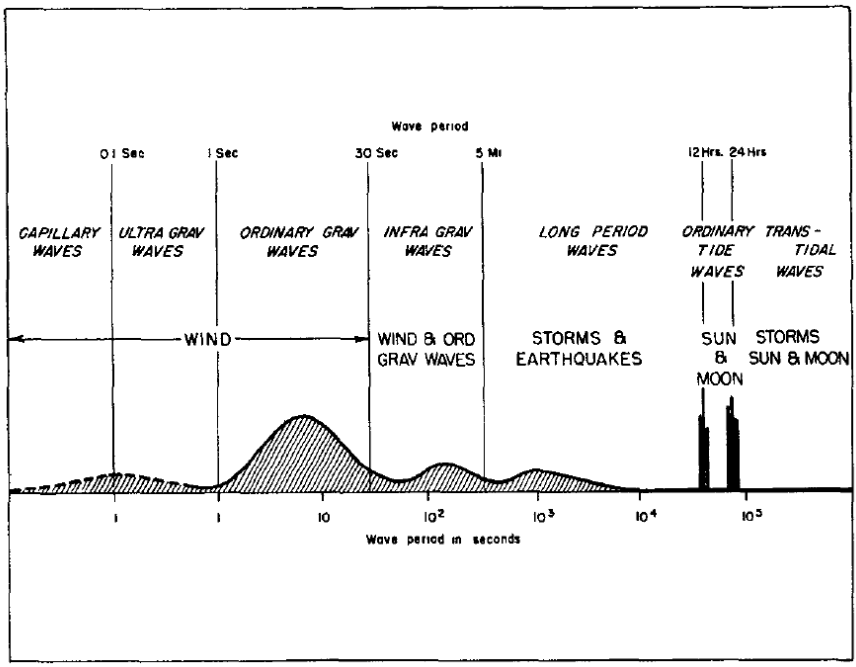

Figure 3.1: Classification of ocean waves according to wave period. The forces responsible for various portions of the spectrum are shown. The relative energy is indicated by the amplitude (y-axis) of the curve. (Garrison, 2015)

wind, where a smaller ratio is indicative of wind waves.

A monochromatic wave is generally characterised by its wave period T, wavelength (λ), wave height H which is twice the wave amplitude ζ, and derived parameters such as the wave steepness $s = H/\lambda$, wave number $k = 2\pi/\lambda$, and the angular wave frequency $\omega = 2\pi/T$. Ocean waves can be represented as a linear summation of monochromatic waves. We can also view the water depth h as a parameter characterising the wave, as the relationship between the wavelength and water depth determines the trajectory of water particles within a wave, and hence the shape of a wave. Consequently, depending on the water depth, ocean waves can be divided into three categories as shown in Fig. 3.3. Deep-water waves travel through water with depth greater than half of the wavelength, where water particles experience an orbital motion not being affected by the seabed. In the wave energy sector, the term 'deep water' usually refers to the water depth equal or greater than 40 m (Pecher and Kofoed, 2016). Shallow-water waves travel through the water depth less than 1/20th of the wavelength, and the trajectory of water particles is flattened becoming elliptical due to the proximity of the seabed. Finally transitional waves fall between the two extremes. The assumption of shallow or deep waves allows for the simplification of the dispersion relation of Eq. (3.19) as given in Section 3.3.3 and in calculation of derived quantities such as wave power

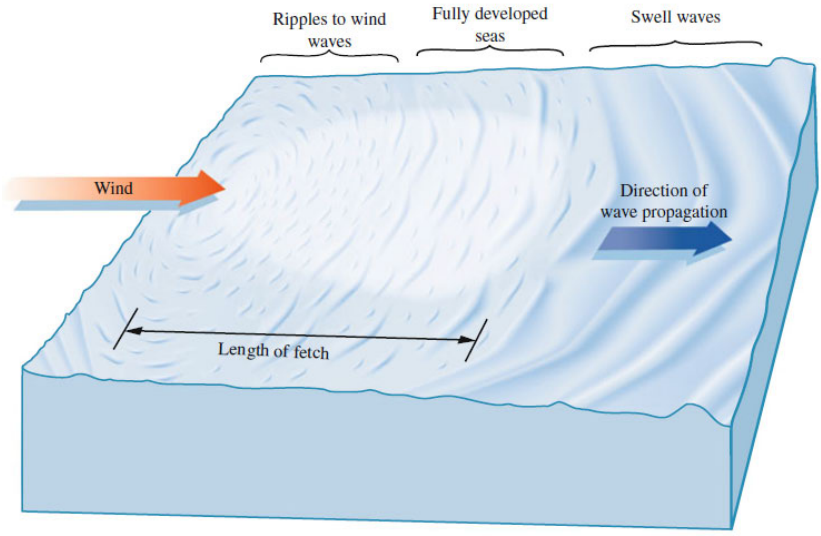

Figure 3.2: Classification of ocean waves according to wave period. The forces responsible for various portions of the spectrum are shown. The relative amplitude is indicated by the curve (Munk, 1950).

Eq. (3.64) given in Section 3.8.

3.2 Wave Modelling Classification

When a wave travels from deep to shallow water as demonstrated in Fig. 3.3, its shape alters due to the increase of its height and decrease of its speed and length. Therefore, deep-water waves with a steepness of s less than 0.01 can be approximated by a sinusoidal wave applying linear potential flow theory (inviscid, incompressible fluid, irrotational flow, and a uniform water depth).

Intermediate or transitional water waves have more non-linear wave profiles due to the sharper crests and flatter troughs. Such waves are usually described by Stokes' wave theory, where the order of non-linearity is directly dependent on the wave steepness. Shallow water waves of long wavelength as compared to the water depth, can be approximated by the cnoidal wave theory (Goda, 2000). The suitability of different wave models depending on the relative water depth and wave steepness shown in Fig. 3.4 proposed by Le Méhauté has been widely accepted in the field (LeMehaute, 1976). It is common to assume that WECs operate in the range of sea states where linear wave theory is applicable. However, at times the wave conditions experienced by WECs can extend into Stokes 2^{nd} and 3^{rd} order theory as reviewed in (Windt et al., 2018). Moreover, for survivability states, all the states shown in Fig. 3.4 are applicable, as well as breaking waves. However, survivability issues are outside of the scope of this thesis and thus we shall focus

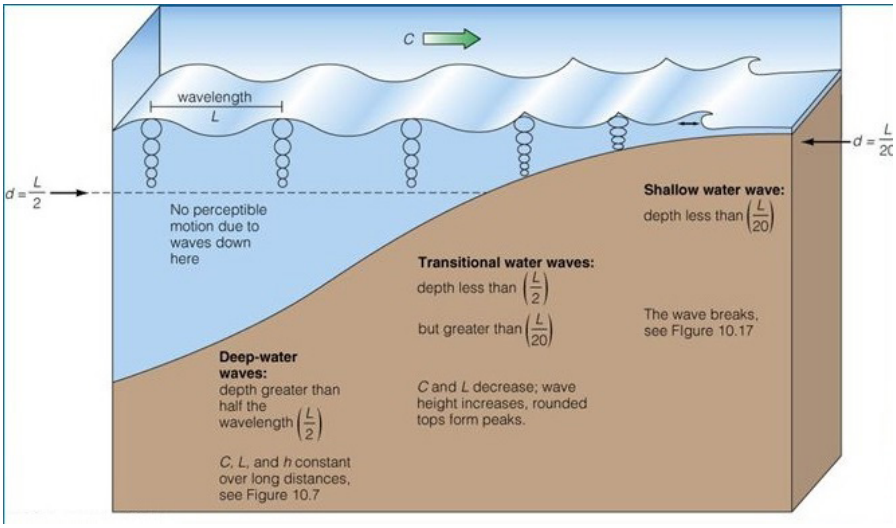

Figure 3.3: Classification of gravity waves according to wave depth (Garrison, 2015).

the attention on linear wave theory.

3.3 Linear Wave Theory

The linear theory of ocean waves, first published in the mid 19th century by George Airy and therefore sometimes referred to as Airy Theory forms the fundamental framework of this thesis. In brief, linear wave theory is a mathematical formulation of the propagation of gravity waves on the surface of an ideal fluid. The assumptions underlying linear wave theory are the following:

- the fluid is inviscid;
- the fluid is incompressible;
- the flow is irrotational;
- the wave amplitude is considered small compared to the wavelength.

Because the velocity can be described as the gradient of a velocity potential, the theory is often referred to as Potential Flow Theory, and will be referred to as such in the rest of the chapter. In this section, a right-handed Cartesian coordinated system with three orthogonal axes: x y and z is adopted. The z axis is pointing upward.

3.3.1 Fundamental equations

Given an incompressible fluid of density $\rho(x, y, z, t)$ and the particle velocity $v(x, y, z, t)$, the two fundamental equations of hydrodynamics are the equation of conservation

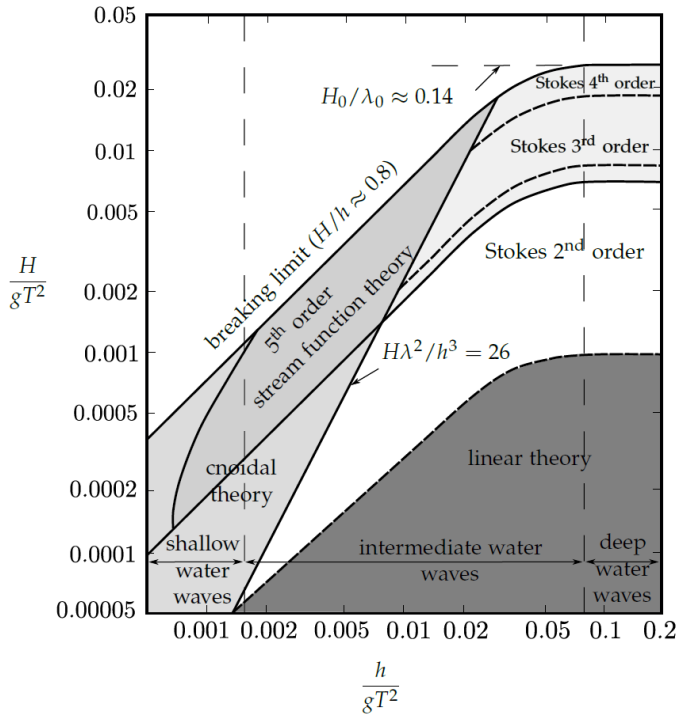

Figure 3.4: Chart of wave model suitability (LeMehaute, 1976).

of mass or the continuity equation:

$$\frac{\partial \rho}{\partial t} + \nabla \cdot (\rho v) = 0, \tag{3.1}$$

and the equation of conservation of momentum known as the Navier-Stokes equation:

$$\frac{\partial v}{\partial t} + (v \cdot \nabla)v = -\frac{1}{\rho}\nabla p + \nu \nabla^2 v + \frac{1}{\rho} f, \tag{3.2}$$

where $p(x, y, z, t)$ is the pressure of the fluid, ν is the coefficient of kinematic viscosity, and f is the external force per unit volume (Newman, 1977). If we assume an ideal fluid that is incompressible, $\rho = const$, inviscid, $\nu = 0$, and with gravity the only external force $f = \rho g$, then Eqs. (3.1) and (3.2) can be simplified to:

$$\nabla \cdot v = 0, \tag{3.3}$$

and

$$\frac{\partial v}{\partial t} + (v \cdot \nabla)v = -\frac{1}{\rho}\nabla p + g. \tag{3.4}$$

Moreover, if we assume irrotational flow, we can write the velocity of a fluid particle as

$$\mathbf{v} = \nabla\phi \tag{3.5}$$

by introducing the scalar quantity called the velocity potential $\phi(x, y, z, t)$. Combining Eq. (3.5) with the Eqs. (3.3) and (3.4) together with several vector manipulations results in the two equations (Falnes, 2002):

$$\nabla^2\phi = \frac{\partial^2\phi}{\partial x^2} + \frac{\partial^2\phi}{\partial y^2} + \frac{\partial^2\phi}{\partial z^2} = 0 \tag{3.6}$$

$$p = -\rho\frac{\partial\phi}{\partial t} - \rho g z - \frac{1}{2}\rho v^2. \tag{3.7}$$

The former, Eq. (3.6) is the well-known Laplace equation that together with the boundary conditions must be satisfied throughout the fluid domain. The solution of the Laplace equation then gives the velocity potential ϕ everywhere in the fluid. The latter, Eq. (3.7), also known the Bernoulli equation for unsteady potential flow, is used to calculate the pressure in the fluid. The term $\rho g z$ is commonly referred to as the *hydrostatic* pressure whilst $\frac{1}{2}\rho v^2$ is known as the *dynamic* pressure term.

3.3.2 Boundary conditions

The three boundary conditions required to solve the Laplace equation are outlined in this paragraph. Two of the boundary conditions are known as *kinematic*, requiring that that fluid particle cannot cross a solid boundary while the other one is known as the *dynamic* boundary condition. Using the schematic in Fig. 3.5, we consider the three principal boundary conditions in the fluid domain: at the free surface η, on the body surface S, and on the sea floor. The dynamic free surface linearised boundary condition states that any particle lying on the free surface will remain there. Assuming the particle velocity components are small compared to the wave velocity and that the free surface elevation is small compared to the wavelength, the condition can be stated as Eq. (3.7):

$$\left[\frac{\partial^2\phi}{\partial t^2} + g\frac{\partial\phi}{\partial z}\right]_{z=\eta} = 0 \tag{3.8}$$

We make use here of the assumption of small wave amplitude and therefore further simplify the equation by setting the free surface at $z = 0$ instead of $z = \eta$. We then define the motion of the water particles on the free surface η as:

$$\frac{\partial\eta}{\partial t}\left[\frac{\partial\phi}{\partial z}\right]_{z=0} = 0. \tag{3.9}$$

The dynamic boundary condition on the free surface rests on the assumption that the pressure outside the fluid is constant. On the body moving with velocity u, the

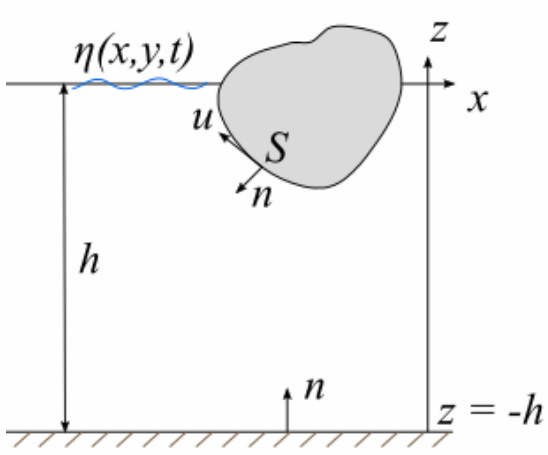

Figure 3.5: Fluid domain for Laplace equation in Potential Flow Theory. The origin is at $z = 0$, h is the water depth, n is the unit normal on wetted body surface and on the sea floor $z = -h$. u is the velocity of the considered point on S.

velocity component normal to the body surface u_n, must be equal to the velocity of the body in the same direction. Therefore the potential of the fluid velocity on the body must satisfy the kinematic boundary condition

$$\frac{\partial \phi}{\partial n} = u_n, \tag{3.10}$$

where n is the unit vector normal to the surface. Finally, the kinematic sea floor boundary condition requires that the fluid vertical velocity z on the sea floor to be zero:

$$\left[\frac{\partial \phi}{\partial z}\right]_{z=-h} = 0. \tag{3.11}$$

On finding the velocity potential ϕ we can derive the three principal quantities often required in wave structure interaction analysis, namely the free surface elevation:

$$\eta(x, y, t) = -\frac{1}{g}\left[\frac{\partial \phi}{\partial t}\right]_{z=0}, \tag{3.12}$$

the hydrodynamic pressure

$$p(x, y, z, t) \approx -\rho \frac{\partial \phi}{\partial t}, \tag{3.13}$$

and the velocity of the fluid

$$v(x, y, z, t) = \nabla \phi. \tag{3.14}$$

3.3.3 Sinusoidal wave solution

For deep water waves, that is where the sea floor has no appreciable effect on the wave particle trajectory, the solution that satisfies the Laplace equation (3.6) and the boundary conditions listed in Section 3.3.2 is a sinusoidal function (Falnes, 2002). This allows us for the separation of the temporal and spatial part of the velocity potential ϕ in the following manner (Alves, 2016):

$$\phi(x, y, z, t) = \hat{\phi}(x, y, z)e^{-i\omega t}. \tag{3.15}$$

Here the sinusoidal time dependence is represented by the unit amplitude $e^{-i\omega t}$, making use of Euler's formula

$$e^{-i\omega t} = \cos\omega t - i\sin\omega t \tag{3.16}$$

The hat operator $\hat{}$ over the velocity potential indicates a complex value. The Laplace equation (3.6) then reads:

$$\nabla^2\hat{\phi} = 0, \tag{3.17}$$

and the three boundary conditions for the velocity potential become:

$$\left[\omega^2\hat{\phi} + g\frac{\partial\hat{\phi}}{\partial z}\right]_{z=0} = 0 \tag{3.18a}$$

$$\frac{\partial\hat{\phi}}{\partial n} = \hat{u} \tag{3.18b}$$

$$\left[\frac{\partial\hat{\phi}}{\partial z}\right]_{z=-h} = 0. \tag{3.18c}$$

The necessity of satisfying the free surface boundary condition of Eq. (3.18)(a) leads to the dispersion relation

$$\omega^2 = gk\tanh(kh), \tag{3.19}$$

For deep water ($kh \gg 1$), Eq. (3.19) simplifies to $\omega^2 = gk$. Conversely, for shallow water ($kh \ll 1$), Eq. (3.19) is approximated by $\omega^2 = ghk^2$.

3.4 Wave-structure Interaction

A body submerged in water is subject to hydrodynamic forces due to the pressure of the surrounding fluid. When the fluid is extensive enough for gravity waves to form on the fluid-atmosphere interface, the bodies experience wave-structure interaction. Because the problem is of particular concern to naval hydrodynamics, the study of floating objects on the sea surface has a long history intimately tied to the history of naval architecture.

As in the study of undisturbed ocean waves, a linear approach is the most common way of resolving the forces and pressures encountered by floating and

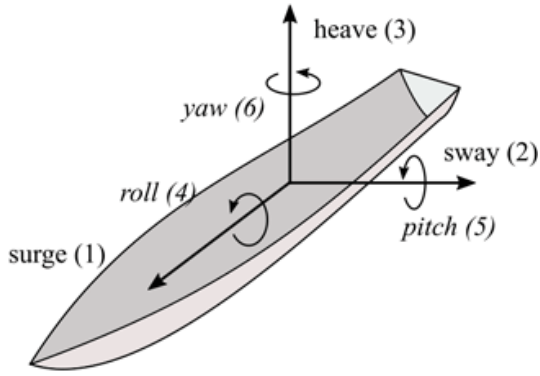

Figure 3.6: The six modes of motion shown for a non-symmetrical body

submerged bodies. In the simplest case it may be assumed that the waves incident upon the body are plane progressive waves of small amplitude, with sinusoidal time dependence. The theoretical results of regular monochromatic waves and the practical applications in real polychromatic sea states are linked by the description of irregular waves as a linear superposition of sinusoidal components (Newman, 1977). This is the method followed in this thesis in modelling wave-structure interaction in irregular waves. The motion of the rigid body is characterised by six components corresponding to six degrees of freedom (DoF) or modes of oscillatory motion (Fig. 3.6). Following naval hydrodynamic convention the modes are defined as follows:

1. surge
2. sway
3. heave
4. *roll*
5. *pitch*
6. *yaw*

and are indicated by the subscript $_k$. It can be noted that the translational DoF, 1-3, are subject to forces whilst the rotational degrees of freedom (4-6) are subject to force moments. The hydrodynamic forces and moments on a body surface S are determined by integrating the fluid pressure over the wetted surface of the body (Newman, 1977):

$$f_{hyd,k} = -\iint_S p n_k dS, \tag{3.20}$$

where n_k is the j-th component of the unit vector normal to the surface of the body as defined in Fig. 3.5. We can utilize the Bernoulli Eq. (3.7) along with Eq. (3.20) for expressing the hydrodynamic force in terms of the velocity potential:

$$f_{hyd,k} = \rho \iint_S \frac{\partial \phi}{\partial t} n_k dS. \tag{3.21}$$

The time dependence can be removed as in Eq. (3.15) resulting in

$$\hat{F}_{hyd,k} = -i\omega\rho \iint_S \hat{\phi} n_k dS. \tag{3.22}$$

3.4.1 Potential decomposition

Because linear theory allows for the principle of superposition, the total complex velocity potential $\hat{\phi}$ can be written as a sum of three different velocity potentials that can be calculated separately:

$$\hat{\phi} = \hat{\phi}_I + \hat{\phi}_D + \hat{\phi}_R, \tag{3.23}$$

where $\hat{\phi}_I$ is the incident, $\hat{\phi}_D$ is the diffracted, and $\hat{\phi}_R$ the radiated velocity potentials, respectively.

The canonical way of calculating the hydrodynamic forces on a moving body is by splitting the problem into the *excitation* problem and the *radiation* problem and solving each one separately (Falnes, 2002).

3.4.2 The excitation problem

If we assume for a moment that the body is fixed then only the incident and diffracted velocity potentials are non-zero. In this case F_e is called the *excitation force or moment* and is defined as:

$$\hat{F}_e = i\omega\rho \iint_S \left(\hat{\phi}_I + \hat{\phi}_D\right) n_k dS, \tag{3.24}$$

The first part of Eq. (3.24), the integral due to the incident velocity potential is known as the *Froude-Krylov* force and represents the force experiences from the oncoming wave, ignoring perturbations on it by the body. The second part of Eq. (3.24) is often termed the *diffraction force*. The fixed body assumption results in the boundary condition Eq. (3.10) applied as:

$$-\frac{\partial \hat{\phi_D}}{\partial n} = \frac{\partial \hat{\phi_I}}{\partial n} \tag{3.25}$$

on the body surface S. In addition, the diffraction velocity potential must also satisfy the far-field condition that satisfies the conservation of energy (Mei et al., 2005):

$$\hat{\phi}_D = \frac{e^{ikr}}{\sqrt{kr}} \text{ as } r \to \infty \tag{3.26}$$

where r is the radial distance away form the body.

$$k = \frac{2\pi}{\lambda} \tag{3.27}$$

The incident velocity potential of a regular progressive wave of amplitude ζ is given by:

$$\phi_I = i\zeta \frac{g}{\omega} \frac{\cosh(k(z+h))}{\cosh(kh)} e^{-ik(xcos\beta + ysin\beta)}, \tag{3.28}$$

where β is the direction of wave propagation relative to the x-axis. k is related to ω by the dispersion relation of Eq. (3.19).

3.4.3 The radiation problem

The forced body oscillation in the absence of an incident wave is known as the *radiation problem* and is resolved by assuming a superposition of radiated waves generated in each oscillation mode j (Falnes, 2002):

$$\hat{\phi}_R = \sum_{j=1}^{6} \varphi_k u_k. \tag{3.29}$$

Here φ_k is complex constant of proportionality $\varphi_k = \varphi_k(x, y, z)$ which represents the complex amplitude of the radiated velocity potential due to the body oscillation in mode j with a unit velocity u_k. The radiated velocity potential must satisfy the boundary condition Eq. (3.10):

$$\frac{\partial \hat{\phi}_R}{\partial n} = \sum_{j=1}^{6} u_k n, \tag{3.30}$$

Equations (3.29) and (3.30) are combined into the following expression:

$$\frac{\partial \hat{\varphi}_k}{\partial n} = n \text{ on } S. \tag{3.31}$$

Analogous to the radiated velocity potential ϕ_R, the proportionality coefficient φ_k must satisfy both the Laplace equation and the kinematic boundary conditions Eqns. (3.8) and (3.11) on the free surface and the sea floor.

$$\left[-\omega^2 \hat{\phi_k} + g \frac{\partial \hat{\phi_k}}{\partial z} \right]_{z=0} = 0 \tag{3.32}$$

$$\left[\frac{\partial \hat{\phi_k}}{\partial z} \right]_{z=-h} = 0. \tag{3.33}$$

The resulting radiation force acting on the body is then given by:

$$\hat{F}_{R,j,k} = i\omega\rho \iint_S \varphi_k \hat{u}_{j,k} n dS. \tag{3.34}$$

The index j, k indicates the force component in the direction of j that is induced by an oscillation in mode k.This expression can be simplified by using the concept of impedance in analogy with electrical engineering. Defining the radiation impedance as

$$Z_{j,k} = i\omega\rho \iint_S \varphi_k n dS \tag{3.35}$$

the equation (3.34) can be re-written as

$$\hat{F}_{R,j,k} = -Z_{j,k}\hat{u}_k. \tag{3.36}$$

$Z_{j,k}$ can be split into the real and imaginary parts:

$$Z_{j,k} = B_{j,k} + i\omega A_{j,k} \tag{3.37}$$

where the real part $B_{j,k}$ is known as the radiation resistance or more commonly radiation damping, while $A_{j,k}$ is known as the added mass. $A_{j,k}$ represents the inertia effect that corresponds to an increase due to the water displaced in the body vicinity when the body moves. $B_{j,k}$ is the resistive term that acts to slow the body motion down as the velocity increases by generating radiated waves in the fluid. The radiation force Eq. (3.34) can therefore be re-written in terms of the added mass and radiation damping coefficients:

$$\hat{F}_{R,j,k} = -B_{j,k}u_k - i\omega A_{j,k}u_k \tag{3.38}$$

This is in fact the most common form of writing the radiation force down for wave energy applications as shall be seen in Sections 3.5, 3.6 and 3.8.

3.5 WEC Equations of Motions in the Frequency-Domain

In this section the principles of Linear Potential Flow Theory are applied to model WEC motion for a single device and subsequently for an array of WECs in the frequency-domain. As we saw in Chapter 2, the frequency-domain approach is the most common way of calculating the forces due to its straightforwardness. However, as discussed in Section 3.8.4, the approach has some inherent limitations that restrict its range of applications for numerical modelling of WECs and WEC arrays.

We begin by writing the equation of motion for a single-DoF floating WEC in Section 3.5.1 and then extend it to an array of floating single DoF WECs. Then we write the linear time-domain formulation that is used to model time-variant processes and weakly non-linear ones in Section 3.6. The equations presented

herein can be easily extended to a multiple DoF system, however for brevity and clarity, and based on the fact that only single DoF WEC systems are modelled in this thesis, we follow the single DoF approach. We utilize z for the displacement and $\hat{z}$ for the complex displacement as the principle type of WEC modelled in this thesis is a heaving cylindrical WEC. It can be noted that whenever possible lower case fonts are utilized to distinguish time-domain quantities while upper case letters are reserved for frequency-domain quantities which are also complex unless specifically indicated otherwise.

3.5.1 Frequency-domain equations of motion for a single degree of freedom WEC

Once all the forces on the WEC are known, its motion can be derived by applying Newton's second law of motion to the system:

$$M\ddot{z} = f_{hyd} + f_{hs} + f_{PTO} + f_v + f_f + f_m. \tag{3.39}$$

Here M is the mass or the moment of inertia of the WEC system depending on the DoF simulated, f_{hyd} is the hydrodynamic force on the system consisting of the excitation and radiation forces detailed in Sections 3.4.2 and 3.4.3, f_{hs} is the hydrostatic or buoyancy force, f_{PTO} is the force of the power take-off mechanism, f_v is the viscous force, f_f is the sum effect of the frictional forces resulting from losses in the mechanical system and finally f_m are the mooring forces. In this thesis the focus is on the first three forces on the r.h.s. of Eq. (3.39). While the other forces are important in certain contexts, they are not the primary drivers of WEC motion, especially for passively controlled systems such as those modelled herein. The last three terms are disregarded for the modelling scope of this thesis. As was performed in Section 3.3.3 the time dependency is removed and re-written in Eq. (3.39) in the frequency-domain form, while also keeping just the terms relevant to this work.

$$M\hat{\ddot{z}} = \hat{F}_{hyd} + \hat{F}_{hs} + \hat{F}_{PTO} + \hat{F}_v + \hat{F}_f + \hat{F}_m. \tag{3.40}$$

Rearranging Eq. (3.40) by putting the acceleration, velocity and displacement proportional terms on the left, the forcing term on the right and writing out the force terms explicitly results in the familiar form of the equation of a forced damped oscillator from classical mechanics:

$$(M + A)\hat{\ddot{z}} + (B + B_{PTO})\hat{\dot{z}} + C\hat{z} = \hat{F}_e \tag{3.41}$$

It can be observed that Eqns. (3.37) and the definitions of the hydrostatic force are used:

$$\hat{F}_{hs} = -C\hat{z}, \tag{3.42}$$

where C is the hydrodynamic stiffness coefficient and $\hat{F}_{PTO}$:

$$\hat{F}_{PTO} = -B_{PTO}\hat{\dot{z}}. \tag{3.43}$$

It can be noted that the in analogy with Eq. (3.43), the PTO force can also contain an acceleration proportional and displacement proportional terms with the coefficients M_{PTO} and C_{PTO} or K_{PTO}, respectively in which case they would be included in Eq. (3.41). However, in this thesis the focus is on so-called *real* or *passively* tuned systems where only the velocity dependent term B_{PTO} is included. The reasoning behind this is that including the M_{PTO} and C_{PTO} would require changing the inertia and spring of a PTO system in real time and is not economically feasible for most current WEC designs.

From Eq. (3.41) we can solve for the complex amplitude displacement $\hat{z}$ in the relevant mode of motion:

$$\hat{z} = \frac{\hat{F}_e}{[-\omega^2(M+A) + i\omega(B+B_{PTO}) + C]}. \tag{3.44}$$

Here A is the added mass and B the radiation or hydrodynamic damping of the WEC. Dividing Eq. (3.44) by the amplitude of the incident wave ζ we obtain an important non-dimensional quantity is derived called the Response Amplitude Operator (RAO) that is the key connection between the WEC motion and the surrounding wave field:

$$RAO \equiv \frac{\hat{z}}{\zeta} = \frac{\hat{F}_e/\zeta}{[-\omega^2(M+A) - i\omega(B+B_{PTO}) + C]}. \tag{3.45}$$

The phase angle φ of the complex WEC motion at angular frequency ω is given by:

$$\varphi = tan^{-1}\left(\frac{(\omega(B+B_{PTO}))}{C-(M+A)\omega^2}\right) - \varphi_e, \tag{3.46}$$

where φ_e is the phase of the excitation force. It is remarked that the basic premise behind the frequency-domain equations introduced in this section is that the forces and motions must be linear and steady-state, otherwise the method of time-separation does not apply. This means that the only types of power take-off, moorings, and other forces must also be linear. In practise however, we can linearise such systems without appreciable loss in fidelity and still apply the frequency-domain approach. As we shall see in Chapter 6, this is one of the key tenets of the methods developed in this thesis for modelling the wave field effects of WECs with realistic PTO systems. Such WEC systems are commonly termed weakly non-linear. Despite its relative simplicity, the frequency-domain model can provide useful insights into the WEC system performance and can assist with a preliminary design of a WEC array.

3.5.2 Frequency domain equations of motion for an array of single degree of freedom WEC

The expressions introduced in Section 3.5.1 are expanded here to a system of WECs oscillating in one DoF, namely an array of WECs. The same assumptions and approximations hold as in the previous section: only those forces and coefficients

relevant to the work presented in this thesis are presented. We start with the damped oscillator equation for motion in the frequency-domain of Eq. (3.41) with the relevant forces expounded:

$$(\mathbf{M}+\mathbf{A})\hat{\ddot{\mathbf{z}}}+(\mathbf{B}+\mathbf{B}_{PTO})\hat{\dot{\mathbf{z}}}+\mathbf{C}\hat{\mathbf{z}}=\mathbf{F}_e. \tag{3.47}$$

Here the relevant motions are $1\times\mathcal{M}$ vectors where each vector component represents the motion of WEC $\mathcal{M}$. $\mathbf{F}_e$ is a $1\times\mathcal{M}$ vector of the excitation forces for each WEC. The hydrodynamic coefficients $\mathbf{M},\mathbf{A},\mathbf{B}$ and the hydrostatic and PTO coefficients $\mathbf{C}$, and $\mathbf{B}_{PTO}$ are all $\mathcal{M}\times\mathcal{M}$ matrices. In the case of $\mathbf{M},\mathbf{C}$, and $\mathbf{B_{PTO}}$ the matrices are diagonal, whereas in $\mathbf{A}$ and $\mathbf{B}$ the off-diagonal elements represent cross-coupling effects. The equation for the complex amplitude displacement (3.44) becomes the following for $\mathcal{M}$ WECs:

$$\hat{\mathbf{z}}=\left[-\omega^2(\mathbf{M}+\mathbf{A})+i\omega(\mathbf{B}+\mathbf{B}_{PTO})+\mathbf{C}\right]^{-1}\hat{\mathbf{F}}_e. \tag{3.48}$$

Here $\hat{\mathbf{z}}$ is the complex amplitude vector of displacements $\hat{z}$ for each body in the WEC array and $^{-1}$ indicates the matrix inverse of the expression in the square brackets. Equation (3.48) can be similarly divided by a vector of the amplitudes ζ of the wave to obtain the vector of RAOs for the WEC array system:

$$\textbf{RAO}\equiv\frac{\hat{\mathbf{z}}}{\zeta}=\frac{1}{\zeta}\left[-\omega^2(\mathbf{M}+\mathbf{A})+i(\omega\mathbf{B}+\mathbf{B}_{PTO})+\mathbf{C}\right]^{-1}\hat{\mathbf{F}}_e. \tag{3.49}$$

The vector of phases for each body can be calculated analogous to Eq. (3.46). Because of the cross-coupling between different WECs in the WEC array, the hydrodynamic coefficients $\mathbf{A}$ and $\mathbf{B}$ need to be calculated in the presence of all N bodies in the array. This is essential for WECs which are closely spaced, yet because for widely-spaced WECs the cross-coupling effects are minimal the coefficients $\mathbf{A}$ and $\mathbf{B}$ can be approximated by sparse matrices in this scenario.

3.6 Equations of the Single DoF WEC Array Motion in the Time-Domain

As was seen in Chapter 2, there are some applications which require us to model non-stationary and non-linear phenomena of the WEC system. Within the framework of linear potential flow theory, we can model a time-domain formulation equivalent of Eq. (3.40) by taking the inverse Fourier transform of the frequency-dependent elements. Including only the relevant terms as described in Section 3.5.1 the resulting equation for an array of $\mathcal{M}$ floating WECs is the following:

$$(\mathbf{M}+\mathbf{A})\ddot{\mathbf{z}}(t))+\int_0^t\mathbf{k}(t-\tau)\dot{\mathbf{z}}(\tau)d\tau+\mathbf{C}\dot{\mathbf{z}}(t)=\mathbf{f}_e(t)+\mathbf{f}_{PTO}(t). \tag{3.50}$$

This expression, also known as the Cummins equation after the person who introduced it in the given form into marine hydrodynamics, is the time-domain expression of Newton's 2^{nd} law (Cummins, 1962). In the above expression $\mathbf{z}(t)$

is the $1 \times \mathcal{M}$ vector of motions of each WEC in the array, $\mathbf{M}$ is the diagonal matrix of masses of each of the WECs, $\mathbf{A}$ and $\mathbf{B}$ are the $\mathcal{M} \times \mathcal{M}$ added mass and radiation damping matrices, respectively, and $\mathbf{C}$, and $\mathbf{B}_{PTO}$ are the $\mathcal{M} \times \mathcal{M}$ diagonal matrices of the hydrostatic and PTO coefficients, respectively. Lastly, on the right side we have the forcing terms: $\mathbf{f}_e(t)$ is the $1 \times N$ vector of the wave excitation forces on each WEC and $\mathbf{f}_{PTO}(t)$ is the vector of the PTO forces on each WEC. Applying the convolution theorem to the kernel of the frequency-domain excitation force in (3.24) and the free surface elevation η gives the excitation force $\mathbf{f_e}(t)$ in the time-domain: (Falnes, 2002):

$$\mathbf{f_e}(t) = \frac{2}{\pi} \int_0^\infty \left[\int_{-\infty}^{\infty} \hat{\mathbf{F}} e^{-i\omega t} d\omega \right] \eta(t-\tau) d\tau. \tag{3.51}$$

The radiation force results in the convolution kernel $\mathbf{k}(t)$ which stems from persistent effects of the body on the free surface (for details see (Falnes, 2002)). Since $\mathbf{K}(t)$ is the inverse Fourier transform of the frequency-domain radiation impedance matrix it can be calculated by a convolution of either the frequency-dependent added mass $\mathbf{A}(\omega)$ or radiation damping coefficient $\mathbf{B}(\omega)$:

$$\begin{aligned} \mathbf{K}(t) &= \frac{2}{\pi} \int_0^\infty \mathbf{B}(\omega) cos(\omega t) d\omega \\ \mathbf{K}(t) &= \frac{2}{\pi} \int_0^\infty \omega \left[\mathbf{A}(\omega) - \mathbf{A}_\infty \right] sin(\omega t) d\omega \end{aligned} \tag{3.52}$$

where the added mass term $\mathbf{A}$ has been split into the frequency dependent part $\mathbf{A}(\omega)$ and the constant added mass matrix at infinity $\mathbf{A}_\infty$. In practise the convolution method is cumbersome and is very slow to compute. As an alternative, the Eq. (3.52) are often represented in *state space* form (see Yu and Falnes (1995) for details). Note that the above equations apply for a system without added PTO damping. Because of its effect on the motion of the WECs, B_{pto} will have to be added to the r.h.s. of equation (3.52).

The critical assumption made in this subsection is that all the hydrodynamic responses are steady-state. In other words the coefficient matrices $\mathbf{A}$, $\mathbf{B}$ and $\mathbf{C}$ are calculated *a priori* and assumed constant throughout the simulation time t. This enables us to utilize a frequency-domain wave-structure interaction solver such as NEMOH (see Section 4.2.1) which greatly speeds up the calculation times compared to a complete time-domain calculation. The forcing terms on the right hand side of Eq. (3.50), however, can be time variable. This enables us to use this particular approach to model non-steady sea states and more importantly real time control where f_{PTO} changes with time non-linearly.

3.7 Modelling WECs in Irregular Seas

In deriving the expressions in the preceding sections it was assumed that the WECs interact with a regular wave of frequency ω of the form given by Eq. (3.15). However, as we instinctively know, real ocean waves are never regular monochromatic.

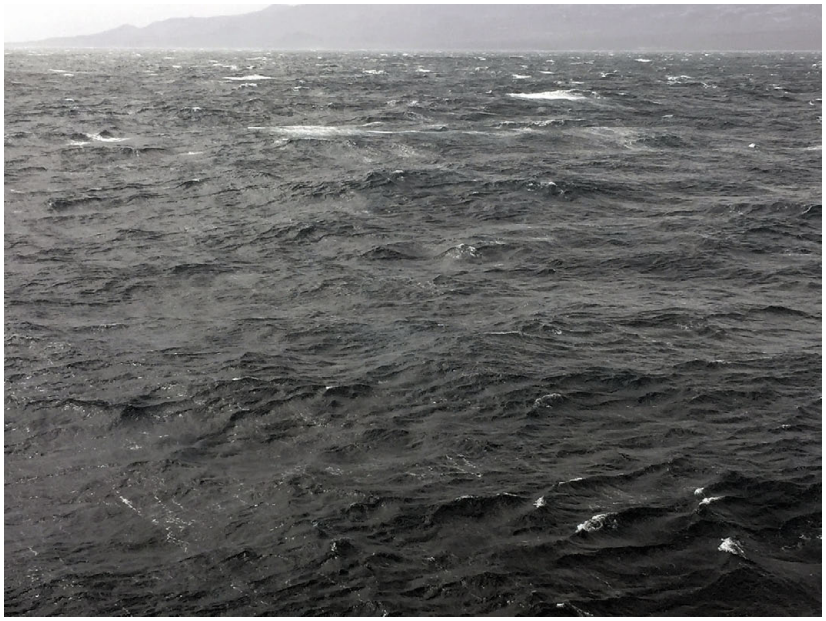

Figure 3.7: Picture of an irregular sea state typical of a majority of the world's oceans. Photo by author.

At first glance real seas can seem a chaotic combination of different size waves coming from different directions as we observe in Fig. 3.7 for example. Fortunately, linear wave theory allows us to model irregular sea states as a linear combination of regular components, each of a frequency ω.

The underlying assumption of this approach, and of linear wave theory in general, is that no transfer of energy occurs between the waves of different frequencies (Mei et al., 2005). This assumption is generally sound for the majority of operational non-storm conditions which form the core of the modelling scenarios in this thesis. The convention in marine hydrodynamics, and by extension wave energy conversion, is to model irregular sea states as a spectral density function or the spectral variance function $S(\omega)$ where the wave frequency distribution is derived from empirical studies of real sea states. Assuming for the moment that the frequency spectrum is continuous, we define the two most commonly used spectral forms. The first, formulated in 1964 by Pierson and Moskowitz (1964), is the Pierson-Moskowitz (PM) spectrum for a fully developed sea state. The PM spectrum,$S_{PM}(\omega)$, mimics the conditions in the open sea where the wind and fetch allows the waves to develop until the breaking limit is reached. The spectrum is commonly formulated as

$$S_{PM}(\omega) = 5\pi^4 \frac{H_{m0}^2}{T_p^4 \omega^5} e^{\left[-\frac{20\pi^4}{T_p^4 \omega^4} \right]} \tag{3.53}$$

where H_{m0} is the spectral significant wave height given by:

$$H_{m0} = 4\sqrt{\int_0^\infty S(\omega)d\omega} \tag{3.54}$$

and T_p is the peak period of the wave. The spectral moment m_0 is defined in Eq. (3.62) in Section 3.8. Since the coastal areas are targeted are exposed to open ocean conditions in the simulations of this thesis, the PM spectrum is utilized for the entirety of the irregular wave simulations in this thesis. An alternative spectral distribution, called JONSWAP (Joint North Sea Wave Observation Project) after the experiment name, was developed based on wave data collected over several year in the fetch-limited North Sea (Hasselmann and Olbers, 1973), and is generally used for such applications. The JONSWAP spectral distribution, S_{JS} is given by:

$$S_{JS}(\omega) = \alpha 5\pi^4 \frac{H_{m0}^2}{T_p^4\omega^5}\gamma^{e\left[-\frac{20\pi^4}{T_p^4\omega^4}\right]}\gamma^{e\frac{-(\omega-\omega_p)^2}{2\sigma^2\omega_p^2}} \tag{3.55}$$

where the parameters $\alpha = 0.0081$ and $\sigma = 0.07$ when $\omega < \omega_p$ and $\sigma = 0.09$ when $\omega > \omega_p$. The γ parameter represents the peakedness of the spectrum. The value of $\gamma = 3.3$ is usually given for the wind seas in closed basins such as the North Sea which the JONSWAP spectrum was found to best represent. To simulate the directional spreading expected in real sea conditions we multiply the omnidirectional Pierson-Moskowitz or JONSWAP spectrum in Eq. (3.53) or (3.55) by a directional spreading function. The most common one and the one we utilize in this thesis is the cos^{2s} spreading function, originally derived by Mitsuyasu et al. (1975) and described by Eq. (3.56):

$$D(\theta) = \frac{1}{\sqrt{\pi}}\frac{\Gamma(s+1)}{\Gamma(s+1/2)}cos^{2s}(\theta - \bar{\theta}), \tag{3.56}$$

where $\bar{\theta}$ is taken to be the mean direction of wave incidence. In this thesis this quantity is represented by β. The wave spreading parameter s is set equal to 10 which is a typical value for the North Atlantic wave climate (Goda, 2000). From $S(\theta)$ we can calculate ζ of each irregular wave component as:

$$\zeta = \sqrt{2\ S_{PM}(H_{m0}, T_p, \omega)D(\theta)\delta\omega\delta\theta} \tag{3.57}$$

where $\delta\omega$ is the angular frequency bin width. The total free surface elevation η for an irregular wave field is then the sum of the product of ζ and the unit amplitude total wave η for each frequency component ω:

$$\eta_{irr} = \sum_{i=1}^{N} \zeta\eta_i. \tag{3.58}$$

Here η_{irr} indicates the total irregular wave field to distinguish it from the regular free surface elevation η for a regular wave.

3.8 Power Output for an Array of WECs

The primary purpose of a WEC is to extract energy from the waves and convert it into useful power, whether mechanical such as in the case of reverse osmosis or most commonly, electrical. Therefore in this section the expressions that are utilized in this thesis to calculate the power of a single WEC and sequentially, an array of WECs are given. Firstly, a brief look at the energy contained in the wave is made to see the theoretical power contained in the waves. Secondly, the theoretical maximum power that a WEC array can convert under optimal conditions is derived. Finally, a focus is made on the equations that will be utilized in obtaining the results presented in the rest of this thesis, namely, the realistic power absorption of a WEC with a passively tuned PTO.

3.8.1 Defining the wave energy resource

As we have noted in Section 3.7, realistic ocean waves are best described as a stochastic process. Therefore, the quantities relevant to the energy contained in the waves also need to be expressed as a distribution. As was seen in Section 3.7, the accepted way of representing realistic waves is through the spectral distribution $S(\omega)$, which can be parametrized by a known spectral shape. It can be noted that when we describe the spectral distribution we describe the frequency spectrum only. The following equations derived in this subsections apply to omnidirectional waves. For short crested or multi-directional seas, the presented expressions also need to be multiplied by the directional distribution that is dependent on the incoming wave incidence angle β as will be expressed in Eq. (3.66) (Folley, 2017).

Firstly, the wave power density $J(\omega)$ for a single wave component is derived:

$$J(\omega) = \rho g S(\omega) \cdot C_g \tag{3.59}$$

where $\rho g S(\omega)$ is the energy in the wave. The speed at which the wave energy propagates depends on the angular wave frequency ω and water depth h and is given by:

$$C_g(\omega) = \frac{\omega}{2k(\omega)} \left(1 + \frac{2k(\omega)h}{\sinh(2k(\omega)h)}\right) \tag{3.60}$$

Utilizing linear superposition as explained in Section 3.7, the average power density for a given sea state defined by the integral over the wave components:

$$J(\omega) = \int_0^\infty \rho g S(\omega) \cdot \frac{\omega}{2k(\omega)} \left(1 + \frac{2k(\omega)h}{\sinh(2k(\omega)h)}\right) d\omega. \tag{3.61}$$

If we define the n_{th}wave spectral moments as:

$$m_n = \int_0^\infty S(\omega)(\omega)^n d\omega \tag{3.62}$$

then the wave energy period, T_e, can be defined as the ratio between the -1st moment and the 0th moment of the wave spectrum:

$$T_e = \frac{m_{-1}}{m_0}. \tag{3.63}$$

From Eq. (3.63) and (3.54), we can define the equation for the directional wave power J in deep water:

$$J = \frac{\rho g^2}{64\pi} {H_{m0}}^2 T_e. \tag{3.64}$$

The wave spectral moments can be utilized to derive additional quantities useful in wave energy conversion. One of them is the relative spreading of the energy with wave frequency, often called the spectral bandwidth ϵ_0, that can be defined as the standard deviation of the period variance density, normalized by the energy period.

$$\epsilon_0 = \sqrt{\frac{m_0 {m_{-2}}^2}{m_{-1}} - 1}. \tag{3.65}$$

The significance of ϵ_0 and alternative measures of wave frequency spreading in assessing the power output of a WEC is detailed in Saulnier et al. (2011). In the context of WEC arrays directionality always plays a role, even for axisymmetric WECs. Therefore, ideally, the directionally resolved wave power density $J(\omega, \theta)$ should be utilized in the calculation of the power output of a WEC array:

$$\begin{aligned} J(\omega,\theta) = \rho g \int_{-\pi}^{\pi} S(\omega,\varphi) \cdot C_g \cdot cos(\theta-\varphi) \delta d\omega d\varphi \\ \begin{cases} \delta = 1, & cos(\theta-\varphi) \geq 0 \\ \delta = 0, & cos(\theta-\varphi) < 0 \end{cases} \end{aligned} \tag{3.66}$$

The binary δ in the above Eq. (3.66) guarantees that only the energy coming from a 180° arc is considered in the wave power calculation.

3.8.2 Theoretical maximum converted power

Next, we formalize some general results on the power absorption of WECs and WEC arrays. Although technically the absorbed WEC power, P shall be referred to as output power in this thesis as we are looking at the conversion from the point of view of the grid and not the waves. These expressions, although not achievable in practise as was explained in detail in Section 2.8 serve as a useful and illustrative upper bound for the realistic values presented in this work.

Firstly, the average power of a system of oscillators which in the given case are the WECs in the array in the frequency-domain is defined, again, by making the assumptions that all motions are harmonic or sinusoidal. For a single WEC operating in one DoF the average power is equal to the product of the hydrodynamic force (see Section 3.4) and the velocity of the WEC:

$$P = \frac{1}{2} \Re \left[\hat{F}_{hyd} \hat{\dot{z}}^* \right]. \tag{3.67}$$

where $\hat{F}_{hyd}$ is given by Eq. (3.22) and * indicates the complex conjugate. For a system of one DoF oscillators *i.e.* a WEC array of WECs operating in one DoF,

Eq. (3.67) becomes the following:

$$P = \frac{1}{2}\Re\left[\hat{F}_{hyd}^{\mathsf{T}}\dot{\hat{\mathbf{z}}}^{*}\right], \tag{3.68}$$

where $\hat{F}_{hyd}^{\mathsf{T}}$ is the matrix transpose of the hydrodynamic forces on each body and $\hat{\mathbf{z}}^{*}$ is the complex conjugate of the column vectors of velocities of each WEC in the array. Using the method performed on the hydrodynamic force in Section 3.4 on the power we write the total average power as the difference of the excitation and the radiation power (Falnes, 2002):

$$P = P_{ex} - P_{rad} \tag{3.69}$$

where P_{ex} is the power absorbed by the WECs from the wave excitation while P_{rad} is the power given off through radiation. Equation (3.69) can be expanded to:

$$\mathbf{P}_{arr} = \frac{1}{2}\Re\left[\hat{\mathbf{F}}_{\mathbf{ex}}^{*} i\omega\hat{\mathbf{z}}\right] - \frac{1}{2}\hat{\mathbf{z}}^{*}\mathbf{B}\omega^{2}\hat{\mathbf{z}}. \tag{3.70}$$

where Eq. (3.38) is used to re-write the radiation force as the complex conjugate product of the WEC velocities $\hat{\mathbf{z}}$ and $\mathbf{B}$. It can be noted that since power is taken as the real part of the product in Eq. (3.68), the imaginary part of Eq. (3.38) does not contribute to the power absorption.

Equation (3.70) can be re-written as:

$$P_{arr,max} = \frac{1}{8}\hat{\mathbf{F}}_{ex}^{*}\mathbf{B}^{-1}\mathbf{F}_{ex} - \frac{1}{2}\left(\hat{\mathbf{z}} - \frac{1}{2}\mathbf{B}^{-1}\mathbf{F}_{\mathbf{ex}}\right)^{*}\mathbf{B}\left(\hat{\mathbf{z}} - \frac{1}{2}\mathbf{B}^{-1}\mathbf{F}_{\mathbf{ex}}\right) \tag{3.71}$$

(for details see Evans (1979)). The theoretical maximum power is reached when the second term is equal to zero and the power is equal to the first term only:

$$P_{arr,max} = \frac{1}{8}\hat{\mathbf{F}}_{\mathbf{ex}}^{*}\mathbf{B}^{-1}\hat{\mathbf{F}}_{\mathbf{ex}}. \tag{3.72}$$

This condition is satisfied when the body motions are equal to the following:

$$\hat{\mathbf{z}} = \frac{1}{2}\mathbf{B}^{-1}\hat{\mathbf{F}}_{ex}. \tag{3.73}$$

Equations (3.72) and (3.73) are the mathematical equivalent of Falnes (2007) famous statement, "The physical law of conservation of energy requires that the energy-extracting device must interact with the waves such as to reduce the amount of wave energy that is otherwise present in the sea". In other words the wave radiated by the system of WECs must interfere destructively with the incident wave such that the radiation part of Eq. (3.72) must completely cancel out. It is important to remark here that the theoretical maximum limit is unreachable in real world scenarios, even for an ideal friction lossless WEC system. Equation (3.73) requires that all motions are optimal, meaning that the complex conjugate of the radiation damping matrix $\mathbf{B}$ is required for all wave frequencies for all WECs. This condition is impossible to achieve in real seas where prefect knowledge of the

future state is required (Falnes, 1995). Moreover, to precisely match the excitation in Eq. (3.70) at all wave frequencies, the PTO system needs to have an adjustable mass, spring and damper, as evidenced from Eq. (3.41) for a single WEC and from (3.47) for an array of WECs. As seen in Chapter 2 in Section 2.8, this requires a complex PTO subject to large forces and motions, rendering the WEC prohibitively expensive. Despite these caveats, the Eqns. (3.72) and (3.73) serve as useful theoretical upper limits to the power absorbed by an array and its motions.

3.8.3 Power output by a resistive (real) PTO

In treating an array of WECs as a black-box system of oscillators, we have defined the theoretical limits on the maximum power absorption in Section 3.8.2. The power absorption and hence the output of real WECs, however, is a function of the PTO system and any mechanical constraints placed on the system as well as the mechanical structure of the WEC itself. Although a spring-damper PTO system that is tuned reactively to allow the PTO to approach the theoretical maximum is possible, in practise such a system has proven often be more expensive to construct and maintain the benefit it provides in terms of the power output (Babarit, 2017). Therefore in this thesis the focus is on passively controlled PTO systems,also known as real-controlled because the real part of Eq. (3.43) is varied. For the PTO force defined by Eq. (3.43) and a single DoF linear WEC modelled in this thesis, the mean output power is given by (Alves, 2016):

$$P = \frac{1}{T}\int_0^T B_{PTO}\dot{z}^2 dt. \tag{3.74}$$

It can be noted that for more sophisticated PTOs that cannot be expressed via a linear model, an alternative expression can be found. The particular case of a hydraulic PTO is explored in Chapter 6. Returning to the frequency-domain and once more assuming that all motions are harmonic we can write Eq. (3.74) as the following:

$$P = \frac{1}{2}B_{PTO}\omega^2|\hat{\dot{z}}|^2. \tag{3.75}$$

Extending the single WEC equation to a WEC array operating in one DoF for arrays of heaving or pitching systems, respectively, the expression (3.75) becomes:

$$\mathbf{P}_{arr,l} = \frac{1}{2}\mathbf{B}_{PTO,l}|\hat{\mathbf{z}}(\omega)|^2\omega^2 \tag{3.76a}$$

$$\mathbf{P}_{arr,l} = \frac{1}{2}\mathbf{B}_{PTO,l}|\hat{\theta}(\omega)|^2\omega^2, \tag{3.76b}$$

where $\hat{\mathbf{z}}$ and $\hat{\boldsymbol{\theta}}$ indicate an $\mathcal{M}\times 1$ column vector of the WEC positions or angular displacement, respectively. $\mathbf{B}_{PTO}$ represents an $\mathcal{M}\times\mathcal{M}$ diagonal matrix with the B_{PTO} coefficients for each WEC on the diagonal. The time-domain equivalent of Eq. (3.76) is given by:

$$\mathbf{P}_{arr,h} = -\frac{1}{T}\int_0^T \mathbf{F}_{PTO}(t)\cdot\dot{\mathbf{z}}(t)dt \tag{3.77a}$$

$$\mathbf{P}_{arr,h} = -\frac{1}{T}\int_0^T \mathbf{T}_{PTO}(t)\cdot\dot{\theta}(t)dt, \tag{3.77b}$$

where the boldface quantities represent $\mathcal{M}\times 1$ column vectors of the forces and velocities of the individual heaving cylindrical WECs of the torques and angular displacements of the individual OSWECs. An important measure of the array effects is the *q*-value, first introduced qualitatively in Section 2.2. Here we present a quantitative definition of the *q*-value as the ratio of $\mathbf{P}_{arr}$ defined in Eq. (3.76) and $\mathcal{M}$ times the single WEC power given in Eq. (3.74) for an array of $\mathcal{M}$ WECs.

$$q = \frac{\mathbf{P}_{arr}}{\sum P_{isol}}. \tag{3.78}$$

where P_{isol} indicates that each of the individual WECs in the denominator operates as if hydrodynamically isolated from one another. The *q-value* is a commonly used metric in wave energy literature to assess the strength of array effects, we find it used in Borgarino et al. (2011b); Child and Venugopal (2010); Child et al. (2011); Stratigaki (2014); Penalba et al. (2017a), for example. It shall be presented along with the values of power output in the following chapters of this thesis. Another common metric of hydrodynamic efficiency utilized in the wave energy literature is the Capture Width Ratio or CWR, also commonly referred to as the capture efficiency Babarit (2017). Although there are various ways to define this parameter, the example of (Babarit, 2015) is here followed and CWR is defined as:

$$CWR = \frac{P}{JW} \tag{3.79}$$

where P is $\mathbf{P}_arr$ the power output of the array (Chapter 6) or $\mathbf{P}_{farm}$ (Chapter 7)) and W is the corresponding characteristic dimension of the WEC array (Chapter 6) or WEC farm Chapter 7.

3.8.4 Limitations to the Linear Potential Flow Theory approach

While linear Potential Flow Theory is a the most versatile approach available to numerical modellers today, with a wide variety of applications and solvers, the method is not without its limitations. We recall that the critical assumptions are a wave amplitude much smaller than the wavelength, the excursion amplitude of the moving WEC is small, and that in realistic seas, energy transfer between frequencies does not occur. Although these assumptions are valid for a majority of WEC array operations, there are several scenarios which entail violations of the aforementioned assumptions. The first is for actively controlled WEC systems. As we alluded to in Section 2.8, such WECs often have large excursion relative to

the wave amplitude ζ and thus the linear assumption of small motion is violated. Furthermore, in such cases the viscous effects, mentioned briefly in Section 3.5.1 can become important. This is also the case for modelling OSWECs under particular wave conditions, as mentioned in Giorgi and Ringwood (2018). Furthermore, for heaving WECs which have a body shape that causes the wetted body surface area to vary with heaving motion, the non-linear Froude-Krylov forces also become time-dependent, a violation of the assumptions of linear Potential Flow Theory. The two aforementioned forces also apply to non-standard shaped WECs, including those that are deformable (Babarit, 2017). The most important case where Potential Flow Theory cannot be applied without making substitutional errors is survival mode, that is WECs and arrays operating in extreme wave conditions. In this case, most assumptions of linear wave theory are violated, therefore numerical approaches such as BEM methods cannot be utilized. Many recent publications have focused on the WEC survivability, (Ransley et al., 2017; Devolder et al., 2017) which have utilized non-linear CFD methods that solve the non-linear Reynolds Averaged Navier-Stokes (RANS) equations.

3.8.5 Conclusion

While non-linear methods are gaining popularity amongst researchers due to increasing computer power, the WEC array problem is still largely within the domain of linear solvers, especially for large multi-WEC arrays. Although non-linear models give the most accurate results, often the speed and underlying simplicity of the model is a more important factor in the solution method selection. Given the needs of a fast, reasonably accurate and straightforward methodology for achieving the balance of calculating WEC array power and *far-field* effects, for the scope of this thesis, linear Potential Flow Theory is the best choice.

Chapter 4

One-way Coupling Between a BEM Solver and a Wave Propagation Model

Abstract

Due to hydrodynamic interaction between WECs in an array, the geometric layout of the WEC array will influence the power production and affect the surrounding area around the WECs. It is essential, therefore, to model both the *near-field* and *far-field* effects of a WEC array. It is difficult to model both by employing a single numerical model that offers the desired precision at a reasonable computational cost, however. In this chapter a coupling methodology is introduced that will allow to model both the *near* and *far*-field effects accurately. This chapter introduces a one-way coupling methodology between the wave-interaction (WSI) BEM solver NEMOH and the mild-slope wave propagation model MILDwave. In a one-way coupling the wave field for each numerical model is calculated independently. In this analysis, the information from NEMOH is fed to MILDwave by imposing a complex wave amplitude and phase at a coupling radius, r_c, *i.e.* taken to be greater than the diameter of a single WEC or the circular area around a WEC array. NEMOH is used to model the motion of the WECs and the *near-field* effects while MILDwave is utilized to model the WEC *far-field* effects. The K_d of the NEMOH-MILDwave coupled model are compared to results from NEMOH for 2 different WEC array test cases. Two alternative methods of passing the information from NEMOH to MILDwave are compared. For a circular coupling region, the sensitivity of the results to r_c is investigated. Finally the choice of the coupling method for the remaining chapters of the thesis and the motivations behind it are given in Section 4.11.

4.1 Introduction

The fundamental principle of the results given in this thesis is that of model coupling. That is the joining of the numerical capabilities of one model to another one in order to produce a result that either model will not be capable of obtaining overall or in a time-efficient manner. For the WEC array problem, the coupling paradigm addresses the balance between sufficient accuracy in modelling individual WEC motion in an array simulated in a large enough numerical domain. The large model domain is capable of including large WEC arrays and the areas surrounding those arrays that might be impacted by the arrays' presence.

Because of hydrodynamic interactions between closely-spaced WECs, in the *near-field* effects, the amount of energy produced by a wave array is not equivalent to the sum of the energy produced by individual WECs. Furthermore, because of the *far-field* effects, the WEC array might have impacts on the adjacent coastline and other sea users. As a consequence, one of the design challenges for wave energy project developers is the optimal placement of WECs that balances the economic needs of the project with the potential deleterious effects on the surrounding environment. The aim is to balance the need to place the WECs in an optimal position to maximize average annual yield while at the same time minimize the far-field effects which might modify the coastal wave field.

As we have reviewed in Chapter 2, to date most modelling has focused on either the first problem (*near-field* effects) or the second (*far-field* effects), in part because of the limitations of numerical tools that are able to model both effects simultaneously. Since a modelling tool needs to balance resolution with computational cost, most models have focused either on resolving the near-field effects at high fidelity but high computational cost or the far-field effects at low fidelity but low cost. The results presented in this chapter introduce and validate the coupling approach by demonstrating its utility in simulating WEC array effects. Pairing models of different resolution and computational cost can enable the modeller to obtain the results at different resolutions for different sub-domains of the problem while keeping the overall computational costs reasonable. The chapter is begun by introducing the numerical tools utilized in the presented coupling, the BEM wave-structure interaction solver NEMOH in Section 4.2.1 and the mild-slope equation wave propagation model MILDwave Section 4.2.2. The one-way coupling technique and compare it to other approaches such as two-way coupling is next defined in Section 4.3.2. Two differing one-way coupling approaches are given in Section 4.3 and results are shown for both methods. A sensitivity analysis of the wave field to the coupling radius is performed in Section 4.10.

4.2 Numerical Tools

First, two numerical solvers that are coupled, the BEM wave-structure interaction solver NEMOH, and the mild-slope equation wave propagation model MILDwave are introduced. The former is used to calculate the WEC motions, forces, and free surface elevations in the *near-field* inner domain while the latter calculates the free

surface in the *far-field* outer domain model (see Fig. 4.4). While generally the two definitions correspond, it is important to note that the inner domain can be as small as the area immediately surrounding the WEC or as large as the whole WEC array or even multiple closely-spaced WEC arrays. The outer domain model can also include portions of the *near-field* zone, especially in the case where we have strong *array effects*.

4.2.1 Boundary Element Method wave-structure interaction solver NEMOH

In the coupling approach herein, the array effects induced by the hydrodynamic interaction between the WECs are resolved using the open-source BEM solver NEMOH (Babarit and Delhommeau, 2015), developed at the École Centrale de Nantes. The current Version v2.03 is based on linear Potential Flow Theory and thus makes the following assumptions:

- The fluid is inviscid;
- The fluid is incompressible;
- The flow is irrotational;
- The wave amplitude is small with respect to the wavelength;
- The amplitude of the body motion is small with respect to its dimension;
- The sea bottom is flat.

As detailed in Section 3.3.1, the flow is described by the velocity potential ϕ. Using the definition given in Eq. (3.5), NEMOH solves the Laplace equation Eq. (3.6) for the complex velocity potential, $\hat{\phi}$ given a set of boundary conditions on the wetted body surface, the free surface, sea bottom and the far-field. This equation is valid in the entire fluid domain, denoted here by Ω. The whole velocity potential problem becomes then a linear Boundary Value Problem (BVP), visually represented in Fig. 4.1. The boundary conditions are given as the set of Eqns. (4.1)

$$\begin{cases} \frac{\partial\hat{\phi}(\Upsilon)}{\partial z} = \frac{\omega^2}{g}\hat{\phi}(\Upsilon) & \forall\Upsilon \in \partial\Omega_F \\ \frac{\partial\hat{\phi}(M)}{\partial z} = 0 & \forall\Upsilon \in \partial\Omega_h \\ \frac{\partial\hat{\phi}(\Upsilon)}{\partial z} = f(\Upsilon) & \forall\Upsilon \in \partial\Omega_S \\ \sqrt{R}(\frac{\partial\hat{\phi}(\Upsilon)}{\partial r} - ik_0)(\hat{\phi} - \hat{\phi}_\infty) \to 0 & r \to 0 \end{cases} \tag{4.1}$$

Here, $\Upsilon(x, y, z)$ is a given point in the fluid domain, $f(\Upsilon)$ is a scalar function, k_0 is the wave number solution of the dispersion relation and $\hat{\phi}_\infty$ is the incident velocity potential at infinity. r_d is the radial distance from the coordinate origin. The boundary conditions are expressed over the different boundary surfaces, where the indices stand for:

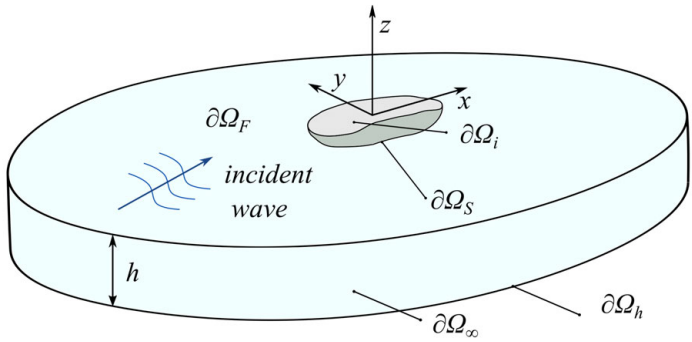

Figure 4.1: Linear boundary value problem resolved in NEMOH (adapted from Babarit and Delhommeau (2015).)

- F: fluid domain boundary
- h: sea bed boundary
- S: floating body boundary
- i: interface of floating body with the free surface

This 3D problem can be transformed into the 2D problem of a source distribution on the body surface using Green's second identity and the appropriate Green function: (Delhommeau, 1989).

Using Green's theorem, it can be shown that (Delhommeau, 1987) the velocity potential is given by:

$$\frac{\Phi}{2}(\Upsilon_t T) = -\frac{1}{4\pi}\iint_{\partial\Omega_B+}\sigma(\Upsilon')G(\Upsilon_t\Upsilon')dS' \tag{4.2}$$

With $G(\Upsilon,\Upsilon')$ the Green function for linearised free-surface hydrodynamics and $\sigma(\Upsilon)$ a source distribution given by:

$$\frac{\sigma}{2}(\Upsilon_t T) - \frac{1}{4\pi}\iint_{\partial\Omega_B}\sigma(\Upsilon')\frac{\partial G(\Upsilon,\Upsilon')}{\partial n}dS' = f(\Upsilon) \tag{4.3}$$

The mathematical problem is then discretised using a Constant Panel Method, leading to a linear matrix problem whose coefficients are the influence coefficients. The Boundary Value Problem (BVP) is numerically solved in the frequency-domain, leading to the full flow field underneath the body. From the flow field, several other quantities are calculated:

- The hydrodynamic coefficients: added mass A and hydrodynamic or radiation damping B;
- The pressure field p on the body surface and the Froude-Krylov forces F_{FK};

- Far-field diffracted and radiated velocity potential in the form of Kochin functions;
- Near-field diffracted and radiated free surface elevation $|\eta_D|$ and $|\eta_R|$;

The free surface elevation η for each frequency component ω is calculated by taking the real part of the complex surface elevation $\bar{\eta}$. It is in turn obtained in NEMOH from the free surface boundary condition Eq. (4.1) for the diffraction problem and the radiation problem, respectively, and summed to η by applying the linear superposition principle of Eq. (3.15).

$$\bar{\eta} = -\frac{1}{g}\left(\frac{\partial \phi}{\partial t}\right)_{z=0} \tag{4.4}$$

where $z = 0$ is the undisturbed free surface. The coefficients of the added mass $A(\omega)$, hydrodynamic damping $B(\omega)$, and hydrodynamic restoring force or buoyancy force $K(\omega)$ which are utilized to calculate the WEC motions while the free surface elevation η is necessary for the coupling with the wave propagation model, MILDwave.

4.2.2 Mild-slope wave propagation model MILDwave

For simulating the *far-field* WEC array effects, the wave propagation model MILDwave is employed Troch (1998); Troch and Stratigaki (2016). MILDwave, developed at the Coastal Engineering Research Group of Ghent University, Belgium, is a phase-resolving model based on the depth-integrated mild-slope equations (Eqs. (4.5a) and (4.5b)) introduced by Radder and Dingemans (1985). This particular model has been used in simulating WEC arrays in a number of recent publications: Beels et al. (2010); Stratigaki (2014); Troch and Stratigaki (2016); Verbrugghe et al. (2016); Balitsky et al. (2017b); Verao Fernandez et al. (2018); Balitsky et al. (2018b) (for details see Section 4.2.2).

4.2.2.1 Governing equations

The mild-slope equations describe the transformation of linear irregular waves with a narrow frequency band over a mildly varying bathymetry (seabed steepness up to 1/3) by (Brorsen and Helm-Petersen, 1998):

$$\frac{\partial \eta}{\partial t} = \frac{\omega^2 - k^2 C C_g}{g}\phi - \nabla \cdot (\frac{C C_g}{g}\nabla \phi_t ot) \tag{4.5a}$$

$$\frac{\partial \phi}{\partial t} = -g\eta \tag{4.5b}$$

Here η and ϕ_t are, respectively, the surface elevation and the total velocity potential at the free water surface. A finite difference scheme on a two-step space-centred, time-staggered computational grid is used to descritize and solve equations (4.5a)

and (4.5b). The domain is uniformly divided in grid cells with dimensions Δx and Δy and central differences are used for spatial as well as time derivatives. Both η and ϕ are calculated in the centre of each grid cell at different time levels, $(n+\frac{1}{2})\Delta t$ and $(n+1)\Delta t$, respectively, leading to the following discretised equations (Brorsen and Helm-Petersen, 1998):

$$\begin{aligned} n_{i,j}^{n+\frac{1}{2}} \cong\, & n_{i,j}^{n-\frac{1}{2}} + \mathcal{B}_{i,j}\phi_{i,j}^{n}\Delta t \\ & - \frac{\mathcal{A}_{i+1,j} - \mathcal{A}_{i-1,j}}{2\Delta x}\frac{\phi_{i+1,j}^{n} - \phi_{i-1,j}^{n}}{2\Delta x}\Delta t \\ & - \mathcal{A}_{i,j}\frac{\phi_{i-1,j}^{n} - 2\phi_{i,j}^{n} + \phi_{i+1,j}^{n}}{(\Delta x)^2}\Delta t \\ & - \frac{\mathcal{A}_{i,j+1} - \mathcal{A}_{i,j-1}}{2\Delta y}\frac{\phi_{i,j+1}^{n} - \phi_{i,j+1}^{n}}{2\Delta y}\Delta t \\ & - \mathcal{A}_{i,j}\frac{\phi_{i,j-1}^{n} - 2\phi_{i,j}^{n} + \phi_{i,j+1}^{n}}{(\Delta y)^2}\Delta t \end{aligned} \tag{4.6}$$

Internal wave generation techniques are used in tandem with absorbing sponge layers at the open boundaries. Waves are generated at an offshore boundary using the source term addition method (Lee and Suh, 1998), adding an additional surface elevation η^* to the calculated value on a wave generation line for each time step. The wave generation line can be straight or a circle. At the domain boundaries waves are numerically absorbed by sponge layers and is obtained by multiplying the calculated surface elevations on each new time step with an absorption function $\mathcal{S}(b)$ that has a value of 1 at the start of the sponge layer and smoothly decreases till a value of 0 at the end Fig. 4.2. Three absorption functions are available in MILDwave:

$$S_1(b) = \sqrt{1 - (\frac{b}{B_s})^2} \tag{4.7}$$

$$S_2(b) = \frac{1}{2}\left(1 + \cos\left(\pi\frac{b}{B_s}\right)\right) \tag{4.8}$$

$$S_3(b) = \frac{1}{\exp((\mu^{-(B_S - b)} - \mu^{-B_s})\ln a_n)} \tag{4.9}$$

with B_s the length of the sponge layer and b the distance from the outside boundary, both expressed in number of grid cells. The absorption function $S_3(b)$ has been designed, based on the absorption function in Larsen and Dancy (1983) to avoid the adapted wave generation and the negative effects from the side sponge layers. $S_3(b)$ equals approximately 1 over a over a longer distance in the beginning of the sponge layer (see Fig. 4.2). It has been found through various testing that $S_2(b)$ gives the best performance in mitigating unwanted wave reflection at the end of the basin opposite the generation line. Consequently this sponge layer function will be used exclusively in the coupled model results presented in this thesis.

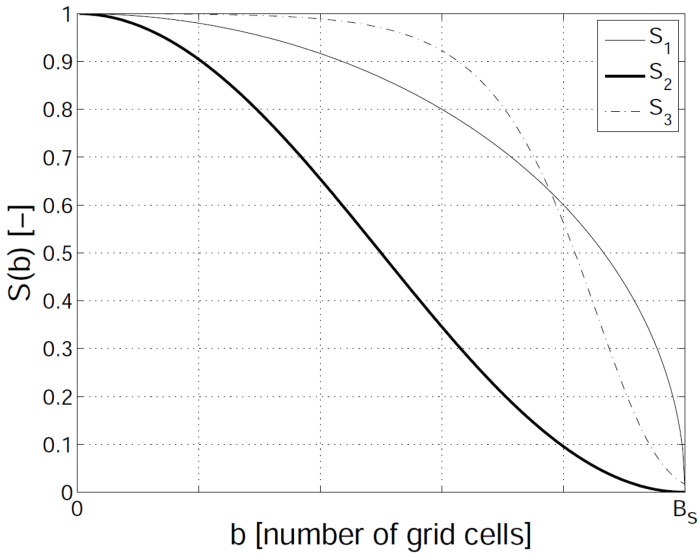

Figure 4.2: Absorption functions $S(\mathrm{b})$ through the sponge layer with length B_s (adapted from (Beels (2009))

4.3 Presenting the Coupling Methodology

A numerical coupling methodology for predicting the wave field around WECs and other floating structures inspired by the work of Stratigaki (2014); Stratigaki et al. (2019); Charrayre et al. (2014a), both of which coupled a wave structure interaction solver to a wave propagation model. The current coupling methodology has been developed to combine:

1. the advantages of wave-structure interaction solvers, which accurately formulate and efficiently resolve the physical processes in wave energy absorption and floating structures;

2. and the benefits of wave propagation models, which efficiently resolve the propagation and transformation of waves over large distances, including bathymetric effects and wave transformation processes when approaching the coastline.

A concurrent similar coupling concept is developed between NEMOH and the wave propagation model OceanWave3D in Verbrugghe et al. (2017b).

4.3.1 General principles

The goal of the coupling methodology is to predict the total wave field, by superposing the *perturbed* (diffracted + radiated) wave field and the incident wave

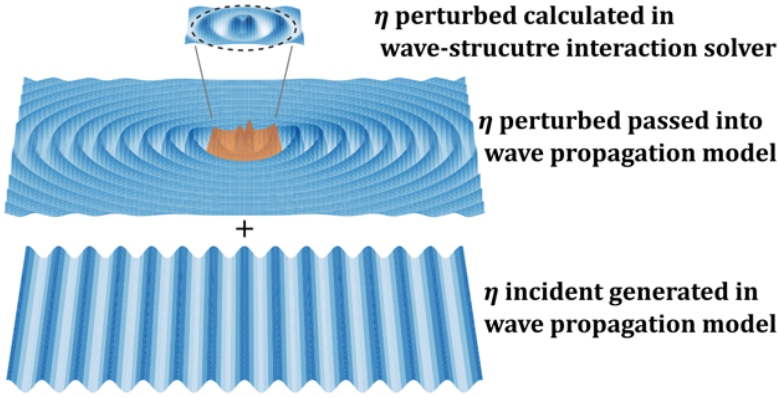

Figure 4.3: 3-D representation of the linear coupling methodology adopted from (Verbrugghe et al., 2018)

field. A frequency-domain wave-structure interaction solver is used within an inner domain around the floating or fixed objects to calculate the perturbed wave field. The propagation and transformation of the incident waves in a large domain is calculated by employing a wave propagation model.

The coupling methodology is applicable to both floating and fixed offshore WECs Stratigaki (2019). The focus in this thesis is on floating and bottom-fixed moving WECs *i.e.* the most computationally demanding case. The general concept is sketched in Figure 4.3. The main coupling procedure is a superposition of two separate simulations: one for the incident wave field and another for the perturbed wave field. The perturbed wave field is a combination of the radiation and diffraction (including wave reflection) and is calculated during a first run in the frequency-domain by the wave-structure interaction solver, within the restricted zone around the WEC, indicated by the dashed circle in Figure 4.3. Note that this zone can be used either around a single WEC or around a cluster of WECs, which is a concept *i.e.* further explored in Chapter 5. Within the wave propagation model, the perturbed field is propagated outwards from a fixed point within the domain. In a separate run, which is termed the *empty basin run*, the incident waves are propagated over the entire domain in the wave propagation model. Only after both runs have finished the wave fields are superimposed giving the total wave field, given the linear superposition principle elucidated in Section 3.4.1.

4.3.2 One-way versus two-way model coupling

Before moving on to the explore the results, it is important to define the present coupling methodology as *one-way* model coupling and to distinguish it from a *two-way* coupling methodology. The two coupling approaches detailed further in

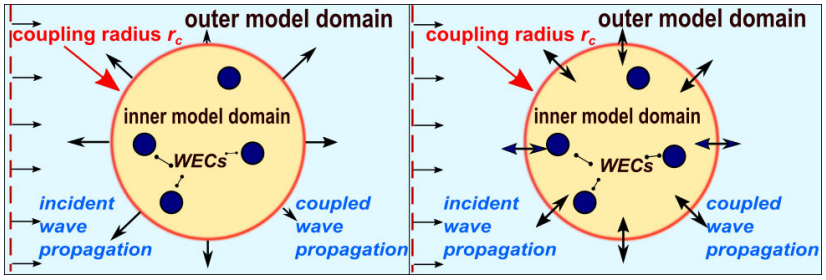

Figure 4.4: Schematic diagram of a one-way coupling (left) and two way coupling (right)

Sections 4.8.1 and 4.8.2 differ only in the type of wave *i.e.* propagated from the inner to the outer domain model. In Fig. 4.4, a schematic drawing of one way and two way coupling is shown. The coupling strategy proposed in this thesis can broadly be categorized as one-way coupling. That is the propagation of model information from the inner model domain to the outer domain model domain without feedback of the results to the inner model from the outer domain model (see Fig. 4.4 for a schematic). In the case the wave amplitudes and phases from NEMOH are coupled into MILDwave on a circle surrounding the WEC array and propagated in the MILDwave computational grid. Other possibilities include a square domain with the caveat that the inner domain corners to not induce irregularities in the outer domain model K_d. In a one-way coupling the wave field for each numerical model is calculated independently, as seen by the blue arrows in Fig. 4.5, and then summed to give the final result. The alternate approach of two-way coupling, requires information to be fed back from the result in the outer domain model into the inner model to give the next iteration. This methodology, although more accurate in principle, is much more time consuming and computationally costly because it requires a re-run of the inner model based on new input parameters. In investigating the WEC array effects in this thesis, it was found that in a majority of the cases such precision is not necessary as the *far-field* effects have a negligible impact on the *near-field* motions of the WECs except in the cases where they are located relatively close, i.e. several WEC diameters away. In this scenario, an alternative approach to a *two-way* coupling is to combine multiple WECs in a single inner domain perturbed field run, as is done in this chapter and in Chapter 5. To perform the coupling runs in this chapter, the information from NEMOH is fed to MILDwave by imposing a complex wave amplitude and phase at a coupling radius, r_c, *i.e.* taken to be greater than the diameter of a single WEC or the circular area around a multi-WEC array. Because the mild-slope equations in MILDwave are solved on a Cartesian grid while the wave phase and amplitude from NEMOH is imposed on a circle, an important parameter of the coupling approach is the proper discretisation of r_c. It is found that the optimal r_c is equal to the grid cell size $\Delta x = \Delta y$ divided by the angular interval Δb, the details of which parameters can be found in Beels et al. (2010); Stratigaki (2014, 2019). The aforementioned condition ensures that the NEMOH values are evenly distributed on a circle defined

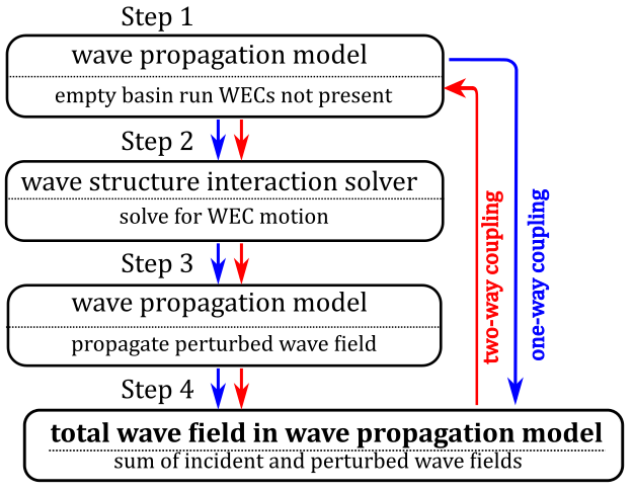

Figure 4.5: Flow chart for *one-way* coupling shown by blue arrows versus *two-way* coupling shown in red.

by r_c with no discontinuities or multiple wave summations to the same grid cell.

4.4 Calculating the Incident Wave Field

The coupled model run commences with running the empty basin to calculate the incident waves in the wave propagation model (Step 1 in Fig. 4.5). It is important to ensure that the phase angle φ is equal to $-\omega t$ at the chosen coupling location. This is necessary since the perturbed wave field is coming from the frequency-domain, where the phase is referenced with respect to the centre of inner domain. This phase matching is ensured by calculating φ in the incident wave run, at the centre of the coupling zone, and subtracting this value from the perturbed wave field phase angle. The wave propagation models are able to simulate shoaling and refraction of incident waves over complex bathymetry. In the case of MILDwave, the slope needs to remain at or below a 1 to 3 ratio (Booij, 1983). The generation of a regular plane waves at the left outer domain model is applied via the following expression:

$$\eta_I(x,y,t) = \Re\{\zeta \cdot e^{-i(\omega t - k(x\cos\beta - y\sin\beta))}\}, \tag{4.10}$$

where η_I is the incident surface elevation, and β is the wave direction. Normally the generation line is placed at the end of the up-wave sponge layer to avoid unwanted reflection and absorption of the incident wave. Waves propagate towards the right side, where the waves are absorbed by the down-wave sponge layer. The top and

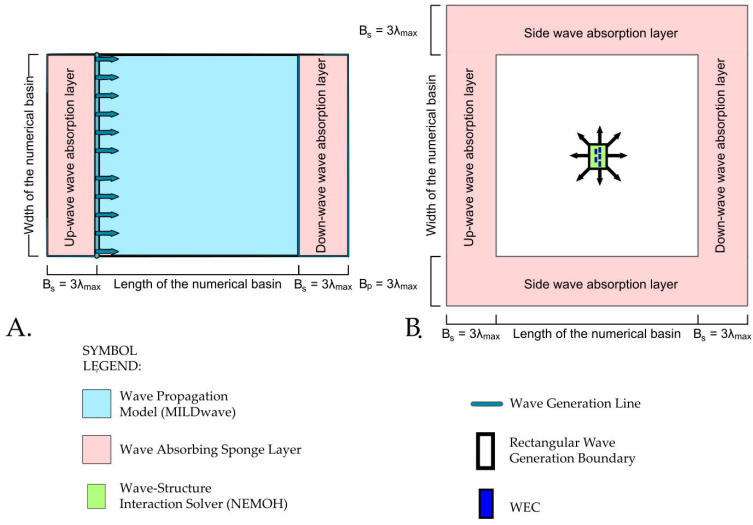

Figure 4.6: Sketch of the incident wave propagation (left) and perturbed wave propagation (right) in MILDwave. The blue line corresponds to the wave generation line, the black rectangle corresponds to the coupling radius generation boundary and the pink areas correspond to absorption zones (sponge layers) down-wave, up-wave and along the sides of the numerical domain.

bottom boundaries can be reflective or absorbing, depending on the settings in the wave propagation model. When reflective boundaries are applied, it is advised to extend the wave propagation domain, perpendicular to the incident wave direction. The incident wave set-up is shown in the left panel in Fig. 4.6. The right panel shows the perturbed wave run.

In the case of irregular incident waves, the superposition principle can be applied. A linear, irregular wave can be represented as a sum of a finite number of regular wave components, each with a characteristic wave height and wave period derived from the wave spectrum. In order to avoid local attenuation of the surface elevation η_I, each regular wave component is shifted with a random phase angle φ_i:

$$\eta_I = \sum_{i=1}^{n} \Re\{\zeta_i \cdot e^{-i(\omega t - k(x\cos\beta - y\sin\beta) - \phi_i)}\} \tag{4.11}$$

where the subscript $_i$ indicates each regular wave angular frequency ω component of the irregular wave. Modelling the wave propagation of irregular waves through a closely-spaced cluster of floating/fixed offshore WECs requires performing multiple coupled simulations with regular waves, each shifted with a random phase angle, and finally superimposing all individual regular wave fields.

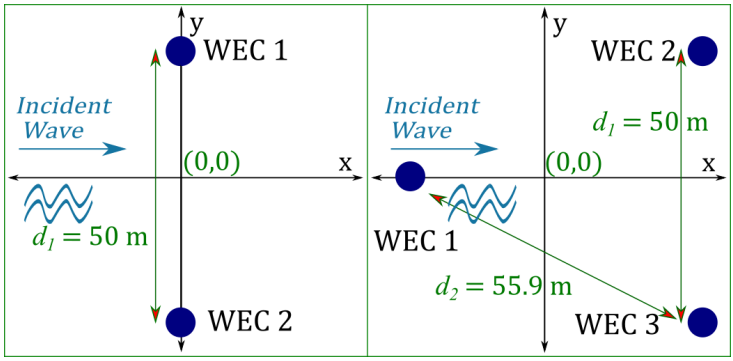

Figure 4.7: Plan view of the 2 and 3 WEC array layouts. The incident wave is coming from the left with a head on incidence of β=0°

4.5 Calculating the Radiated and the Diffracted Wave Fields

The perturbed wave field is the superposition of the radiated and diffracted field and is calculated in the inner domain by the wave-structure interaction solver NEMOH. This is shown graphically as Step 2 in Fig. 4.5. Two alternative approaches to coupling the perturbed field to the wave propagation model MILDwave are discussed in Section 4.8. However, the calculation for both inputs, performed in the wave-structure interaction solver NEMOH is the same and is detailed below. First, a frequency-domain simulation is performed in the BEM solver NEMOH in a domain with a fixed bottom. The body motions and static and dynamic pressures are calculated via the Laplace Eq. (3.6) and the boundary conditions Eq. (4.4) outlined in Section 4.2.1. The dynamic pressure is integrated over the floating body to obtain the radiation and diffraction forces. These quantities depend on the WEC shapes, the degree(s) of freedom, the wave period and the local water depth. Making use of Eq. (4.4) and the linear superposition principle, we can calculate the diffracted and radiated free surface elevations η by transforming the frequency-domain output complex amplitude values to the time-domain.

$$\begin{aligned} \eta_D &= |\hat{\eta}|e^{i\varphi_D} \\ \eta_R &= \sum_j^{\mathcal{M}} i\omega|\hat{z}||\hat{\eta}|e^{i\varphi_R} \end{aligned} \tag{4.12}$$

The inner domain $\hat{\eta}$ are calculated on a grid which is chosen smaller and finer than the wave propagation grid, giving a greater accuracy. In the next step, shown as Step 3 in Fig. 4.5, the diffracted and radiated waves, as calculated in the previous step, are propagated in the wave propagation model with varying bathymetry. In Section 4.8 it is demonstrated that coupling the summed perturbed wave from NEMOH is advantageous to coupling the individual radiated and diffracted waves

to the outer domain model model MILDwave. The coupled perturbed wave is then imposed inside a circular region with a radius r_c and then propagated outwards. A study of the sensitivity of the results to r_c is performed in Section 4.10.

4.5.1 The wave field in NEMOH

As we are interested in the accuracy of the coupling approach and testing of the fidelity of linear models in general is outside the scope of this thesis, we shall establish NEMOH as the benchmark against which to measure the results, because as mentioned in Section 4.4, the grid resolution is finer than that of the wave propagation model and the ability to model array effects intrinsically means that expected result of the coupling should approximate the NEMOH solution as closely as possible where the domains match. To perform the analysis we choose a NEMOH domain larger than the coupling region, out to 200 m in the x and y direction from the centre. The coupled MILDwave-NEMOH domain for this investigation will match the NEMOH domain with the exception of the region inside the coupling radius r_c which in both cases is equal to the wave field in NEMOH as we manually impose it as described in Section 4.5. The grid settings for both NEMOH and MILDwave are set with $\delta x = \delta y \equiv 2m$ for the regular wave runs and $\delta x = \delta y \equiv 3m$ for irregular waves to account for the need to model high period waves in the wave propagation model. Since NEMOH gives only the radiated and diffracted free surface elevations, a complex incident wave $\hat{\eta}_I$ of amplitude equal to ζ given by Eq. (4.14) is added to the sum of the perturbed $\hat{\eta}$ in the simulated NEMOH domain:

$$\hat{\eta}_I(x, y, t) = \zeta \cdot e^{-i(\omega t - k(x\cos\beta - y\sin\beta))} \tag{4.13}$$

where β is the direction of wave propagation. The sum of η_D η_R and η_I gives the total free surface elevation $\eta_t ot$ everywhere in the simulation domain. In NEMOH, the phase angles of the diffracted and radiated wave are referenced to the centre of the domain, and the wave is normalized by an incident wave amplitude of 1.0; therefore the NEMOH free surface elevations need to be multiplied by the modelled incident wave amplitude ζ.

To obtain the irregular wave field in NEMOH we sum N frequency components and multiply them by ζ_i, the weighted amplitude *i.e.* derived from a given spectral representation S_f via Eq. (3.57):

$$\hat{\eta}_{I,irr}(x, y, t) = \sum_{i=1}^{N} \zeta_i e^{-i(\omega t - k(x\cos\beta - y\sin\beta)}, \tag{4.14}$$

where f_i is the angular wave frequency and Δf_i is the frequency bin width for each frequency component i. In this thesis we utilize the S_{PM} spectral representation given by Eq. (3.53).

4.6 Results Representation

Before diving into the results, a few remarks about the presentation of the results in this thesis is given. For the regular wave cases in this and the following chapters Chapters 5 and 6 the contour plots of the results are presented in all points of the domain by calculating the K_d, defined as the ratio between the numerically calculated total wave, H_t, and the incident wave height, H_I:

$$K_d = \frac{H_t}{H_I} = \frac{\sqrt{8 \cdot \sum_t^{\Delta t} \eta_t ot(x,y)^2 \cdot \frac{dt}{\Delta t}}}{H_I} \tag{4.15}$$

where $\eta_t(x,y)$ is the resulting total surface elevation in each simulation time step dt and Δt is the time window over the K_d is computed. The contour plots of the irregular wave results in this chapter and the following Chapters 5 and 6 are presented as the K_d for irregular waves, defined as the ratio between the numerically calculated significant wave height, $H_{m0,tot}$, and the incident significant wave height, $H_{m0,I}$:

$$K_d = \frac{H_{m0,tot}}{H_{m0,I}} = \frac{4 \cdot \sqrt{\sum_t^{\Delta t} \eta_t(x,y)^2 \cdot \frac{dt}{\Delta t}}}{H_{s,i}} \tag{4.16}$$

where $H_{m0,tot}$ is $2\zeta_i$ for the total wave calculated at a point in the domain and $H_{m0,I}$ is $2\zeta_i$ of the incident wave.

To compare the accuracy of the two approaches in Section 4.8, plots of the percent difference in the K_d between the coupled NEMOH-MILDwave and NEMOH is shown. The percent difference is defined as:

$$\frac{K_{d,MW} - K_{d,NEM}}{K_{d,NEM}} \cdot 100. \tag{4.17}$$

where the subscripts $_{MW}$ and $_{NEM}$ stand for MILDwave and NEMOH, respectively. Where indicated, the black solid ellipses or boxes indicate with approximate scale the sizes and locations of the WECs and blank regions indicate coupled wave fields which are not part of the analysis. For clarity we shall drop the $\hat{}$ symbol from all graphics and discussions when referring to the wave amplitude.

For the cross-section figures in Section 4.8.3, the location of the cross-sections in the domain are shown by red dashed lines. In this view the incident wave is coming from the left with $\beta = 0°$. The zone in the red boxes is the near-field zone which is modelled separately in NEMOH and is not part of the coupled model analysis.

4.7 The Wave Field around single WECs and WEC arrays in NEMOH

In this results section, the contour plots of the regular and irregular free surface elevation modifications due to the presence of the 2-WEC and 3-WEC array of the

heaving cylindrical WECs detailed are presented in terms of the K_d as outlined in Section 4.6.

The WEC is a heaving circular cylinder with a radius of 5 m and a draft of 2 m, representative of a range of current prototypes. In this chapter, for the sake of simplicity, the PTO of each WEC is modelled as a resistive damper with a value of $3.6 \times 10^5 kgs^{-2}$, which is representative for a resistive PTO of the WEC type we model. More realistic PTO cases will be presented further in Chapter 6. Here the PTO damping value is set constant for each of the WECs in the array. The results for one WEC are shown for both wave periods in Fig. 4.8 and for 2 and 3 WEC arrays in Fig. 4.9, where the normalized wave field K_d is calculated via Eq. (4.15) with the perturbed η given by Eq. (4.4) and the incident η given by Eq. (4.13). The two wave periods were chosen because they:

(a) represent a common modelling scenario for WEC deployment off the European Atlantic coast and

(b) because the PTO coefficient is set to maximize the power output at these periods.

In this chapter and in this thesis in general, the wave field generated by the BEM code NEMOH is utilized as the benchmark where applicable. Although it has important constraints as outlined in Section 3.8.4, NEMOH accurately resolves array interactions within the paradigm of linear theory.

4.7.1 The regular perturbed wave field in NEMOH

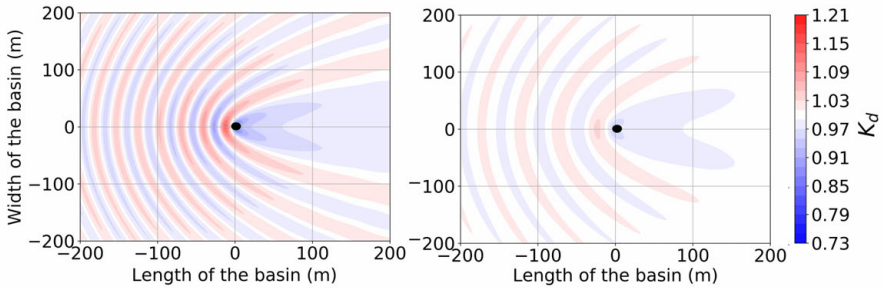

Figure 4.8: The K_d in the NEMOH domain for a single WEC for a regular wave of H = 2 m and T = 6 s (left) and T = 8 s (right).

The first results presented are the absolute values of the total wave field calculated in NEMOH via Eq. (4.4) for the single WEC and the 2 and 3 WEC array layout exhibited in Fig. 4.7 for a regular wave of H = 2 m and T = 6 s and T = 8 s.

The wave field displayed is the sum of the incident, diffracted, and radiated waves. For the one WEC case shown in Fig. 4.8, the parabolic pattern of the

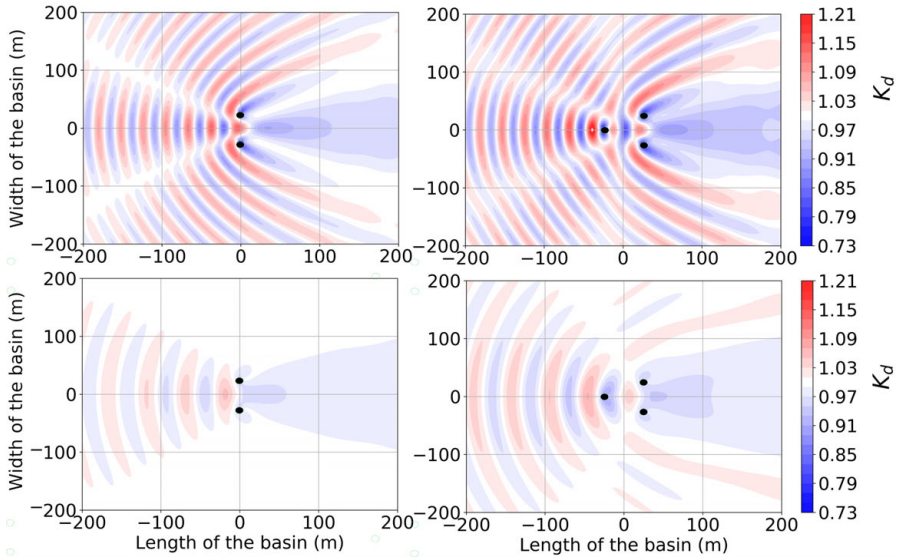

Figure 4.9: The K_d in the NEMOH domain for a 2-WEC array (left), and a 3-WEC array (right) for a regular wave of H = 2 and T = 6 s (top) and T = 8 s (bottom).

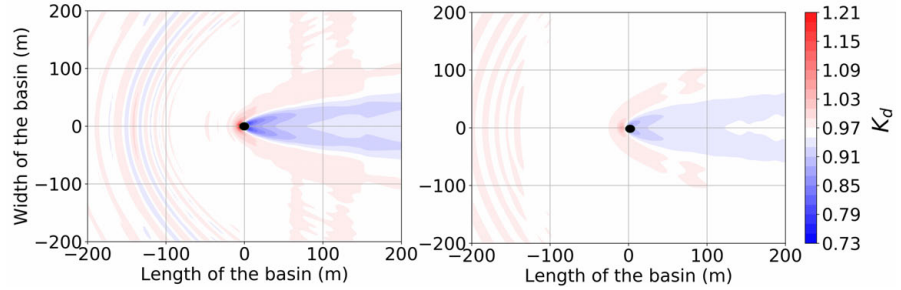

Figure 4.10: The K_d in the NEMOH domain for a single WEC for an irregular wave of H_{m0} = 2 m and Tp = 6 s (left) and Tp = 8 s (right).

incident wave interacting with the wave diffracting in front and around the WEC is visible. The diffraction effect is primarily influenced by the size of the buoy relative to the wave and for the case of the r = 5 m buoy for all three periods the buoy is significantly smaller than the wave length, so diffraction is similar for all the examples. The array results in Fig. 4.9 generally mirror the pattern of the single WEC but with more complicated interaction patterns, especially next to and in between the WECs in what is termed the 'near-field' zone in this thesis. While the diffraction is dependent on the body shape more than the wave period, the radiation is strongly dependent on the latter. Therefore the large decrease in the

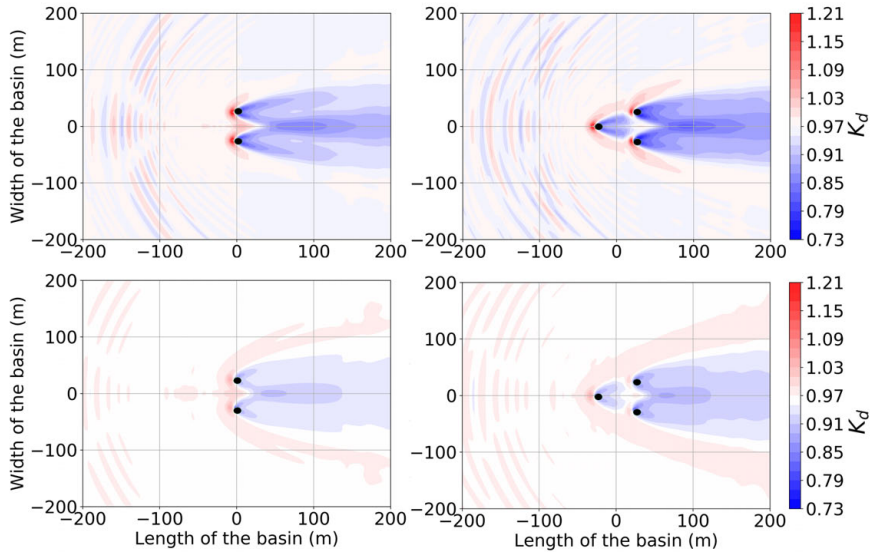

Figure 4.11: The K_d in the NEMOH domain for a 2-WEC array (left) and 3-WEC array (right) for an irregular wave of $H_{m0} = 2$ m and Tp $= 6$ s (top) and Tp $= 8$ s (bottom).

perturbed wave between T $= 6$ s and T $= 8$ s is due to the radiation of the former case. The radiation decreases markedly as the wave period moves away from the resonance period of the WEC which is $T_r \equiv 3.3$ s. For the single WEC it is a circular area of enhanced amplitude oscillations, while for the two and three WEC arrays the pattern manifests as 'rays' of amplitude modification that emanate from the individual WEC positions.

4.7.2 The irregular perturbed wave field in NEMOH

Attention is next turned to the irregular wave results for the same three cases presented for regular waves in Section 4.7.1. The irregular total amplitude of the free surface elevation K_d is calculated from the sum of the multi-component irregular incident wave of Eq. (4.14) and the sum of the perturbed waves calculated from Eq. (4.4) from ϕ_D and ϕ_R which are then normalized by the PM spectral distribution of Eq. (3.53), with $N = 20$ frequency components, which, according to analysis of existing work in (Pastor and Liu, 2014) is sufficient for WEC motion simulation.

The biggest difference between the regular wave results in Figs. 4.8 and 4.9 and the irregular wave results in Figs. 4.10 and 4.11 is the reduction in the parabolic wave patterns of positive and negative interference. Also a decrease in K_d behind the WEC or arrays of WECs is observed, in the 'wake zone'. The irregular wave case K_d is reduced by up to 15% for the 3-WEC array case for Tp $= 6$ s, which is a significantly greater reduction than the 10% observed behind the 3-WEC array

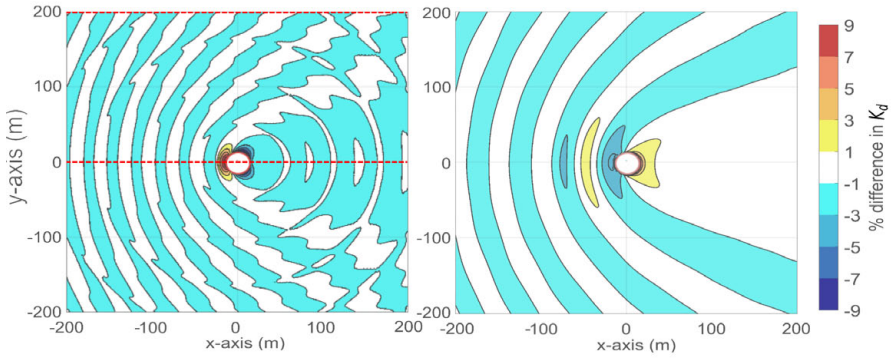

Figure 4.12: Percent difference of the radiated + diffracted coupling approach in the absolute value of the K_d in the NEMOH domain for a single WEC for a regular wave of H = 2 m and T = 6 s (left) and T = 8 s (right). Percent error expressed relative to NEMOH benchmark free surface elevation.

for the same T = 6 s regular wave case. Note also that the net areas of positive interference in the domain are greatly reduced, roughly approximated by the warm colours in the contour plots. Unlike the regular wave cases, there is no beneficial relationship between the incoming wave and the perturbed wave that results in the areas of beneficial interaction witnessed in Figs. 4.8 and 4.9. The key takeaway is that irregular waves tend to not only reduce the power performance of the individual WECs and arrays, as will be demonstrated in Chapter 5 in Section 5.6, but that the net effect of the presence of the WECs in an irregular wave field is a reduction in the near-field K_d with a significant effect in lee of the array. As we can see in this and the previous section Section 4.7.1, the NEMOH domain cannot be extended to study these effects without either:

(a) a decrease in the resolution which will negatively impact the resolution of the individual WECs or

(b) a significant increase in the computational time needed.

This is precisely the reason for the coupling to the wave propagation model, the results of which can be ran over a much larger area without the need to make the aforementioned compromise. But before delving into the results over a large domain, one needs to establish the accuracy of the coupling methodology by comparing the coupled domain one-to-one with the NEMOH domain. In the next several sections, Sections 4.8, 4.8.1 and 4.8.2 we will dive into different coupling approaches and arrive at the one which gives the best results in the shortest time. The results of this approach will then be presented in Section 4.9 for the same scenario as in Section 4.5.1.

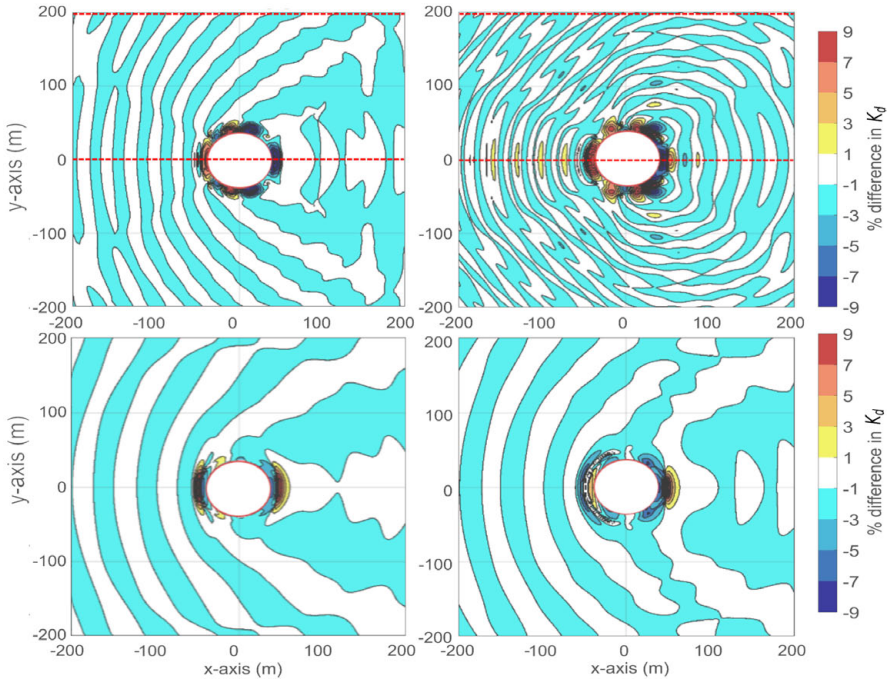

Figure 4.13: Percent difference of the radiated + diffracted coupling approach in the absolute value of the K_d in the NEMOH domain for a 2-WEC array (left), and a 3-WEC array (right) for a regular wave of H = 2 m and T = 6 s (top) and T = 8 s (bottom). Percent error expressed relative to NEMOH benchmark free surface elevation.

4.8 Alternate Approaches to Coupling the Perturbed Wave

As mentioned in Section 4.3.2 and Section 4.7.1, before settling on the preferred coupling method which will be utilized in the rest of thesis, we explore two alternatives in coupling the free surface elevation η from the NEMOH inner domain to the MILDwave outer domain model in this section. To do so, we select 3 test cases: 1 WEC and a small 2 and 3-WEC closely-spaced arrays. The test configuration is shown in Fig. 4.7.

4.8.1 Coupling the radiated and diffracted waves

The first approach calculates the diffracted and radiated wave fields in NEMOH and adds the respective waves to the incident wave field in MILDwave. In this case the diffracted wave η_D Eq. (4.13)(a) and η_R Eq. (4.13)(b), the radiated wave, are each imposed the MILDwave computational grid cells of r_c and propagated radially. Note that this procedure requires two separate runs of MILDwave in Step

3 of Fig. 4.5: one to propagate the radiated and one to propagate the diffracted waves, respectively. To ensure the phase equality between the inner and outer domain model, we must make sure that the phases of each of the η at the centre of the coupling domain match. To compare the accuracy of the coupling approach, we present the results as plots of the percent difference between the K_d of the coupled model and the NEMOH K_d for a one WEC and two and three WEC arrays for a regular wave the modelled periods of T = 6 s and T = 8 s in Fig. 4.12 for one WEC and in Fig. 4.13 for the 2 and 3 WEC arrays, the same scenario which was demonstrated in NEMOH in Section 4.5.1. Note that the inner domain region, shown by the white circle, is excluded from the analysis because it represents the NEMOH imposed wave field as explained in Section 4.5 and does not elucidate the coupled model performance. The overall trend we see is a slight overestimate by the coupled model of the magnitude of the interactions, manifested in the predominance of negative error values shown in blue. An exception is the case of a single buoy for 8 s where there is a slight underestimate at the back of the WEC, that may be a result of the comparatively low radiation of this configuration. There is a notable difference in the behaviour between T = 6 and T = 8 seconds where the former displays slightly greater errors. This is expected, as the modelled WEC has a resonance period at 4.6 s which is closer to 6 s than to 8 s and consequently the array interaction effects which determine the % error tends to be more pronounced at this wave period.

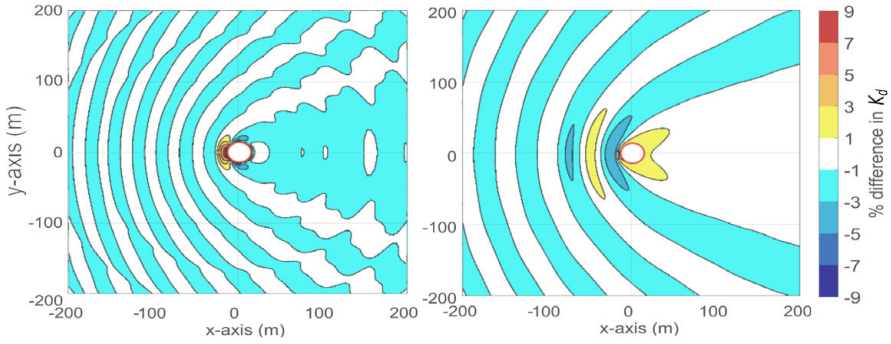

Figure 4.14: Percent difference between of the perturbed coupling approach in the absolute value of the K_d in the NEMOH domain for a single a single WEC for a regular wave of H = 2 m, T = 6 s (left) and T = 8 s (right).

4.8.2 Coupling the perturbed wave

The second approach couples the incident wave from MILDwave to the perturbed wave created by summing the radiated and diffracted η from NEMOH before coupling it to MILDwave. It differs from the technique detailed in Sec. 4.8.1 only in that the η values superimposed at the radius r_c and propagated in MILDwave

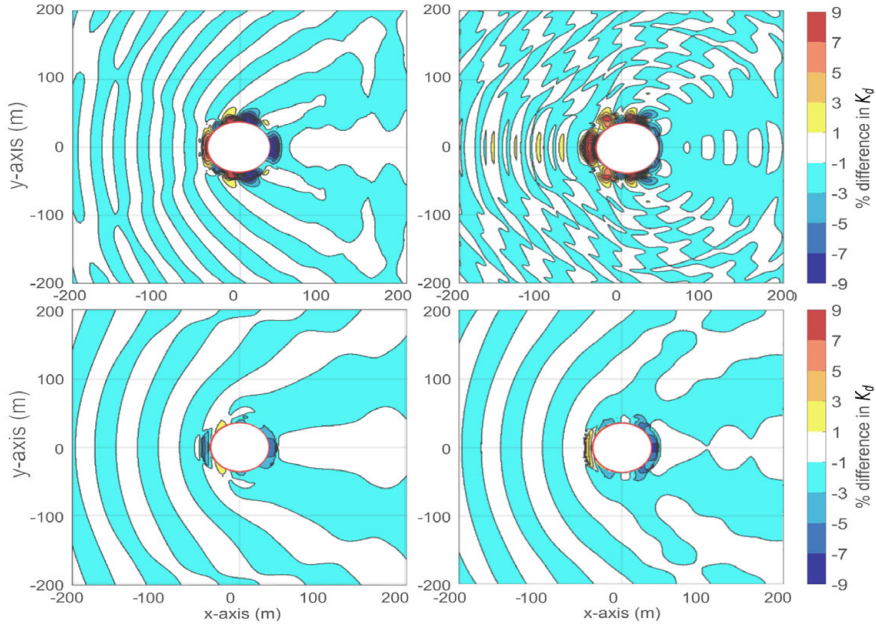

Figure 4.15: Percent difference of the perturbed coupling approach in the absolute value of the K_d in the NEMOH domain for a 2-WEC array (left), and a 3-WEC array (right) for a regular wave of H = 2 m, T = 6 s (top) and T = 8 s (bottom).

are those of the NEMOH perturbed wave. In contrast with the approach of Section 4.8.1, this procedure requires only one run of MILDwave in Step 3 of Fig. 4.5. We again ensure the correct phase relationship by setting the incident wave phase to be equal to the perturbed wave phases at r_c.

The percent difference in K_d for the second coupling approach is illustrated in Fig. 4.14 and Fig. 4.15 for the one WEC and array cases, respectively. We can observe that the overall pattern of the error in K_d closely matches that observed in Figs. 4.12 and 4.13 for the coupling approach in Sec. 4.8.1. In fact for T = 8 s they are identical outside of the near-field region. Of note is the apparent decrease in the positive anomaly in lee of the single buoy and a matching decrease in the negative anomaly in front of the single buoy at T = 6 for the perturbed case in Fig. 4.15 as compared with the radiated plus diffracted case in Fig. 4.13. In contrast, the difference in the errors for the arrays of two and three buoys is very small. This pattern can be explained by the fact that for the single buoy the perturbed wave pattern is determined largely by the radiated wave. It is apparent, therefore, that the difference in the performance of the two coupling techniques is in the way they model radiation, with the modelled diffraction essentially unchanged.

4.8.3 Cross-sections at the domain centre and at a lateral distance of 200 m

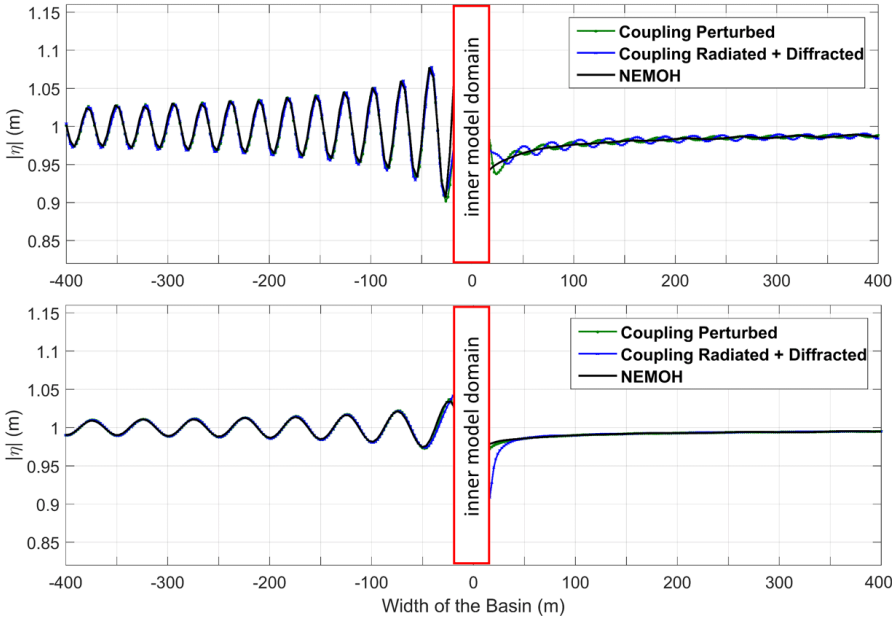

Figure 4.16: Cross-section of the K_d at $y = 0$ for 1 WEC for a regular wave of H = 2 m, T = 6 s (top) and T = 8 s (bottom).

To provide further detail in the performance of the two coupled approaches detailed in Section 4.8.1 and Section 4.8.2 we show cross-sections at $y = 0$ and $y = 200$ m in Figs. 4.16 to 4.21. In each of the figures the result for a regular wave of H = 2 m T = 6 s is shown in the top panel while that for H = 2 m T = 8 s is displayed in the bottom panel. Our first observation is that even though the general pattern for each configuration is repeated as the wave period increases the magnitude of the interaction decreases. Consequently, the difference between the two coupling methods is greater for T = 6 s than for T = 8 s. As was explained in Section 4.8.1, this is due to the enhanced interaction close to the modelled WEC resonance period. We also observe that at the cross section away from the array centres at $y = 200$ m for T = 6 s, there is notable decrease in the difference between the coupled K_d and the NEMOH result while the magnitude of the effects is essentially unchanged at the centre cross-section. For T = 8 s this difference is not visible as both coupling methods closely follow the base result. Observe that behind the WECs (the right side of the figures), for the cross sections at $y = 0$, the perturbed coupling approach K_d closely follows that of NEMOH while the radiated and diffracted coupling approach leads to oscillations that are not present in the benchmark data. Observe that these deviations increase as we move from 1 WEC to 2 and 3 WEC arrays. Furthermore, the radiated plus diffracted approach

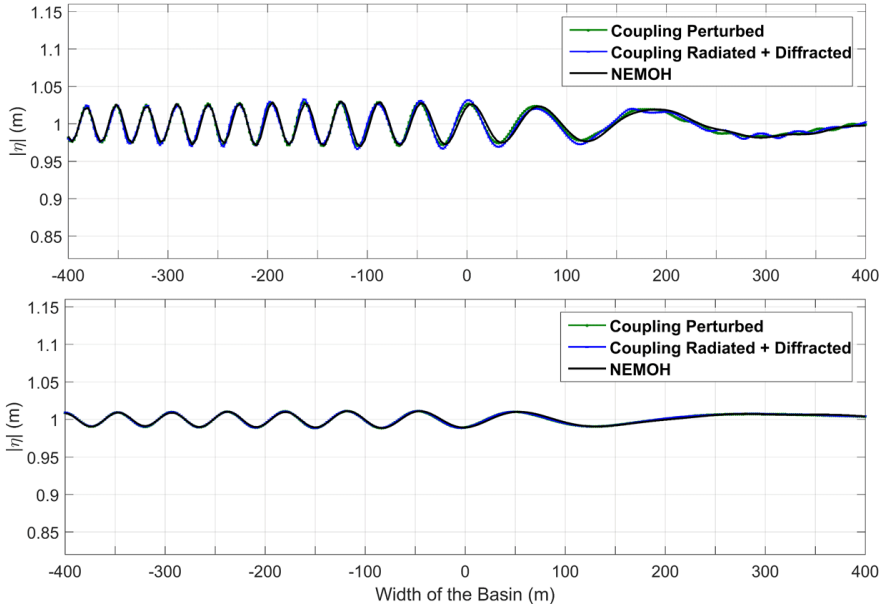

Figure 4.17: Cross-section of the K_d at $y = 200$ for 1 WEC for a regular wave of H = 2 m, T = 6 s (top) and T = 8 s (bottom).

results in a significant decrease in the wave field immediately in lee of the coupling zone while the perturbed method closely follows the NEMOH results and does not. At the same time, for the cross-sections at $y = 200$ m, the deviations are not significant, leading to essentially equal results.

4.9 The coupled wave field in MILDwave using the perturbed wave approach

4.9.1 Calculating the perturbed wave field in MILDwave

Having witnessed a very small difference between the two coupling approaches in the previous Sections 4.8.1 and 4.8.2, it was decided to use the perturbed wave method because of the increased efficiency in eliminating an extra run in Step 3 in Fig. 4.5. In the simulation the grid cell size is set to equally spaced $\delta = x = \delta = y \equiv 2$ m for the regular wave results and $\delta = x = \delta = y \equiv 3$ m for the irregular waves. The perturbed wave is calculated via the sum of the radiated and diffracted wave elevations as described in (4.12) in Section 4.5 for each regular wave.

$$\eta_P = \eta_D + \eta_R \tag{4.18}$$

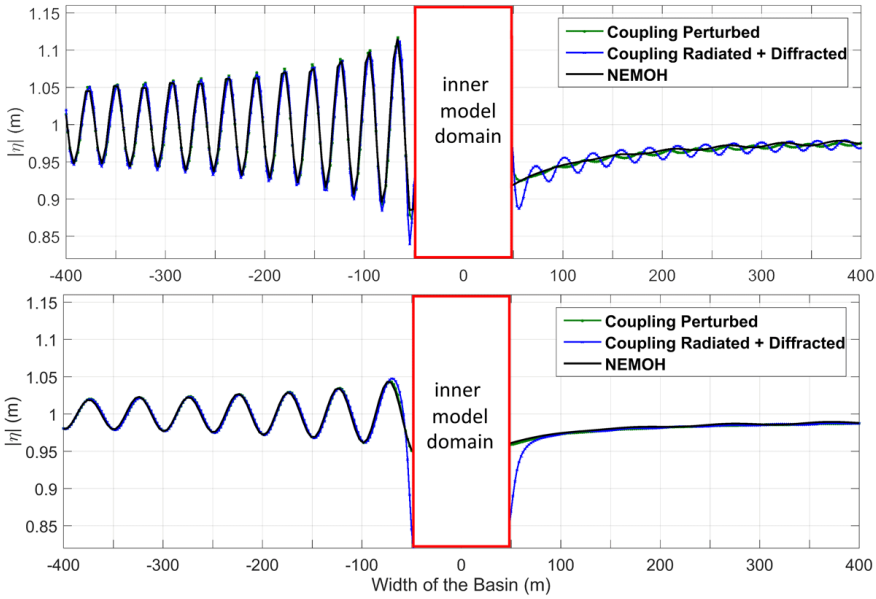

Figure 4.18: Cross-section of the K_d at $y = 0$ for a 2-WEC array for a regular wave of H = 2 m, T = 6 s (top) and T = 8 s(bottom).

In the irregular wave case, each perturbed wave $\eta_{pert,irr}$ is a finite sum of N regular perturbed wave components each calculated via (4.18):

$$\eta_{pert,irr}(x,y,t) = \sum_{i=1} \zeta_i |\eta_{pert}| \cos(\varphi_{pert,i} \ - \omega_i t) \tag{4.19}$$

where $|\eta_{pert}|$ is the absolute value of the perturbed free surface elevation and $\varphi_{pert,c,i}$ is the phase at the centre of the coupling domain of each perturbed frequency component. Each amplitude ζ_i is derived from the spectral distribution S_f (Eq. (3.57)) via Eq. (3.53). $\varphi_{pert,c,i}$ is selected randomly between $-\pi$ and π to avoid local attenuation of the surface elevation.

4.9.2 Calculating the total wave field in MILDwave

The total wave field of the coupled domain is obtained as the sum of the incident and perturbed waves. For the regular wave case this is a simple sum of Eqs. (4.10) and (4.18) with the incident wave generated in a separate run of MILDwave with a plane wave propagating at the desired incident wave angle β, in what is termed the Empty Basin (EB) run. For the irregular waves, the total wave field is the sum of the sums in Eqs. (4.11) and (4.19). The sums are performed at each wave frequency separately, as a consequence, each coupled results requires N runs of the Empty Basin run and N runs of the perturbed wave, where N is the number

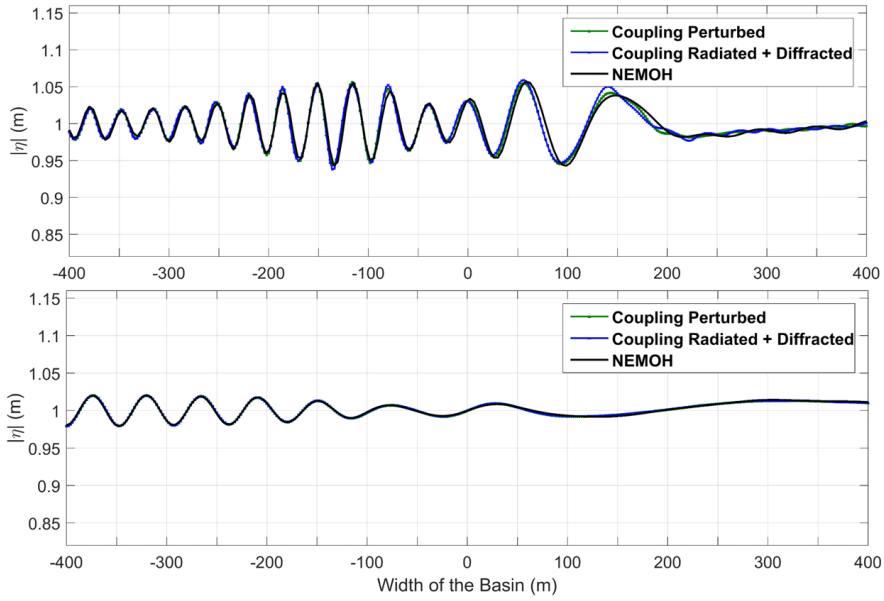

Figure 4.19: Cross-section of the K_d at $y = 200$ for 2-WEC array for a regular wave of H = 2 m, T = 6 s (top) and T = 8 s (bottom).

of frequency complements of the irregular waves. In this thesis, we aim to strike a balance between illuminating the important effects of wave interactions with WECs and the rapidity of the calculations, therefore a compromise frequency resolution of $N = 20$ components was chosen.

4.9.3 The coupled regular wave field in MILDwave

The total wave field as simulated in MILDwave for the same H = 2 m and T = 6 s and T = 8 s regular wave is illustrated in Figs. 4.22 and 4.23 and for a $H_{m0} = 2$ m Tp = 6 s and $H_{m0} = 2$ m and Tp = 8 s. As in Section 4.5.1, the location of the WECs is indicated by black ellipses. For the single WEC case we observe that the coupled MILDwave run faithfully reproduces the interference pattern between the incident and the perturbed wave in Fig. 4.22 and the difference in the magnitude between T = 6 s and T = 8 s which was interpreted in Section 4.7.1. The cross-section of the coupled MILDwave η at the x-axis ($y = 0$) is plotted in Fig. 4.25 for the 1-WEC case. We do observe that MILDwave tends to slightly overestimate the magnitude of the interactions yet the magnitude of the overestimation is no more than to 1% in front of the WEC in front of the WECs, in the area of the highly variable η. Behind the WECs in the 'wake zone', the coupled MILDwave result is remarkably similar to the NEMOH results as soon as we move away from the area immediately surrounding the WECs which is inside the coupling radius of 50 m. Also of note is the slight difference in the wake zone shape immediately in

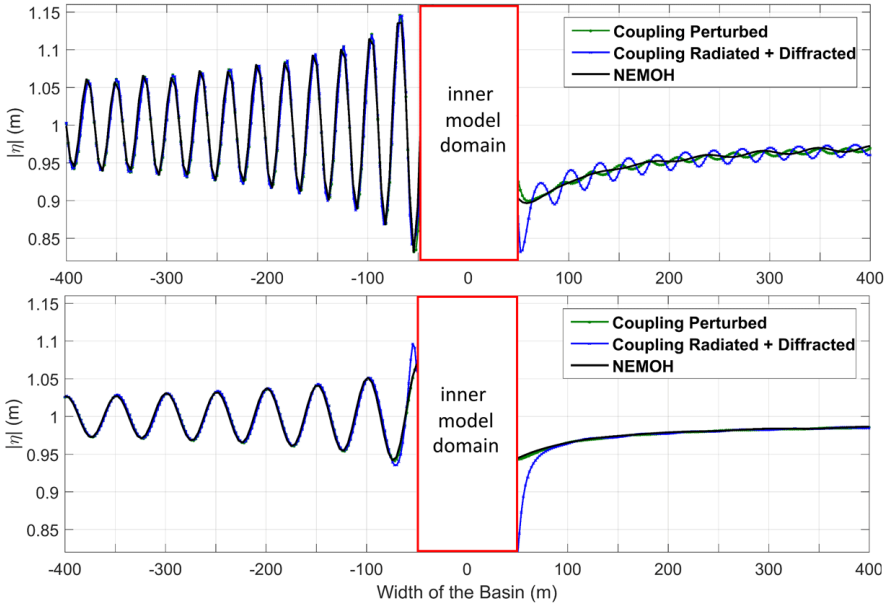

Figure 4.20: Cross-section of the K_d at $y = 0$ for a 3 WEC array for a regular wave of H = 2 m, T = 6 s (top) and T = 8 s(bottom).

lee of the coupling zone *i.e.* seen in the contour plots Fig. 4.23. This is due to the way the perturbed wave field is imposed in MILDwave in the generation circle and also due to the fact that MILDwave has a finite resolution of $\delta_z = \delta_y \equiv 2$ m whereas in NEMOH the wave field is calculated directly from the much finer discretisation of the WEC via the Green's functions. The same excellent agreement is seen for the WEC array case of Fig. 4.23 the coupled result is remarkably similar to the wave field plotted in NEMOH in Fig. 4.9, with only slight deviations in the immediate vicinity of the WECs inside and around the coupling circle and an overall increase in the magnitude of the anomalies of less than 2% inside the coupling radius. Away from the WECs the agreement is near perfect with only a slight overestimation in the η of 1% or less. This can also be observed in the cross-sections at the y-axis which compare the NEMOH total wave and the MILDwave coupled total wave for the 2 and 3 WEC case for both simulated wave periods in Fig. 4.26. Note that for the 1 WEC case and 3 WEC case a WEC is on the x-axis and therefore its location is shaded out while for the 2-WEC array both WECs are off the x-axis as diagrammed in Fig. 4.7 The aforementioned small discrepancies notwithstanding, the similarity is remarkable, with the coupled MILDwave model flawlessly representing the main features of the complicated interaction pattern. Given that this result can be extended to the far-field domain, this congruency demonstrates the viability and usefulness of the coupled model approach

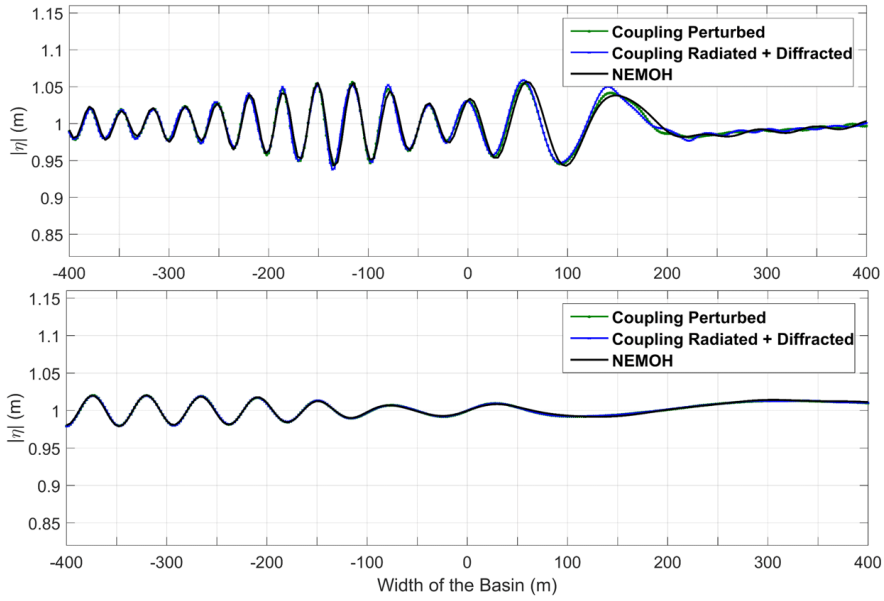

Figure 4.21: Cross-section of the K_d at $y = 200$ for a 3 WEC array for a regular wave of H = 2 m, T = 6 s (top) and T = 8 s (bottom).

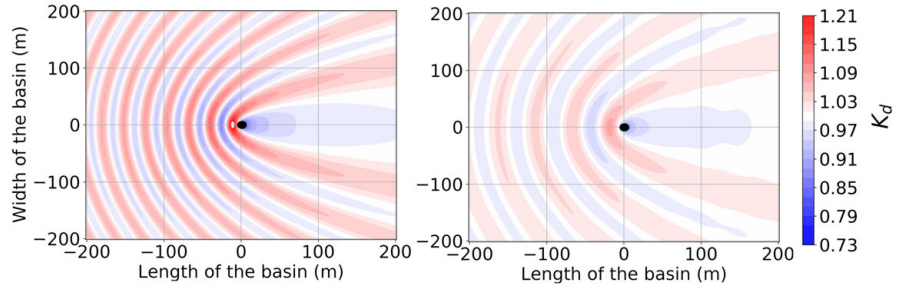

Figure 4.22: The absolute value of the K_d in the coupled MILDwave domain for a single WEC for a regular wave of H = 2 and T = 6 s (left) and T = 8 s (right).

4.9.4 The coupled irregular wave field in MILDwave

We will now turn the attention to the irregular wave field case by presenting the same 3 cases of 1, 2 and 3 WECs in the 200 m by 200 m domain that was analysed for the regular wave case in Section 4.9.3, for H_{m0} = 2 m Tp = 6 s and H_{m0} = 2 m and Tp = 8 s. The single WEC result is shown in Fig. 4.24 while that for the 2 and 3-WEC arrays is seen in Fig. 4.28. The cross section on the x-axis

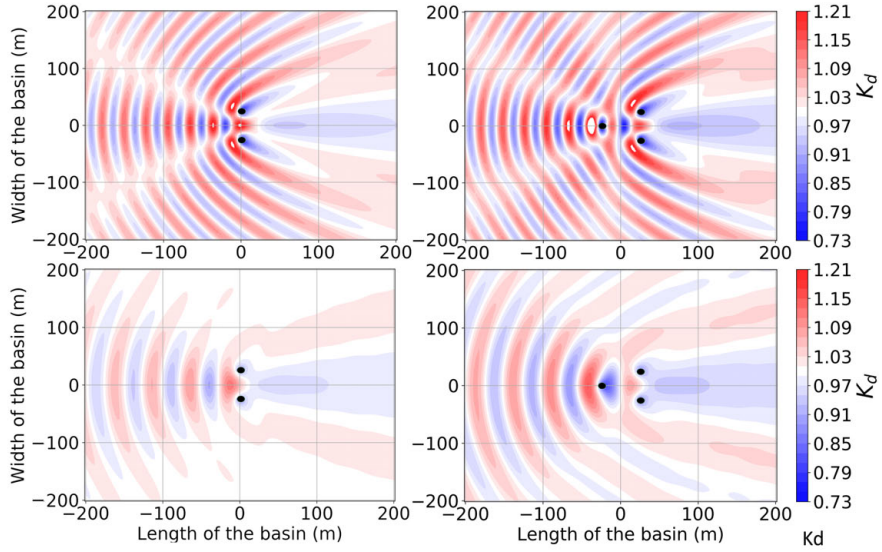

Figure 4.23: The absolute value of the K_d in the coupled MILDwave domain for a 2-WEC array (left), and a 3-WEC array (right) for a regular wave of H = 2 m and T = 6 s (top) and T = 8 s (bottom).

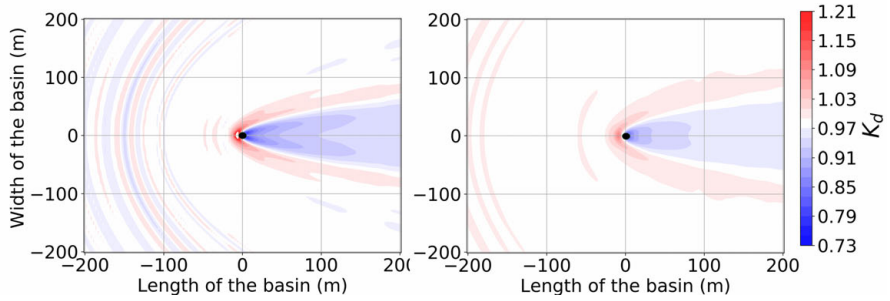

Figure 4.24: the absolute value of the K_d in the NEMOH domain for a single WEC (left), a 2-WEC array (centre), and a 3-WEC array (right) for an irregular wave of H_{m0} = 2 m and Tp = 6 s (top) and Tp = 8 s (bottom).

is plotted for the 1-WEC case in Fig. 4.29. The agreement with the NEMOH results given in Fig. 4.8 is even better than in the regular wave case, with the differences barely perceptible. The one area where the discrepancy between the coupled MILDwave and the NEMOH η is inside the coupling radius of 50 m and should not be considered in the analysis of the model results as the focus is on the model performance away from the coupling zone. Observe that in the irregular wave case, the shape of the wake is accurately reproduced in both the Tp = 6 s

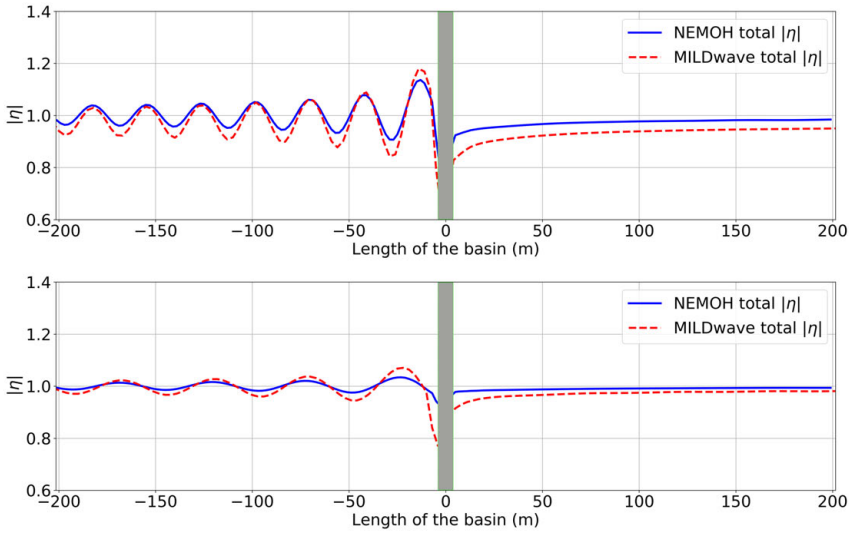

Figure 4.25: Cross-section of the K_d at $y = 0$ for one WEC at the centre of the domain for a regular wave of H = 2 m T = 6 s (top) and T = 8 s (bottom).

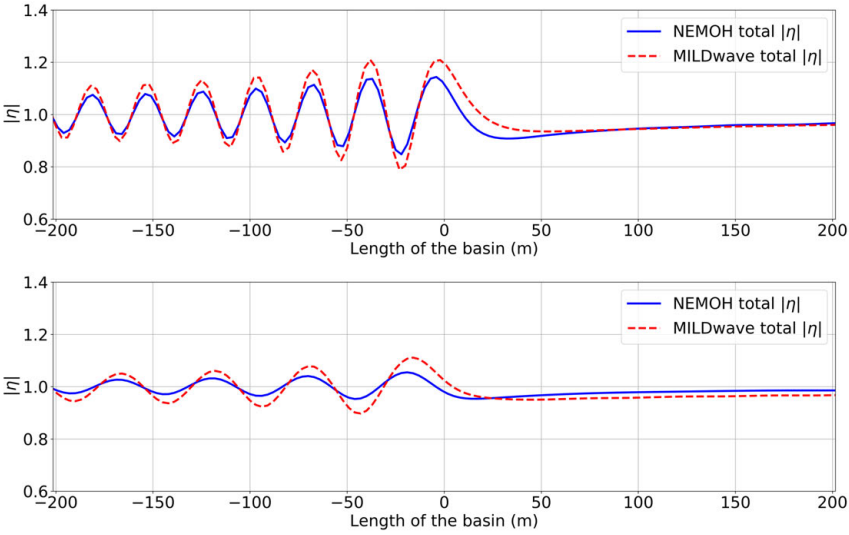

Figure 4.26: Cross-section of the K_d at $y = 0$ for a 2 WEC array for a regular wave of H = 2 m T = 6 s (top) and T = 8 s (bottom).

and the Tp = 8 s result. The 2 and 3-WEC array results of Fig. 4.28 are also remarkably similar to the equivalent NEMOH wave field given in Fig. 4.9. This can

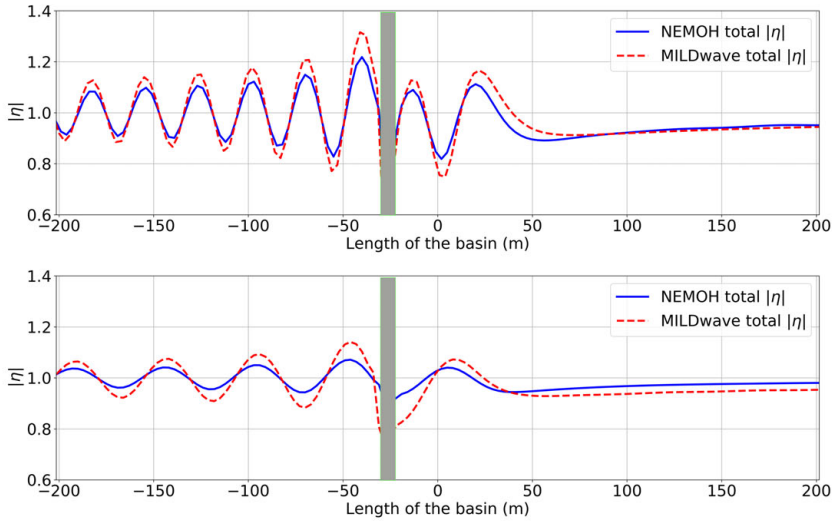

Figure 4.27: Cross-section of the K_d at $y = 0$ for a 2 WEC array for a regular wave of H = 2 m T = 6 s (top) and T = 8 s (bottom).

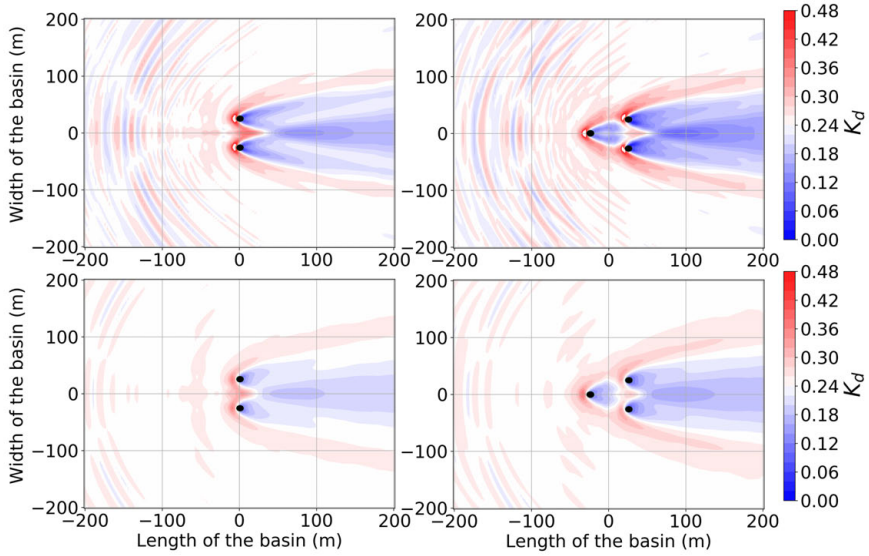

Figure 4.28: The K_d in the coupled MILDwave domain for a single WEC (left), a 2-WEC array (centre), and a 3-WEC array (right) for an irregular wave of H_{m0} = 2 m and Tp = 6 s (top) and Tp = 8 s (bottom).

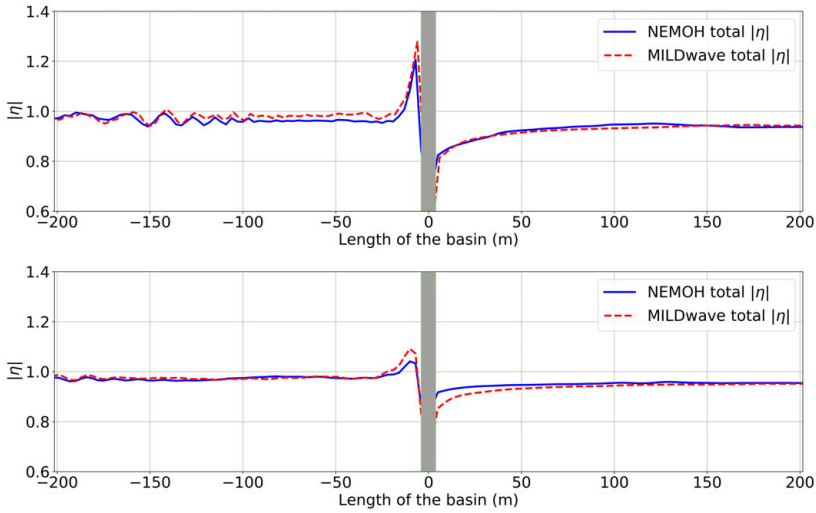

Figure 4.29: Cross-section of the K_d at $y = 0$ for one WEC at the centre of the domain for a regular wave of H = 2 m T = 6 s (top) and T = 8 s (bottom).

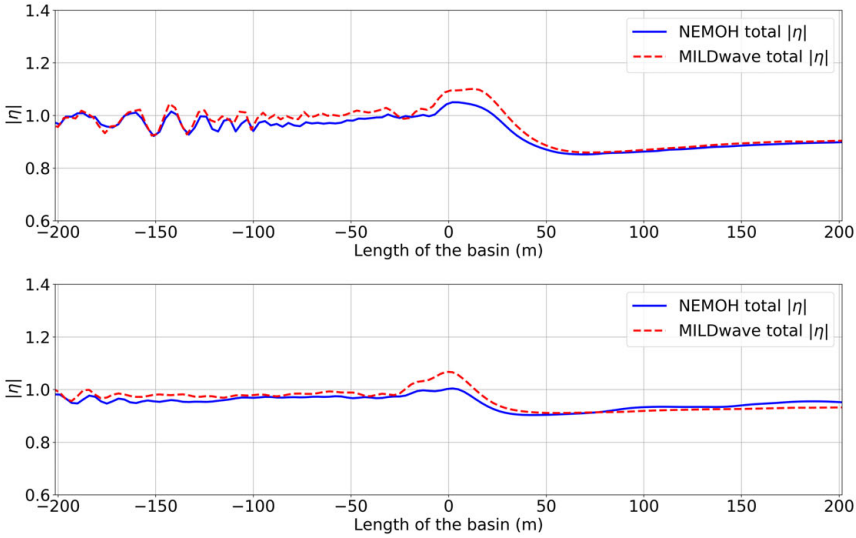

Figure 4.30: Cross-section of the K_d at $y = 0$ for a 2-WEC array for an irregular wave of H_{m0} = 2 m, Tp = 6 s (top) and Tp = 8 s (bottom).

also be observed in the cross-sections at the y-axis in Figs. 4.30 and 4.31 where the total wave in NEMOH is plotted together with the total wave of the coupled

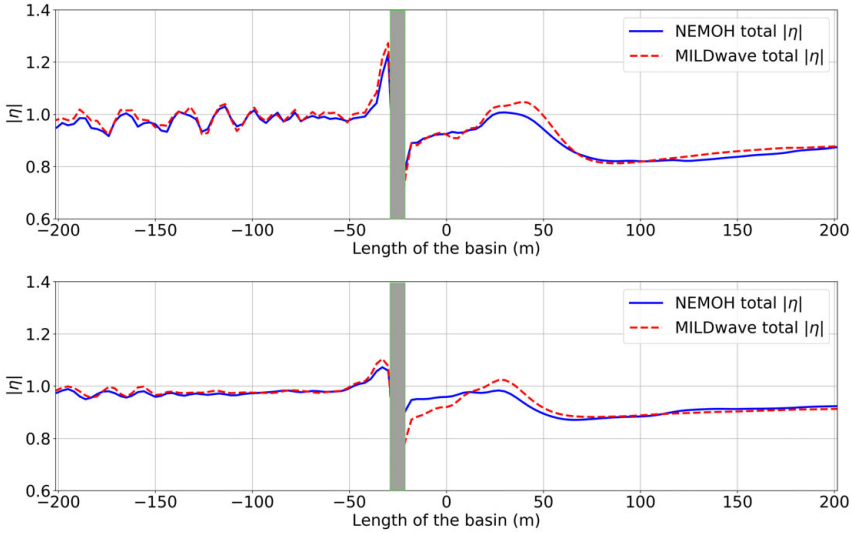

Figure 4.31: Cross-section of the K_d at $y = 0$ for a 3-WEC array for an irregular wave of $H_{m0} = 2$ m, Tp $= 6$ s (top) and Tp $= 8$ s (bottom).

MILDwave result. Note that the difference between the two models is much less for the irregular wave case, owing to the smoothing nature of the spectral distribution which decreases the sharp peaks and troughs of the WEC array interactions and also serves to smooth any slight offsets in the phase of the perturbed wave relative to the incident wave.

As was previously remarked in Section 4.7.2, the biggest difference between the regular and irregular wave results presented here is the lack of areas of positive interference, especially in front of the WEC arrays, and an increase in magnitude of the wake zones in lee of the arrays, manifested in the reduction of η. Note the interesting results *i.e.* reproduced in Fig. 4.28 for the 3 WEC array where the reduction in η due to the front array is offset by the reflection in front of the 2 back WECs. This indicates that the array configuration is indeed energy maximizing, in that the performance of the back arrays is not negatively influenced by the presence of the front one. We shall study these connections in more detail in the following Chapter 5. Note that by maximizing the power output of the array, the absorption of the wave energy is concurrently enhanced; the result is the large wake we see in lee of the 3-WEC array, especially for Tp $= 6$ s which as we mention in Section 4.7.1 is closer to the resonance period of the WEC and thus the WEC is able to extract more energy from the wave at the lower periods as compared with the T $= 8$ s case. Overall, the coupled results demonstrate a remarkable agreement between the chosen benchmark NEMOH BEM result and the coupled MILDwave wave propagation case. As we will demonstrate in Chapter 7, this will enable us to faithfully reproduce array effects over larger domains that include multiple WEC

arrays.

4.10 Influence of the Coupling Radius r_c

One of the motivations for coupling various models is balancing the computational cost with the need to model an entire domain with a reasonable accuracy. WEC arrays are particularly suitable candidates for this approach in that the complexities of the hydrodynamic interactions are only present in the near-field zone. Therefore, the same precision is not necessary for modelling the far-field, where the effects due to the radiation and diffraction are not as pronounced. Although the times to compute the small arrays in BEM for this particular study are relatively short since we only model one wave frequency and one wave direction, this is not the case when we seek to model larger arrays, as the computational costs for a BEM model increases as $\mathcal{O}(N^3)$ panels, where the number of panels is proportional to the number of bodies in the array. In contrast, the time to model an entire basin of 1200 m by 1200 m in MILDwave is 10 min on a 8GB RAM Intel i7 2.80G GHz PC, regardless of the number of WECs present.

A further constraint imposed by standard BEM models is that they cannot represent varying bathymetry. While this assumption is realistic for closely-spaced WECs, in intermediate and shallow waters for separating distances greater than a few hundred meters the bathymetry effects will be significant. Indeed, recent studies have have demonstrated the influence of varying bathymetry to be greater than the array interaction effects for WEC array scenarios in shallow water regions as was demonstrated clearly in (Charrayre et al., 2014b; Verao Fernandez et al., 2017, 2018; Tomey-Bozo et al., 2019). As we have pointed out in Section 4.3, the coupling radius r_c is the key parameter that forms the circular boundary between the inner and outer domain model models. A larger coupling radius generally results in more accuracy in modelling the array interaction effects but at the expense of both increased computational cost and the inability of describing varying bathymetry in the area enclosed by r_c. Consequently, we seek to minimize r_c under the conditions of keeping the error small and enclosing the entire array. We demonstrate the influence of r_c for the case of a wave radiated by a single buoy at T = 8 s in Fig. 4.32 which is the target sea state for the type of WEC array modelling we seek to do. We observe that the agreement between the coupled radius is excellent with the exception of the smallest r_c which is several percentage points above the target K_d. This discrepancy indicates that in the modelled case the inter array effects extend beyond $r_c = 10$ m, as would naturally be expected for a $r = 5$ m WEC. We can conclude that for the modelled WEC type, a coupling radius greater than or equal to two WEC diameters provides the desired accuracy. Other types of WECs such as OSWECs where the near-field array effects are greater and will require a larger r_c for increased coupled model accuracy. Moreover, as mentioned previously, the coupling radius will also need to be large enough to include all closely-spaced WECs in an array. Although the notion of what constitutes *closely spaced* for intra-array spacing in an array is debated, see for example Babarit (2010); Bacelli et al. (2013) for a discussion, for the purpose of this thesis we define WEC arrays

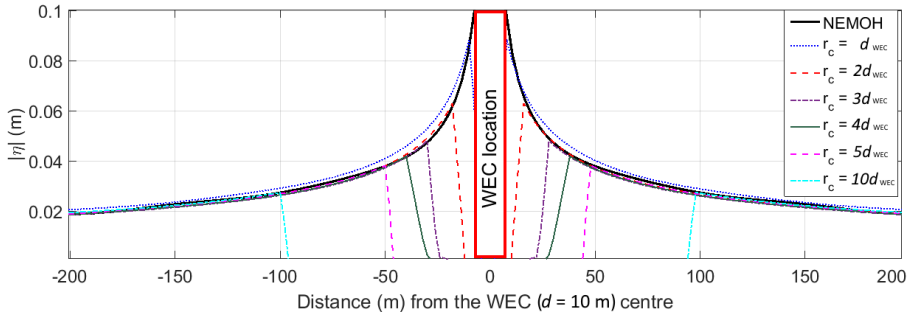

Figure 4.32: Cross-section at y = 0 demonstrating K_d of the radiated waves for $r_c = d$, 2d, 3d, 4d, 5d, AND 10d for a 10 m d WEC. The black line shows the K_d calculated in NEMOH.

as closely-spaced where the WECs are spaced less than four WEC diameters apart.

4.11 Conclusion

In this chapter we have demonstrated the validity of a one-way coupling methodology between the BEM WSI solver NEMOH and the mild-slope wave propagation model MILDwave via a typical WEC modelling scenario of 1 heaving cylindrical WEC and an array of 2 and 3 heaving cylindrical WECs. We have shown that outside of the zone in close proximity to the WECs the coupled models are in excellent agreement with the BEM solution and is within 2% for regular waves and less than 1% for the irregular wave cases demonstrated. It has been also shown that the most accurate and also the fastest way of coupling the BEM model to the wave propagation model is via the perturbed wave approach described in Section 4.9.1. This coupling approach produces a slightly better agreement with NEMOH for areas close to r_c than the approach of separately coupling the radiated and the diffracted waves. Further, given that the separate coupling of radiation and diffraction requires two distinct runs of MILDwave, the perturbed coupling strategy is the preferred technique for future work. Although we have shown the results for one particular set of models for the case of regular and irregular waves, the coupling procedure presented in this paper can be extended to other models and for modelling different WEC types. As an example, the case of the OSWEC in the coupled model will be presented in Chapter 7, along with a varying bathymetry. For coupling of depth-resolving models such as OceanWave3D (Verbrugghe et al., 2018), the concept of the coupling radius can be expanded to a coupling 'hollow cylinder' where the information from the inner model is exchanged with the outer domain model at each depth layer. Using the superposition principle, irregular and multi-directional waves can be modelled by calculating each frequency and direction separately, in which case the benefits of a fast solver like MILDwave will become more apparent. The restrictions of the presented coupled methodologies, along with the requirements of linear wave theory outlined in Chapter 3, namely the

assumption of constant depth inside the coupling radius r_c in the immediate vicinity of the WECs, and the mild-slope restrictions on the bathymetry surrounding the WEC array zone are in line with realistic deployment scenarios for the current generation of WEC arrays.

Chapter 5

Factors Altering the Power Output and the Wave Field of a WEC Farm

Abstract

One of the key challenges in designing a WEC array is that the devices hydrodynamically interact with one another. Therefore their positioning will impact both the power output of a given wave energy project and any potential effects on the surrounding areas. The wave energy array developer then must optimize the location of the WECs to maximize power output whilst at the same time minimizing capital cost and any potential deleterious external effects. A number of recent studies have shown that one potential solution is that instead of positioning the WECs uniformly in a WEC farm, they can be placed in dense clusters of several devices with space available in between for navigation. In this chapter a hypothetical WEC farm consisting of two WEC array of 5 devices each is investigated. In this chapter the focus is on the key factors influencing the WEC farm power output via hydrodynamic interactions, namely: WEC array separation distances, the angle of wave propagation and the effect of regular vs. irregular waves. To accomplish this goal, a the novel coupling methodology introduced in the previous Chapter 4 between the BEM model NEMOH and the wave propagation model MILDwave is applied. To investigate the WEC array effects with a farm, henceforth termed *inter-array* effects in analogy with the *intra-array* effects which are hydrodynamic interactions of WECs within an array, we introduce a state-of-the-art iterative method which enables the order-arbitrary calculation of these interaction effects. The basis of the method is the iterative calculation of the perturbed wave by order of iteration. In this chapter, the notion of WEC array 'independence' is likewise defined within a WEC farm. The usage of this information to further simplify the calculation of the *inter-array* effects and the WEC farm power calculations.

5.1 Introduction

Ocean wave energy is a promising source of clean electricity that has the potential to make a significant contribution in reducing the world's dependence on fossil fuels. However, in order for it to follow the path of offshore wind and become a commercially viable power source, significant cost reductions must be made. Because of physical restrictions on the size of individual wave energy converters (WECs), it is the established view of the wave-energy community that WECs have to be deployed in farms to be economically viable (Babarit, 2017). To benefit from developing offshore infrastructure and the maritime support industry, such farms need to have a power rating in the order of hundreds of mega watts. With the most promising current WEC technology, this corresponds to farms of hundreds of WECs. How these WECs are grouped and arranged within a WEC farm to maximize profitability while minimizing detrimental effects is still an open question.

For a key group of WECs nearing commercial deployment, *i.e.*, heaving axi-symmetrical point absorbers, a number of recent studies have numerically and experimentally investigated the layout and spacing of WECs within WEC farms (Borgarino et al., 2011b; Göteman et al., 2015; Stratigaki, 2014; Stratigaki et al., 2015; Penalba et al., 2017b). Although the terms "WEC farm" and "WEC array" are used interchangeably, we define a "WEC farm" as comparable in size to an offshore wind farm that may consist of a large number of sparsely separated WECs or clusters of densely packed WECs, which we hereby term "WEC array" following the definition proposed in Chapter 1. All of the aforementioned investigations utilized potential flow theory, specifically the Boundary Element Method (BEM), to resolve intra-array effects, *i.e.*, those between the WECs in the array. While effective for arrays with a small number of WECs, BEM modelling becomes computationally demanding as the number of WECs and modelled frequencies increase.

We follow an alternative approach whereby a WEC farm comprising two WEC arrays is modelled using a one-way coupling technique between BEM model NEMOH (Babarit and Delhommeau, 2015) and wave propagation model MILDwave (Troch, 1998; Troch and Stratigaki, 2016). One-way coupling means that the perturbed wave field is only propagated from the inner domain to the outer domain, as evidenced in Fig. 5.1. In the investigation, the inner domain is the WEC arrays' near field, while the outer domain spans the entire farm area and the far-field. We used the BEM model in the near-field area of the WEC arrays and the wave propagation model in the far-field WEC farm area external to the WEC arrays (see Fig. 5.1).

A key feature of the proposed one-way coupling technique is that waves are propagated from the near-field model domain (NEMOH) to the far-field model domain (MILDwave) via a transfer of information on a wave-generation circle inside a coupling radius r_c. A schematic of these domains and the clustered layout is presented in Fig. 5.1. Wave loading in NEMOH is determined by the wave conditions in the domain at the WEC array location. If the effect of one array on another is sufficiently small, then these disturbances in the wave field due to the interaction can be ignored; therefore the arrays can be simulated by using the same incident wave conditions. If the WEC arrays are sufficiently close, allowing for mutual hydrodynamic interaction, however, the effect of the perturbed (radiated and

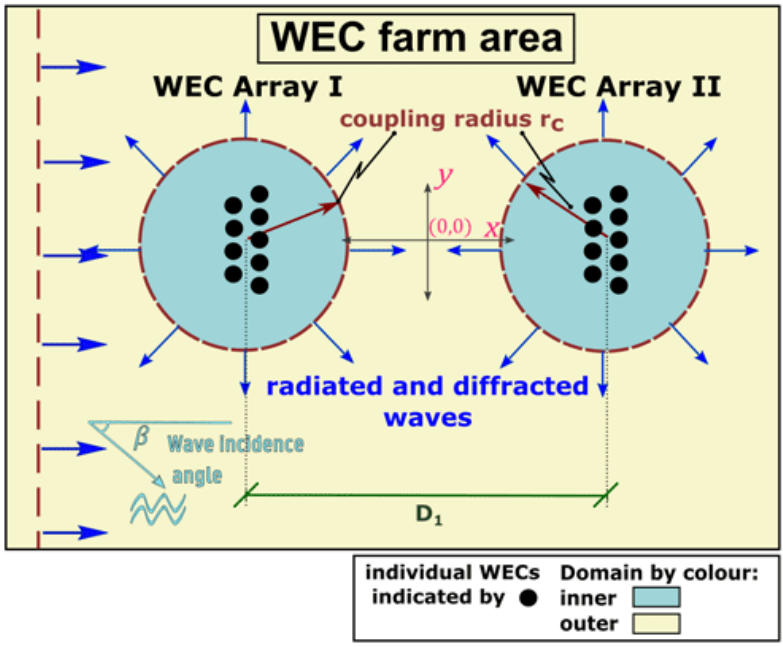

Figure 5.1: Schematic of the clustered WEC farm layout.

diffracted) waves from one array on another needs to be taken into account. Such an approach would, of course, require multiple simulations and would take longer to perform. The crucial question then is at what distance we can consider two arrays to be sufficiently hydrodynamically independent to model them as isolated. Depending on the wave type, wave incidence angle, and inter-array separation distance, we explore the magnitude of the effect of the presence of one array in the proximity of another on the total WEC farm power output.

Two closely spaced staggered arrays of nine-point absorber-type heaving WECs are modelled using the aforementioned coupling technique. We investigated various inter-array separation distances for a range of wave-incidence angles for regular waves and various inter-array separation distances in irregular waves. The power output for the different configurations of the WEC farm is calculated and compared to that of a WEC farm of hydrodynamically independent WEC arrays, i.e., those operating in isolation. The minimum inter-array separation distance, D, for which two WEC arrays in a farm can be considered as hydrodynamically independent is defined for each simulated wave period. As the focus is on operational sea states, in this work we operate on the paradigm of linear potential theory, as detailed in Section 5.2.

5.2 Theoretical Background

As is the case for the rest of this document, the investigation in this chapter assumes Linear Potential Flow Theory. For a detailed discussion and a list of assumptions see Section 3.3. These assumptions allow us to make use of the superposition principle in:

(a) enabling the coupling between NEMOH and MILDwave

(b) allowing the modelling of irregular waves as a superposition of regular wave components

(c) allowing the consecutive summation of the perturbed waves to calculate the inter-array effects

It is also important to remember the restrictions imposed by Linear Potential Flow Theory, outlined in Section 3.8.4, the most important of which is to remember that the methods introduced in this chapter apply to WEC array operational states and not to extreme conditions in survival mode which might preclude the use of linear theory. The details of the BEM solver NEMOH are given in Section 4.2.1 while those for MILDwave are presented in Section 4.2.2

5.2.1 Boundary Element Method solver

In the coupling technique, the intra-array effects, induced by the hydrodynamic interaction between the WECs, are resolved by simulating the WEC motions using open-source potential flow BEM solver NEMOH (Babarit and Delhommeau, 2015) which was introduced in Section 4.2.1 in Chapter 4. We remind here that NEMOH solves the fluid flow via the Laplace equation Eq. (3.6) which is simplification of the Navier-Stokes equations with the assumptions of Linear Potential Flow Theory. Equation (3.6) is solved by means of Green's functions, as detailed in Babarit and Delhommeau (2015). The resulting potential flow of the fluid ϕ, allows us in turn to calculate the free surface elevations via Eq. (3.9) which is the free surface kinematic boundary condition. For further details on the methodology, see Section 4.2.1.

It is also worth remarking that NEMOH outputs the complex free surface elevation that consists of the real part which is the instantaneous free surface elevation η and the instantaneous phase φ. Since we are interested in the net effects of the WEC array interactions, we take the absolute value of the complex $\hat{\eta}$ to obtain the average free surface amplitude. For brevity we drop the $\hat{}$ symbol over the η symbol when referring to the absolute value of the K_d. In NEMOH the radiation and diffraction potentials ϕ_R and ϕ_D are calculated.

5.2.2 Mild-slope wave propagation model

For simulating the far-field effects, e.g., sometimes referred to as the 'wake zone' in the lee of the array, the wave propagation model MILDwave was employed(Troch, 1998; Troch and Stratigaki, 2016) in the outer domain. MILDwave, developed at

the Coastal Engineering Research Group of Ghent University, Belgium, is a phase-resolving model based on depth-integrated mild-slope equations (Equations (4.5a) and (4.5b)) in the form proposed by Radder and Dingemans (1985). The mild-slope equations (Equations (4.5a) and (4.5b)) are solved using a finite-difference scheme that consists of a two-step space-centred, time-staggered computational grid, as detailed in (Brorsen and Helm-Petersen, 1998). Further details on MILDwave are given in Section 4.2.2 in Chapter 4.

5.3 Coupling Methodology

5.3.1 Modelled WECs

The WEC type modelled in this chapter is a flat circular cylinder with a diameter of 10 m and a draft of 2 m which was also examined in Chapter 4. The shape was selected based on its overall dimensions being similar to several promising WEC technologies, namely, Seabased, Oscilla Power, and SINN Power Wave National Renewable Energy Laboratory (2017). All three WECs are in the planning stages of a pre-commercial WEC array. The Power Take Off (PTO) of each WEC is modelled as a resistive damper with a B_{PTO} value of 3.6×10^5 kg s^{-2}, which is representative for a resistive PTO of the WEC type we model targeting a sea state with a peak period of 8 s. This would correspond to a facsimile of the wave-climate period encountered in parts of the North Atlantic where WEC array demonstration projects are in the planning stages (Electric Supply Board (ESB), Ireland, 2019). The natural or resonance period of the WEC, T_r, is equal to 4.6 s and, for simplicity, the value of B_{PTO} was set identical to each of the WECs in an array. Further details are provided in Section 4.7.1

5.3.2 WEC Array and WEC Farm Layout

To simulate a realistic array of WECs, we chose a staggered configuration that has been shown in a number of numerical studies of heaving WECs (Child and Venugopal, 2010; Child et al., 2011; Ruiz et al., 2017a), to maximize power in both regular and irregular sea states. Similar results for staggered configurations were shown in experimental studies in (Stratigaki et al., 2014; Stratigaki, 2014; Stratigaki et al., 2015). For each of the WEC farm configurations, we simulate two nine-WEC arrays as shown in Fig. 5.2 within the farm shown in Fig. 5.1 at various inter-array separating distances D_1 from each other. The array orientation was held constant, while the angle of the incoming waves relative to the x-axis, β, was set at $0°$, $45°$, and $90°$. A schematic of the farm layout is shown in Fig. 5.1. In this investigation, water depth is held constant at 40 m.

5.3.3 Coupling of NEMOH to MILDwave

In order to model the inter-array effects in a WEC farm in an efficient manner and with reasonable accuracy, a one-way coupling method introduced in Chapter 4 is employed. In brief, the perturbed wave field is calculated in the BEM code

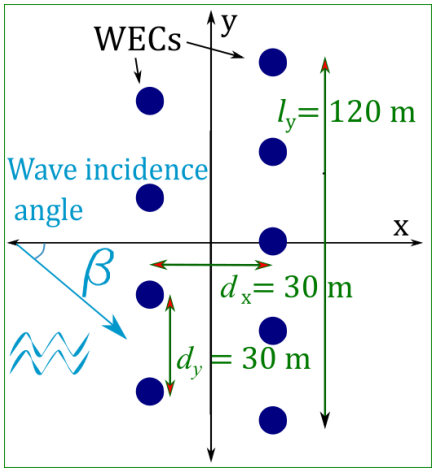

Figure 5.2: Plan view of the Wave Energy Converter (WEC) array layout for nine heaving buoys. The incident wave makes heading β with the x-axis; d_x and d_y are the x and y intra-array separation distances; and l_y is the length of the array orthogonal to the wave incidence of $\beta = 0°$.

NEMOH and is propagated into the depth-integrated wave model MILDwave on a circle large enough to enclose the near-field domain that surrounds the WECs. Based on the aforementioned analysis in Section 4.10, we set the coupling radius r_c at the smallest possible value which results in a discrepancy of less than 2% in K_d between NEMOH and MILDwave K_d.

For the present investigation the value of r_c is set at 100 m which includes all the WECs in one array. The MILDwave grid resolution is set at $\Delta x = \Delta y = 1$ m and the outside boundary conditions are Sponge Layers which are calibrated to minimize reflection as detailed in Section 4.2.2.

5.3.4 Iterative method to calculate the total wave field in a WEC farm consisting of multiple WEC arrays

To assess the effects of the two WEC arrays within a WEC farm on each other, and in order to evaluate the total power output of the WEC farm, we need to calculate the total perturbed wave field in the MILDwave domain. As Linear Potential Flow Theory is presumed in this study, we use the superposition principle to sum up the total wave field by combining an iterative approach with the coupling method presented in Section 5.3.3. The technique employed is illustrated in Fig. 5.3. Note that the arrows indicating propagating waves (λ) are shown for illustrative purposes: in fact the summation is made over the average free surface elevations η in the frequency domain. The initial step (Step 1) was to propagate the incident wave field in the empty numerical basin in MILDwave to obtain the undisturbed free surface elevation. In Step 2, the incident wave field was used as input into NEMOH, whence the 1^{st}iteration of the perturbed wave of WEC Array I, $1i$, was

evaluated. In Step 3, the average wave amplitude at the location of the centre of Array I, was used as input into NEMOH to calculate the 1^{st} order perturbed wave of WEC Array II, p_{1ii}. In Step 4, the process in Step 2 was repeated, with p_{1ii} as the new input perturbed wave. Finally, in Step 5, the same process was performed for the 2^{nd} iteration perturbed wave of WEC Array I, p_{2i}. Since the input perturbed wave field in each subsequent step was reduced by approximately an order of magnitude, for all practical purposes this process could be terminated at Step 4 without any appreciable loss in accuracy, even for closely spaced cases where interaction is maximized. Therefore, Step 5 is only displayed for a complete description of the proposed coupling method.

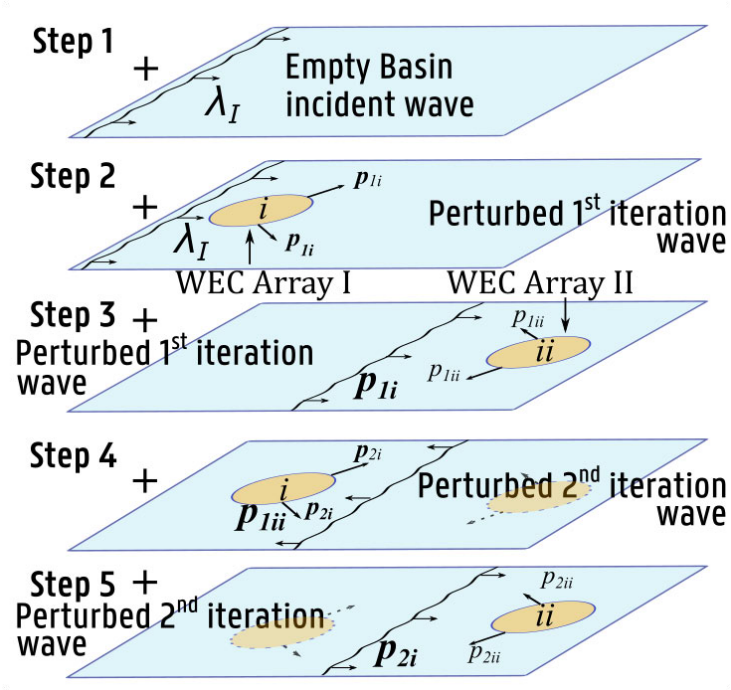

Figure 5.3: Procedure for determining the perturbed wave field for a regular wave input. Incident wave λ is coming from the left.

5.3.5 Coupling irregular waves

In this chapter, we model an irregular long-crested sea state using a non-directional Pierson-Moskowitz spectrum $S_{PM}(H_{m0}, T_p, \omega)$ (see Eq. (3.53) with $N = 20$ frequency components. Total free surface elevation η_i for an irregular wave field is then the sum of the frequency component amplitude ζ_i (Eq. (3.57)), and unit amplitude total free surface elevation η_i, obtained by using the procedure in Fig. 5.3 in Section 5.3.4 for each frequency component i as given by Eq. (3.58).

5.4 Determining the Power Output of a Nine-WEC Array

To evaluate the influence of the inter-array interaction effects on the performance of a WEC farm, we compute the total power produced by the two WEC arrays after having obtained the modified wave field in the WEC farm using the approach outlined in Section 5.3.4. For each WEC array, using the amplitude of the total modified wave field at the locations of the WECs as the input, we calculate the power output by simulating the WEC motions in NEMOH using Equation (5.1) for regular waves for each frequency component i.

$$P(\omega,\beta) = \frac{1}{2}\sum_{j=1}^{\mathcal{M}} B_{PTO}\omega^2 \left|\hat{Z}_j(\omega,\beta)\right|^2 \tag{5.1}$$

Here, $\mathcal{M}$ is the number of WECs in the array, ω is the wave angular frequency, $\hat{Z}_j$ is the complex heave Response Amplitude Operator (RAO) of WEC j, and B_{PTO} is the PTO damping coefficient, set equal to 3.6×10^5 kg s^{-2} for each WEC. For modelling irregular wave cases, we modelled the power output as the sum of the power at each wave component frequency i calculated by Equation (5.1) weighted by the non-directional Pierson–Moskowitz spectrum $S_{PM}(f)$:

$$P_{irr} = 2\sum_{i=1}^{N} \Delta\omega S_{PM}(H_{m0}, T_p, \omega) p_(\omega,\beta) \tag{5.2}$$

In Equation (5.2), $\Delta\omega$ is the frequency bandwidth of the spectrum discretisation and $N = 20$. The total power output of the WEC farm is the sum of the power produced by the two WEC arrays. For a WEC array in regular waves, the power output is modelled for three wave incidence angles β: $0°, 22.5°$, and $45°$. In exploring the effect of irregular waves in a WEC farm, only the head on incidence angle $\beta = 0°$ was simulated. Although B_{PTO} was set constant and at the same value for both regular and irregular wave cases, sensitivity analysis was performed with varying values of B_{PTO}, which showed that the constant of 3.6×10^5 kg s^{-2} chosen for this paper results in the maximal power for one WEC for a variety of wave conditions. For simplicity, in this investigation we utilize a simple linear PTO coefficient which is kept constant for each WEC in the array and for each wave type and period. An optimization study of various PTO systems including varying the PTO linear coefficient between regular and irregular waves is performed in the following chapter Chapter 6.

5.5 Regular Wave Results

5.5.1 K_d around two WEC Arrays within a WEC Farm in regular waves

We begin the analysis by qualitatively looking at the coupled total wave fields of the two array WEC farms produced by the iteration method outlined in Section 5.3.4.

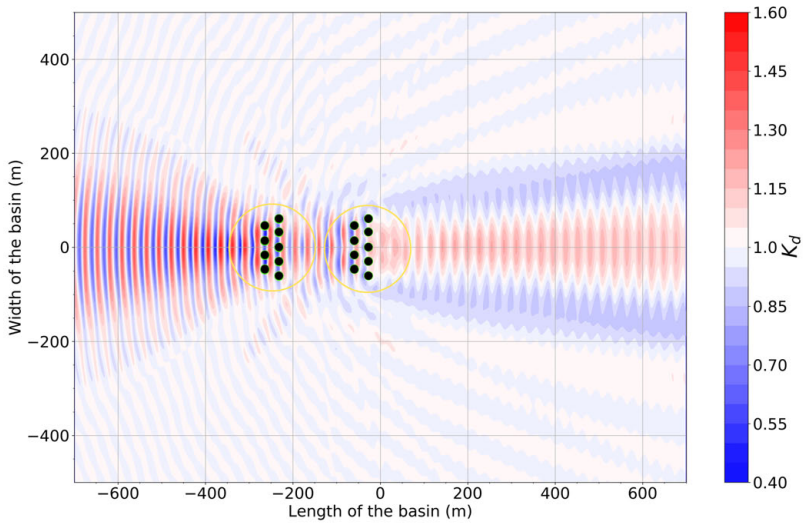

Figure 5.4: K_d around two WEC arrays, I (left) and II (right), of nine heaving cylindrical WECs for regular waves of H = 2 m and T = 6 s. Inter-array separation distance D_1 = 200 m or $2r_c$. Wave incidence angle $\beta = 0°$. The yellow circle indicates the extent of the inner (NEMOH) domain and is likewise indicated in the rest of the contour plots in this chapter.

Representative results are shown in this section in Figs. 5.4 to 5.6 for a regular wave of H = 2 m and T = 6 s, T = 8 s , and T = 10 s, respectively, for a head-on incidence angle $\beta = 0°$ for a inter-array separation distance of D_1= 200 m. We note that the wave field shown inside the yellow circle of radius r_c is the inner-domain NEMOH η, initialized by the η given by the MILDwave Empty Basin at the end of Step 4, as shown in Fig. 5.3 in Section 5.3.4. In an initial glance at the figure, we notice a strong contrast between the results for T = 6 s and the other two simulated periods, namely, T = 8 and T = 10 s. For the former, both the magnitude and the extent of the disturbances in the wave field due to the presence of the array are quite notable. We also observed strong positive K_d anomalies on the $y = 0$ axis that were not present at T = 8 s and T = 10 s. The positive anomalies at T = 6 s were due to interference between radiation and the diffraction of the WEC array optimized for $\beta = 0°$. Note that this constructive interference is nearly absent for the other two wave periods which demonstrate a significant reduction in the η or wake, in the same area in lee of the WEC arrays. As was also mentioned in the previous chapter in Section 4.7.1, this is due to the radiation of the given WEC type at a period of T = 6 s which is closer to its resonance period of T_r = 3.3 s. The combined effect of the radiation of the WECs in the two arrays at a relatively close inter-array separation distance D_1 is enough to counterbalance the shadowing of the incoming wave due to the diffraction and absorption of the same WECs. In Figs. 5.7 to 5.9, the parallel results for a inter-array separation distance of D_1= 600 m are demonstrated for a regular wave of H = 2 m and T =

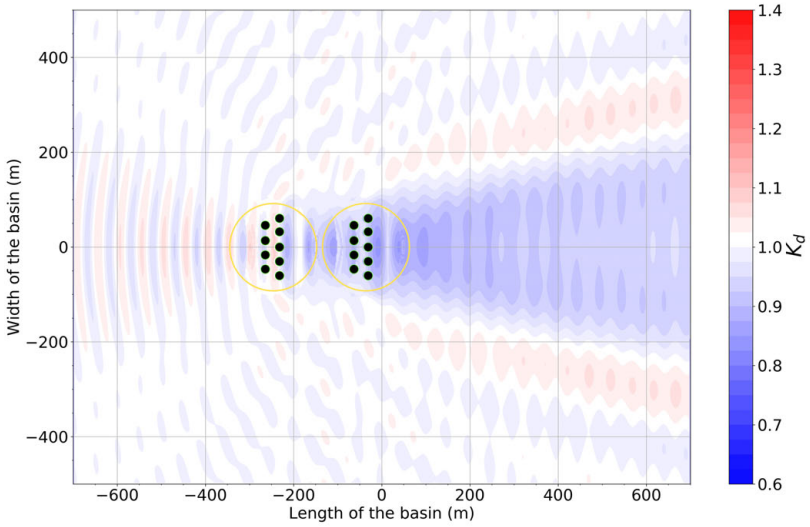

Figure 5.5: K_d around two WEC arrays, I (left) and II (right), of nine heaving cylindrical WECs for regular waves of H = 2 m and T = 6 s. Inter-array separation distance D_1 = 200 m or $2r_c$. Wave incidence angle $\beta = 0°$.

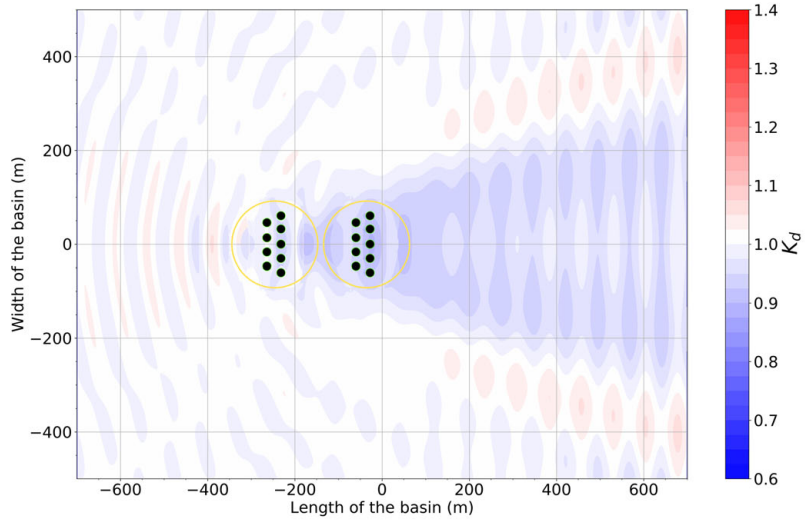

Figure 5.6: K_d around two WEC arrays, I (left) and II (right), of nine heaving cylindrical WECs for regular waves of H = 2 m and T = 6 s. Inter-array separation distance D_1 = 200 m or $2r_c$. Wave incidence angle $\beta = 0°$.

6 s , T = 8 s , and T = 10 s, respectively, for a head-on incidence angle $\beta = 0°$.

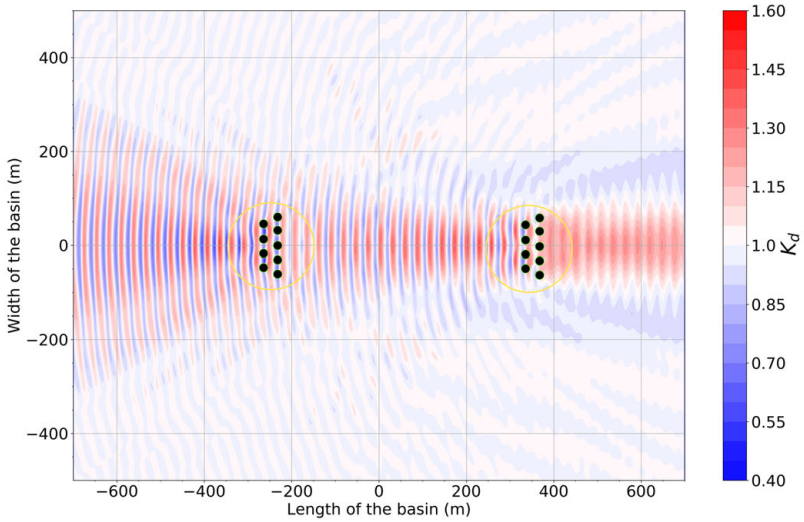

Figure 5.7: K_d around two WEC arrays, I (left) and II (right), of nine heaving cylindrical WECs for regular waves of H = 2 m and T = 6 s. Inter-array separation distance $D_1 =$ 200 m or $2r_c$. Wave incidence angle $\beta = 0°$.

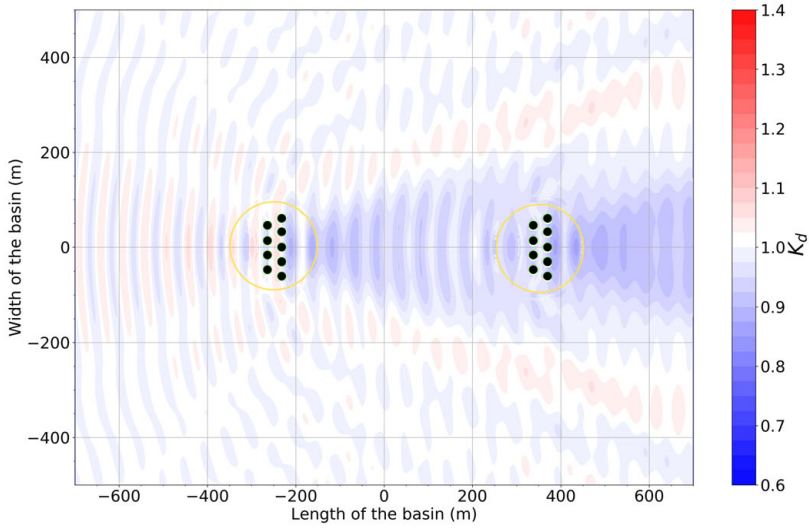

Figure 5.8: K_d around two WEC arrays, I (left) and II (right), of nine heaving cylindrical WECs for regular waves of H = 2 m and T = 6 s. Inter-array separation distance $D_1 =$ 200 m or $2r_c$. Wave incidence angle $\beta = 0°$.

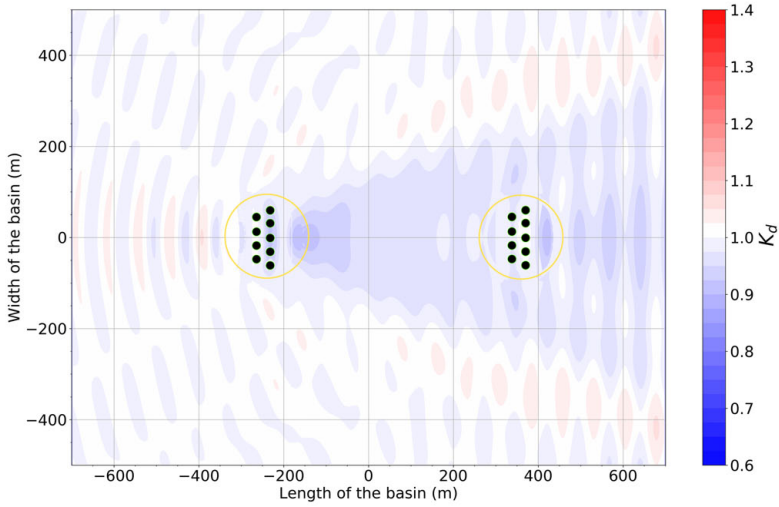

Figure 5.9: K_d around two WEC arrays, I (left) and II (right), of nine heaving cylindrical WECs for regular waves of H = 2 m and T = 6 s. Inter-array separation distance D_1 = 200 m or $2r_c$. Wave incidence angle $\beta = 0°$.

The same general interference pattern of positive and negative anomalies in η is observed as for the D_1= 200 m separation in Figs. 5.4 to 5.6. We remark that, in Fig. 5.8 and Fig. 5.9, behind the second array, there is a reduction in K_d for T= 10 s and little change for T = 8 s. In contrast, for the T = 6 s wave in Fig. 5.7, there is a net positive anomaly in η in the same location. This outcome can be explained in part by the more favourable position of Array II with respect to Array I that enabled it to radiate more waves for the case of larger separation distance. Such disturbances in K_d can be correlated with the WEC farm's performance as is shown in Section 5.5.2. In terms of the magnitudes of the anomalies in the wave field, there was again a marked contrast between the case of T = 6 s and that of the other two periods. For the former, the positive anomalies reached a value of 1.35, meaning that, in places, the presence of the WEC arrays increased the undisturbed wave field by up to 35%. The same negative anomaly was not as strong, as the region of marked decrease in K_d was mitigated by the positive anomalies in K_d due to the radiation of WEC array II. In contrast, for T = 8 s and T = 10 s, the greatest positive effects were no more than 10%, and there was a symmetry in the values of the maximum positive and negative K_d anomalies that deviated around 10% from the mean value of K_d. These results show the potential for radiation from WEC arrays to mitigate the effect of shadowing by the same arrays. We must note however, that the figures shown in this section are for the worst case scenario of WEC arrays aligned with the incoming wave direction. As we can see from the anomalies in η, we expect the results for off-axis incidences β to be superior in terms of the leeward WEC array locations. This is in fact shown in the next section Section 5.5.2 in the power curves.

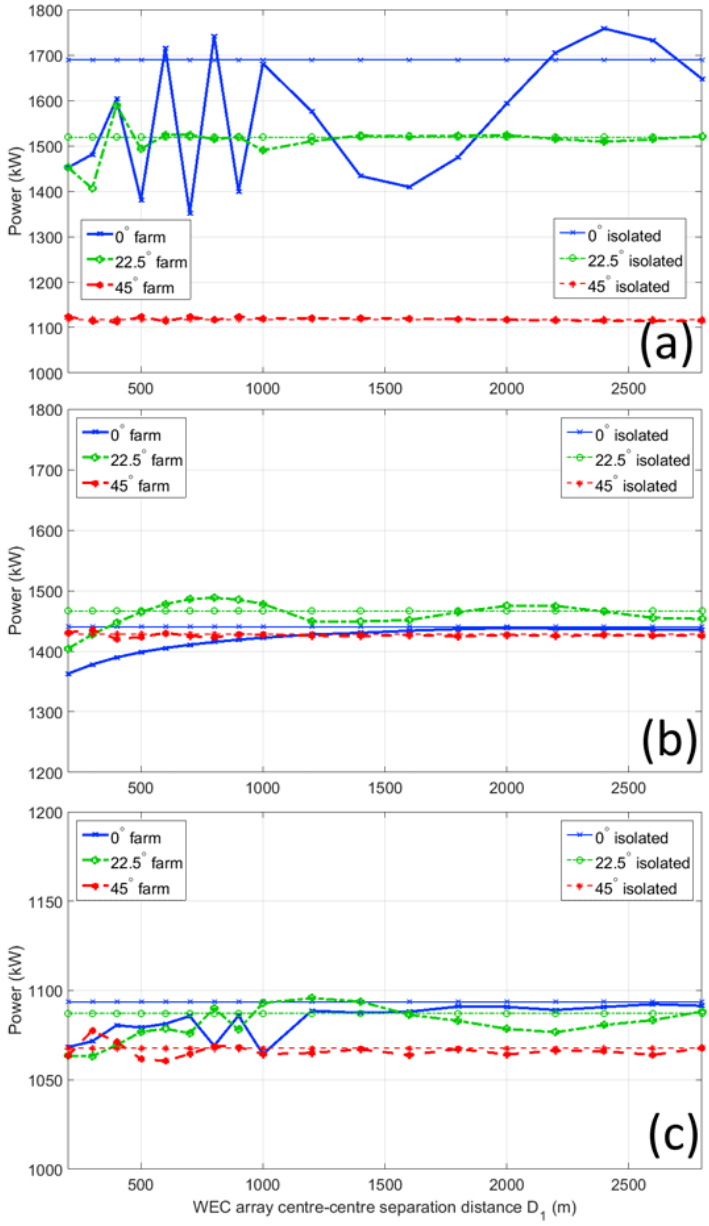

Figure 5.10: Power output of the WEC farm for various inter-array separation distances D_1 for regular waves of T = 6 s, (**a**) T = 8 s (**b**), and T = 10 s (**c**) for $\beta = 0°$ (solid line) 22.5° (dash-dot line), and 45° (dash line) thin horizontal lines indicated 2 × P_{array}. Thick lines indicate P_{farm}.

5.5.2 Power output of a WEC farm composed of two WEC arrays in regular waves

In the next two subsections, we expand on the qualitative observations made in Section 5.5.1 by quantifying the power output by a WEC farm composed of two WEC arrays separated by distance D_1 for incident waves of T = 6 s, T = 8 s, and T = 10 s. The procedure outlined in Section 5.4 in Fig. 5.3 was employed to calculate the power output of the two-array WEC farm for a range of separation distances D_1. Total average power output is displayed in the graphs in Fig. 5.10 for each period and wave incidence angle β. The thinner level lines are P_{isol}, the power output of a farm of hydrodynamically isolated WEC arrays, or 2× the power of a single nine-WEC array, while the thick lines represent P_{farm}, the power output of the hydrodynamically coupled WEC farm. The results are also presented in a non-dimensional manner in Fig. 5.11, where P_{farm} normalized by P_{isol} on the y-axis is plotted versus the non-dimensional ratio of D_1/d, where d is the WEC diameter. The ratio of P_{farm}/P_{isol} is analogous to the $q - value$, a commonly used metric to assess array effects within individual WEC arrays as mentioned in Section 2.7.1 and Section 3.8.3.

We first take note of the oscillating nature of the power output, with values both above and below the line showing the power output of arrays operating in isolation. The oscillations decreased in magnitude as we moved the arrays away from each other. Observing the trend from Fig. 5.10a to Fig. 5.10c, we noted the absolute value of the power output decreasing with increasing period. This is an expected trend given the behaviour of the disk-shaped buoy with resistive control in regular waves that maximizes the motion close to the resonance period, T_r, of 4.6 s. Note also that, in addition to the decrease in P_{farm} with wave period T, there is a slight decrease with increasing incidence angle β for T = 6 s and T = 10 s, especially in the case of the former. This is a consequence of the WEC arrays' shape, as seen in Fig. 5.2, where an increasing intra-array wake on the second row of WECs for each WEC array was observed, as β increases toward 45°, at which angle the WEC array effectively becomes aligned.

5.5.2.1 Wave incidence at $\beta = 0°$

In Fig. 5.10, we plotted the power output for increasing separation distance D_1 between Arrays I and II for three incidence angles, β= 0° (solid lines), β = 22.5° (dash-dot lines), and β = 45° (dashed lines). Fig. 5.10a shows the result for T = 6 s, Fig. 5.10b for T = 8 s, and Fig. 5.10c for T = 10 s. Observe that the result for T = 6 s for β = 0° shows the greatest power oscillations. This should come as no surprise, seeing that, in Fig. 5.7 there is a strong rapidly oscillating pattern of K_d in front of and in between the WEC arrays. Note also that, despite a single peak giving higher power output than the case of WEC arrays operating in isolation, the rest of the points fall well below the line of $P_{isolated}$. This trend demonstrates that the optimized staggered WEC array configuration results in substantial power extraction from the incoming waves, and that when one WEC array wakes another, the effect is strongly negative. This deleterious effect on power of placing one WEC

array in lee of another is mirrored in the results for T = 8 s (Fig. 5.10b) and T = 10 s (Fig. 5.10c).

5.5.2.2 Wave incidence at β = 22.5° and 45°

In this subsection, we compared and contrasted the reposes of the WEC farm power output for WEC array off-axis wave incidence. The key message of the curves in Figs. 5.7 to 5.9 is that, unlike the result for $\beta = 0°$, the array off-axis graph shapes do not greatly vary across the three tested periods. In other words, the WEC farm exhibits similar behaviour in power output across the three modelled wave peak periods. The power output of the WEC farm for $\beta = 22.5°$ is always higher than for $\beta = 45°$, with the magnitude of oscillations about the P_{isol} also less for $\beta = 45$ °.

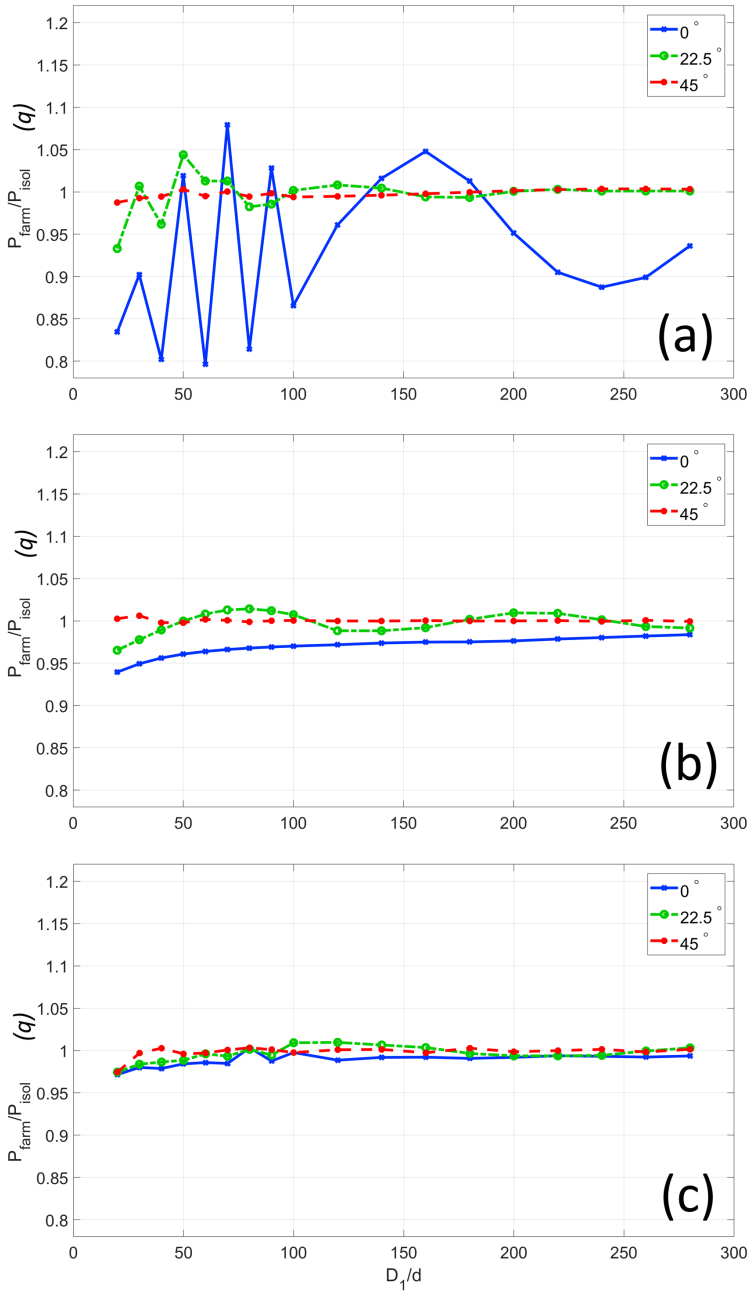

Figure 5.11: Ratio of P_{farm}/P_{isol} for non-dimensional distance D_1/d, where d is the diameter of the WEC shown for regular waves of T = 6 s (**a**), T = 8 s (**b**), and T = 10 s (**c**) for $\beta = 0°$ (solid line) 22.5° (dash-dot line), and 45° (dash line).

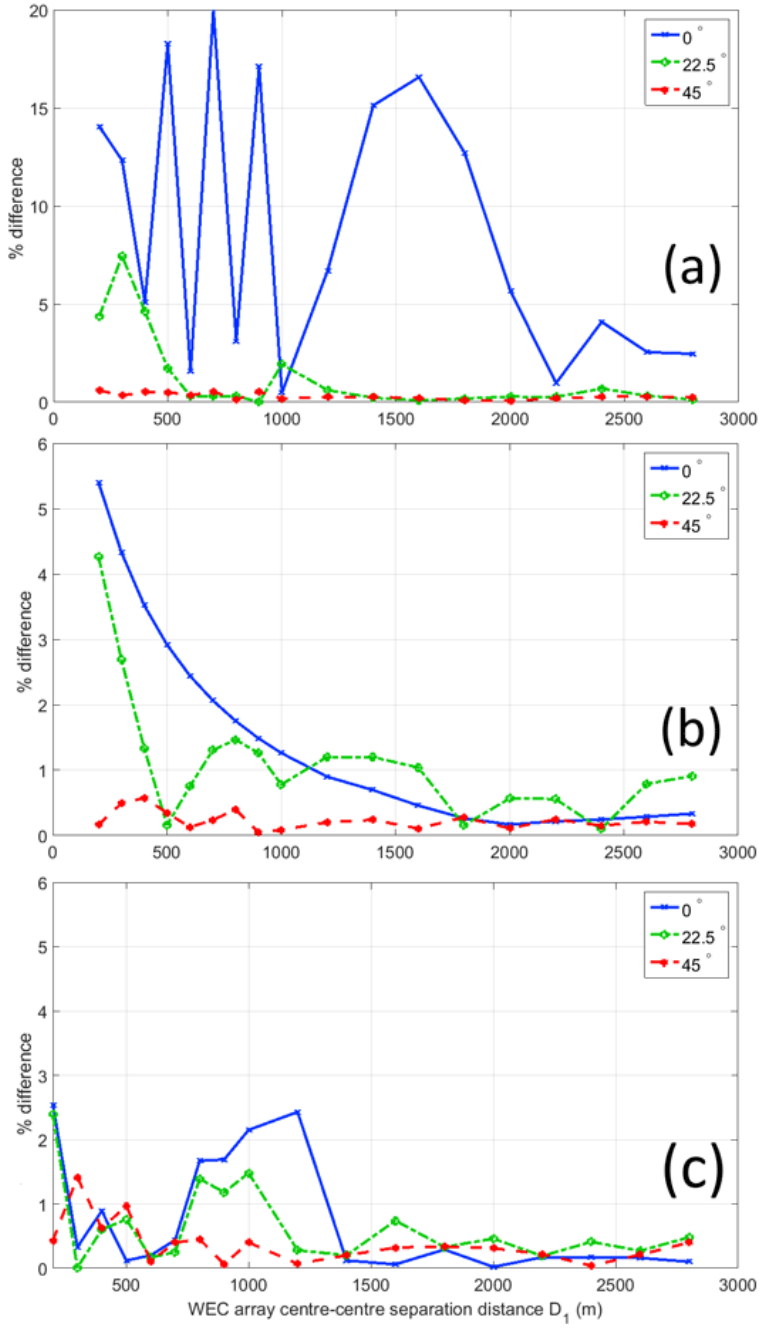

Figure 5.12: Percent difference between P_{farm} of two WEC arrays separated by inter-array distance D_1 and P_{isol} for regular waves of T = 6 s (**a**), T = 8 s (**b**), and T = 10 s (**c**), for 0° (solid line) 22.5° (dash-dot line) and 45° (dash line).

We point out that, although for T = 6 s the power of the WEC farm at β = 22.5° is generally lower than that for a head-on wave ($\beta = 0°$), this is not true for T = 8 s and T = 10 s. For T = 8 s, the power output for β=0° and β= 22.5 ° of both P_{isol} and (P_{farm}) is higher than for $\beta = 0°$. For T = 10 s, P_{farm} with $\beta = 22.5$ ° is lower than the value of P_{isol} in head-on waves, but is higher than the result for P_{farm} with β=0°. Again, we can link this result to the K_d plots in Section 5.5.1, where $\beta = 22.5$ ° is generally in an area of positive interference and low variability compared to $\beta = 0°$. Note that, for $\beta = 45$ °, P_{farm} is consistently lower than for $\beta = 0$ ° and $\beta = 22.5$ °. This outcome is explained in Section 5.8. Note that, by looking at Fig. 5.11, the graphs converge toward unity as we increase the relative distance, a result expected from theory and presented in many studies,

among them (Babarit, 2010; Borgarino et al., 2011b; Child and Venugopal, 2010; Ruiz et al., 2017b). However, from a practical point of view, it is important to remark that presenting the results in this manner hides the absolute difference in power. For example, for the closest separation distances for T = 6 s, the ratio P_{farm}/P_{isol} is below 0.95 for $\beta = 22.5°$ and $\beta = 45°$, and is greater than 0.95 for T = 8 s and T = 10 s. However, the improved relative performance comes at the cost of significant decrease in absolute power, as witnessed in Fig. 5.10.

5.5.3 Quantifying the percent difference between P_{farm} and P_{isol}

While in Section 5.5.2 we explored the trends in WEC farm power output in absolute terms, in order to answer the question posed in the introduction of this paper, namely, that of the error introduced by assuming WEC array independence, we needed to quantify the percent difference between P_{farm} and $P_{isolated}$. We calculated the percent difference between P_{farm} and P_{isol} for the three regular waves for the three wave incidence angles. As expected from analysing power output in Section 5.5.2, the relatively large errors for T = 6 s and $\beta = 0°$ stand out compared to the rest of the data. We see that the error was as large as 20% for $D_1 =$ 700 m, and did not consistently decline below 10% until D_1 of 2000 m. This is a consequence of strong interference between the perturbed waves of the two arrays when they were aligned with the wave direction and with each other.

For $\beta = 22.5°$ and $\beta = 45°$, we noted that the percent error was below the 5% threshold for the former and 1% for the latter, meaning that the array effect played a minor role in modifying the behaviour of P_{farm}. Still, the trend was a decrease in the magnitude of the percentage difference, with an increase in array–array separation distance.

To see this trend more clearly, we could plot the power in graphic format in Fig. 5.12. Here, the decreasing asymptotic trend is obvious save for the anomalous result of $\beta = 0°$ for T = 6 s. The strong oscillations in the graph for $D < 1000$ m are a consequence of the resolution in x of the D_1, where the strongly varying graph oscillating about P_{isol} is sampled frequently enough to capture the peaks and troughs of the perturbed waves of the two arrays. For $D_1 > 1000$ m, the lower resolution in x only shows the envelope of the trend. For the other eight cases, the frequency of the variability was not as strong; therefore, the curves look to be

smoother over the entire range of separation distances.

5.6 Irregular wave results

In this section, we present the results for an irregular wave incident on the WEC farm in Fig. 5.1. As mentioned in Section 5.3.5, the irregular waves in the study are modelled on a Pierson–Moskowitz spectrum with no directional spreading. The peak periods analysed are $T_p = 6$ s, $T_p = 8$ s, and $T_p = 10$ s, matching the period of the regular wave cases. Each irregular wave result is a weighted sum of the coupled wave field at each modelled frequency. Since the dependency of the wave field on the incidence wave angle yields a similar pattern for irregular waves as for regular waves, we only present results for wave incidence $\beta = 0°$. We begin, as in Section 5.5, by looking at the total coupled wave fields for the farm in Section 5.6.1 and then explore the WEC farm power output in Section 5.6.2.

5.6.1 K_d around two WEC arrays within a WEC farm in irregular waves

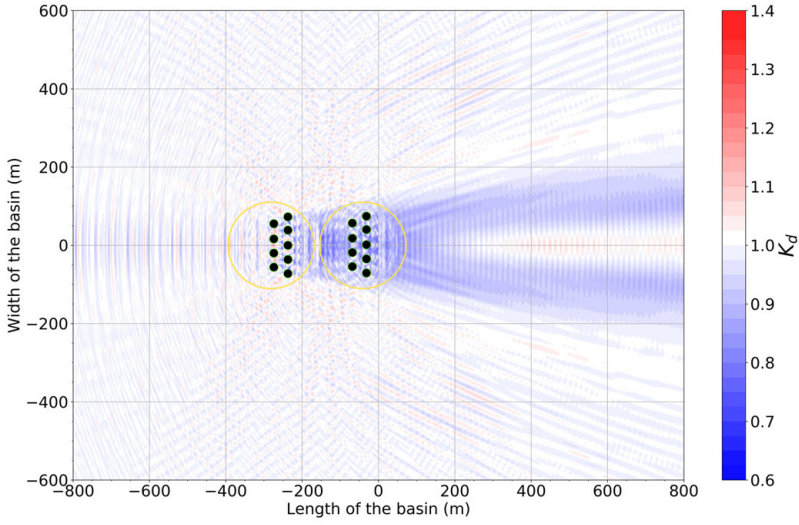

Figure 5.13: Total wave field around two WEC arrays, I (left) and II (right), of nine heaving buoys for Pierson–Moskowitz irregular waves of $H_{m0} = 2$ m, $T_p = 6$ s. Inter-array separation distance $D_1 = 200$ m or $2r_c$. Wave incidence angle $\beta = 0°$.

The irregular wave results for $T_p = 6$ s and $T_p = 8$ s are plotted in Figs. 5.13 and 5.14 for $D_1 = 200$ m, and in Figs. 5.15 and 5.16 for $D_1 = 600$ m. The contour plots shown the value of the K_d at each point in the domain as defined by Eq. (4.16). The total wave field is obtained as the sum of the undisturbed (incident) and the perturbed wave field at 20 different frequency components as explained in

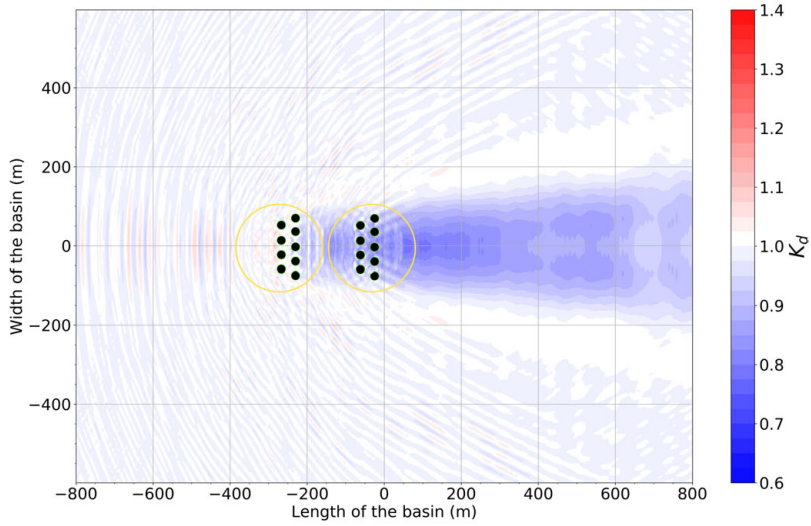

Figure 5.14: Total wave field around two WEC arrays, I (left) and II (right), of nine heaving buoys for Pierson–Moskowitz irregular waves of $H_{m0} = 2$ m, $T_p = 8$ s. Inter-array separation distance $D_1 = 200$ m or $2r_c$. Wave incidence angle $\beta = 0°$.

Section 5.3.5. The chief difference we noted in comparing the irregular wave results in the figures for the irregular K_d to the regular counterparts in Figs. 5.4 to 5.6 and Figs. 5.13 and 5.14 is the decrease in the overall magnitude of the interaction, as would be expected for the case where wave energy was not concentrated at one frequency but was, instead, spread out. Moreover, we could observe an absence of significant areas of positive interactions, such as those encountered for a regular wave case in the Fig. 5.4 and 5.7, in the bands surrounding the wake of the arrays, at approximately 20° to 30° off the y-axis. At the same time, the wake was quite strong, notably for $T_p = 8$ s. For T = 6 s, we could explain the decreased wake by the ability of the WECs in the array to radiate, acting to immediately offset the decrease in the wave height in lee of the arrays. This contrast between the two modelled wave periods is starkest for the arrays separated by 200 m in Fig. 5.13 and Fig. 5.14, where we observe a region of neutral or positive K_d from 200 to 800 m behind the arrays for $T_p = 6$ s, and only negative anomalies in K_d for $T_p = 8$ s. As is expected for multi-frequency sea states, the interaction pattern witnessed in Figs. 5.13 and 5.14 and Figs. 5.15 and 5.16 is more complex than that of the regular wave fields in Figs. 5.4 and 5.5 and Figs. 5.4 and 5.5. Nonetheless, the majority of the array effect of the particular array configurations are in the region immediately on the array axis or slightly off it. This is the reason for the significant effects on power absorption for the arrays in a head-on sea state detailed in Section 5.5.2.1 and witnessed in Fig. 5.10(a) and 5.12 (a). In the next section Section 5.6.2, we explore the power output for the analogous case in irregular waves for various array separation distances D_1.

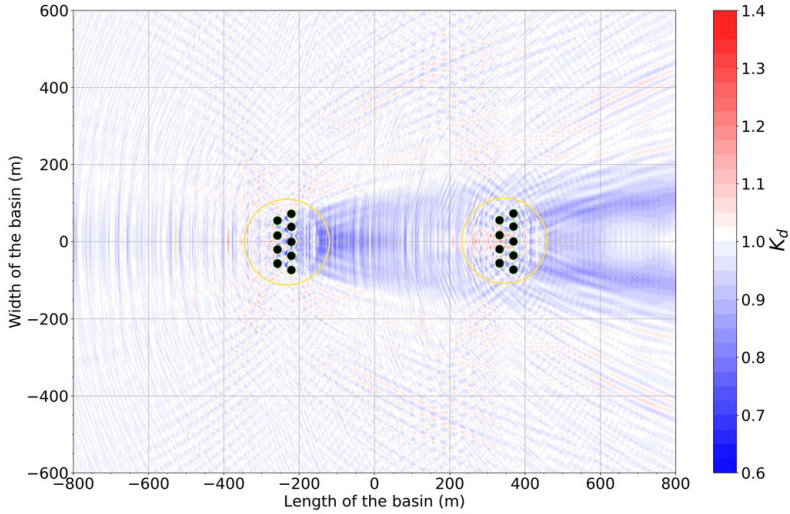

Figure 5.15: Total wave field around two WEC arrays, I (left) and II (right), of nine heaving buoys for Pierson–Moskowitz irregular waves of $H_{m0} = 2$ m, $T_p = 6$ s. Inter-array separation distance $D_1 = 600$ m or $6r_c$. Wave incidence angle $\beta = 0°$.

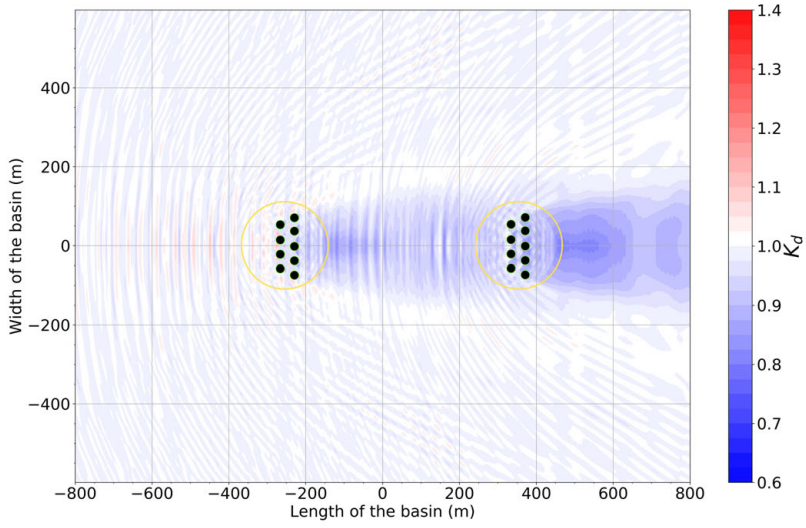

Figure 5.16: Total wave field around two WEC arrays, I (left) and II (right), of nine heaving buoys for Pierson–Moskowitz irregular waves of $H_{m0} = 2$ m, $T_p = 8$ s. Inter-array separation distance and $D_1 = 600$ m or $6r_c$. Wave incidence angle $\beta = 0°$.

5.6.2 Power output of a WEC farm composed of two WEC arrays in irregular waves

When one compares the result in Fig. 5.17 to the corresponding regular wave cases in Fig. 5.10, one can remark two large differences. The first is that for the case of an irregular wave, all of the array effects were detrimental to the power absorption of the WEC farm. This is further highlighted in Fig. 5.18, where the P_{farm}/P_{isol} ratio was below unity for all plotted non-dimensional distances. Such was not the case for the regular wave for T = 6 s in Fig. 5.10a, where there were certain distances for which the power output of the interacting WEC farm was greater than that of the isolated one. The second difference was that total power output for the three irregular wave peak periods was lower than for the corresponding regular wave periods.

This is not surprising, as the efficiency of a heaving WEC decreased when the energy was spread out over many frequencies in the irregular wave case. We also observed that, unlike the regular wave case where the power output was highest for T = 6 s, for the irregular wave case power was highest for $T_p = 8$ s. This difference in the behaviour of the WEC farm could be due to the fact that for a Pierson-Moskowitz spectrum, which we used here to model the irregular waves, as the peak period increases, the frequency spectrum also narrows. Thus, the spectrum is widest for $T_p = 6$ s and narrowest for $T_p = 10$ s. Therefore, the difference between the energy bandwidth was greatest between T = 6 s and $T_p = 6$ s. This effect is enough to decrease the performance of the heaving WECs by a factor of 3, and reverse relative power output vis-a-vis T = 8 s. Even if we did not explicitly model off-axis wave incidences β for irregular waves, we expected the results to mirror those for regular waves in that power output would be improved compared to the case of $\beta = 0°$, but not much greater than unity. This can be easily seen in the representative K_d for the irregular wave for Tp = 6 s in Figs. 5.13 and 5.14 for D_1= 200 m and for D_1= 600 m in Figs. 5.15 and 5.16, where the 'wake zone' extends out to ±15 degrees on either side of $\beta = 0°$ behind the WEC arrays.

5.7 Defining 'Hydrodynamic Independence' in a WEC Farm Composed of Two WEC Arrays

We have seen in Sections 5.5.1 and 5.6.1 that the various factors in play influencing the power output of a WEC farm lead to a very complicated pattern of interaction that can be hard to discern. It is natural, then, to ask how we can extract practical information from such data that can both serve to optimize the WEC farm layout for a specific goal, as well as to accurately calculate the wave fields around the WEC arrays. For this reason, we attempt to simplify the problem of calculating hydrodynamic interactions in a WEC farm by quantifying the significance of the interactions by first setting the value of 5% as an 'independence' threshold. Consequently, we define a WEC farm of two WEC arrays as hydrodynamically 'independent' if the power output was within ±5% of the power output by two independent WEC arrays that operate in isolation (the case of $2 \times P_{array}$).

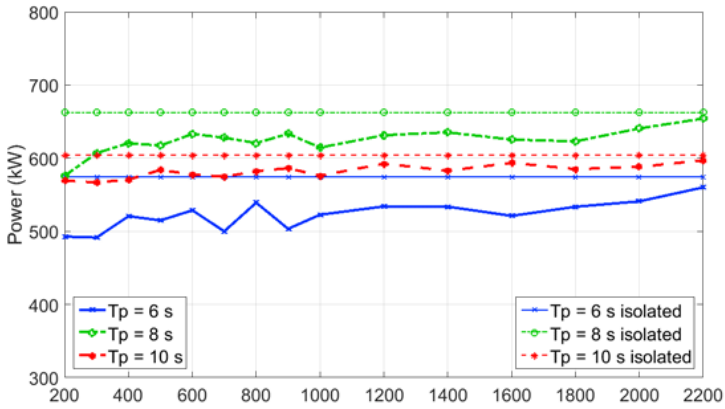

Figure 5.17: Power output of a WEC farm for various inter-array separation distances D_1 for irregular waves of Tp = 6 s , Tp = 8 s , and Tp = 10 s for 0° (solid line), 22.5° (dash-dot line), and 45° (dashed line). Thin horizontal lines indicate P_{isol}. Thick lines indicate P_{farm}.

We recall here that in the hydrodynamically independent case, power output was computed for each WEC array in isolation, specifically that the undisturbed wave field is used as input for the motion equations of the WEC array. The power output for the case where there was interaction between the WEC arrays was determined by the iterative procedure outlined in Section 5.3.4. Therein, the input wave field is the sum of the incident and perturbed waves from both arrays. For the case of irregular waves outlined in Section 5.3.5, wave field summation is performed over each frequency ω. In order to visualize this concept, we turn back to Figures 5.12 and 5.19, where we plotted the percent difference between P_{farm} and P_{isol} for regular and irregular waves, respectively. Starting with the regular wave cases in Fig. 5.12, we immediately observe that only for the case of T = 6 s and $\beta = 0°$ was the difference consistently greater than 10% for a range of separation distances D_1. For the rest of the investigated regular cases, the difference was small, and, in fact, for T = 10 s only the $\beta = 22.5$ ° waves resulted in a difference larger than 1% in power output. For T = 8 s, for all three wave incidence angles, the percent difference was below the 5% 'hydrodynamic independence' threshold. We can therefore safely assume array 'independence' for an overwhelming majority of the regular wave cases presented in this study.

For the irregular wave scenarios for $\beta = 0°$ in Fig. 5.19, we see a slightly different but marked decrease trend in the difference between P_{farm} and $2 \times P_{arr}$ with increasing D_1. While the case of $T_p = 6$ s is still the 'worst' in terms of percent difference because of the frequency spread of the Pierson–Moskowitz waves, the percent difference for $T_p = 6$ s was greater than that for T = 8 s. For $T_p = 10$ s, the percent difference was less than 5% for all separation distances greater than 400 m. Although we did not model them in this investigation, based on Figs. 5.13 and 5.14 and Figs. 5.15 and 5.16, we could surmise that, for the 'off-axis' wave incidence angles, the difference between $2 \times P_{arr}$ and P_{farm} would again be smaller.

A more complex modelling scenario with irregular wave results for multiple arrays and incidence angles β will be presented in Chapter 7. In summary, making the assumption of array 'independence' in a WEC farm, where the WEC arrays are modelled as isolated, is safe as long as one array is not directly in lee of another. Moreover, for D_1 greater than 1000 m, all modelled cases except for those of waves of T = 6 s and $T_p = 6$ s were below the 5% threshold and could be deemed 'independent', allowing for a significant reduction in modelling complexity without loss of fidelity.

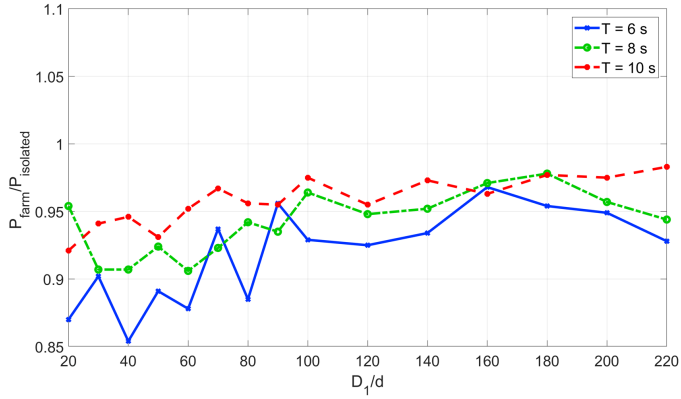

Figure 5.18: Ratio of P_{farm}/P_{isol} for non-dimensional distance D_1/d, is the diameter of the WEC shown for irregular waves of $T_p = 6$ s (solid line), $T_p = 8$ s (dash-dot line), and $T_p = 10$ s (dashed line).

5.8 Discussion

In Section 5.7 we saw that the separation distance between the WEC arrays in a WEC farm is not the only factor that plays a role in determining the extent to which two WEC arrays are hydrodynamically linked. However, the asymptotic behaviour of WEC array interaction with respect to array separation distance D_1 is evident in Figures 5.10, 5.12, 5.17, and 5.19. It should be noted that the extent of the separation distance that we have modelled is limited from a practical standpoint to 2800 m, and several studies(Babarit, 2010; Borgarino et al., 2011b) show that, in regular waves, two WECs can have an appreciable hydrodynamic influence on each other, even when they are separated by more than 5 km. Here, it is important to remark that, in those particular investigations and in others that showed similar strong interactions at large separation distances, the modelled WECs were optimally tuned to magnify WEC motions. As a consequence , we should expect the perturbed waves from WECs tuned in such a manner to be greater than those of linearly resistively tuned WECs of the type that we modelled in this paper.

Of the factors influencing the strength of both WEC farms, wave field modification and its power output, D_1, had the largest influence. However, as we saw in Section 5.5.2, the period of the modelled wave has an appreciable influence on inter-array iteration, especially close to the resonance period of the WECs. For irregular waves, as witnessed in Section 5.6.2, the difference between the three peak periods was not as strong given the frequency spreading inherent in the Pierson–Moskowitz spectrum we used in the model. We also demonstrated the linking of influence of the wave incidence angle and D_1 to the power output. Not only did the overall magnitude of the interaction effects decrease as the wave incidence changed from a $\beta = 0°$ heading to $\beta = 45°$, but the variability over the range of D_1 decreased as well. This was a result of the relative position of the WEC arrays; when one array was not directly shadowing another, the likelihood of a decrease in performance of a WEC array located down-wave was reduced. Consequently, for incidence angles K_d away from 0°, the waves that interacted with WEC array II located down-wave were closer to the undisturbed incident wave. Of note is the suboptimal performance of $\beta = 45°$ observed in Fig. 5.10, specifically for the case of T = 6. The 'underperformance' of $\beta = 45°$ could be explained by the fact that, at this wave incidence angle, the staggered configuration became aligned, and the back row of the array was strongly shadowed by the front row, as can be witnessed in Fig. 5.2. As the staggered configuration of the WECs became roughly aligned for the waves with $\beta = 45°$, there was a significant 'wake effect' inside the WEC array, but not at the WEC-farm level. This is why there was also less oscillation in power output over the WEC farm separation distances D_1 for $\beta = 45$ °. These results remind us that, in order to construct an optimized WEC farm, both the design of the micro elements, i.e., the layout of the individual WECs in a clustered array, and the macro elements, *i.e.* the WEC farm layout composed of larger units, should be considered.

We should remark an important point about the trends seen in Fig. 5.10 and Fig. 5.17. In particular, WEC farm interaction is beneficial to only a small subset of the regular wave cases modelled, and is never beneficial for irregular waves. This outcome is largely due to WEC type and the limitations of the linear resistive PTO modelled in this investigation. As was shown in a number of previous studies Child and Venugopal (2010); Balitsky et al. (2014); Penalba et al. (2017b); Ruiz et al. (2017b), one needs to implement active frequency-dependent control in order to fully take advantage of WEC motions to induce beneficial hydrodynamic interactions between WECs and, by extension, between WEC arrays. While we observed an overall decrease in the magnitude of inter-array interactions as we increased the array separation distance consistent with the $1/\sqrt{2}$ asymptotic trend defined in (Babarit, 2010), there was significant difference in the smoothness of the power-output curve between the various tested wave periods and incidence angles β. It should be pointed out that the result was mainly due to the configuration choice of individual WEC arrays that were optimized for a certain incident wave direction, specifically, β=0°. Thus, when placed one behind another, the power output of the WEC farm substantially decreased.

The observed response of the WEC farm exactly mirrors the trend that was demonstrated for individual WECs placed at increasing intra-array distances from

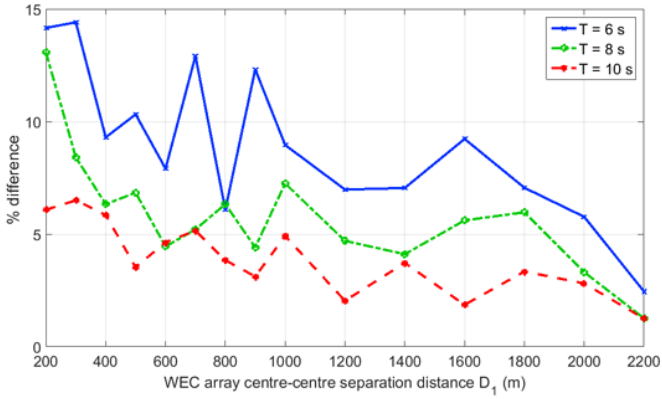

Figure 5.19: Percent difference between P_{farm} of two WEC arrays separated by inter-array distance D_1 and $2 \times P_{arr}$ for irregular waves of Tp $= 6$ s (**a**) Tp $= 8$ s (**b**) and Tp $= 10$ s (**c**) for 0° (solid line), 22.5° (dash-dot line), and 45° (dashed line).

each other, such as in (Babarit, 2010; Borgarino et al., 2012; Garcia Rosa et al., 2015). In these papers, the net power in a WEC array trends to the sum of the power of isolated WECs as the separation distance becomes larger. In the investigation, we were able extend said observation to WEC farms composed of multiple arrays. Note that a similar conclusion was reached in Borgarino et al. (2012), where the authors separated a WEC farm into two clusters of WECs, concluding that offsetting array clusters so that one is not directly behind another is the best array layout design strategy.

However, in Borgarino et al. (2012), the authors employed a BEM solver to simultaneously calculate all interactions, an approach that has limits as the number of simulated WECs increases. In contrast, the coupling method permitted us to model arbitrary large numbers of WECs, provided they were split into individual clustered arrays. As was noted in the introduction, this constraint could almost certainly be applied to WEC farms from practical and economical considerations. As we have shown in Section 5.7, unless WECs are closely spaced and are directly aligned with the incoming wave direction, such clusters can be assumed 'independent' with only a small error in the WEC farm power output estimate.

5.9 Conclusion

In this chapter, an iterative coupling method between the near-field BEM solver NEMOH and far-field wave propagation model was applied to examine the WEC array interaction effects in a WEC farm composed of heaving resistive WECs. The method provides a robust and efficient means of calculating the wave field around compact WEC arrays and, in turn, allowed us to estimate the total power output of a WEC farm. Although the coupling gives accurate results to an arbitrary degree of precision, even a few orders of interactions require a complicated web

of iterations as explained in Section 5.3.4 in Fig. 5.3. Hence, it is natural to seek further simplification of hydrodynamic calculations. If we can assume that two WEC arrays (I and II) in a farm are hydrodynamically independent, i.e., they behave as isolated, then the power absorbed by each WEC array can simply be computed in one iteration. The total wave field in a farm could then be calculated as the sum of two perturbed wave fields generated by WEC Arrays I and II, where the motion of both arrays is forced only by the incident wave.

We saw that the primary determinant for the power output of a WEC farm composed of linearly resistive heaving WECs for a given regular or irregular wave period is separation distance D_1. Nonetheless, wave incidence angle β plays a significant role in determining not only the total power output of a WEC farm for a given wave period but also the attenuation of the array effects with D_1. It should be mentioned that, in this investigation, we focused on a narrow subset of modelling scenarios, namely, that the study was performed for heaving WECs with a linearly resistive PTO. Although we expect the same overall trends to hold for various classes of WECs, it is evident that, for actively controlled WECs that are able to be tuned for a particular sea state, WEC motion and, by extension, the perturbations in the wave field would be increased in magnitude and felt over a larger distance away from the array. It will be the topic of a future investigation to model a more realistic type of WEC, where each WEC's PTO is subject to active control. Finally, we should note that, although we have demonstrated the coupling technique of Section 5.3.4 and the power-output trends in Sections 5.5.2 and 5.6.2 for a WEC farm composed of only two WEC arrays, the method could easily be extended to WEC farms composed of multiple arrays as will be shown in Chapter 7.

In this chapter, it was also shown that, for both regular and irregular waves, for a large majority of cases, two WEC arrays in a farm could be considered hydrodynamically independent for the purposes of assessing the power output of a WEC farm. In this case, a simple and fast coupling method consisting of only one summation for each array could estimate power output with high accuracy. In Section 5.7, we investigated the error magnitude *i.e.* introduced into the calculation by making the assumption of hydrodynamic independence of the WEC arrays. We observed that the error introduced by the array independence assumption was within 5% for all cases except for only the closest separation distances D_1 for T $=$ 6 and $T_p = 6$ for $\beta = 0°$.

As was noted in Section 5.6, in this work we did not explicitly model off-axis wave incident angles β for irregular waves. The work of the research group on short-crested irregular wave modelling of WEC arrays has been accepted for publication as of the date of this thesis. Additionally, as we alluded in the discussion in Section 5.8, the results depend on the type of modelled PTO. To this end, the group is integrating various realistic PTO types into the coupled modelling via a PTO module. These results are presented in the following chapter Chapter 6.

If we extend the scope beyond purely hydrodynamic considerations and consider the economic constraints of a commercial WEC farm, we can see that separating WEC farms into hydrodynamically independent clusters of WECs can have advantages beyond simplifying power-output calculations. By concentrating many WECs in close proximity, a WEC farm developer can save on the cost of marine cables that

are known to be a significant expense item for offshore energy projects. Furthermore, spacing constraints, such as leaving navigation channels for operations and maintenance navigation and other sea users in between the WEC arrays, naturally result in a clustered layout for the WEC array. Based on the results obtained in this paper, we can consider such a WEC farm to be composed of 'independent' arrays and apply the present coupling method to the problem of technoeconomic optimization of WEC farms *i.e.* necessary for the commercial viability of wave energy.

Chapter 6

The implementation of a Time-Domain Power-Take-off (PTO) into a coupled model

Abstract

The Power Take-Off (PTO) system is the key component of a Wave Energy Converter (WEC) that distinguishes it from a simple floating body because the uptake of the energy by the PTO system modifies the wave field surrounding the WEC. Consequently the choice of a proper PTO model of a WEC is a key factor in the accuracy of a numerical model that serves to validate the economic impact of a wave energy project. Simultaneously, the given numerical model needs to simulate many WEC units operating in close proximity in a WEC farm, as such conglomerations are seen by the wave energy industry as the path to economic viability. A balance must therefore be struck between an accurate PTO model and the numerical cost of running it for various WEC farm configurations to test the viability of any given WEC farm project. Because hydrodynamic interaction between the WECs in a farm modifies the incoming wave field, both the power output of a WEC farm and the surface elevations in the 'near field' area will be affected. For certain types of WECs, namely heaving cylindrical WECs, the PTO system strongly modifies the motion of the WECs. Accordingly, the choice of a PTO system affects both the power production and the surface elevations in the 'near field' of a WEC farm. In this chapter, we investigate the effect of a PTO system for a small wave farm that we term 'WEC array' of 5 WECs of two types: a heaving cylindrical WEC and an Oscillating Surge Wave Energy Converter (OSWEC). These WECs are positioned in a staggered array configuration designed to extract the maximum power from the incident waves. The PTO system is modelled in WEC-Sim, a purpose-built WEC dynamics simulator. The PTO system is coupled to the open-source wave structure interaction solver NEMOH to calculate the average wave field η in the 'near-field'. Using a WEC-specific novel PTO system model, the effect of a hydraulic PTO system on the WEC array power production and the near-field is compared to that of a linear PTO system. Results are given for a series of regular wave conditions for a single WEC and subsequently extended to a 5-WEC array. We demonstrate the quantitative and qualitative differences in the power and the 'near-field' effects between a 5-heaving cylindrical WEC array and a 5-OSWEC array. Additionally, it is shown that modelling a hydraulic PTO system as a linear PTO system in the case of a heaving cylindrical WEC leads to considerable inaccuracies in the calculation of average absorbed power, but not in the near-field surface elevations. Yet, in the case of an OSWEC, a hydraulic PTO system cannot be reduced to a linear PTO coefficient without introducing substantial inaccuracies into both the array power output and the near-field effects. The implications of the results compared to previous research on WEC arrays which used simplified linear coefficients as a proxy for PTO systems discussed.

6.1 Introduction

Due to hydrodynamic interactions between individual WECs and closely-spaced groups of WECs, determining the power output of a WEC farm is not a trivial matter. As experimental studies are costly and time consuming, the chief design tool for assessing WEC farms is numerical modelling. There are many variables influencing the estimated power output, amongst them the site wave climate and bathymetry, WEC farm layout and the Power Take-off (PTO system) of each WEC. Modelling them in parallel leads to significant demands on computational power, and often leads to unclear conclusions. An additional complication for the numerical modellers is that many of the aforementioned variables are interdependent; it is therefore essential to understand the significance of each of the variables underlying the chosen numerical model.

For a given WEC type and incident wave, a critical parameter that influences the WEC motion and the power output of a WEC farm is the PTO system. Because of the variety of technical solutions and complexity of modelling the inherently non-linear behaviour of a majority of viable PTO systems in WECs, a plurality of previous investigations have assumed a simple mechanical damper as a proxy for the PTO system.

Some examples for farms of heaving cylindrical WECs are found in (Child and Venugopal, 2007; Charrayre et al., 2014b; Göteman et al., 2015; Ruiz et al., 2017a,b) and for Oscillating Surging Wave Energy Converters (OSWECs) in (Yu et al., 2014a; Zhao et al., 2013; Schmitt et al., 2016; Tay and Venugopal, 2017; Henry et al., 2018). Concurrently, due to step improvements in hydrodynamic modelling software, there has been a jump in the number of numerical investigations that have modelled single WECs (Paredes et al., 2013; Schmitt and Elsaesser, 2015; Devolder et al., 2016; Verbrugghe et al., 2018) and small farms of WECs (Devolder et al., 2018a; Bharath, 2018) with fully non-linear hydrodynamics. Yet, as pointed out in Penalba et al. (2018) for the case of heaving point absorbers and in (Schmitt et al., 2016) for OScillating Wave Energy Converters (OSWECs), the errors due to a simplified PTO model can override any improvements made by more accurate hydrodynamic models. A particular concern with many existing PTO modelling efforts is that the most common PTO system type developed for commercial WEC prototypes, a hydraulic PTO system, is inherently non-linear (de O. Falcão, 2008; Folley and Whittaker, 2009a). A few recent studies, notably (Cargo et al., 2012; So et al., 2015; Sell et al., 2017; Penalba et al., 2018; Yu and Jenne, 2018) have implemented realistic hydraulic PTO models with non-linear dynamics. However, these studies were limited in their scope to single WECs and not WEC farms, furthermore, many of the models are quite complicated in their implementation.

In this chapter the goal is to implement a realistic hydraulic PTO model for two types of promising WEC technologies, namely heaving cylindrical WECs and OSWECs, in an array composed of 5 WECs. Although the terms WEC farm and WEC array are used interchangeably, as in the rest of the thesis, we will follow the precedent set in (Balitsky et al., 2018b) and term a small farm of closely-spaced WECs a *WEC array*. The impact of the hydraulic PTO system on the power output

and the 'near-field' surface elevations of the 5-WEC array is compared to that of the base case of a linear PTO system. Both PTO systems are simulated using WEC-Sim (Yu et al., 2014a), a dynamical simulator for WECs built in the Matlab Simulink platform. The PTO model is coupled to the open-source wave-structure interaction solver NEMOH (Babarit and Delhommeau, 2015) using the perturbed wave field imparted by the motion of the WECs in WEC-Sim.

Previously, a similar approach was presented in (Stratigaki, 2014; Balitsky et al., 2017b; Verbrugghe et al., 2017b) for the case of a wave-structure interaction solver coupled to a wave propagation model using a basic linear PTO model. WEC-Sim has been utilized in modelling hydraulic PTOs in a number of recent studies (So et al., 2015; Yu and Jenne, 2018). In the present study only the near-field zone is simulated with a future goal of coupling to a wave propagation model in order to model the impact of a WEC farm (consisting of one or multiple WEC arrays) in the 'far-field'. In referencing the near-field we refer to the area inside the WEC array immediately surrounding the WECs, while the far-field can refer to areas outside the immediate area of the WEC array up to several km away. The modifications of the wave field in the presence of multiple bodies are referred to as 'array effects', that are synonymous with 'farm' or 'park effects' used in some literature (Beels et al., 2010; Babarit, 2013; Charrayre et al., 2014a; Penalba et al., 2017b).

We begin by providing the details on the two numerical PTO system interpretations used in the study in Section 6.2 and specify the regular wave test matrix of the simulations in Section 6.3.2. We then present the results for a single WEC for the power in Section 6.4.1, the near-field K_d in Section 6.4.2, and compare the performance and effects of a hydraulic PTO system to a linear PTO system in Section 6.4.2.3. Next we present the corresponding results for the 5-WEC arrays of heaving cylindrical WECs and OSWECs in Sections 6.5.4 and 6.5.5 and Section 6.5.5.3. Finally, we highlight the key messages of the research in the discussion in Section 6.6, and make conclusions with a view toward a continuation of the work undertaken in this chapter in Section 6.7.

6.2 PTO Model Development

6.2.1 Equations of motion

To model the WECs with a given PTO system, in this investigation we utilize the open source mechanical solver WEC-Sim developed by Sandia National Laboratory in collaboration with the National Renewable Energy Laboratory (NREL) in the US (Yu et al., 2014a). WEC-Sim operates within the Matlab Simulink environment. For 1 DoF WEC displaced a distance z from equilibrium, WEC-Sim solves for the WEC motion in the time-domain using the Cummins equation (6.1):

$$\mathrm{M}_t\ddot{z}(t) = f_e(t) + f_{rad}(t) + f_{hs}(t) + f_{PTO}(t) + f_v(t) + f_m(t) \tag{6.1}$$

In the case of a floating WEC oscillating in heave, $\mathrm{M}_t = \mathrm{M} + A_{33\infty}$ where M is the generalised mass matrix and $A_{33\infty}$ is the asymptotic value of the heave added mass. On the right hand side, $f_e(t)$ is the excitation force, $f_{PTO}(t)$ is the

PTO force, $f_{hs}(t)$ is the hydrostatic force, $f_{rad}(t)$ is the force vector of radiation, $f_v(t)$ are the forces that can be modelled as viscous or friction losses in the system, and $f_m(t)$ is the force vectors resulting from the mooring connections. The excitation force is calculated as $f_e(t) = \mathcal{F}^{-1}\{F_e(\omega)\eta(\omega)\}$, where $\eta(\omega)$ is the Fourier transform of the surface elevation and $F_e(\omega)$ is the frequency-domain exciting force transfer function. $f_{hs}(t)$ is the hydrostatic force which is equal to the inverse Fourier transform of $K_{33}Z(\omega)$ where K_{33} represents the hydrostatic stiffness and $Z(\omega)$ the frequency-domain displacement of the heaving cylindrical WEC. The hydrodynamic coefficients representing A, the added mass of the device, B, the hydrodynamic damping and K, the hydrodynamic spring or stiffness, are calculated in the frequency-domain in NEMOH for each relevant degree of freedom for the given WEC type. Note that henceforth all capital letters represent frequency-domain complex quantities whilst small case letters represent real-valued time-domain quantities. For the regular waves simulated herein, the radiation force $f_{rad}(t)$ can be calculated in the steady state form for a given frequency ω by the following equation (6.2):

$$f_{rad}(t) = -A(\omega)\ddot{z} - B(\omega)\dot{z}. \tag{6.2}$$

In this chapter, we do not model $f_v(t)$ and $f_m(t)$ since they are assumed to be negligible, therefore those terms are set equal to zero. The OSWEC described in section 6.3.1 is simulated using the same Eq. (6.1), with the substitution of torques for the forces and the pitch angular displacement $\theta(t)$ for the heave displacement $z(t)$ and the coefficients in heave for the coefficients in pitch. Two different types of power take-off systems will be further discussed: a linear and hydraulic PTO system, the former being the most popular way of simplifying a PTO system while the latter being one of the most used PTO systems in commercial WEC designs.

6.2.1.1 Linear PTO system

The most common way of simulating the effect of the PTO system of a wave energy converter is by modelling its dynamics as linear. This means the PTO system is modelled as a spring-damper-mass system with stiffness coefficient K_{PTO} and damping coefficient B_{PTO}. However, because of the practical difficulty of changing the mass of the PTO system in real-time, it is often assumed the mass is unchangeable, resulting in the spring-damper system as represented in Figure 6.1 for the heaving cylindrical WEC. For practical reasons, a PTO with a variable stiffness is often difficult to implement, therefore a further simplification is warranted where we set the stiffness coefficient K_{PTO} to zero. In the following calculations, the PTO system will be modelled as linear damper, resulting in the following expression for the PTO force:

$$f_{PTO,l}(t) = -B_{PTO,l}\dot{z}(t) \tag{6.3}$$

with $B_{PTO,l}$ the linear PTO damping term. The linear PTO influences the dynamics of the heaving cylindrical WEC: it exerts a force, $f_{PTO,l}(t)$, oppositely

directed to the WEC's velocity, $\dot{z}(t)$. The instantaneous power $P_{inst,l}$ absorbed by the linear PTO system is calculated as:

$$P_{inst,l}(t) = -f_{PTO,l}(t)\dot{z}(t) = B_{PTO,l}\dot{z}^2(t) \tag{6.4}$$

When assuming that the waves are sinusoidal the motion of the WEC can be expressed as the real part of a complex value: $\Re\left\{Z(\omega)e^{-i\omega t}\right\}$, where from this point capital letters will represent the complex form of a certain quantity. The average power P_l absorbed by a heaving cylindrical WEC with a linear PTO system in one wave period is given as

$$P_l = \frac{1}{2}B_{PTO,l}|Z(\omega)|^2\omega^2 \tag{6.5}$$

The expression above is used to find the optimum value for $B_{PTO,l}$ resulting in the maximum average absorbed power P. This leads to

$$B_{PTO,l} = \sqrt{B_{33}^2 + \left(\omega(m + A_{33}) - \frac{K_{33}}{\omega}\right)^2} \tag{6.6}$$

with m the WEC's mass, A_{33} the added mass in heave, B_{33} the heave component of the hydrodynamic damping and K_{33} the hydrostatic stiffness in heave. The same procedure can be repeated for the OSWEC with a linear PTO system: the PTO-torque $\mathcal{T}_{PTO,l}$ is calculated as follows:

$$\mathcal{T}_{PTO,l}(t) = -B_{PTO,l}\dot{\theta}(t) \tag{6.7}$$

with $B_{PTO,l}$ the linear damping coefficient in $[Nm/(rad/s)]$ for the OSWEC and $\dot{\theta}(t)$ the pitch velocity of the OSWEC $[rad/s]$. The optimal value for $B_{PTO,l}$, resulting in the maximum average absorbed power, is given by

$$B_{PTO,l} = \sqrt{B_{55}^2 + \left(\omega(I + A_{55}) - \frac{K_{55}}{\omega}\right)^2}. \tag{6.8}$$

Here, I represents the OSWEC's moment of inertia about its hinge, A_{55} represents the added moment of inertia in pitch, B_{55} the pitch component of the hydrodynamic damping and K_{55} the flap buoyancy torque. The average absorbed power by an OSWEC with a linear PTO system is then expressed as:

$$P_l = \frac{1}{2}B_{PTO,l}|\Theta(\omega)|^2\omega^2 \tag{6.9}$$

with $|\Theta(\omega)|$ the amplitude of the pitch motion.

6.2.1.2 Hydraulic PTO system

Although the linear damper is a convenient way of modelling the effects of the PTO system, it is in some cases an oversimplified representation of the realistic PTO system. Realistic full scale WECs are often equipped with a hydraulic PTO system, which can be modelled numerically using WEC-Sim for both a heaving cylindrical WEC and an OSWEC. A schematic representation of a heaving cylindrical WEC equipped with a hydraulic PTO system is given in Fig. 6.1.

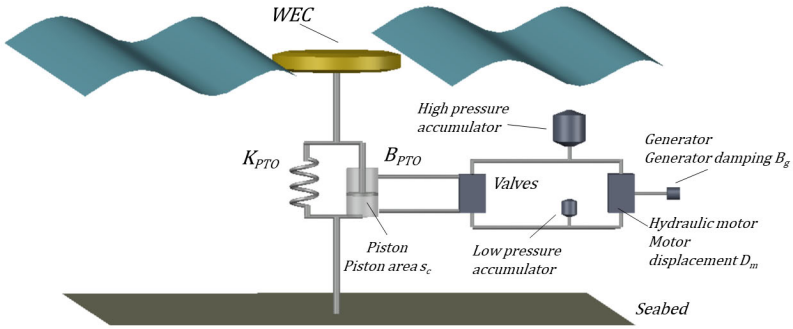

Figure 6.1: Schematic representation hydraulic PTO for heaving cylindrical WEC

In the case of a heaving cylindrical WEC, the hydraulic PTO system converts the heaving motion in a pressurized fluid flow. This fluid flow is translated in rotational energy by the variable displacement motor. The motor's axle is connected to a generator's axle, which generates electricity (So et al., 2015). The provided model calculates the hydraulic PTO force, $f_{PTO,h}$ with:

$$f_{PTO,h}(t) = -sign(\dot{z}(t)) \cdot (p_h(t) - p_\ell(t))s_c \tag{6.10}$$

with p_h and p_ℓ respectively the pressure in the high and low pressure accumulator, whereas s_c represents the piston area. Accumulators smoothen the peak flows into a quasi-constant flow towards the hydraulic motor (Verbrugghe et al., 2015). The PTO-force exerted by the hydraulic PTO system always has the opposite sign as the velocity of the heaving cylindrical WEC. The volume flow Q_{piston}, resulting from the up- or downward piston movement is given by:

$$Q_{piston}(t) = s_c\dot{z}(t) \tag{6.11}$$

Rectifying valves ensure unidirectional flow further in the hydraulic system. This makes fluid flow from the piston into the high pressure accumulator and then

further to the hydraulic motor. Fluid leaving the hydraulic motor flows towards the low pressure accumulator. The incoming volume flow in the high pressure accumulator, Q_{in}, is calculated as:

$$Q_{in} = Q_{piston} - Q_{motor}. \tag{6.12}$$

with Q_{motor} flowing into the hydraulic motor - see Eq. (6.15). The total fluid volume inside the accumulator at time t_j equals $V_{in}(t_j)$ and is calculated with:

$$V_{in}(t_j) = V_{in}(t_{j-1}) + Q_{in}(t_j) \cdot dt. \tag{6.13}$$

It is assumed that initially there is no fluid inside the accumulator, so $V_{in}(0)$ equals 0. The total volume of the accumulator equals V_0, which allows the calculation of the pressure inside the accumulator as follows, according to an isentropic process of the air in the accumulator:

$$p_h(t_j) = \frac{p_{precharge}}{(1 - \frac{V_{in}(t_j)}{V_0})^{\gamma}} \tag{6.14}$$

with $p_{precharge}$ the initial pre-charge pressure in the accumulator and γ the adiabatic index, set equal to 1.4. The compressibility of the fluid is neglected. The calculation of the pressure in the low pressure accumulator, $p_l(t_j)$, is done similarly. The fluid volume flow originating from the motor is determined by:

$$Q_{motor}(t) = \omega_m(t)\alpha D_m \tag{6.15}$$

In this formula, ω_m represents the angular velocity of the hydraulic motor, whereas α represents the swashplate angle which is the instantaneous motor displacement divided by the maximum motor displacement. D_m represents the nominal motor displacement. The product αD_m represents the volume needed for one revolution of the hydraulic motor, expressed in $[m^3/rad]$. In MATLAB Simulink, the angular velocity of the hydraulic motor, ω_m, is calculated by integrating the following expression:

$$\dot{\omega}_m(t) = \frac{(p_h(t) - p_\ell(t))\alpha D_m - \mathcal{T}_g(t) - \mathcal{T}_f(t)}{I_{mg}}, \tag{6.16}$$

where $\mathcal{T}_g$ is the generator torque, $\mathcal{T}_f$ the torque due to friction, and I_{mg} the total mass moment of inertia of the motor/generator. The generator torque changes linearly with the motor's angular velocity, ω_m, with a damping coefficient of the generator, B_g:

$$\mathcal{T}_g(t) = B_g\omega_m(t). \tag{6.17}$$

It is assumed that this damping coefficient B_g is constant. The efficiency of the generator depends on its torque $\mathcal{T}_g$ and its angular velocity ω_m. A table for the generator efficiency is provided by WEC-Sim for different combinations of $\mathcal{T}_g$ and ω_m. The average absorbed power by the hydraulic PTO of a heaving cylindrical WEC over one wave period T is expressed as:

$$P_h = -\frac{1}{T}\int_0^T f_{PTO}(t)\cdot \dot{z}(t)dt \tag{6.18}$$

The equation (6.18) is the absorbed power without taking into account losses in the hydraulic motor and electric generator. The average electrical power will be less than the power at the piston, P_h, since friction in the hydraulic motor and the efficiency of the generator are taken into account in WEC-Sim. In section 6.3.4 and further, only the average absorbed power at the piston P_h will be considered. WEC-Sim also provides the ability to implement a hydraulic PTO system for an OSWEC. The principle of a hydraulic PTO system applied to a pitching flap is sketched in Fig. 6.2. In Fig. 6.2, a positive pitching angle θ corresponds to a clockwise movement of the flap, which implies a shortening of the PTO-bar equipped with the PTO system. This shortening in its turn creates a pressure difference on both sides of the piston. The pitching motion thus induces a linear movement in the piston. Once this linear motion is calculated in Simulink, the force f_{PTO} can be calculated and will be multiplied with the lever arm length ℓ around the hinge in order to find the torque $\mathcal{T}_{PTO}$:

$$\mathcal{T}_{PTO}(t) = f_{PTO}(t)\cdot \ell(t). \tag{6.19}$$

How the force f_{PTO} is calculated is explained in section 6.2.1.2, in Eq. (6.10), since the hydraulic PTO system for the OSWEC mainly contains the same components as the one for the heaving cylindrical WEC. How the pitching motion of the flap is converted in a linear movement of the piston is briefly explained below. This conversion involves some geometric parameters – see Fig. 6.2 :

- $\theta(t)$, the varying pitch angle
- g, the offset height of the PTO-bar connection with the seabed
- c, the distance between the flap-hinge and connection with the PTO-bar
- $b(t)$, the length of the PTO-bar, varying in time. For $\theta = 0$, $b = b_{ini}$.
- $r(t)$, the vertical distance between the connection points of the PTO-bar, varying in time
- $\beta(t)$, the angle between the PTO-bar and the vertical direction, varying in time
- $\ell(t)$, the length of the lever arm (or the distance of the hinge to the PTO-bar), variable in time

In Fig. 6.2 the length r varies in time and is evaluated by $r(t) = c \cdot \cos(\theta(t)) - g$, while angle $\beta(t)$ can be calculated as $\beta(t) = \arccos(r(t)/b(t))$. The length of the lever arm ℓ, i.e. the perpendicular distance from the PTO-bar to the hinge can be determined using:

$$\ell(t) = \sin(\theta(t) + \beta(t)) \cdot c \tag{6.20}$$

The instantaneous absorbed power can be either determined by multiplying $\mathcal{T}_{PTO}$ with the angular velocity $\dot{\theta}$ or by multiplying f_{PTO} with the linear velocity of the piston at each time step, as in Eq. (6.18). Similarly as for the heaving cylindrical WEC, only the total absorbed power P_h at the piston will be considered. The average absorbed power by the hydraulic PTO system of an OSWEC over one wave period is expressed as:

$$P_h = -\frac{1}{T}\int_0^T \mathcal{T}_{PTO}(t) \cdot \dot{\theta}(t) dt \tag{6.21}$$

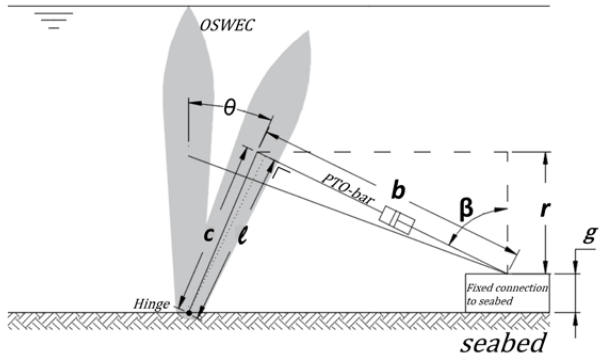

Figure 6.2: Hydraulic PTO system working principle of a generic OSWEC

6.3 Modelled WECs and Input Wave Conditions

In this investigation we present the results for full scale WECs for a series of regular waves of varying heights and periods. The WEC types are outlined in Sec. 6.3.1 and the input wave conditions are shown in Table 6.2 in Section 6.3.2.

6.3.1 Modelled WEC types

The two types of full-scale WECs modelled in this study are a heaving cylindrical buoy and a pitching bottom fixed flap, which is often termed OSWEC (Yu et al.,

Table 6.1: Characteristic dimensions and natural periods per WEC

WEC type	WEC dimension (m)		wave period,T (s)
heaving cylindrical WEC	radius	10	5.46
OSWEC	width	20	17.0

2014b). The heaving cylindrical WEC type is a flat cylinder with radius (r) of 10 m and a draft (h_z) of 2.0 m (see Fig. 6.3). The shape was selected based on its overall dimensions being similar to several promising WEC technologies, namely that of Carnegie Wave (Carengie Clean Energy, 2018) and SINN Power (SINN Power GmbH, 2018). Moreover, as noted in a recent study, (Shadman et al., 2018), such a flat disk shape provides a balance between the power absorption, WEC bandwidth, and material cost considerations. Note that in the case the buoy is not fully submerged as in the case of the Carnegie CETO^{TM}and is instead floating at equilibrium position with a draft of $h_z = 2.0$ m. The natural or resonance period of the WEC in heave , $T_{r,33} \equiv 5.46$ s. The second is a bottom-fixed surface-piercing OSWEC with a width (w) of 20 m, a height (h) of 12 m, a draft (h_z) of 10 m, and a thickness (δx) of 1.0 m (see Fig. 6.3). The OSWEC is similar to several pre-commercial WEC technologies, specifically the WaveRoller, developed by Finnish company AW-Energy. The natural pitch period of the OSWEC, $T_{r,55} \equiv 17$ s.

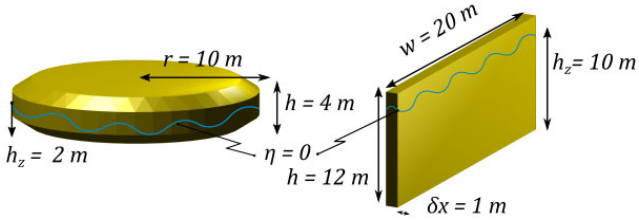

Figure 6.3: Heaving cylindrical WEC (left) and pitching OSWEC (right) schematic. The wavy line indicates the undisturbed free surface elevation η.

6.3.2 Input wave conditions

In order to demonstrate the utility of the presented PTO model coupling, regular waves of two wave heights and four wave periods are simulated as shown in Table 6.2. Note that the chosen wave heights represent a moderate wave climate typical of operating conditions in the North Atlantic (Varing et al., 2017). Therefore such events as overtopping of WECs are not taken into account. Each PTO system configuration presented in Section 6.3.1 and each WEC type in Sec. 6.3.1 is modelled for all wave conditions. In the following sections 6.3.3 and 6.3.4, we determine the optimal PTO system coefficient for each WEC and PTO system type for each wave condition defined in Table 6.2.

Table 6.2: Test matrix of regular wave conditions

wave height, H (m)	natural period,T (s)			
1.0	6.0	8.0	10.0	12.0
2.0	6.0	8.0	10.0	12.0

6.3.3 Optimal PTO system coefficients: linear PTO

In section 6.3.3 it was stated that an optimal value exists for the linear PTO system damping coefficient $B_{PTO,l}$, resulting in the maximum average absorbed power. These damping coefficients are first calculated for the specific case of the heaving cylindrical WEC with Eq. (6.6), for the dimensions described above. The theoretically found values are summarized in Table 6.3. To calculate the corresponding coefficients for the OSWEC, (6.8) is applied for the OSWEC with the prescribed dimensions of Fig. 6.3. Results for the optimal linear PTO damping coefficients are given in Table 6.3.

Table 6.3: Optimal linear B_{PTO} coefficients for a heaving cylindrical WEC ($10^6\times$ kg/s) and OSWEC ($10^6\times$ $(kg \cdot m^2)/s$)

T (s)	6	8	10	12
heaving cylindrical WEC	1.12	2.25	3.46	4.65
OSWEC	128.0	98.40	69.70	51.0

6.3.4 Optimal PTO system coefficients: hydraulic PTO

6.3.4.1 Optimal hydraulic PTO system coefficients for a heaving cylindrical WEC

It was proven that an optimal linear damping coefficient exists when a linear PTO system is applied. Since the PTO-force of a hydraulic PTO system, $f_{PTO,h}$ is no longer linearly dependent on the velocity of the heaving cylindrical WEC, no straightforward relationship for an optimal configuration of the hydraulic PTO system can be expressed. In order to find optimal PTO system parameters, a similar approach as in (Cargo, 2013) is followed: a hydraulic PTO system damping term $B_{PTO,h}$ is defined and it is checked for an optimum value. Note however that this damping coefficient $B_{PTO,h}$ cannot be used to calculate the PTO-force $f_{PTO,h}$ by multiplying $B_{PTO,h}$ with the WEC's velocity. It is a coefficient that takes into account the different parameters of the hydraulic PTO system that influence the performance of the WEC, with the same dimensions as the linear damping term $B_{PTO,l}$ $[kg/s]$:

$$B_{PTO,h} = (\frac{s_c}{D_m})^2 B_g \tag{6.22}$$

$B_{PTO,h}$ can be changed by modifying the piston area, s_c, the motor displacement, D_m or the generator damping, B_g, see Fig. 6.1. In practice it is most convenient

to alter the motor displacement D_m (Cargo, 2013), e.g. by installing a variable displacement motor as hydraulic motor. It is assumed that the swashplate angle α equals unity. Since only D_m will be varied in the following procedure, it is assumed that s_c and B_g are constant: s_c is set as $0.0707m^2$ and B_g as 6 $\frac{Nm}{rad/s}$, respectively, based on a prior analysis. Figure 6.4 proves the existence of an optimal value for $B_{PTO,h}$ for different wave periods in regular waves. Similarly as for the linear PTO system, the optimal value for $B_{PTO,h}$ increases with increasing wave period T. Due to the inherent non-linearities of the hydraulic PTO system, a different optimal value for $B_{PTO,h}$ could be expected for a different wave height H at the same wave period T. However, only a small change was observed in the optimal value for $B_{PTO,h}$ when altering the wave height H from 1.0 m to 2.0 m. The same conclusion was made in (Cargo, 2013). Since the average absorbed power P_h stays rather constant close to the optimal value for $B_{PTO,h}$, the effect of a small change in $B_{PTO,h}$ close to its optimum value on P_h is negligible. Therefore, the $B_{PTO,h}$ coefficients summarized in Table 6.4 will be used for both $H = 1.0m$ and for $H = 2.0m$. The optimal hydraulic PTO system damping coefficients for

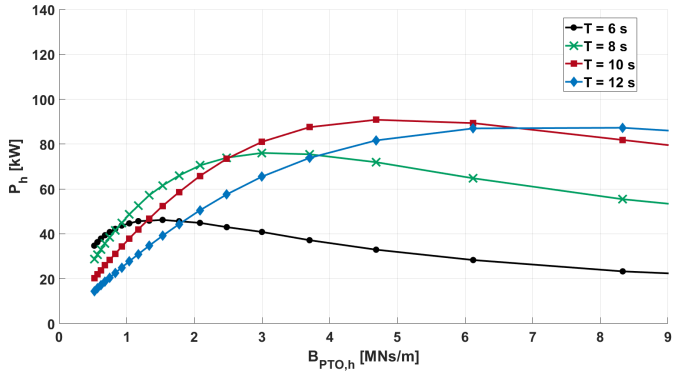

Figure 6.4: Average absorbed power P_h as function of hydraulic damping coefficient $B_{PTO,h}$ for the heaving cylindrical WEC for four different wave periods and for a wave height $H = 1.0m$.

the heaving cylindrical WEC for the studied wave conditions are summarized in Table 6.4.

6.3.4.2 Optimal hydraulic PTO system coefficients for the OSWEC

Section 6.2.1.2 also described the application of a hydraulic PTO system to an OSWEC. Similarly as for the heaving cylindrical WEC, optimal hydraulic parameters will be found for the OSWEC with dimensions as given in section 6.3.1. The piston area was set equal to $s_c = 0.1257m^2$ while the generator damping B_g is set to $10\frac{Nm}{rad/s}$, both values resulting from a prior analysis. Note that additional geometric parameters have to be considered when studying the optimal configuration for an OSWEC with a hydraulic PTO system - see section 6.2.1.2 and Fig. 6.2. The

hydraulic PTO system applied to the OSWEC exerts a torque, $\mathcal{T}_{PTO}(t) = f_{PTO}(t) \cdot \ell(t)$, depending on the PTO-force f_{PTO} and the lever arm ℓ, calculated as in equation 6.20. The latter depends on the following geometric parameters: g, c and b as defined in Fig. 6.2. This implies that, contrary to the case of the heaving cylindrical WEC, not only the characteristics of the hydraulic PTO system, but also the initial geometric parameters g, c and b_{ini} have to be chosen carefully. The reasoning followed in the procedure of optimizing the hydraulic PTO system will briefly be explained below. It is firstly assumed that an optimal PTO-torque exists for each wave period, $\mathcal{T}_{PTO,opt}$. When then e.g. c increases, ℓ will increase as well, keeping all other parameters constant. This will result in a lower $f_{PTO,opt}$ in order to achieve the same $\mathcal{T}_{PTO,opt}$. f_{PTO} can be lowered by increasing D_m. Changing the motor displacement will result in a different pressure difference between the accumulators and a different motor speed.

The geometric configuration of the hydraulic PTO system for the OSWEC can thus be chosen in such a way that allows the most convenient hydraulic motor parameters. It may be expedient to limit the motor speed or the pressure difference to a certain value, which can be realized by adapting the motor displacement accordingly. A brief numerical analysis has shown that higher values for c and thus higher motor optimal displacements D_m result in lower pressure differences. However, this distance c will probably have to be limited as well due to practical considerations. When looking at sketches of the WaveRoller OSWEC, the hydraulic PTO system seems to be very close to the seabed. After a brief analysis, it was chosen to put c equal to 3.0 m, g to 1.5 m and b_{ini} to 5.0 m. D_m was varied in order to find an optimal value that results in the maximum P_h. In order to express an equivalent $B_{PTO,h}$ for the OSWEC (similarly as was done for the heaving cylindrical WEC), following formula is used, resulting in a coefficient with the same dimensions as the linear damping term for the OSWEC:

$$B_{PTO,h} = c \cdot b_{ini} (\frac{s_c}{D_m})^2 B_g. \tag{6.23}$$

Figure 6.5 shows the average absorbed power P_h for different values of $B_{PTO,h}$ for the four considered wave periods described in Section 6.4.2 and a wave height $H = 1.0m$. The optimal value for $B_{PTO,h}$ decreases with increasing wave period, for this range of wave periods. The same conclusion was made for the OSWEC with a linear PTO system: the optimal value for $B_{PTO,l}$ decreases with increasing wave period.

Table 6.4: Optimal hydraulic damping coefficients $B_{PTO,h}$ for a heaving cylindrical WEC ($10^6\times$ kg/s) and OSWEC ($10^6\times\ m^2 \cdot kg/s$).

	T (s)	6	8	10	12
heaving cylindrical WEC	H = 1.0 m	1.5	3.25	4.7	8.3
OSWEC	H = 1.0 m	275	175	121	95

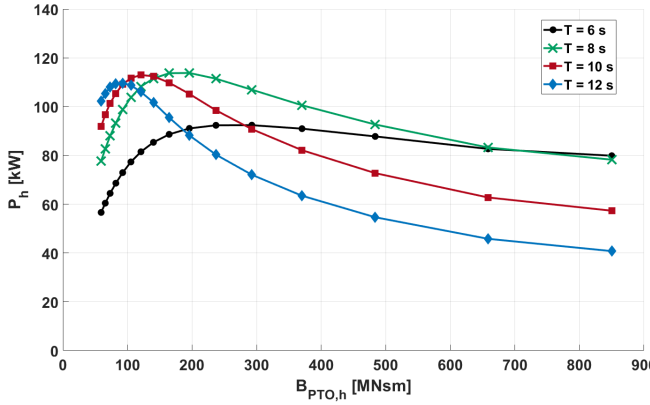

Figure 6.5: Average absorbed power P_h as function of hydraulic damping coefficient $B_{PTO,h}$ for the OSWEC for four different wave periods and for a wave height $H = 1.0m$.

6.4 Comparing the Effects of a Linear to a Hydraulic PTO System for a Single Heaving Cylindrical WEC and a Single OSWEC

6.4.1 Comparing the average power output for each WEC vs type of PTO system

The average power output for a single WEC of each type is calculated via Eq. (6.5) or Eq. (6.9) for the linear PTO system and via Eq. (6.18) or (6.21) for the hydraulic PTO system. Note that for the latter PTO system type the losses in the generator will not be taken into account to provide a fair comparison with the linear results, as noted in Sec. 6.2.1.2.

The B_{PTO} settings used are described in Sections 6.3.3 and 6.3.4. Results for the modelled wave conditions of Table 6.2 for the linear PTO system are shown in Table 6.5 and for the hydraulic equivalent in Table 6.6. We note that the results for H = 2.0 m are almost exactly 4 times the results for H = 1.0 m, indicating that the non-linear influence of the hydraulic PTO system in these operational wave conditions is minimal. Therefore we will focus on the results for a H = 1.0 m wave, which we plot in the bar charts in Figs. 6.6 and 6.7. The percent difference is defined by equation (6.33). We observe that for the heaving cylindrical WEC, the average power output is always greater with the hydraulic PTO system than with the linear PTO system while, in comparison, for the OSWEC the situation is reversed.

$$\frac{P_h - P_l}{P_l} \cdot 100. \tag{6.24}$$

It can be seen that there is a notable increase in the average power output for

Table 6.5: Average power output for a single WEC for a linear PTO system. Heaving cylindrical WEC: top two rows. OSWEC: bottom two rows.

WEC type	wave height H (m)	average power output linear P_l (kW) wave period T (s) 6.0	8.0	10.0	12.0
heaving cylindrical WEC	1.0	47.98	65.94	72.86	72.04
	2.0	191.91	263.78	291.46	288.14
OSWEC	1.0	106.5	132.8	131.6	126.8
	2.0	425.9	531.0	526.5	508.8

Table 6.6: Average power output for a single WEC for a hydraulic PTO system. Heaving cylindrical WEC: top two rows. OSWEC: bottom two rows.

WEC type	wave height H (m)	average power output hydraulic P_h (kW) wave period T (s) 6.0	8.0	10.0	12.0
heaving cylindrical WEC	1.0	50.15	77.40	90.05	85.34
	2.0	200.61	311.36	364.6	344.15
OSWEC	1.0	92.56	114.3	113.1	109.4
	2.0	368.0	452.6	448.0	434.4

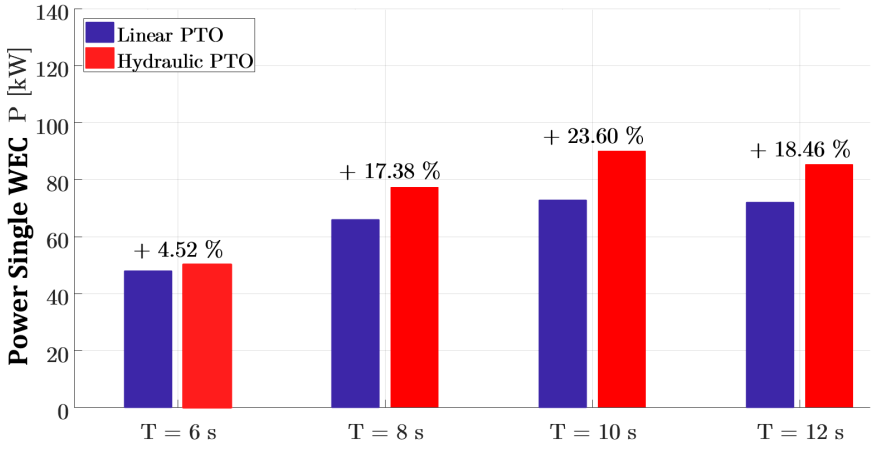

Figure 6.6: Bar chart showing the power output for one heaving cylindrical WEC with linear PTO system (P_l) (purple) and hydraulic PTO system (P_h)(red) with the percentage difference between the two.

the hydraulic PTO system (P_h) versus the linear (P_l) for the case of the heaving cylindrical WEC for periods $T \geq 8.0s$. For these wave conditions, the hydraulic

PTO system is able to damp the motion of the WEC to more effectively match the phase of the incident wave condition. Such is not the case with the OSWEC, where the natural pitching period of the WEC is higher than the investigated wave periods and the hydraulic PTO system is not performing optimally, *i.e.* it cannot 'speed up' the relative motion. We must note, however, that the linear PTO system for the OSWEC, although it shows on average a 15% improvement in the power performance of the WEC, may be making unrealistic assumptions about the motion of the OSWEC that may result in an artificially increased average power output. Observe that in all cases the average power output for the OSWEC is much higher than for the heaving cylindrical WEC, indicating that the OSWEC is more efficient in absorbing the power of the incoming waves; how this power absorption affects the wave field will be explored in the next section 6.4.2.

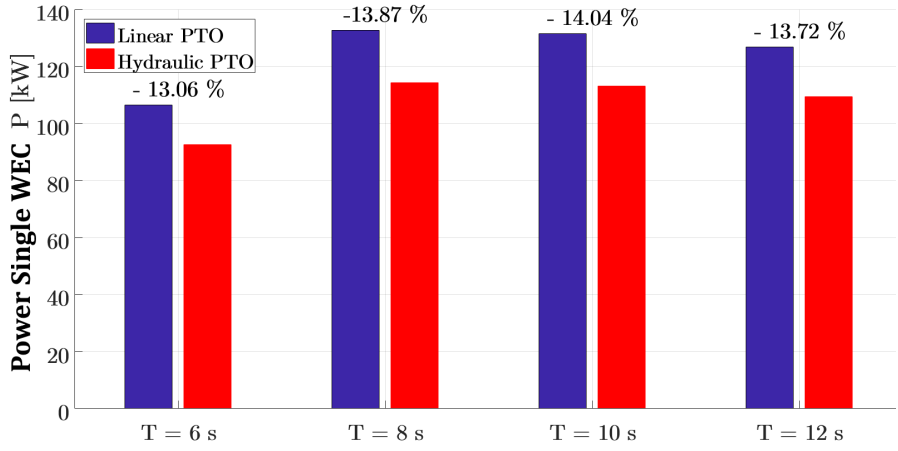

Figure 6.7: Bar chart showing the power output for one OSWEC with linear PTO system (P_l) (purple) and hydraulic PTO system (P_h)(red) with the percentage difference between the two.

6.4.2 Analysing the wave field around one WEC

6.4.2.1 Calculating the total and perturbed wave fields

To calculate the wave field around a single WEC for a wave height H, we sum the complex incident unidirectional regular wave field, calculated at each point via Eq. (6.25)

$$\zeta(x, y) = \frac{H}{2} e^{-i(kx)} \tag{6.25}$$

to the perturbed wave field consisting of the radiated and diffracted wave fields.

Both are calculated from their respective potentials via the kinematic free surface boundary condition Eq. (3.9). The radiated wave field is given by Eq. (6.26)

$$\eta_R = -\frac{ZH}{\zeta}\frac{i\omega\phi_r}{2g}. \tag{6.26}$$

Here ϕ_r is the radiated velocity potential and the ratio of the body displacement Z to the wave amplitude ζ is the response amplitude operator (RAO) which is calculated in Eq. (6.27):

$$\frac{Z}{\zeta} = \frac{F_e}{-\omega^2(M+A)^2 - i\omega(B_{PTO}+B)+C} \tag{6.27}$$

The modulus of the complex RAO calculated in Eq. (6.27) is the amplitude of the WEC's position divided by the wave amplitude:

$$|RAO| = |\frac{Z}{\zeta}| \tag{6.28}$$

Eq. (6.27) is only valid when modelling a WEC with a linear PTO system. In Eq. (6.27) F_e is the excitation force, M the mass of the device, and A, B and C , the added mass, hydrodynamic damping, and hydrodynamic spring or stiffness coefficients, respectively, determined in NEMOH for each of the relevant degrees of freedom. The B_{PTO} is the linear $B_{PTO,l}$ coefficient in table 6.3 for each wave period and WEC type. It is important to mention that the use of the hydraulic PTO coefficient $B_{PTO,h}$, as described in 6.3.4.1 and 6.3.4.2, in Eq. (6.27) will lead to incorrect results. The coefficient $B_{PTO,h}$ was composed in order to combine all significant factors influencing the average absorbed power P_h, to check if an optimum value of the average absorbed power exists and to study the trend of this coefficient over a range of periods. Since the RAO for a WEC with a hydraulic PTO system cannot be calculated analytically, this RAO is determined using numerical time-domain simulations. For a given wave period and wave height, the WEC's displacement is calculated numerically using WEC-Sim. The modulus of the RAO is calculated with Eq. (6.28), whereas the RAO's phase is determined as in Eq. (6.29):

$$\varphi = \omega \cdot \Delta t, \tag{6.29}$$

where Δt represents the time shift between the WEC's displacement profile and the surface elevation profile. As the WEC's position $z(t)$ is not sinusoidal when equipped with a hydraulic PTO system, the following method is used for the calculation of the time shift Δt:

$$\Delta t = argmax_\tau \int_0^T z(t) \cdot \zeta(t-\tau)dt. \tag{6.30}$$

The RAO phase φ will be positive since the WEC's motion is delayed with respect to the incoming wave ($\Delta t \leq 0$). The complex value of the RAO is now determined as:

$$\frac{Z}{\zeta} = |\frac{Z}{\zeta}|e^{i\varphi}. \tag{6.31}$$

The diffracted wave amplitude η_d is given by Eq. (6.32)

$$\eta_D = -\frac{i\omega\phi_D\zeta}{g}, \tag{6.32}$$

where ϕ_D is the diffracted velocity potential. We calculate the wave field around a single WEC for each of the incident wave conditions presented in table 6.2. In the two sections following, Sections 6.4.2.2 and 6.4.2.3, we show representative results from the 24 cases simulated. The contour plots are shown in terms of the K_d, Eq. (4.15), as detailed in Section 4.5.1. Note that the tally takes into account the fact that for the linear PTO system the result for H = 1.0 m and H = 2.0 m are the same.

6.4.2.2 The influence of the WEC type on the wave field

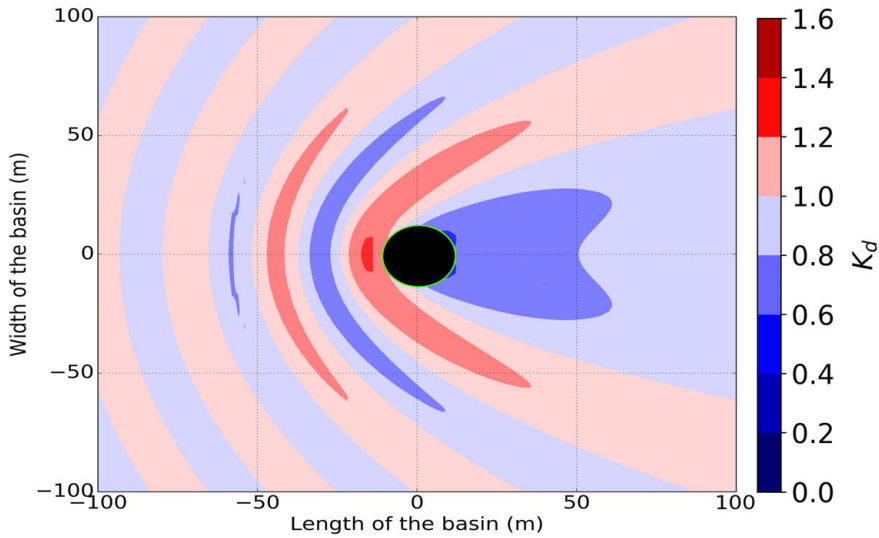

Figure 6.8: Modulus of the total surface elevation K_d for a heaving cylindrical WEC (left). Incident wave of H = 1.0 m T = 6.0 s propagating from the left.

Before diving into the complicated patterns seen in the 'near-field' wave field of the array, we model a single WEC in the numerical domain to clarify the impact of WEC type and PTO system type on the wave field. The two WEC types presented in Sec. 6.3.1 have a substantially different impact on the incoming waves as witnessed in the plots of the modulus of total wave field K_d, in Fig. 6.8 for one heaving cylindrical WEC (left) and an OSWEC (right) for a linear PTO system for the same incident wave of H = 1.0 m and T = 6.0 s.

One observes right away that the perturbation effect for the OSWEC is much greater than that of the heaving cylindrical WEC, both in magnitude and extent away from the WEC. This difference is largely a consequence of the diffraction potential of the OSWEC since it presents a barrier to the entire water column compared to the small-draft heaving WEC which presents much less resistance to the incoming waves. As an example, we can observe this difference in Fig. 6.10 for a H = 1.0 m T = 10.0 s for a heaving cylindrical WEC and for an OSWEC, respectively.

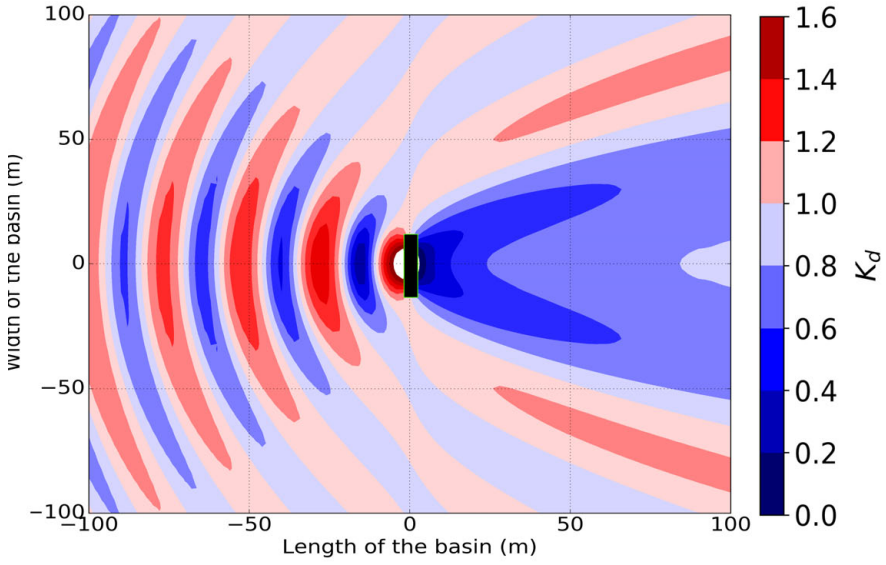

Figure 6.9: Modulus of the total surface elevation K_d for an OSWEC. Incident wave of H = 1.0 m T = 6.0 s propagating from the left.

Moreover, the difference in the radiated wave field is significant as well, especially as we move to higher wave periods, where the OSWEC responds more to the incoming wave whereas the heaving cylindrical WEC is essentially riding on top of the water column. This is significant in the study because it is indeed the radiation which we can influence throughout the PTO model as will be witnessed in the next subsection.

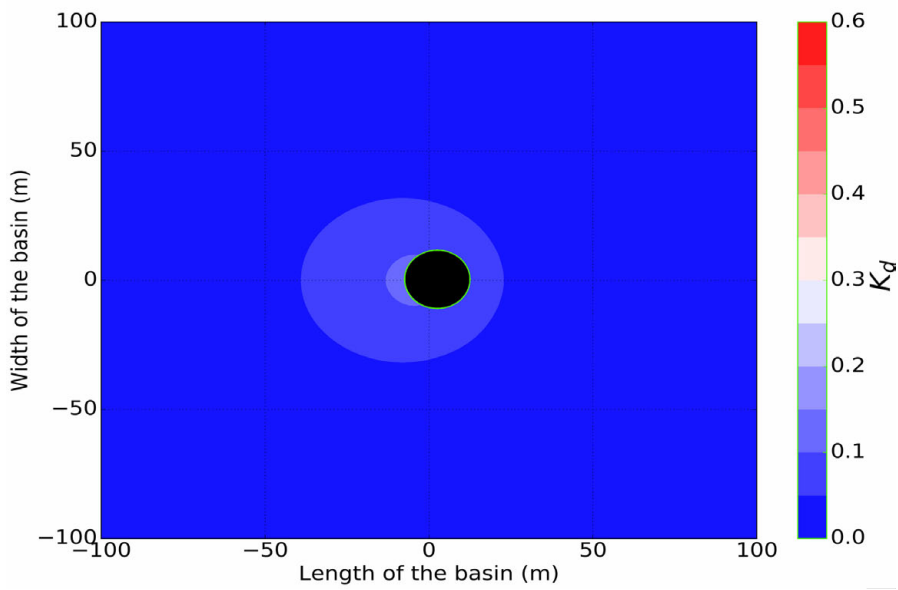

Figure 6.10: Modulus of the diffracted surface elevation K_d for a heaving cylindrical WEC. Incident wave of H = 1.0 m T = 10.0 s propagating from the left.

6.4.2.3 The influence of the PTO system type on the wave field for a single WEC

As mentioned in the previous paragraph in Sec. 6.4.2.2, the discrepancy between the radiation of the two WECs is less than the difference in diffraction for a given wave. However, it is still significant, and as the radiated wave field is a function of the PTO system as well as the WEC type, we do see a divergence in the perturbed wave field between the different PTO system types. This is noted in a plot of the percent difference between the total K_d for the linear and the hydraulic PTO system first for the heaving cylindrical WEC in Fig. 6.12 and the OSWEC in Fig. 6.13 for a H = 1.0 m, T = 8.0 s wave. The percent difference in the K_d for the two PTO types is defined as:

$$\frac{K_{d,h} - K_{d,l}}{K_{d,l}} \cdot 100. \tag{6.33}$$

We observe that the variability between the two PTO system types is less than 5 % for the heaving cylindrical WEC whilst that for the OSWEC is closer to 10 % in the region near the device. This is not demonstrated in the results in the power output (P_{farm}) however, where in Tables 6.5 and 6.6 in Section 6.4.1 for the H = 1.0 m, T = 8.0 s wave, the difference between P_l and P_h is 17 % and only 14 % for the OSWEC. Moreover, $P_h - P_l$ is positive for the heaving cylindrical WEC while the addition of a hydraulic PTO system actually reduces the power output for an OSWEC. This situation is mirrored for the other wave periods where the

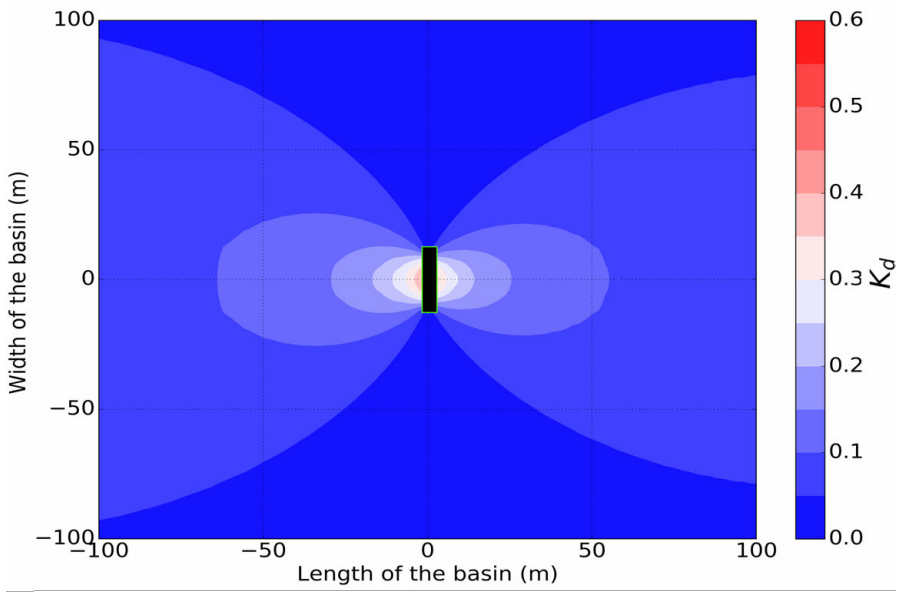

Figure 6.11: Modulus of the diffracted surface elevation K_d for an OSWEC. Incident wave of H = 1.0 m T = 10.0 s propagating from the left.

increase in the perturbed wave field for the OSWEC compared to that of the the heaving cylindrical WEC does not induce an increase in the power output of the OSWEC P_h.

6.5 The Power Output and the Near-field for an Array of 5 WECs with a Hydraulic PTO

6.5.1 WEC Array Layout

As seen in the results for a single WEC in Section 6.4, the perturbed wave field around a single WEC strongly depends on both the WEC type and the PTO system modelled. In this section we extend the results to an array of 5 WECs with a view toward the modelling of a commercial scale WEC farm consisting of multiple WEC arrays. To this end we model two different 5-WEC arrays: one consisting of heaving cylindrical WECs (Fig. 6.14) and the other of pitching OSWECs (Fig. 6.15). The intra-array separation distances d_x and d_y are set to 40 m, which is the $2\times$ the diameter of the heaving cylindrical WEC and the width of the OSWEC. The array configurations of both WEC types are staggered, an arrangement that was clearly shown to be power-maximizing in a number of numerical and experimental studies such as in (Beels et al., 2010; Child and Venugopal, 2010; Child et al., 2011; Stratigaki, 2014; Ruiz et al., 2017a; Balitsky et al., 2017b, 2018b). In this

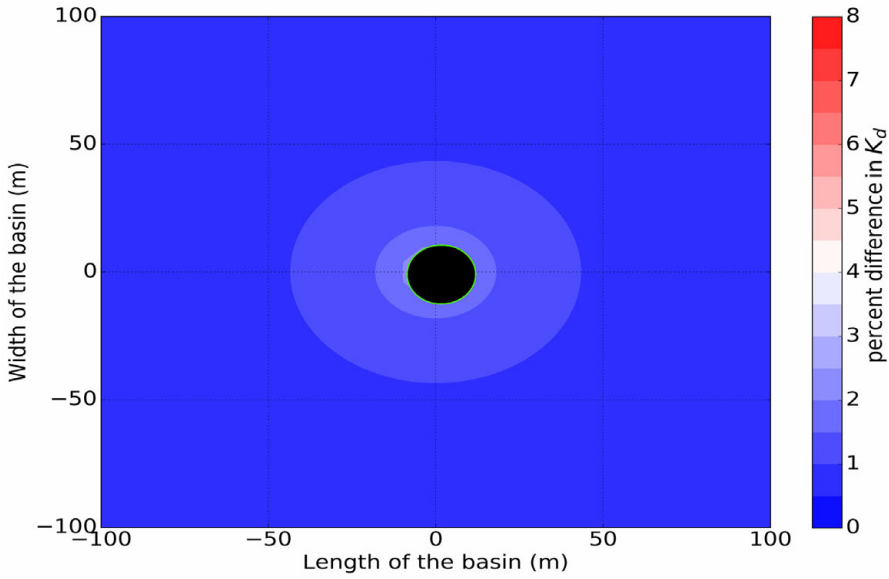

Figure 6.12: Percent difference (eq (6.33)) in the total wave field between the hydraulic and linear PTO system for a heaving cylindrical WEC. Incident wave of H = 1.0 m, T = 8.0 s propagating from the left

investigation the water depth is set at 30 m for the heaving buoy and 10.0 m for the OSWEC.

6.5.2 Iterative approximation for the WEC array near-field

To assess the effects of multiple WECs in a WEC array or multiple WEC arrays in a WEC farm on the power output ($\mathbf{P}$) of the farm, we need to calculate perturbed wave field in the *near-field* domain. As we assume linear theory in the work, we can use the superposition principle to sum up the total wave field by utilising an iterative approach first developed in (Balitsky et al., 2017a). In the case of a single array presented in this chapter we substitute individual WECs for a WEC array in the calculation of the sum of the wave fields. Therefore, the approach described in Fig. 5.3 is valid, with the substitution of a single OSWEC for a WEC array. The initial step (Step 1) is to propagate the incident wave in the empty numerical basin (no WEC present) to obtain the undisturbed surface elevation. In Step 2 the incident surface elevation is used as input into NEMOH whence the 1st iteration perturbed wave of WEC I, p_{1i}, is evaluated. In Step 3, the average wave amplitude at the location of p_{1i} is used as input into NEMOH to calculate the 1st iteration perturbed wave of WEC II, p_{1ii}.

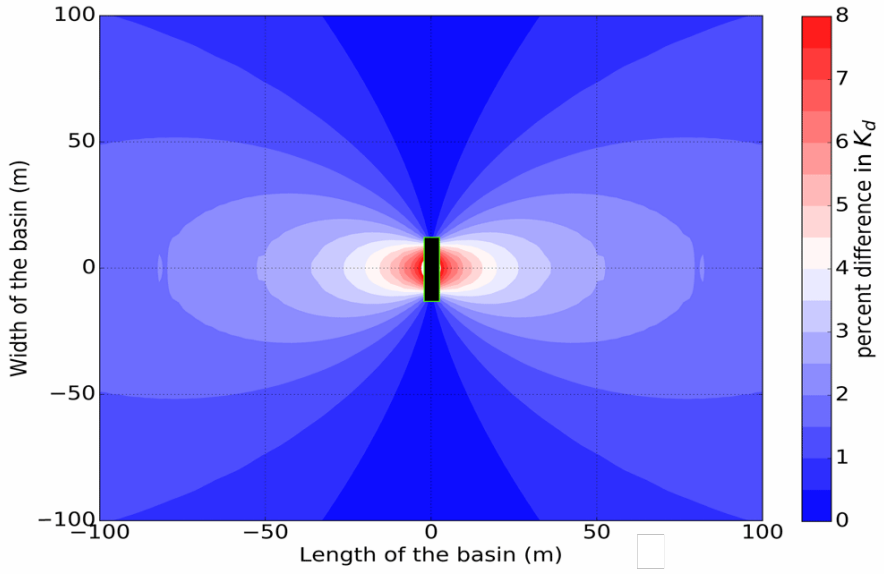

Figure 6.13: Percent difference (eq (6.33)) in the total wave field between the hydraulic and linear PTO system for an OSWEC. Incident wave of H = 1.0 m, T = 8.0 s propagating from the left

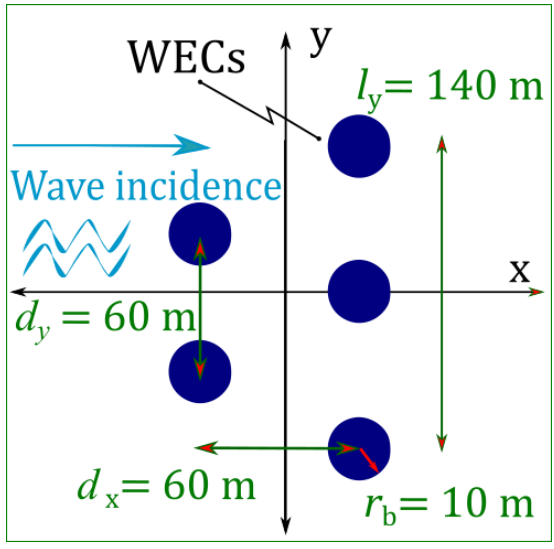

Figure 6.14: Plan view of the array layout for five heaving cylindrical WECs. The incident wave propagates from the left.

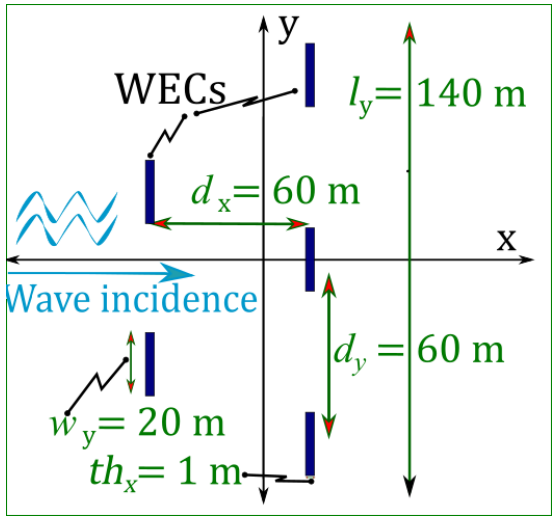

Figure 6.15: Plan view of the array layout for five pitching OSWECS. The incident wave propagates from the left.

6.5.3 Power output calculation for an array of 5 WECs

In evaluating the influence of the 5-WEC array interaction effects on the performance of a wave farm, we compute the total power output by the two WEC arrays, after having obtained the modified wave field in the WEC array using the approach outlined in Section 6.5.2. The power of each array is calculated by the following equations depending on the PTO system and WEC type. For the linear PTO system, we extend equations (6.5) and (6.9) to $\mathcal{M}$ WECs operating in one DoF to Eq. (6.34),

$$\mathbf{P}_l = -\frac{1}{2}\mathbf{B}_{PTO,l}|\mathbf{Z}(\omega)|^2\omega^2, \tag{6.34a}$$

$$\mathbf{P}_l = -\frac{1}{2}\mathbf{B}_{PTO,l}|\boldsymbol{\theta}(\omega)|^2\omega^2, \tag{6.34b}$$

where $\mathbf{Z}$ and $\boldsymbol{\theta}$ indicate an $\mathcal{M} \times 1$ column vector of the WEC's position or angular displacement respectively. $\mathbf{B}_{PTO,l}$ represents an $\mathcal{M} \times \mathcal{M}$ diagonal matrix with the B_{PTO} coefficients for each WEC on the diagonal. For the hydraulic PTO system, the equations equivalent to (6.18) and (6.21) are given in Eq. (6.35):

$$\mathbf{P}_h = -\frac{1}{T}\int_0^T \mathbf{F}_{PTO}(t) \cdot \dot{\mathbf{z}}(t)dt, \tag{6.35a}$$

$$\mathbf{P}_h = -\frac{1}{T}\int_0^T \mathcal{T}_{PTO}(t) \cdot \dot{\boldsymbol{\theta}}(t)dt. \tag{6.35b}$$

Here as in Eq. (6.34), the boldface quantities represent $\mathcal{M} \times 1$ column vectors of the forces and velocities of the individual heaving cylindrical WECs of the torques and angular displacements of the individual OSWECs. As mentioned in Sec. 6.5.2, for each WEC in the array, the motions and the forces used in Eqns. (6.34) and (6.35) are calculated with the input wave equal to the incident wave plus the 1st order WEC array perturbed wave at the location of the given WEC. The magnitude of the η used for calculating the power $\mathbf{P}$ in Eqns. (6.34) and (6.35) is taken as the average of the 1st order modified η on a region immediately surrounding the WEC. In addition to calculating the power of each array, we also give the $q-value$, defined in Eq. (3.78) in Eqs. (6.5), (6.9), (6.18) and (6.21) for the heaving cylindrical WEC or the OSWEC, respectively. Furthermore, the CWR of the array as defined by Eq. (3.79) is given in Tables 6.7 and 6.8. Note the characteristic width W for both WEC array types is 140 m.

6.5.4 Power output for an array of 5 WECs

Table 6.7: Average power output for an array of 5 WECs for a linear PTO system. Heaving cylindrical WECs: top three rows. OSWECs: bottom three rows.

WEC type	value	wave height H (m)	average power output linear $P_l(kW)$ wave period T (s)			
			6	8	10	12
Heaving cylindrical WEC	ARRAY	H = 1.0	234.5	325.5	315.3	304.4
	SINGLE × 5	H = 1.0	239.9	329.7	364.3	360.2
	q	H = 1.0	0.98	0.99	0.87	0.85
	CWR	H = 1.0	0.28	0.29	0.23	0.18
OSWEC	ARRAY	H = 1.0	1002	1737	1283	854.3
	SINGLE × 5	H = 1.0	532.3	663.6	657.8	634.2
	q	H = 1.0	1.88	2.62	1.95	1.35
	CWR	H = 1.0	1.19	1.55	0.92	0.51

The 5-WEC array power output for the linear PTO for the two WEC types is displayed in table 6.7 for the modelled wave periods from table 6.2 for H = 1.0 m and in the bar chart Fig. 6.16. The corresponding results for the hydraulic PTO are displayed in 6.8 and Fig. 6.17. The *q* value for the various configurations, defined in Eq. (3.78), is displayed in the third and sixth data row. As we have witnessed in Section 6.4.1, the deviation from linear behaviour due to the increase from H = 1.0 m to H = 2.0 m is very small, therefore the focus of attention will be on the results for H = 1 m with knowledge that the results for H = 2.0 m show similar patterns and behaviours.

As in the single WEC case, one observes a significant increase in the power output of the 5-OSWEC array versus a 5-heaving cylindrical WEC array with the power of the former producing up to 3 × more power for a wave period of 8.0 s. Note that as in the single WEC case analysed in Section 6.4.1, the heaving cylindrical WEC array produces more power with increasing wave period while in

the case of the OSWEC array, the peak power occurs for T = 8.0 s, with a decrease for higher wave periods. This reduction is more significant in the array case than in the single wave case, a fact *i.e.* reflected in the decreasing q values as the period increases. This behaviour can be directly linked to the increase in the K_d in the 'near-field' zone, as we will observe in Section 6.5.5.2. For the heaving cylindrical WEC, the q values are also decreasing for wave periods greater than 8.0 s, but with the difference that each q value is consistently below unity. It is clear from the data that in the case of the modelled 5-WEC array configuration, placing the OSWECs in an array is much more advantageous to their performance than for the heaving cylindrical WECs. We must remark however, that in realistic wave conditions with frequency and directional spreading it is near impossible to achieve the phase relationships that lead to high q values and consequently, we expect the relative difference in the array power output between the two types of WECs to diminish. The same remarks can be made about the CWR in Table 6.7. Observe that the CWR values are significantly lower for the array of heaving cylindrical WECs than for the OSWECs. This corroborates the results found in Babarit (2015) for the single WECs of the same type. Observe, however, that the values for the OSWEC are greater than unity for the lower two periods. Although this might appear on the high side, one must note that the CWR metric presented in this chapter is of a staggered array and is expected to be greater than that for a line of devices with the same characteristic width. Moreover, as mentioned in Section 6.2, the linear PTO model tends to exaggerate the motion of the WECs, especially in regular waves and where losses are not taken into account. Given the slightly lower CWR

Table 6.8: Average power output for an array of 5 WECs for a hydraulic PTO system. Heaving cylindrical WECs: top three rows. OSWECs: bottom three rows.

WEC type	value	wave height H (m)	average power output hydraulic P_h (kW) wave period T (s)			
			6	8	10	12
Heaving cylindrical WEC	ARRAY	H = 1.0	245.7	387.3	389.3	358.3
	SINGLE × 5	H = 1.0	250.77	386.99	450.26	426.69
	q	H = 1.0	0.98	1.00	0.86	0.84
	CWR	H = 1.0	0.29	0.35	0.28	0.21
OSWEC	ARRAY	H = 1.0	867	1618	1238	868.8
	SINGLE × 5	H = 1.0	462.8	571.7	565.4	547.2
	q	H = 1.0	1.87	2.83	2.19	1.59
	CWR	H = 1.0	1.03	1.44	0.88	0.51

for the hydraulic PTO 5-OSWEC array, one can surmise that the hydraulic PTO presents a more 'realistic' modelling case where the power capture is reduced as a consequence of reduced OSWEC motion. At the same time, the case of the 5-HPA array is the reverse, indicating that a linear PTO approximation does not lead to exaggerated WEC motion in the studies cases.

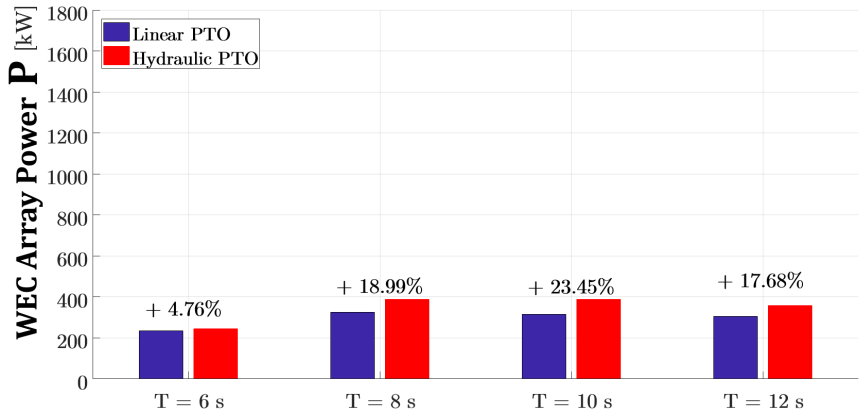

Figure 6.16: Bar chart showing the power output for a 5-heaving cylindrical WEC array with linear PTO system (purple) and hydraulic PTO system (red) with the percentage difference between the two calculated by Eq. (6.33).

6.5.5 The near-field K_d for an array of 5 WECs

In this section we present the results for the *near-field* wave field for an array of 5 heaving cylindrical WECs, arranged in the configurations displayed in Figs. 6.14 and 6.15 for the wave periods listed in table 6.2 for a wave height H of 1.0 m. The results are presented in Section 6.5.5.1 and Section 6.5.5.2 as the modulus of the surface elevation K_d. Using this metric we show both the total wave field to see the connection between the surface elevation and the array power output, and the perturbed wave field which only displays the array effects, *i.e.* deviations from the incident wave field brought about by the interactions with the WEC arrays. Because of the quantitative differences in the wave fields for a heaving cylindrical WEC and an OSWEC, the presentation of the results is split into two subsections 6.5.5.1 and 6.5.5.2, where in each subsection we take an in-depth look at the 'near-field' wave amplitude η in terms of the K_d.

6.5.5.1 The perturbed K_d for an array of heaving cylindrical WECs

First thing, we take a look at the wave field of an array of 5 heaving cylindrical WECs for a linear PTO system for T = 6.0 s and T = 8.0 s. In Figs. 6.18 and 6.20 the total K_d and in Figs. 6.19 and 6.21 the perturbed K_d fields are plotted for the named wave periods. Notice that the magnitude of the changes in the total K_d due to the presence of the array are much greater for the case of T = 6.0 s. This can be seen even more clearly in a comparison of the perturbed K_d for the same two wave periods between Fig. 6.19 and Fig. 6.21, where the perturbed wave field is nearly 2 $\times$ greater in magnitude near the WECs. However, it would be

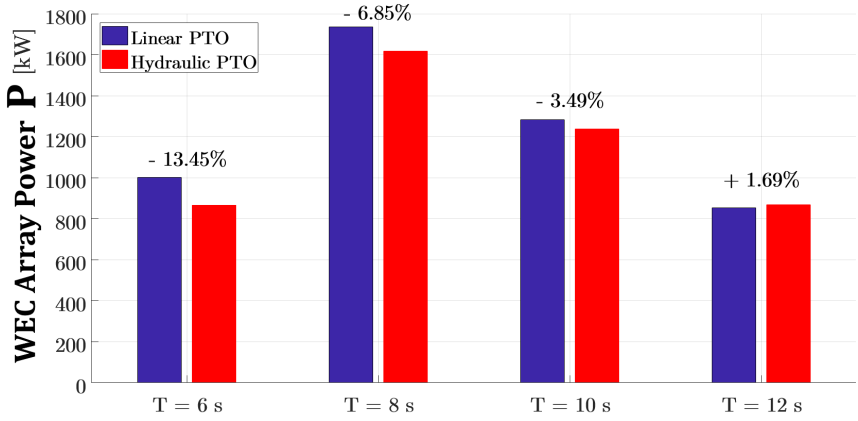

Figure 6.17: Bar chart showing the power output for a 5-OSWEC array with linear PTO system (purple) and hydraulic PTO system (red) with the percentage difference between the two calculated by Eq. (6.33).

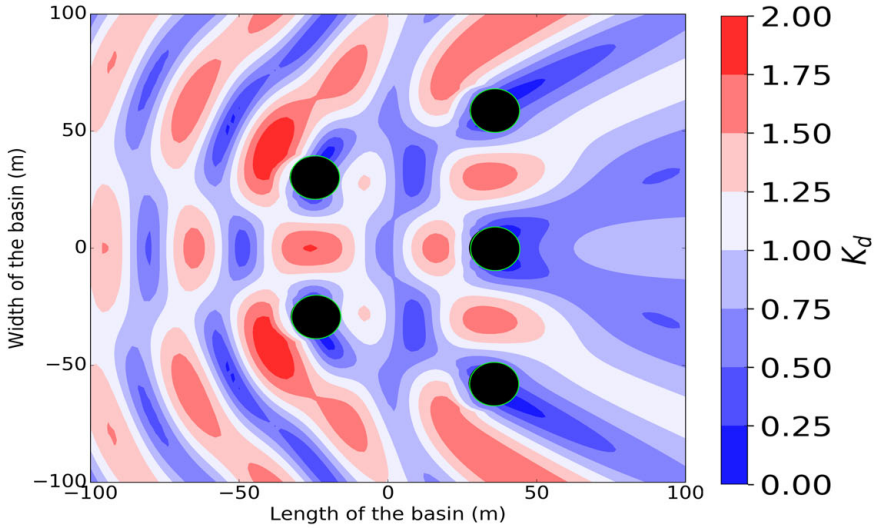

Figure 6.18: The total K_d for a heaving cylindrical WEC for a wave of H = 1.0 m, T = 6.0 s for a linear PTO system. Incident wave propagating from the left.

incorrect to assume that this difference is linearly proportional to the difference in the power output $\mathbf{P}$ of the array at these wave periods, as will be elaborated on in

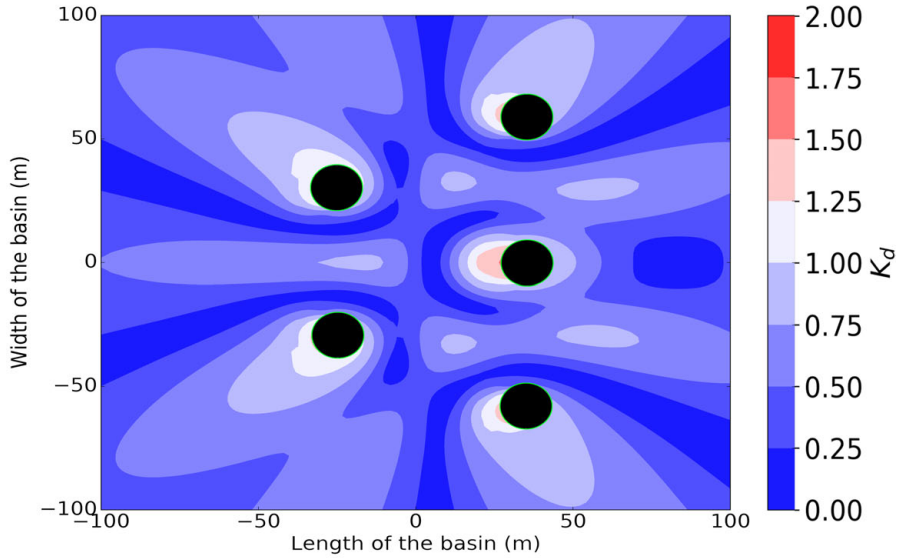

Figure 6.19: The perturbed K_d for a heaving cylindrical WEC for a wave of H = 1.0 m, T = 6.0 s for a linear PTO system. Incident wave propagating from the left.

Section 6.6.

Moving on to the two higher wave periods, T = 10.0 s and T = 12.0 s, the interaction of the incident wave field with the WEC array markedly decreases. We can observe this in a contour plot of the total and the perturbed wave field for T = 10.0 s for the heaving cylindrical WEC array with a linear PTO system in Figs. 6.22 and 6.23. We note that although the perturbed wave field is barely perceptible, it does result in a slight enhancement of the total wave field which creates an area of higher total K_d in front of the array. For T = 12.0 s the shape of the interaction zones is similar to those of T= 10.0 s but the magnitude of the array effects are minimal and consequently, these wave fields are not displayed in the interest of brevity.

6.5.5.2 Results for an Array of OSWECs

We next move on to explore the results of the simulations for the 5-OSWEC Array. Analogous to Sec. 6.5.5.1 we first look at the total near-field K_d for T = 6.0 s and T = 8.0 s, which are the wave periods with the greatest 'array effect' and the highest power output $\mathbf{P}$. In Figs. 6.24 and 6.26, we plot the total K_d and in Figs. 6.26 and 6.27, the perturbed K_d for the two wave periods in question. Observe that the magnitude of both fields is much greater than that of the heaving cylindrical WEC shown in Figs. 6.18 to 6.20 for both T = 6.0 s and T= 8.0 s. Moreover, we observe a large difference in the locations of 'hot spots' and 'cold

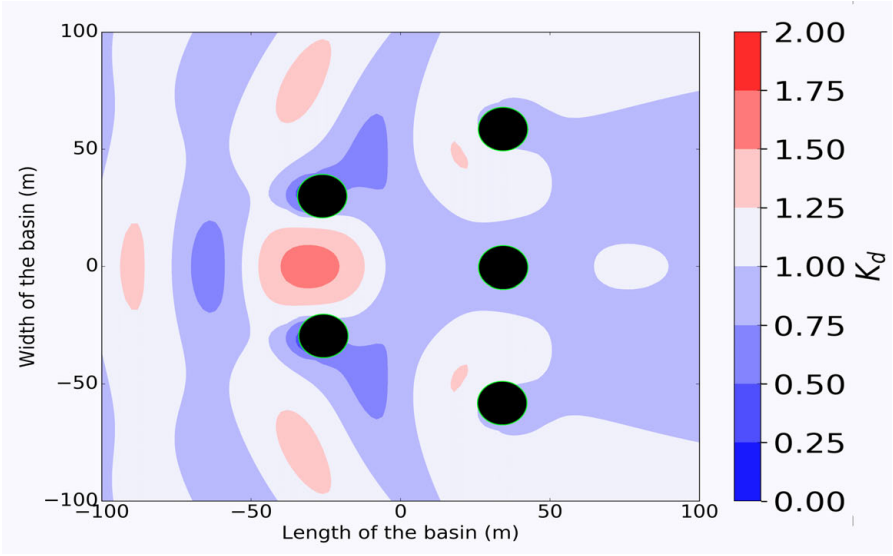

Figure 6.20: The total K_d for a heaving cylindrical WEC for a wave of H = 1.0 m, T = 8.0 s for a linear PTO system. Incident wave propagating from the left.

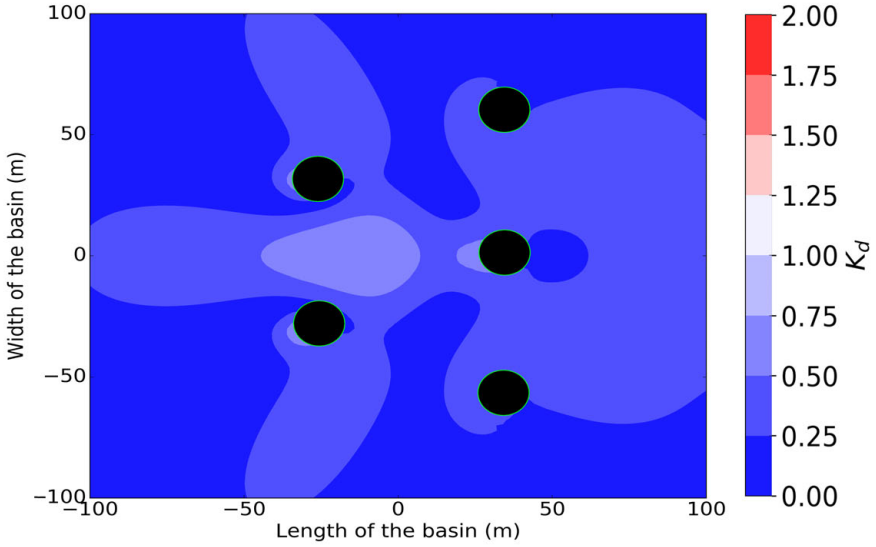

Figure 6.21: The perturbed K_d for a heaving cylindrical WEC for a wave of H = 1.0 m, T = 8.0 s for a linear PTO system. Incident wave propagating from the left.

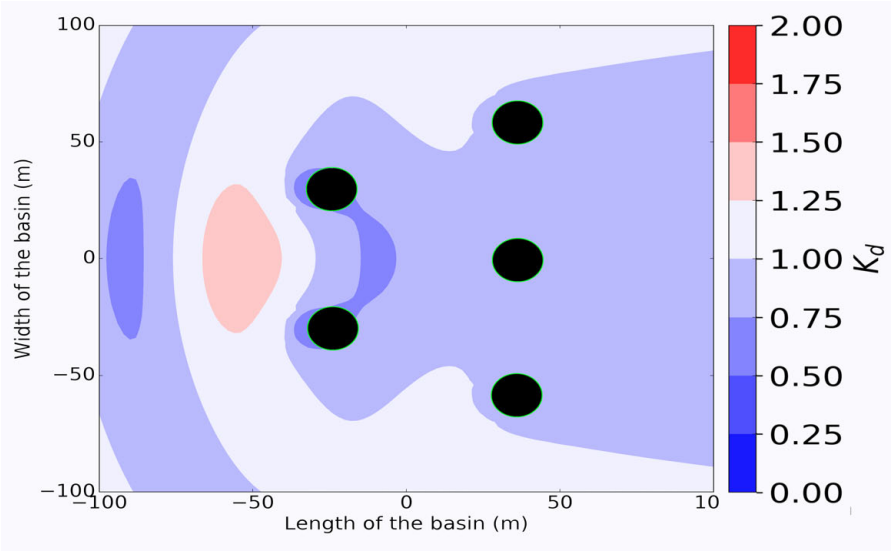

Figure 6.22: The total K_d for a heaving cylindrical WEC for a wave of H = 1.0 m, T = 10.0 s for a linear PTO system. Incident wave propagating from the left.

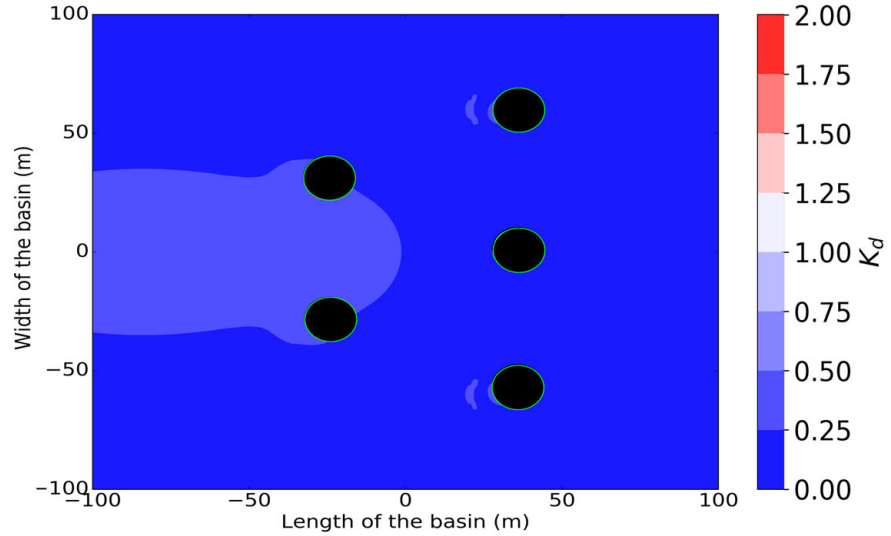

Figure 6.23: The perturbed K_d for a heaving cylindrical WEC for a wave of H = 1.0 m, T = 10.0 s for a linear PTO system. Incident wave propagating from the left.

spots', which are areas of strong positive or negative anomalies in K_d between T

= 6.0 s and T = 8.0 s. In other words the areas with destructive interference between the incident and the perturbed wave leads to a decrease in K_d or vice versa with constructive interference between the incident and perturbed waves. This is important in understanding the interaction between the wave period and the power output $\mathbf{P}$ that we will discuss in Section 6.6.

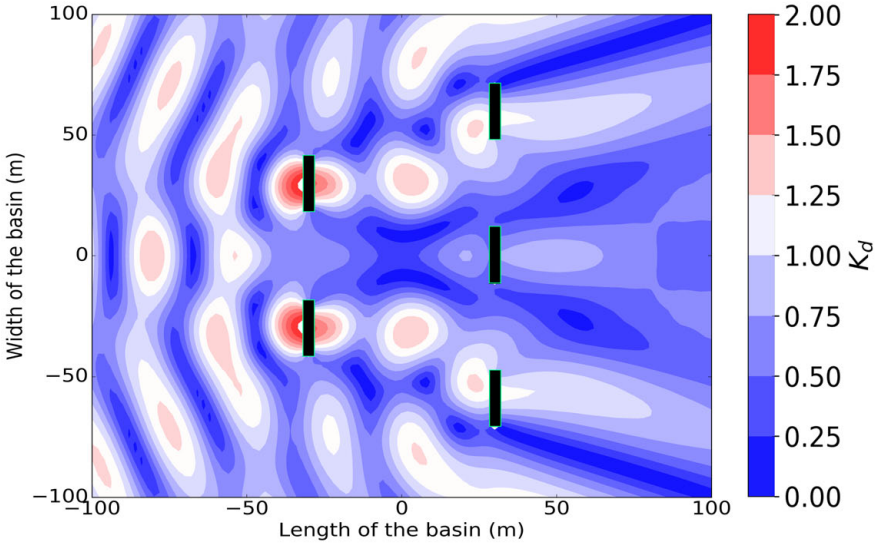

Figure 6.24: The total K_d for an array of OSWECs for a wave of H = 1.0 m, T = 6.0 s for a linear PTO system. Incident wave propagating from the left.

As with the heaving cylindrical WEC, the two largest wave periods T = 10.0 s and T = 12.0 s display smaller perturbations in the near-field zone. Unlike for the heaving cylindrical WEC, however, they are still significant, as we can witness in Figs. 6.28 and 6.30 for the total K_d and in Fig. 6.31 for the perturbed K_d for an OSWEC with a linear PTO system. This perturbation effect is mirrored in the positive q values in Tables 6.7 and 6.8 for both T = 10 s and T = 12 s, unlike in the case of the heaving cylindrical WECs. Again, notice the strong change in the locations of the positive and negative anomalies in the total wave field between Fig. 6.28 and Fig. 6.30. As will be seen in Section 6.5.5.3, these are the two wave periods where the hydraulic PTO system power performance in a OSWEC array is close to or slightly exceeding the linear PTO system WEC array case, unlike the single WEC case in Section 6.4.1 where the reverse is true.

6.5.5.3 Comparing the effect of a linear PTO system to a hydraulic PTO system for a wave field around a 5-WEC array

In this section we compare the effect of the linear and hydraulic PTO system on the near-field of the array. As in Sections 6.5.5.1 and 6.5.5.2, we show the outcomes

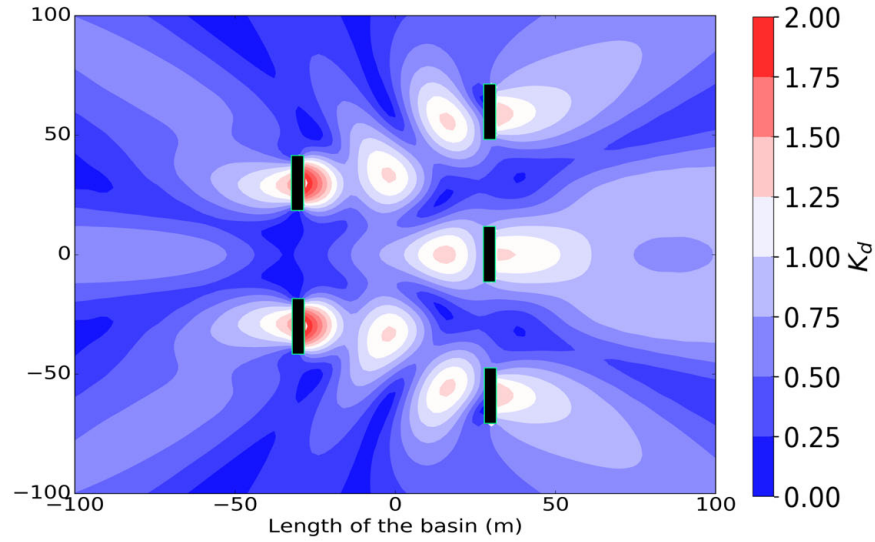

Figure 6.25: The perturbed K_d for an array of OSWECs for a wave of H = 1.0 m, T = 6.0 s for a linear PTO system. Incident wave propagating from the left.

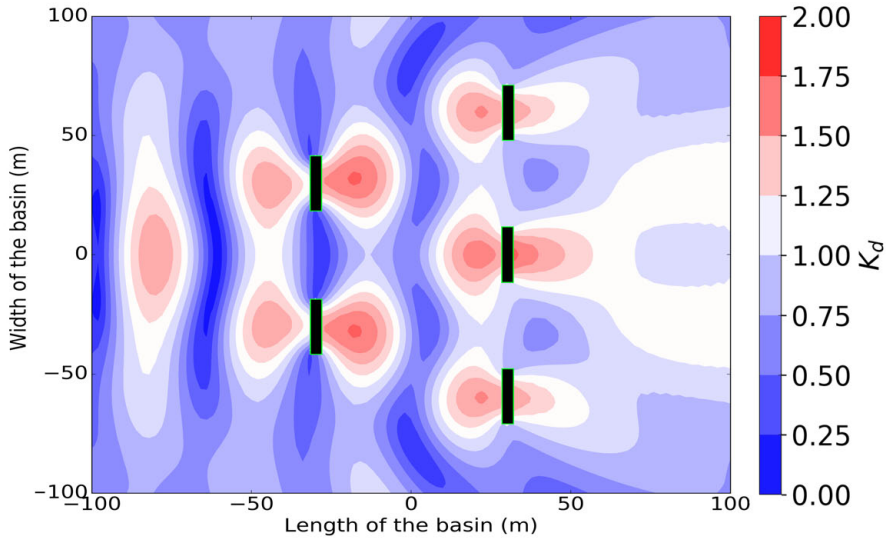

Figure 6.26: The total K_d for an array of OSWECs for H = 1.0 m, T = 8.0 s for a linear PTO system. Incident wave propagating from the left.

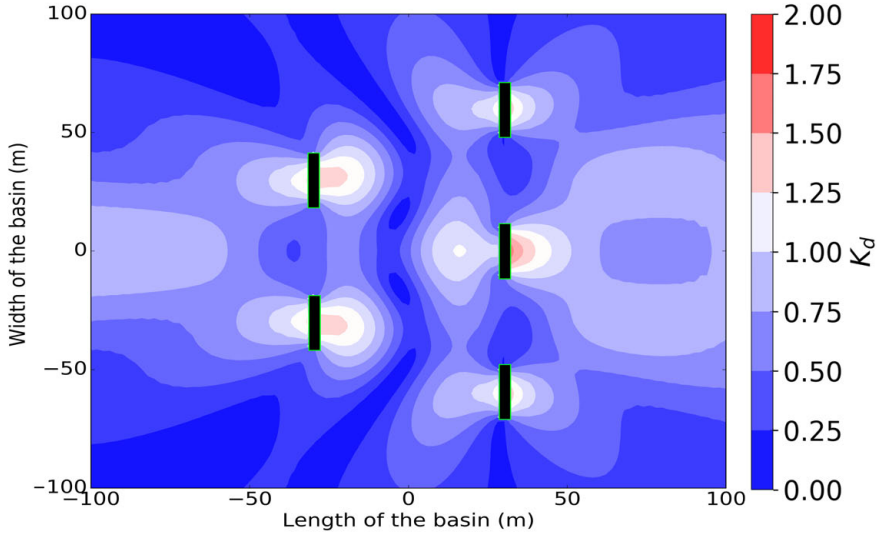

Figure 6.27: The perturbed K_d for an array of OSWECs for H = 1.0 m, T = 8.0 s for a linear PTO system. Incident wave propagating from the left.

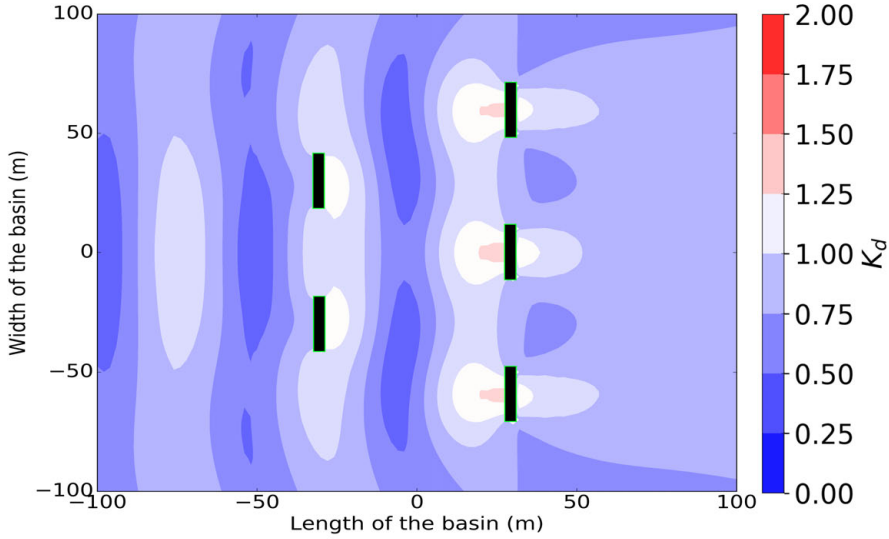

Figure 6.28: The total K_d for an array of OSWECs for a wave of H = 1.0 m, T = 10.0 s for a linear PTO system. Incident wave propagating from the left.

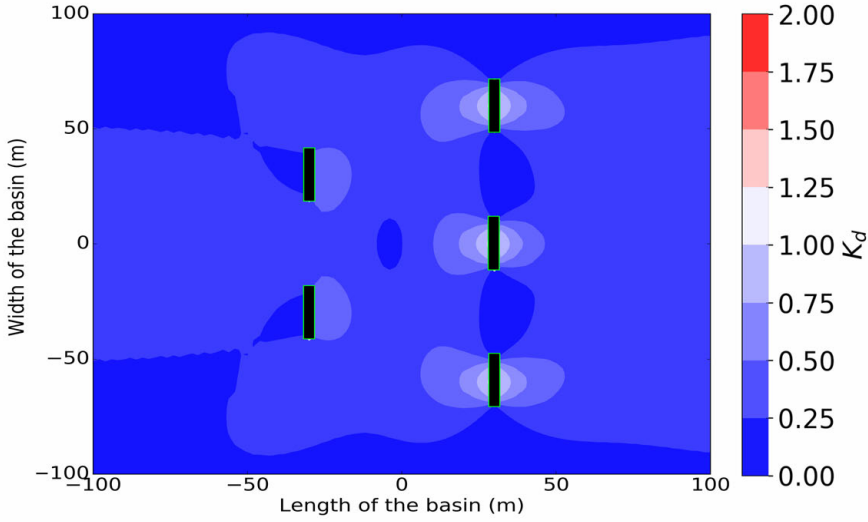

Figure 6.29: The perturbed K_d for an array of OSWECs for a wave of H = 1.0 m, T = 10.0 s for a linear PTO system. Incident wave propagating from the left.

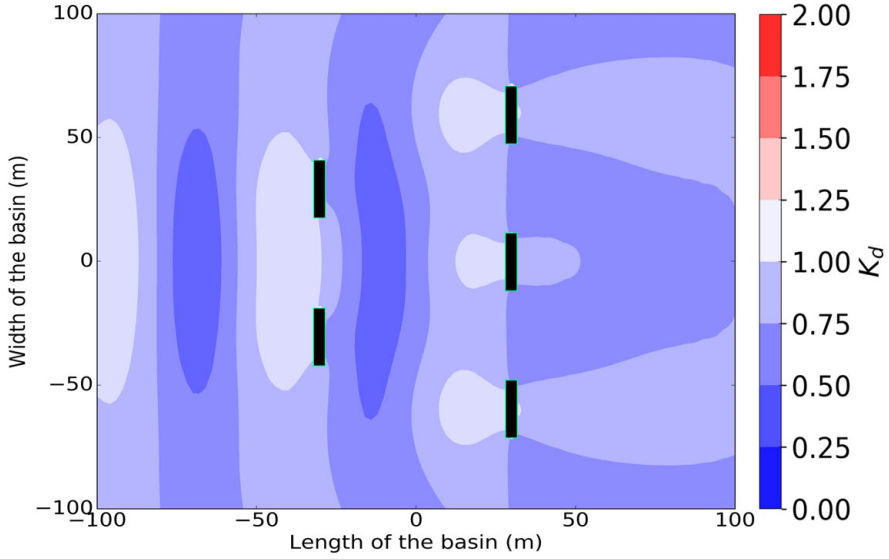

Figure 6.30: The total K_d for an array of OSWECs for a wave of H = 1.0 m, T = 12.0 s for a linear PTO system. Incident wave propagating from the left.

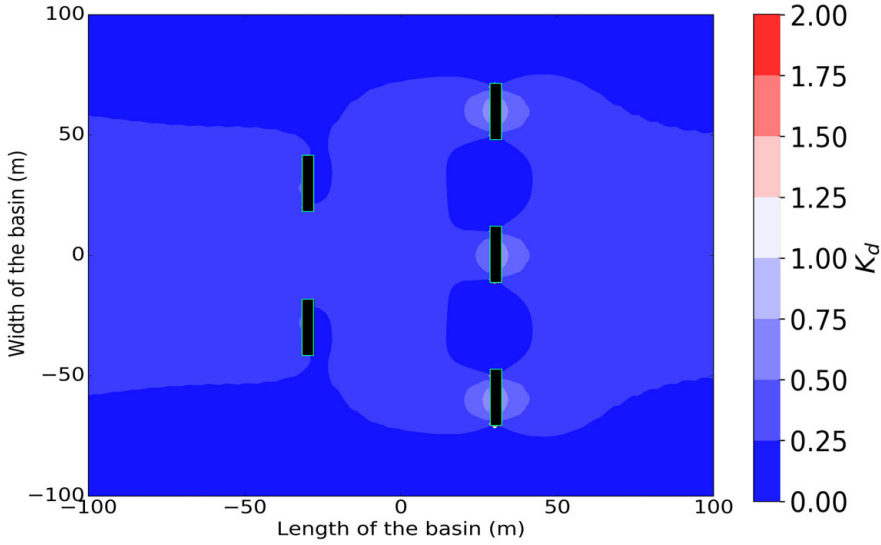

Figure 6.31: The perturbed K_d for an array of OSWECs for a wave of H = 1.0 m, T = 12.0 s for a linear PTO system. Incident wave propagating from the left.

for both the total and perturbed wave fields, but instead of plotting K_d, we plot the percent difference between the K_d of the WEC with hydraulic and the linear PTO system. This is similar to Figs. 6.12 and 6.13 for the a single WEC. We start by looking at the effect of the hydraulic PTO system for the case of the heaving cylindrical WEC. In Fig. 6.32 we plot the difference between the total K_d for a heaving cylindrical WEC for the 4 modelled wave periods as defined by Eq. (6.33). The first observation we make is the marked decrease in the K_d difference as we increase T from 6.0 s to 12.0 s. While for the 6.0 s wave the difference barely exceeds 15 % for areas on the perimeter of the body, for the rest of the wave periods the differences are considerably less, dipping below the 5% threshold of the T = 12.0 s case. Note that whereas for the two shorter wave periods the areas of positive and negative change have a complicated pattern based on the interaction between the radiated waves of each body, for the T = 10.0 s and T = 12.0 s cases there is a general trend of a higher K_d for the hydraulic PTO system for the front rows and lower for the back row, especially for the back middle WEC. Observe that this slight overall decrease in K_d does not adversely affect the heaving cylindrical WEC array performance, as we saw in Tables 6.7 and 6.8 in Section 6.5.4, where the performance of the heaving cylindrical WEC array is significantly better than that of the single WECs. Contrary to the heaving cylindrical WEC array, the difference of the PTO system greatly modifies the wave field of the 5-OSWEC array. In comparing Fig. 6.33 to Fig. 6.32, we see that the percent difference is much greater, in fact more than 100% for the 8.0 s case.

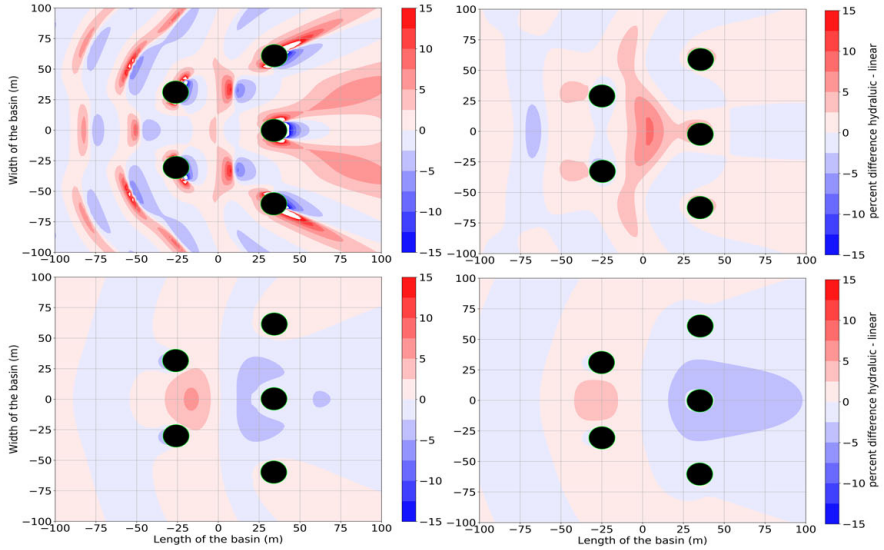

Figure 6.32: Percentage difference between the K_d produced by a heaving cylindrical WEC with a hydraulic PTO vs. a linear PTO system for a wave of H = 1.0 m and wave periods of T = 6.0 s (top left) T = 8.0 s (top right) T = 10.0 s (bottom right) T = 12.0 s (bottom left). Incident wave propagating from the left.

One also observes that unlike for the heaving cylindrical WEC array example, the differences in K_d do not markedly decrease with increasing wave period. We see that difference is the greatest for T = 8 s but that it is also greater for T = 12.0 s than for T = 10.0 s. What we see then is that there is a strong effect the hydraulic PTO system on the WEC array wave field, and by comparing the contour plots in Fig. 6.33 to the values for the average absorbed power of the OSWEC array in Tables 6.7 and 6.8, we also notice that the difference in K_d is not always proportional to the difference in power. For example, we notice that the magnitude and extent of the positive anomalies for T = 12.0 s is greater than that for T = 10.0 s but that the hydraulic PTO system 5-OSWEC array produces less power for the higher period. In general, we see that the difference from linear to hydraulic PTO system has a strong effect on the total wave field, but that the quality of the difference is greatly dependent on the wave period. We note that for the T = 8.0 s case in particular, there is an overall reduction in the surface elevation in lee of the array for the hydraulic PTO system compared to the linear PTO system, a fact *i.e.* reflected in the increase of the *q* value from 2.62 to 2.83. We can also observe that for the T = 10.0 s and especially the T = 12.0 s case that there is a net increase in K_d inside the array area and a slight decrease outside of it. Again, we see this confirmed in the *q* values in Tables 6.7 and 6.8 where they increment from 1.95 to 2.19 for the T = 10.0 s and from 1.35 to 1.59 for the T = 12.0 s wave.

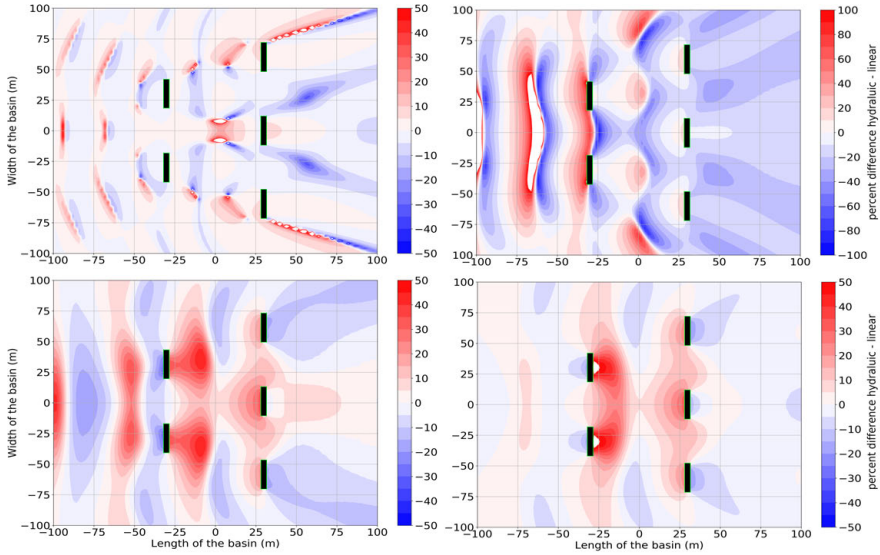

Figure 6.33: Percentage difference between the K_d produced by an OSWEC with a hydraulic PTO vs. a linear PTO system for a wave of H = 1.0 m and wave periods of T = 6.0 s (top left) T = 8.0 s (top right) T = 10.0 s (bottom right) T = 12.0 s (bottom left). Incident wave propagating from the left.

6.6 Discussion

In the results for the 5-WEC arrays in Section 6.5 was seen the interplay between the efficacy of the WEC array from the point of view of average absorbed power and the array wave field K_d. The primary determination we can make is that the array effects are much stronger for the 5-OSWEC array case than for the heaving cylindrical WEC array case. Consequently, the effect of the change of the PTO system on the near-field surface elevations is much more significant for the OSWEC than for the heaving cylindrical WEC as highlighted in Figs. 6.32 and 6.33 in Section 6.5.5.3. As remarked in Fig. 6.16 in Section 6.5.4, the effect of the change in PTO on the power output of the array is likewise quite different between the 5-heaving cylindrical WEC array and the 5-OSWEC array. And yet it is not strictly related to the change in the magnitude of the array effects. The addition of a hydraulic PTO significantly increases the power output of the heaving WEC array, especially at the higher wave periods. Meanwhile for the OSWEC array, there is a net decrease in the array power output with a change from a linear to a hydraulic PTO system for all periods except for T = 12 s. The interplay between the impact of the PTO systems of the two WEC types placed a closely-spaced WEC array on the array power and on the near-field K_d are conceptualized in the flow chart in Fig. 6.34. The arrow thickness represents the relative magnitude of the effect of each PTO type on the phenomena where the arrows are directed.

As with the magnitude, the location of the greatest changes in the near-field K_d differs between the 5-heaving cylindrical WEC and the 5-OSWEC array. Observe that the areas of positive and negative % difference in K_d are very distinct, with the hydraulic PTO system increasing the apparent K_d behind the heaving cylindrical WEC array while for the OSWEC array the change from a linear to a hydraulic PTO reduces the K_d behind the WECs. This is not a surprise given that the OSWEC, which operates in shallow water and fills the entire wave column, presents a bigger obstacle to the oncoming waves that results in much greater wave diffraction as observed in Figs. 6.12 and 6.13. It is also the case that the OSWEC produces a stronger radiated wave field. The sum of the two effects results in strong areas of constructive and destructive interference that we observe in the mean free surface elevations in the single OSWEC case in Fig. 6.8 (left) and in the array of 5 OSWECs in Figs. 6.24, 6.26, 6.28 and 6.30. Note especially the enhancement in the wave fields for T = 8.0 s for the OSWEC where the perturbed field is up to 50 % greater around the bodies.

This is manifested in the power output $\mathbf{P}$ of the 5-OSWEC array at this wave period in Tables 6.7 and 6.8: $\mathbf{P}$ is the highest value among all wave periods for the OSWEC and also with the highest q value, for both PTOs. In contrast, the perturbed wave field for the heaving cylindrical WEC for T = 8.0 s is quite small, only differing by a few centimetres from the undisturbed K_d as we see in the in Fig. 6.21. Moreover, the impact of the change in the PTO system of the heaving cylindrical WEC is not necessarily reflected in the power output of the heaving cylindrical WEC array. As an example, the 5-heaving cylindrical WEC array outputs the most power at a wave period of T = 8.0 s for a linear PTO system, for a hydraulic PTO system the power is higher for wave period of T = 10.0 s. Since the near-field array effects and the power output of a 5-heaving cylindrical WEC array are not directly linked, these changes are not reflected in Fig. 6.32 where we see a relative decrease in the near-field K_d between the case of a wave period of T = 8 s and T = 10 s.

When we observe the areas of positive or negative change based on a substitution of a linear for a hydraulic PTO system, in Fig. 6.32, we note a decrease in the change in K_d for the higher wave periods, indicating that the hydraulic PTO system is indeed extracting more energy from the wave field than the linear PTO system. However, the magnitude of these effects is close to the 5% threshold and can essentially be neglected in a 1^{st} order modelling approach. Conversely, we have noted in Section 6.5.5.3 that the addition of a hydraulic PTO system to the OSWECs in an array tends to 'pull' in the energy from the surrounding areas to the 'near field'. This is especially true for higher wave periods and is reflected in the relative increase in the power output of an OSWEC array with a hydraulic PTO system compared to the same isolated WEC. In the case of the OSWEC array, the effects are an order of magnitude stronger. We note the present results show the same differences in the strength of the array effects between the heaving cylindrical WEC and the OSWEC arrays as in those presented in (Verao Fernandez et al., 2017).

We presume that such contrasting behaviour is a reflection of the differences in the underlying hydrodynamics of the WEC-PTO system of the 2 WEC types.

For the heaving cylindrical WEC case, the primary driver of an increment in the power output of a hydraulic PTO system is the increase in the PTO system force, while for the OSWEC the hydraulic PTO system has a greater impact on the WEC motion. Indeed, the K_d of near-field area of the OSWEC array increases with the hydraulic PTO system, especially for the long wave periods T = 10.0 s and T= 12.0 s. Unlike the heaving cylindrical WEC case, we also note that a change in the PTO system reduces the K_d in lee of the WEC array, augmenting the areas of destructive interference. This might be important in considering the impact on surrounding WEC arrays and coastal processes. Still, a change in PTO system for

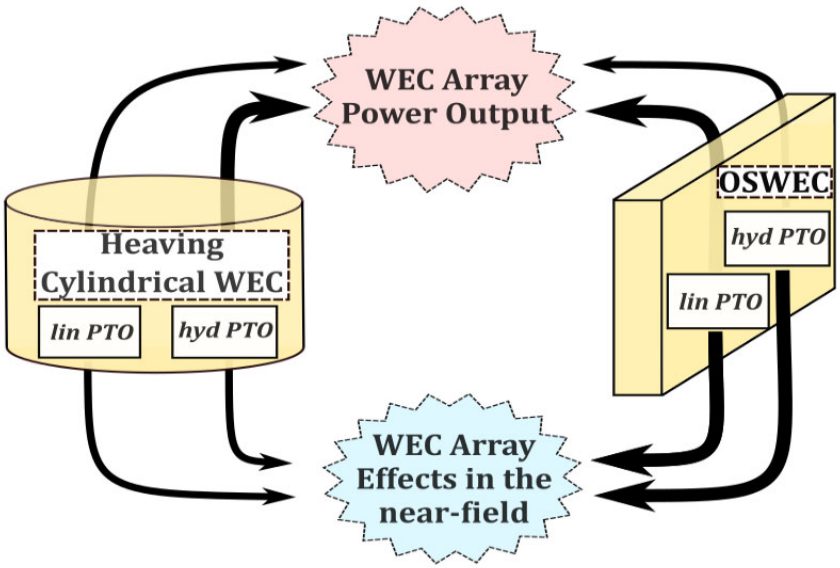

Figure 6.34: Schematic diagram showing the relationship between the PTO system impacts of the two types of WECs in an array. Thick arrows represent strong influences on the indicated parameters while thin arrows represent weak influences.

the OSWEC results in an improvement for only the T = 12.0 s, with a relative decrease in the power output for the other wave periods compared to the linear PTO system case. We must remark here that for the OSWEC case, for both the single WEC and the array, the linear PTO model can exaggerate the performance of the OSWEC since we are not taking into account the strong non-linearities inherent in the dynamics of this WEC type. This has been pointed out in (Schmitt et al., 2016; Giorgi and Ringwood, 2018) amongst others. Therefore, if we were to chose a more sophisticated model for the OSWEC, the relative 'underperformance' of the hydraulic PTO system might disappear.

It must be mentioned here that in this study we are using a linear hydrodynamic model in simulating the WEC arrays for regular waves from a single direction. It has been shown in literature and in the own research that these assumptions would

tend to overestimate both the power output and the perturbations in the near-field K_d. We note that a heaving cylindrical WEC, being axi-symmetric, is much less sensitive to changes in the direction of the incoming wave than the OSWEC. We also remark that for the case of the OSWEC, the linear PTO model might lead to an overestimation of the power and the differences we observe between a 5-OSWEC array power output with a linear and hydraulic PTO model might be in part be due to such assumptions. Therefore we use the linear model more as a 'benchmark' to compare with previous studies such as (Charrayre et al., 2014b; Verao Fernandez et al., 2017; Ruiz et al., 2017b; Balitsky et al., 2018b) rather than a realistic PTO system representation to include in an OSWEC array simulation.

6.7 Conclusion

In this chapter we have presented a model of arrays of 5 WECs of two WEC types with contrasting hydrodynamics, a heaving cylinder WEC and an OSWEC driven by the surge component of the wave force. In the wave structure interaction-PTO model, we simulated single WECs and arrays with linear and hydraulic PTO systems, calculating both the power output of the WEC array and near-field K_d of the WEC array using an original iterative method that enables a fast calculation of both quantities. We have elaborated on the distinct hydrodynamic behaviour of the heaving cylindrical WEC and the OSWEC.

We noted the differing effects of changing of a WEC PTO system between a single WEC case and an array case as summarized by Fig. 6.34. Pertaining to power output P for the single heaving cylindrical WEC case, we conclude that the hydraulic PTO system brings a significant increase in the power output compared to a linear PTO system with up to 25% improvement for a H $=$ 1.0 m T $=$ 10.0 s wave. For an array of 5 heaving cylindrical WECs the result is similar, with the increase due to the hydraulic PTO system mirroring that of the single WEC case. In both cases the impact of the heaving cylindrical WEC array on the near-field is minimal, with the only significant modification of the wave field at a wave period of T $=$ 6.0 s. By extension then, a change in the PTO type for a heaving cylindrical WEC array produces no substantial changes to the near-field surface elevations. Therefore, if these effects are the primary target of a given investigation, a hydraulic PTO system can be modelled as a linear PTO system without loss of fidelity.

Conversely, for a single OSWEC, a hydraulic PTO system tempers the performance, with a reduction in the power output P across all wave periods around 14 %. Intriguingly, the situation for a 5-OSWEC array is different, with the hydraulic PTO system only having a strong negative effect on power output for a T $=$ 6.0 s wave. For the other wave periods the change in PTO system does not result in a large decrease in the power output, indeed for T $=$ 12.0 s it slightly increases. We can see, therefore, that for the case of a 5-OSWEC array the array effects play a strong role in modifying the WEC array power output. There is a two-fold conclusion then for modelling the OSWECs. Firstly, a single OSWEC with a specific PTO system cannot be expected to reflect the behaviour of said PTO system in an

array. Secondly, the difference between the two types of PTO systems modelled is great enough such that one cannot substitute one PTO system for another without introducing substantial error. As a practical consideration, most existing models of array PTO systems are simulated as linear PTO systems. Although a hydraulic PTO system is more difficult to model in practise, the results have shown that for the case of the OSWEC array with a hydraulic PTO system, it cannot be simplified down without introducing substantial error into both the array power output and the near-field effects. In both of the aforementioned cases, the WEC array modeller can use the conceptual schematic introduced in Fig. 6.34 as a guideline for choosing which assumptions to make.

It is part of the ongoing research to gradually increase the complexity and sophistication of both the hydrodynamic and the PTO models with the counterbalance of having a fast and intuitive solution for WEC array modelling. It is the next step of the research to utilize the presented coupled models in a realistic WEC farm simulation using real sea states to test the limitations of the present research mentioned at the end of the discussion in Section 6.6. Furthermore, the aim of this thesis is to expand the calculation of the perturbed wave field to the 'far-field' area away from the WEC farms to study coastal effects and interactions with a changing bathymetry.

Chapter 7

A simple wave to wire model for analysis of WEC farm effects

Abstract

In this chapter the modules developed in the previous chapters are integrated into a wave-to-wire (W2W) model which links a Boundary Element Method (BEM) solver to a WEC motion solver which are in turn coupled to a wave propagation model. The hydrodynamics of the WEC are resolved in the wave structure interaction solver NEMOH, the PTO is run in the WEC simulation tool WEC-Sim, and the resulting perturbed wave field is coupled to the mild-slope propagation model MILDwave. The W2W model is run for verified for a realistic wave energy project consisting of a WEC farm composed of 10 5-WEC arrays of OSWECs. The investigated WEC farm is modelled for a real wave climate and a sloping bathymetry based on a proposed OSWEC array project off the coast of Bretagne, France. Each WEC array is arranged in a power-maximizing 2-row configuration that also minimizes the inter-array separation distance d and the arrays are located in a probable staggered energy maximizing configuration that also reduces along-shore WEC farm extent. The WEC farm power output and the near and far-field effects are simulated for irregular waves with various significant wave heights wave peak periods and mean wave incidence directions β based on the site wave climatology. The PTO system of each WEC in each farm is modelled as a closed-circuit hydraulic PTO system optimized for each set of incident wave conditions, mimicking the proposed site technology, namely the WaveRoller® OSWEC developed by AW Energy Ltd. The investigation in this chapter provides a proof of concept of the proposed W2W model in investigating potential commercial WEC projects.

7.1 Introduction

In this thesis the reader witnessed the development of various numerical tools and investigated diverse facets of the WEC array problem, specifically the complex interplay between the WEC array power and the WEC array effects on the surrounding area. It is now possible to pull together the various developments in the previous chapters, including:

- coupling between the BEM solver NEMOH and the mild-slope wave propagation model MILDwave (Chapter 4)
- development of an iterative technique to model WEC farms composed of clustered WEC arrays (Chapter 5)
- development of a realistic time-domain PTO module (Chapter 6)

in a wave-to-wire model suite. Unlike existing wave-to-wire models such as (O'Sullivan and Lightbody, 2015; Bailey et al., 2016), which focus on a specific WEC technology, or those such as (Penalba and Ringwood, 2018a,b) that deal with a single objective of power maximization, the model proposed in this thesis has the dual goal of accurately representing the wave field around the array and at the same time allowing a fast and accurate calculation of the power output of a given WEC array project.

In this chapter we test the wave-to-wire model introduced above for a realistic scenario of a proposed commercial WEC array project, namely the WATTMOR proposal developed by the energy companies DCNS and Fortum in partnership with the Finnish company AW Energy utilizing the WaveRoller® technology (Kasanen, 2015). WaveRoller is an OSWEC that has been successfully deployed over various generations and independently certified by the ratings agency Lloyd's register (AW-Energy Oy, 2019). The WEC farm investigated in this chapter is to be located in the Baie d'Audierne near Pouldreuzic in Bretagne, France at a latitude of 47.93°N and a longitude of 4° 44'W. The project location is shown in Fig. 7.1 on a map of the western part of the Finistère peninsula of Bretagne.

The realistic deployment scenario will consists of modelling the following four WEC array project aspects:

a a wave climate representative of the site

b a realistic sloping bathymetry

c a WEC with approximate dimensions to the proposed WEC technology to de deployed

d a hydraulic PTO system mirroring that of the proposed WEC

e a probable WEC farm layout that seeks to maximize power absorption over a limited coastal length.

The wave climate utilized by the model is derived from 9 years of actual buoy data from buoy 05605 (Belle-île) of the French buoy network provided by CANDHIS

CEREMA Eau, mer et fleuves - ER/MMH (2019) located in 45 m of water depth. Note that the only the wave heights and wave period are investigated here. They represent a moderate wave climate typical of operating conditions in the North Atlantic (Varing et al., 2017). Consequently, such events as overtopping of the OSWECs and survival mode such as submergence are not taken into account in this thesis.

The site bathymetry, based on surveys carried out for the WATTMOR project, as shown in Section 7.2.2, is approximated in this study by a slope of 1/200 which easily fits within the criteria for the application of MILDwave as detailed in Section 4.2.2. The modelled WEC is an OSWEC of dimensions equal to the one investigated in Chapter 6 and is based on the publicly available information on the WaveRoller® technology. The PTO system is reproduced in WEC-Sim as a simplified yet accurate hydraulic time-domain simulation which has been introduced in (Balitsky et al., 2018b) and detailed in (Balitsky et al., 2018a). The WEC farm layout η is determined via an iterative method first developed in (Balitsky et al., 2018b) and expounded in this thesis in Chapter 5.

Results will be presented in two parts: firstly a pilot-scale example of a 10-OSWEC farm consisting of 2 5-OSWEC arrays placed on an shore-orthogonal axis in Section 7.6, the second the full commercial scale consisting of a gridded 50-WEC farm of 10 5-WEC arrays in Section 7.7. The power output and the wave field of the WEC farms will be presented for the seasonal wave conditions based in the wave data calculated in Section 7.2.3. For the full-scale layout, the power output will be analysed for spring, winter and summer wave conditions in Tables 7.5 to 7.7, respectively. In the discussion in Section 7.8, we will comment on the interaction between the bathymetry and the wake effects of the WEC farm's arrays and the influence of the wave conditions. Finally, in the conclusions section Section 7.9, we shall summarize the results of the chapter with a view toward assessing the coastal impacts of potential wave energy projects, especially those located relatively close to the shore.

7.2 Characteristics of the WEC Array Project Site

7.2.1 Study location and geographical context

The hypothetical WEC farm investigated in this thesis is placed in the Baie d'Audierne near Pouldreuzic in Bretagne, France at a latitude of 47.93°N and a longitude of 4° 44'W in a region of gently sloping bathymetry close to major sea ports. The overview map showing the study area within the context of the surrounding region is shown in Fig. 7.1. The W2W model domain chosen for this investigation, indicated by the orange rectangle in Fig. 7.2, overlaps the commercial project area shown in the red box in the same figure. The reasoning for taking a orthogonal cross-section is that we are primarily interested in the transformation of the waves over the sloping bathymetry and its impact on the WEC array power production and the far-field effects on the coast. Furthermore, with the seaward boundary set at a 35 m depth (see Section 7.2.2 for details), the incoming wave will be minimally impacted by shoaling and thus can serve as a good proxy for the offshore

Figure 7.1: Map locating the investigation domain at the proposed WATTMOR project site in the Baie d'Audierne and the CANDHIS buoy 05605 (Belle-île) which serves as the source of the wave data off the coast of Bretagne, France

wave incidence.

The WEC farm layout and the depth profile are shown in Fig. 7.4. Note that the horizontal scale is shrunk for clarity. The individual array domains modelled in NEMOH are shown as green, numbered *i* through *x*. The location for the hypothetical WEC farm investigated in this chapter was chosen for a number of reasons. Firstly, as mentioned in the introduction, the site currently under investigation for a possible commercial WEC array project, namely WATTMOR (Kasanen, 2015). Secondly, the wave climate at the site is representative of the North Atlantic wave climate which covers the majority of the European coastline (Varing et al., 2017). Furthermore, Europe is currently home to the largest number of existing and proposed WEC array projects (European Marine Energy Centre Ltd., 2019). Thirdly,

the characteristics of the bathymetry, with a gentle slope and isobaths nearly parallel to the coastline, easily lend themselves to modelling with a mild-slope equation based wave propagation model.

Finally, at the given site, we also have an energetic wave climate capable of supporting an economically viable wave energy conversion technology as will be detailed in Section 7.2.3 and one where there is a strong match between the chosen OSWEC device operating conditions and the mean wave climate Kasanen (2015). Geographically, the site is in close proximity to large ports such as Brest, Douarnenez and Quimper, which are able to provide the necessary access and know-how for the deployment and maintenance of a WEC array project. Lastly, the location of a wave measuring buoy with a high resolution long-term recording history approximately 100 km away and in a similar depth to the deep end of the modelling domain enables us to utilize real wave data in the modelling.

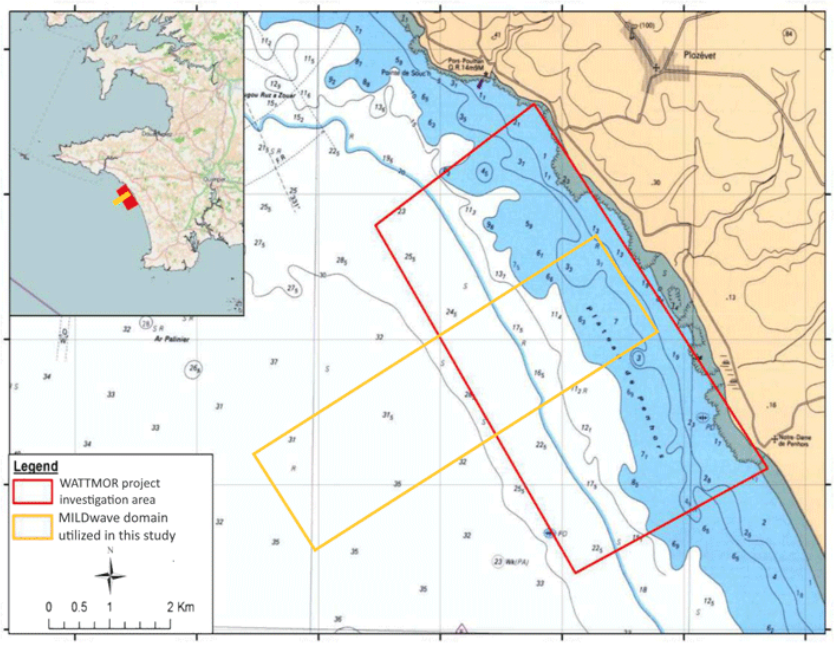

Figure 7.2: Detailed map showing the project area (red box) and the W2W model domain investigated in this chapter (orange box)

7.2.2 Site bathymetry and approximation

The site bathymetry is presented in Fig. 7.2 and in Section 7.2.2, with the latter giving the high resolution survey data specifically collected for the WATTMOR project. As we observe in Section 7.2.2, the chosen model domain is very well approximated by a shore-orthogonal slope, with only a few variations that are well

within the margin of approximation. Moreover, the site sea bottom consists of mostly fine sand which tends to shift in response to the waves and currents, therefore a slope is also the most accurate representation of the average bathymetric profile over a WEC Array project lifetime of several decades. The rationale for choosing the same depth for the submergence of the OSWECs is that the commercial scale equivalent, namely the WaveRoller OSWEC (AW-Energy Oy, 2019), has a fixed size. Although the information provided by the developer in (AW-Energy Oy, 2019), the OSWEC is deployable from 8 to 15 meters. Given the difficulty of manufacturing different size components one does not foresee it being economical to design a separate device for these depths. At the same time, the performance of a device which is continuously submerged decreases substantially.

Therefore, the conjecture is that the OSWEC will be fixed to an inert gravity base which would ensure the correct submergence depth so that the it is surface piercing. In the case of the gravity base the local depth immediately surrounding the OSWEC is decreased to 10m which is the modelled depth in NEMOH. An alternative NEMOH configuration has been performed where the where the water is allowed to move under the OSWEC. It has been found that the power output of an OSWEC submerged in 15 m versus 10 m is only 6% greater for waves of $H_{m0} =$ 2 m, $T_p = 6$ s, and 5% for a wave of $H_{m0} = 2$ m, $T_p = 12$ s wave. However, this modelling does not account for the supporting structure which is likely to reduce the power output and put it more in line with the 10 m depth results presented in the thesis. Based on the presented consideration the modelling scenario is deemed to be representative of the realistic case study herein modelled.

7.2.3 Analysis of the wave climate at the investigation site

The proposed WEC array project location sits 100 km away from the nearest long term wave measuring buoy with an interrupted data record, station 05602 - Belle-île, maintained by the Centre d'Archivage National de Données de Houle In Situ (CANDHIS), that is a partnership between the Grand Port Maritime de Nantes St-Nazaire, l'École Centrale de Nantes, and the French public agency CEREMA (Centre d'études et d'expertise sur les risques, l'environnement, la mobilité et l'aménagement). The location of the buoy and the investigation area of this chapter are shown in Fig. 7.1.

The wave rider buoy, located at 47°17.1'N and 3°17.1'W, at a depth of 45 m, has been providing continuous half-hourly directional wave data since its deployment in 2010. In this investigation, we utilize 9 years of data from December of 2010 to March of 2019. The data is provided each half and hour over the 9 year period. Of the measurements provided by the buoy, we have utilized the spectrally-derived significant wave height,H_{m0}, the peak wave period T_p, and the mean wave direction from true North, θ_m which will be utilized to derive the incoming wave direction β relative to the shore-orthogonal rectangular domain axis. The wave data is analysed and split into four seasonal bins, namely winter, spring, summer, and autumn, based on meteorological convention, *i.e.* winter is December-February. The bulk average of the aforementioned quantities is given in Table 7.1 along with the overall 9-year averages. There are a few evident trends we can note from this

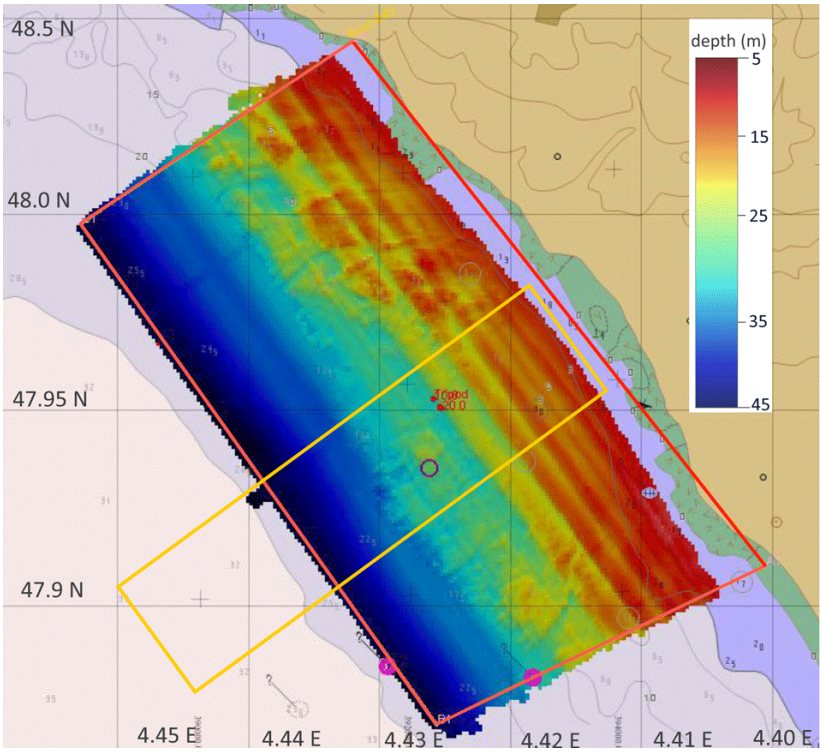

Figure 7.3: Map showing the detailed bathymetric survey of the project area (red box)

Table 7.1: Summary statistics of the wave climate at the Belle île measurement buoy located at 47°17' N and 3°17' W for a 9 year period Oct. 2010 - Mar 2019.

	wint	spr	sum	aut	year
$H_s(m)$	2.55	1.75	1.20	1.80	1.87
$T_p(s)$	11.71	10.45	8.71	10.54	10.34
$\theta_w(^\circ)$	261.74	263.32	270.12	263.16	264.48

table. Firstly, this is a relatively energetic sea state without a significant inter-year variation in the three major parameters. The mean winter H_{m0} and T_p are significantly higher than the summer values. We also notice the small divergence between the spring and autumn values, with only a 4% difference in H_{m0}, less than 1% difference in the T_p, and an even smaller difference of 0.5% in the mean wave direction. Likewise, the spring and autumn averages are very close to the overall annual average of the three quantities. Such a climate is characteristic of the North Atlantic and other sites at similar latitudes in the northern hemisphere without influence from the southern hemisphere such as the North East Pacific.

The wave data motivates the choice of modelling 3 different sea states, namely the winter, summer, and overall average that can also stand as a proxy for the

spring and autumn wave conditions, which is elucidated Section 7.3.1. We also remark the small variations of the mean wave direction θ_m of only 8° between the summer and winter values. The small variations in the mean incident wave directions are very favourable for an OSWEC array of the type modelled in this study, as the performance of these WECs has been shown to decrease for oblique wave incidences (Tay and Venugopal, 2017; Henry et al., 2018). While a longer data set would have yielded more clues about the inter-annual variability of the wave climate at the study location, the consistency of the available data means the performed analysis closely represents the site wave climate over a medium-term project duration.

7.2.4 WEC farm and clustered WEC array layout

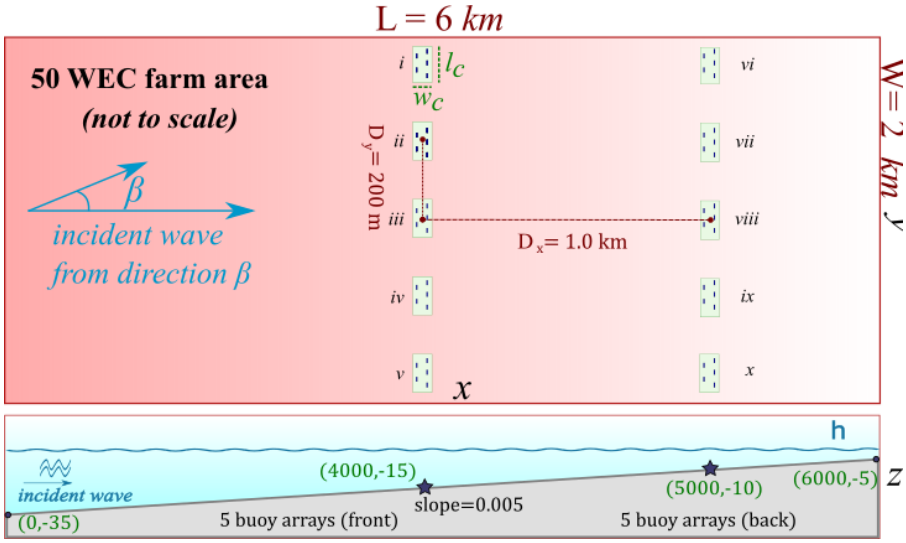

Figure 7.4: 50 WEC farm schematic shown. Top and side views. Note the area outside of the 2 row of OSWEC arrays is not shown to scale to increase visibility

The full-scale WEC farm, shown in top view and in profile in Fig. 7.4, consists of two rows of staggered arrays facing the prevailing wave direction, separated by 1 km. The WEC farm bathymetry is modelled as a slope of 1/200 with the depth ranging from 35 m at the offshore (WSW) side to 5 m at the near-shore (ENE) side. The location of the front WEC array row is at a depth of 15 m while the back row is situated at a depth of 10 m. Both depths are within the operating range of the proposed OSWEC technology, as mentioned in (Kasanen, 2015). The 1 km WEC farm row separation distance allows the back row to avoid the worst shadowing behind the front row, as we will witness in Section 7.7. The side to side separation distance between the centres of adjacent WEC arrays is 200 m, which is sufficient to minimize the lateral array effects of OSWECs.

The WEC farm domain displayed in Fig. 7.2 is orthogonal to the shoreline, or

240° from true North. This means the WEC arrays are located 24° off the average incidence wave direction and 30° off the summer wave incidence. To simulate a realistic array of WECs, we have chosen a staggered configuration as has been previously utilized in both Chapter 5 and Chapter 6. The configuration, along with the dimensions of the WEC arrays is displayed in Fig. 7.5. For the case of a compact WEC array, this configuration is power maximizing in the sense that the worst shadowing effects of one WEC on the other are avoided for a small β, as was shown in Borgarino et al. (2011b), for example.

It should be mentioned that the investigations of Tay and Venugopal (2017) and Tomey-Bozo et al. (2019) specifically deal with closely spaced OSWEC arrays in real sea states, mirroring the scope of the work in this chapter, both use a staggered inter-array configuration. As will be seen in the results displayed in the three tables in Section 7.7, the array orientation relative to the WEC farm axis is held constant while the angle of the incoming waves relative to the x-axis, β, is rotated for the wave directions modelled in Table 7.3. This choice is also realistic given that the OSWEC technology will likely be deployed parallel to the isobaths, which in the chosen scenario are also parallel to the shore.

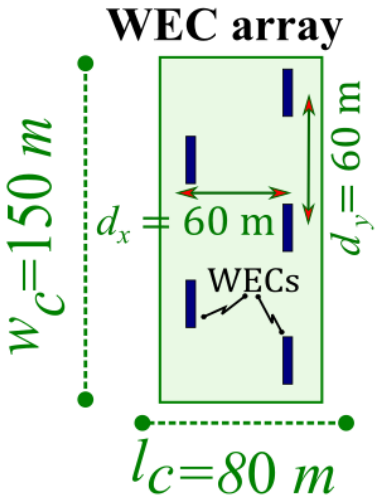

Figure 7.5: 5-WEC Array. Top view.

7.3 Wave-to-wire model methodology

7.3.1 Modelled scenarios

In order to ascertain the influence of the wave climate on the WEC farm operation, we subject the assumed wave farm to a variety of realistic wave conditions based on the wave climate data presented in Section 7.2.3. Before simulating the realistic multi-frequency sea states, we investigate the WEC farm response for a regular

wave of H = 2 m and T = 10 s, which is close to the mean annual values for the wave climate, to gain insight into the behaviour of the WEC farm. The shore-normal incidence angle $\beta = 0°$ is simulated as a 'base case' scenario, against which the effects of the site average $\beta = 20$ ° is compared. The regular wave parameters are summarized in Table 7.2. In simulating the wave climate based on the project

Table 7.2: WEC farm regular wave modelled scenario

$H_{m0}(m)$	T (s)	$\beta(°)$
2.0	10.0	0
2.0	10.0	20

site buoy data given in Section 7.2.3 we utilize some of the trends inferred from the analysis in Section 7.2.3 to simplify the modelling. Namely, as we observed from the data in Table 7.1, the spring and autumn average wave climate is nearly identical. Therefore, in this investigation we chose to model only 3 distinct wave conditions, namely the summer, winter, and autumn wave regimes, with the respective H_{m0}, T_p, and θ_m. The wave parameters simulated to obtain the results in Sections 7.6 and 7.7 are given in Table 7.3. The incoming wave incidence angle β is calculated as the difference between the WEC farm x-axis which is 241° from North, and the 3 mean wave incidences θ_m. Note that directional spreading is not modelled in this investigation.

Table 7.3: WEC farm modelled scenarios

simulated case	wint	sum	aut
$H_{m0}(m)$	2.55	1.20	1.80
$T_p(s)$	11.71	8.71	10.54
β (°)	-20.0	-30.0	-22.0

7.3.2 NEMOH BEM model parameters

The WEC array domain, corresponding to the green area in Section 7.6 and Fig. 7.4 and detailed in Fig. 7.5, is simulated in the BEM Wave Structure Interaction solver NEMOH. In brief, the interactions between the 5 bodies are solved using the Green's function method given the meshed surfaces of the WEC everywhere in the domain. The radiated and diffracted free surface elevations η are separately obtained for the WEC motions due to the diffracted and the radiated potentials via the free surface boundary condition Eq. (3.18). The depths simulated in NEMOH are 15 meters, to account for the same depth of submergence of the OSWEC. Further details on NEMOH are given in Section 4.2.1 in Chapter 4 and in (Babarit and Delhommeau, 2015).

7.3.3 MILDwave wave propagation model parameters

The W2W entire domain, shown by the rose gradient in Fig. 7.4 and bounded by the yellow box in Fig. 7.2 and Section 7.2.2, is simulated in MILDwave, a phase-resolving wave propagation model developed at the Coastal Engineering Research Group of Ghent University, Belgium. The model resolves the Berkhoff form of the Mild-Slope equations given by Eqs. (4.5a) and (4.5b) in the 6 km x by 2 km y domain shown in Fig. 7.4 with the grid resolution set to $\delta x = \delta y \equiv 5m$, which is sufficiently small to model the smallest peak wave period simulated, namely $T_p =$ 8.71 s. MILDwave is run over an inclined bathymetry as shown in the profile in Fig. 7.4 with a slope of $1/200$ with depths ranging from 35 m offshore to 5 m near-shore. Sponge layers of width 300 m of the Elliptical type given by Eq. (4.9) are placed at the ends of the domain parallel to the y-axis to minimize wave reflection. For the case of the empty basin run, the lateral boundaries parallel to the x-axis, are periodic, meaning that information leaving one end of the numerical domain enters the opposite end and thus the required model length in this direction is reduced. For details of the implementation of the periodic boundaries in MILDwave, see (Vasarmidis et al., 2019). For the coupled runs, the boundaries are sponge layers, as described in Section 4.2.2. Given the large domain and the multiple frequencies simulated, multiple instances of MILDwave are run in parallel to speed up calculation.

7.3.4 Coupling of NEMOH to MILDwave

In order to model the far-field effects in an efficient manner with a reasonable accuracy, the one-way coupling methodology presented in this thesis and detailed in Chapter 4 is employed between NEMOH and MILDwave. In brief, the perturbed wave field is calculated in the BEM code NEMOH and is propagated into the depth-integrated wave model MILDwave on a rectangle large enough to enclose the near-field domain that contains the WECs. Based on the sensitivity analysis performed in Chapter 4, we chose a rectangle with a length of 80 m and width of 150 m (see Fig. 7.5). The coupling methodology allows us the flexibility of coupling multiple inner domains to the outer domain; this is utilized in preparing the results in Section 7.7, where the 10 NEMOH domains containing the WEC arrays are coupled into MILDwave simultaneously.

7.3.5 Simulating irregular sea states

Because buoy spectral data is not available for the analysis site, we must chose a spectral representation to model the frequency distribution of an irregular sea state. Although various spectral parametrization exist, since the proposed site is in the open ocean, and not fetch-limited for the prevailing wave directions, we select a omni-directional Pierson-Moskowitz spectrum $S_{PM}(H_{m0}, T_p, \omega)$ with $N = 20$ frequency components, which according to an analysis of existing work in Pastor and Liu (2014) is sufficient for WEC motion simulation. The Pierson-Moskowitz distribution is given in Eq. (3.53).

7.3.6 Modelled OSWECs

The type of WECs simulated in this chapter is a bottom-fixed surface-piercing OSWEC with a width (w) of 20 m, a height (h) of 12 m, a draft (h_z) of 10 m, and a thickness (δx) of 1.0 m (see Fig. 6.3 (right)). The WEC is activated by the surging force of the waves in the shallow water wave regime, with the wave force driving a pitching motion about the base attachment which we set at the sea bottom for the 10 m depth and assuming a mounting structure that results in the same submergence profile for the 15 m depth deployment. The OSWEC is similar to several pre-commercial WEC technologies, specifically the WaveRoller device (AW-Energy Oy, 2019). The natural pitch period of the OSWEC, $T_{r,55} \equiv 17$ s.

7.3.7 Hydraulic PTO system and derivation of the optimal coefficients for irregular waves

The Power Take-Off (PTO) of each modelled WEC is a hydraulic system described in detail in Section 6.2.1.2 in Chapter 6 and constructed in the Matlab Simulink® environment then simulated in WEC-Sim, an open source purpose-built WEC dynamics simulator developed jointly by Sandia Laboratories and the National Renewable Energy Laboratory in the USA (Yu et al., 2014a; So et al., 2015). A schematic of the hydraulic system parameters is presented in Fig. 6.2. As was done in (Cargo et al., 2014) and in (Balitsky et al., 2018a), a hydraulic PTO system damping term $B_{PTO,h}$ is defined and checked for an optimum value. This $B_{PTO,h}$ is a coefficient that takes into account the parameters of the hydraulic PTO system that influence the performance of the WEC and has the same dimensions as the linear damping term $B_{PTO,l}$ given in Eq. (6.8) in Chapter 6: [(kg $\cdot$ m^2)/s] for an OSWEC. For a single OSWEC in regular waves $B_{PTO,h}$ is given in Eq. (7.1) with c being the distance between the flap-hinge and the connection with the PTO-bar and b_{ini} the length of the PTO-bar for $\theta = 0$.

$$B_{PTO,h} = c \cdot b_{ini}(\frac{s_c}{D_m})^2 B_g \tag{7.1}$$

For an OSWEC, the optimum value for $B_{PTO,h}$ for a given frequency ω is searched for by varying the motor displacement D_m, since it is the most convenient parameter to alter in practice. In the regular modelled wave case given in Table 7.2, $B_{PTO,h} = 121 * 10^6 kg \cdot m^2/$s.

For an irregular wave simulation, the bulk hydraulic equivalent PTO coefficient is derived by taking the spectrally-weighted sum of the hydraulic motor displacements D_m over the N frequency components:

$$D_{m,irr} = \frac{\sum_{i=1}^{N} D_{m,i}(\omega_i) \cdot S_{PM}(\omega_i)}{\sum_{i=1}^{N} S_{PM}(\omega_i)} \tag{7.2}$$

where $D_{m,i}$ is the motor displacement for frequency ω_i and $S_{PM}(H_{m0}, T_p, \omega)$ is the Pierson-Moskowitz spectral distribution used in this investigation and given by

Eq. (3.53) in Section 7.3.5. The irregular bulk hydraulic coefficient is then given by:

$$B_{PTO,h,irr} = c \cdot b_{ini}(\frac{s_c}{D_m, irr})^2 B_g \tag{7.3}$$

The choice was made to average out the motor displacements D_m instead of the hydraulic damping coefficient $B_{PTO,h}$, since D_m is the parameter that is actually modified. Furthermore, since the optimal $B_{PTO,h}$ for periods higher than 10 s decreases rapidly with increasing period. Thus, applying the weighted average in Eq. (7.2) to $B_{PTO,h}$ instead of D_m would have resulted in an unrepresentative value of $B_{PTO,h,irr}$. Each PTO coefficient in the OSWEC array is calculated by running WEC-Sim with the hydrodynamic coefficients given by the Wave Structure Interaction solver NEMOH. The optimal B_{PTO} coefficients for the three simulated wave states in Table 7.3 in Section 7.3.1 are given in Section 7.3.7. Note that the coefficients are the same across the 5 OSWECs in each array for each simulated wave condition: because the gradual slope of the curve of the OSWEC power output over the optimal hydroalic coefficient $B_{PTO,h}$ in Fig. 6.5 the influence of the adjacent bodies on $B_{PTO,h,irr}$ is minimal. It also must be mentioned that the non-linear influence of the significant wave height on $B_{PTO,h,irr}$ was found to be minimal, therefore the coefficients depend only on T_p.

Table 7.4: Optimal hydraulic damping coefficients $B_{PTO,h,irr}$ for a single OSWEC ($10^6 \times m^2 \cdot kg/s$).

T_p (s)	8.71	10.54	11.71
$B_{PTO,h,irr}$	198.7	145.6	121

7.4 Calculating the power output of a WEC farm composed of multiple WEC arrays

To ascertain the influence of the WEC intra-array interaction effects on the performance of a WEC farm, we compute the sum of the output power produced by the WEC arrays, after having obtained the modified wave field in the WEC farm using the approach outlined in Section 5.3.4. The procedure is outlined in the following list:

1. the wave field inside each array is computed in NEMOH using Eq. (4.4)
2. the power of each WEC in the array is calculated in WEC-Sim using the amplitudes output by NEMOH and summed for the $\mathcal{M}$ bodies
3. the power of the array is multiplied by the average wave field in the coupled 1st order perturbed MILDwave W2W model at the array perimeter
4. the power of the WEC farm is then the sum of the power of all constituent WEC arrays.

For each WEC array, using the amplitude of the total η at the locations of the WECs as the input determined in item 1 above, the WEC array power output is calculated in item 2 by simulating the OSWEC motions in WEC-Sim using Eq. (7.4) for each frequency component i.

$$\mathbf{P}_{i,h}(\omega,\beta) = -\frac{1}{T}\sum_{j=1}\mathcal{M}\int_0^T \mathcal{T}_{i,PTO}(t)\cdot\dot{\boldsymbol{\theta}}_{\boldsymbol{i}}(t)dt. \tag{7.4}$$

Here, M is the number of bodies in the array, $\mathcal{T}_{i,PTO}$ is a column vector of torques of each OSWEC, $\dot{\boldsymbol{\theta}}_{\boldsymbol{i}}$ is a column vector of the angular velocities of each OSWEC, ω is the wave angular frequency. The simulations are performed in WEC-Sim with the amplitude given by the total η at the WEC location determined by the procedure in Section 5.3.4. For simulating irregular wave scenarios, the power output is given by the sum of the power at each wave component frequency i, calculated by Eq. (7.4) weighted by the omnidirectional Pierson-Moskowitz spectrum $S_{PM}(f)$ given in Eq. (3.53)

$$\mathbf{P}_{array,irr} = 2\sum_{i=1}^{N}\Delta\omega S_{PM}(H_{m0},T_p,\omega)\mathbf{P}_{i,h}(\omega,\beta) \tag{7.5}$$

In Eq. (7.5), $\Delta\omega$ is the frequency bandwidth of the spectrum discretisation and the number of frequency components $N = 20$. To obtain the total power output of the WEC farm in item 3 above, we run the iterative procedure of Section 5.3.4 to obtain the total 1^{st} order η and subsequently multiply the value obtained in Eq. (7.5) by the value of the η at the perimeter of the array. Because the WEC array inner domain region includes the WEC bodies and the immediate surrounding area which is subject to the limitations of the linear BEM calculation, we chose the mean value of η on the perimeter of the WEC array regions to provide a representative value of the total wave field perturbed by the far-field array effects of the surrounding WEC arrays. Finally P_{farm} is given as the sum of $\mathbf{P}_{array}$ given by Eq. (7.4) for regular waves and Eq. (7.5) for irregular waves:

$$\mathbf{P}_{farm} = \sum_{k=1}^{\mathcal{N}}\mathbf{P}_{array}, \tag{7.6}$$

where $\mathcal{N}$ is the number of WEC arrays in the farm.

7.5 Results Representation

To assess the impact of the WEC arrays on each other and on the surrounding wave field, contour plots of the absolute value of the complex wave amplitude $|\eta|$ are plotted in Section 7.6 and Section 7.7. $|\eta_r|$ is defined by the following equation:

$$|\eta|_r = \frac{H_t}{H_I}\cdot\frac{H_I}{2} = \sqrt{2\cdot\sum_{t}^{\Delta t}\eta(x,y)_t^2\cdot\frac{dt}{\Delta t}} \tag{7.7}$$

for the regular wave contour plots. Unlike in the case of the contour plots of the K_d presented in Chapters 4 to 6, where the differences in the wave height chosen were not part of the analysis, in this chapter the difference is a representative of the wave climate. Therefore the non-dimensional K_d is not a sufficient assessment tool and the dimensional quantity $|\eta|$ is selected. Note that while the energy content of the $|\eta|$ for the same regular wave height and irregular significant wave height is not the same, we only compare the two for a qualitative and not quantitative analysis. As an example to highlight the differences in the areas of the hot spots and the wake zones between the two sets of cases investigated. Note that the area inside of the light orange boxes is the inner model coupling domain as explained in Section 7.3, and is shown for completeness only. In this study we do not consider the inner domain values in the analysis of the coupled wave field. This rule will apply to the contour plots presented in this and the subsequent section Section 7.7.

For the irregular wave results in Sections 7.7.1 to 7.7.3, the contour plots display the absolute value of the complex wave amplitude $|\eta_{irr}|$ given by:

$$|\eta|_{irr} = \frac{H_{m0,t}}{H_{m0,I}} \cdot \frac{H_{m0,I}}{2} = 2 \cdot \sqrt{\sum_{t}^{\Delta t} \eta_{irr}(x,y)_t^2 \cdot \frac{dt}{\Delta t}} \tag{7.8}$$

analogous with the regular wave $|\eta|$ given in Eq. (7.7). The inner NEMOH domain of the WEC arrays is shown by orange rectangles in all the contour plots of $|\eta|$. Note that the absolute value of the wave amplitudes $|\eta|$ demonstrated herein are not normalized by the incident waves to show the absolute difference in the three wave climates. Warm coloured areas indicate $|\eta|$ greater than the mean free surface elevation for a given H_{m0} while cold colours indicate wave elevations below the mean.

7.6 Results for a exploratory 2-array 10 OSWEC farm

As a first step to modelling the full 50 WEC farm in a 6.0 km by 2.0 km domain, a reduced size 10 WEC farm consisting of 2 WEC Arrays in a 1.0 km by 2.0 km domain is modelled for the same wave climate as the 50 WEC farm. The OSWEC array locations are at the same depths as the full scale farm modelled in Section 7.7 and are located at 15 m depth (front array) and 10 m (back array), maintaining the sloping profile of the full scale WEC farm domain. A schematic of the exploratory 10 OSWEC farm is shown in Section 7.6. Although there are considerable difference between regular and irregular wave results, as was shown for example in Section 4.9.4 in Chapter 4, the main features of the array effects of the WEC farm are apparent for a regular wave, particularly the influence of wave directionality.

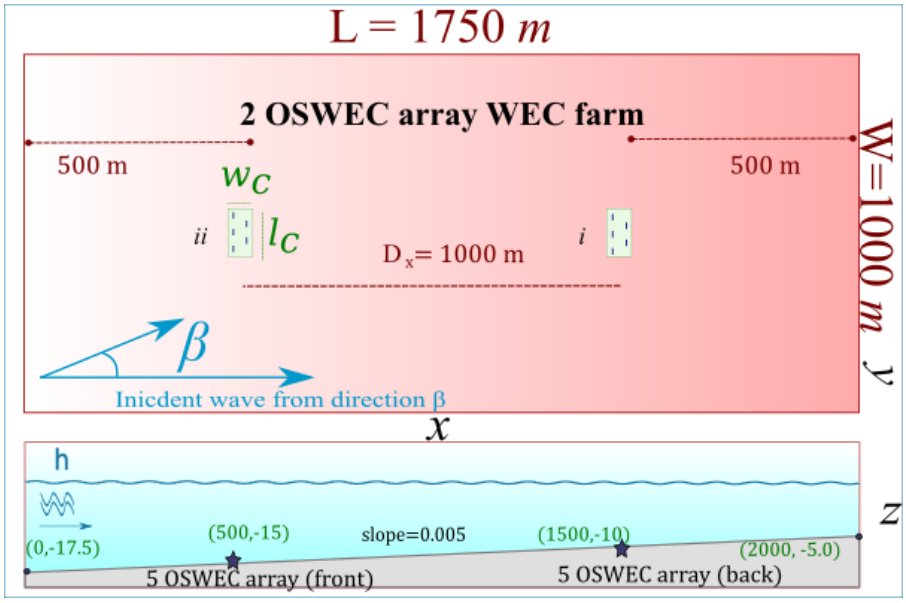

Figure 7.6: Exploratory 10 WEC farm for validation of the wave-to-wire model shown to scale. Top and side views

7.6.1 The 10-OSWEC farm η for a regular wave at $\beta = 0°$ incidence

The first result shown is a contour plot of $|\eta|$ for the regular wave of H $=$ 2 m and T$=$ 10 s, representative of the mean site wave climate with a $\beta = 0$ °, given in Table 7.2 in Section 7.3.1. Looking at Fig. 7.7, the first that is apparent is the very strong interference pattern between the two WEC arrays in the WEC farm. Analogous with the contour plots of the K_d in the previous chapters, there are areas of enhancement of $|\eta|$ or 'hot spots' and areas of reduction in $|\eta|$ which are referred to as the 'wake zone' or the zone of 'shadowing'. The largest wake zone is observed behind the front WEC array, that is the one which is located on the left side of the basin in water depth of 15 m. There is a large area of reduction of up to 40% of the incident wave field in a region several hundred meters behind the array location and extending to about twice the width of the WEC array in the y-direction. In contrast, behind the second WEC array one does not see such a pronounced wake zone, instead one observes a hot spot aligned with the x-axis. The primary reason for this discrepancy is that the back WEC array is located in a shallow region of only 10 m water depth. There is significant wave reflection behind it with the shallow bathymetry zone which one can infer from the profile in Section 7.6. In addition, as a consequence of the interaction of the refraction of the OSWEC arrays and the sloping shallow bathymetry, large areas of positive anomalies are found on the shoreward boundary at a vertical distance of 500 km away from the WEC array centres. Also note the significant interference

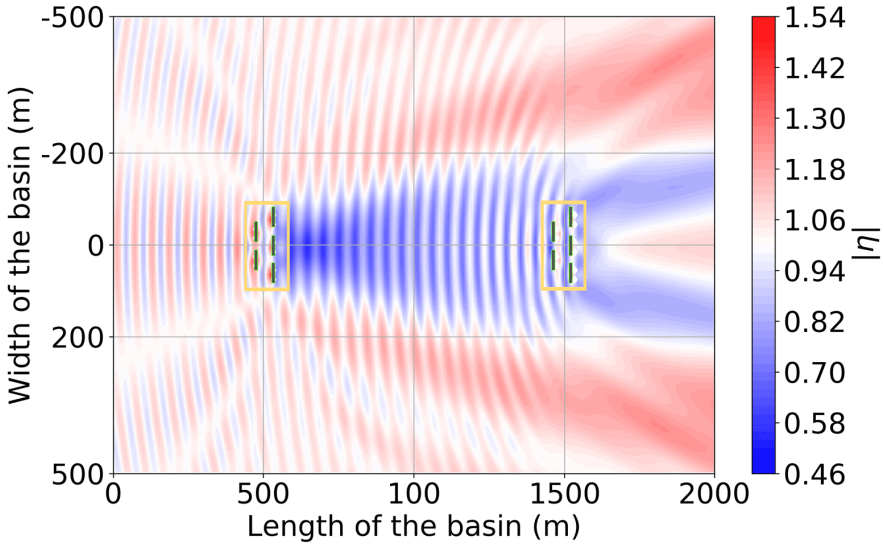

Figure 7.7: Coupled $|\eta|$ for H = 2.0, T = 10.0 s, and $\beta = 0$ ° for a 10 OSWEC 2-Array farm

effects between the perturbed waves of the WEC array and the incident wave that is manifested in the strong interference pattern between and seaward of the two OSWEC arrays.

7.6.2 The 10-OSWEC farm η for a regular wave at β = -24° incidence

The next scenario modelled is the 10-OSWEC farm displayed in Section 7.6 for H = 2 m and T = 10 s but with an incidence angle β = - 24°. This is the regular wave representative of the mean site conditions observed at the WEC array project site as detailed in Section 7.3.1. Again, as pointed out at the beginning of Section 7.6, the study models this scenario to highlight the difference in the behaviour of a WEC farm aligned with the incoming incident wave versus one that is off-angle, such as the case for the average wave climate of the investigated WEC farm project site.

As expected, the observed total $|\eta|$ in Fig. 7.8 is quite different from the one shown in Fig. 7.7. Note the asymmetry in the interference patterns and the areas of positive versus negative anomalies. One sees that the majority of the area below the y-axis is a wake zone, while above the y-axis there is a large area of hotspots with an increase in $|\eta|$ close to 20% as one moves toward the shallower region on the right side of the domain. Naturally this is due to the wave incidence angle of β = -24 °, in which one would expect most of the reduction in $|\eta|$ from the WEC arrays to occur on the left bottom side, opposite the wave incidence. Yet

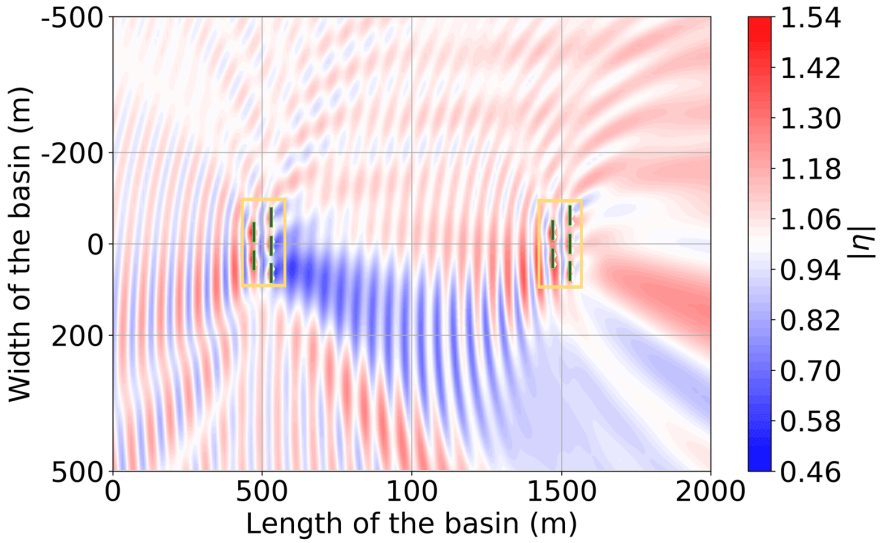

Figure 7.8: Coupled absolute total wave amplitude $|\eta|$ for H = 2.0 m , T = 10.0 s and β = -24 ° for a 10 OSWEC 2-array farm over the sloping bathymetry shown in Section 7.6.

the pattern is complicated by the fact that there is significant reflection from the OSWECs which also creates the strong 'rays' of interference at an angle 90 ° counter-clockwise from the incidence. β in the modelled case is approximately equal to β = -110 °. Note that the maximum enhancement in η is greater than β = 0° case in Section 7.6.1 but that the area of such enhancement is very limited, negating the possibility of using this fact for an optimal positioning of WECs. As one witnesses in Section 7.6.3 in the complementary results for the irregular wave case, this constructive interference is nearly absent. This fact has significant consequence for the power output of WEC arrays in a WEC farm with angled incidence waves. The power output of the WEC array will be reflected at incidence angles different from those wave incidence as the authors will see for the full WEC farm results with off-axis incidence angles β in Section 7.7.4.

7.6.3 The 10-OSWEC farm η for an irregular wave at $\beta = 0°$ incidence

In this section we present the irregular wave results for the same modelling scenario introduced in the previous Sections 7.6.1 and 7.6.2, where the regular wave of H = 2 m T = 10 is substituted by an irregular wave with a H_{m0} = 2 m and T_p = 10 s, where the frequency distribution given by the Pierson-Moskowitz parametrization given in Eq. (3.53). One can observe the significant differences between the results presented herein and the regular wave results of Section 7.6.1. Firstly, the strong pattern of constructive and destructive interference is greatly reduced, owing to

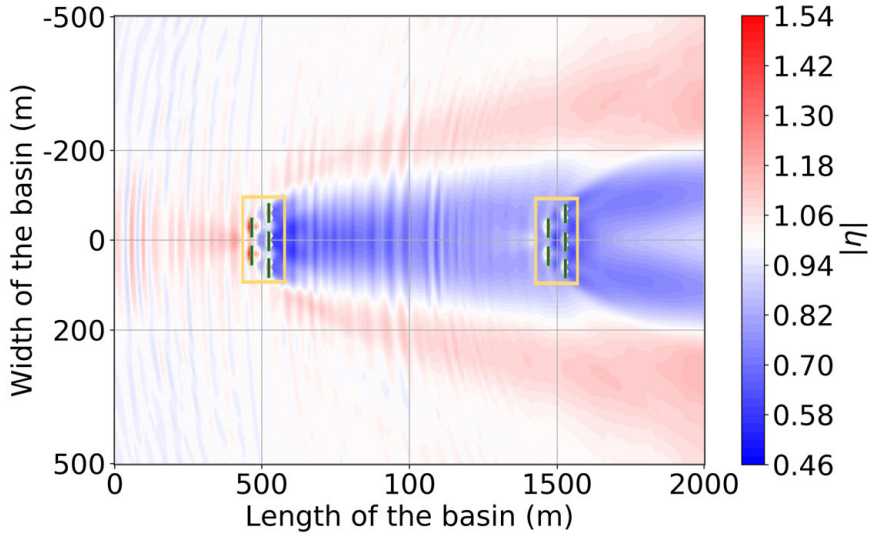

Figure 7.9: Coupled total wave amplitude$|\eta|$ for H_s = 2.0 m, T_p = 10.0 s and $\beta = 0$ ° regular wave for a 10 WEC 2-Array farm over a sloping bathymetry shown in Section 7.6.

the smoothing effect of the multi-frequency sea state. Furthermore, there is a significant reduction in the magnitude of the 'hot spots', particularly one in the lee of the 2 WEC arrays at the x-axis. The wake zones, meanwhile, wave not reduced in magnitude or extent, but in fact have a more extensive area of reduced $|\eta|$. This phenomenon is part of the reason that one sees a near-field influence of constructive influence on the power output for the OSWEC farm modelled in the full scale farm results in Section 7.7.4.

7.6.4 The 10-OSWEC farm η for an irregular wave at β = -24° incidence

Analogous with the comparison made in the previous Section 7.6.3 between the regular and irregular results for $\beta = 0°$, the qualitative differences between the $\beta = 24°$ results for regular and irregular waves are significant. In Fig. 7.10 one can observe that the majority of the domain is either in a neutral zone, that is no change in the η due to array effects, or indeed in the wake zone. Note how the strong wave reflection that is so prominent to the left bottom side of the OSWEC arrays is absent in the irregular wave results. This outcome is due to the fact that the OSWEC is much more reflective to a single component T = 10 s wave than a multi-frequency T_p = 10 s wave. As in the regular wave case one sees a skewing of the wake zone, where the back WEC array is not any more in the wake zone of the front one as in Fig. 7.7. This is a potential benefit for a aligned WEC farm configuration such as the one presented here. The results will be mirrored in the

values of the power output exhibited in Tables 7.5 to 7.7.

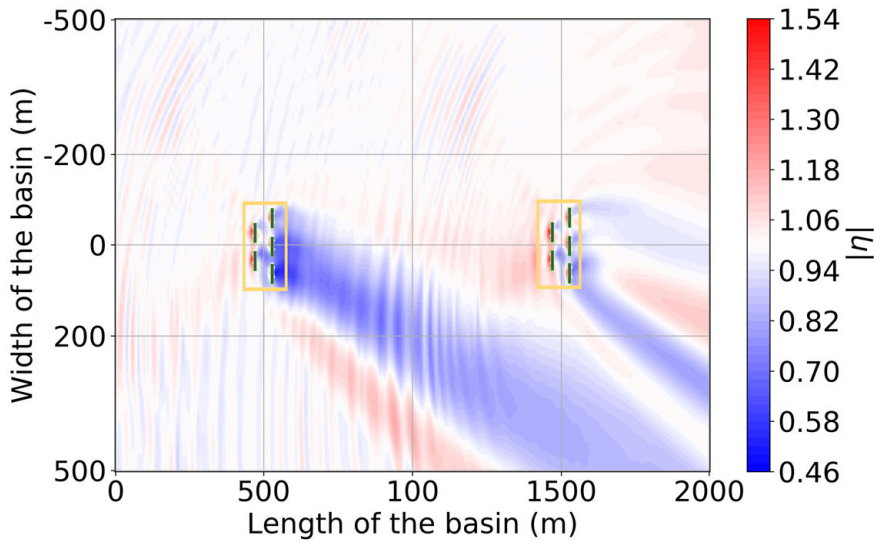

Figure 7.10: Coupled $|\eta|$ for H = 2.0 T = 10.0 s and β = -24 ° regular wave for a 10 WEC 2-Array farm over a sloping bathymetry shown in Section 7.6.

7.7 Results for a 10-array 50-WEC farm

In this section we demonstrate the key results of the chapter: the wave field and the power output of the 50 WEC farm which is illustrated in Fig. 7.4. The total size of the modelled domain is 6 km by 2 km, with the depth ranging from 35 m on the left or seaward side to 5 m on the right or shoreward side. In subsections Sections 7.7.1 to 7.7.3 the mean $|\eta_{irr}|$ for the three seasonal wave climates of Section 7.3.1 is displayed in Figs. 7.11 to 7.13. Then the nominal power output of the WEC farm is presented in Tables 7.5 to 7.7 in Section 7.7.4. A short discussion on the relative power output is given in Section 7.7.6.

7.7.1 The 50-OSWEC farm η for a the site winter climate

The coupled values of the total $|\eta|$ for the mean site winter wave climate of H_{m0} = 2.55 m, T_p = 11.71 s, and β = -20 ° are shown for the WEC farm domain in Fig. 7.11. The first effect one notices from the contour plot, Fig. 7.11, is the large wake zone behind the 1st and the 2nd row of the WEC farm. In contrast with the regular wave case for the small WEC farm presented in Figs. 7.7 and 7.8, but mirroring the small basin irregular wave results in Figs. 7.9 and 7.10, there are almost no areas of hot spots. Instead one finds only a narrow band of positive η

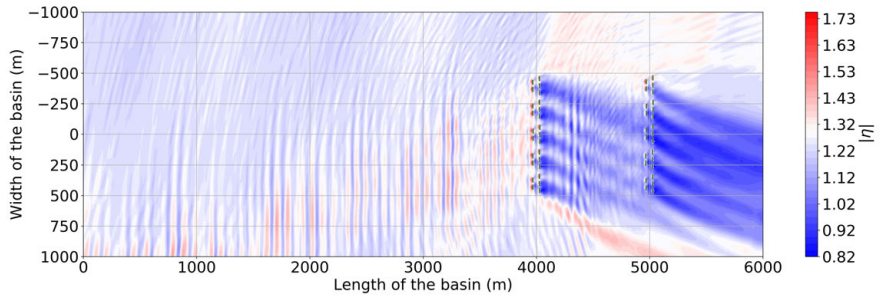

Figure 7.11: Coupled total $|\eta|$ for the mean winter wave H_{m0} = 2.55 m, T_p = 11.71 s, and β = -20 ° for a 50 WEC 10-Array farm.

anomalies parallel to the wave incidence of β = -20° from the front WEC array row. The wake zone, however is extensive: the average wave amplitude at nearly all of the shore side (left hand side) domain boundary is reduced by roughly 0.4 m, which is nearly 25 % of the incoming H_{m0} of 2.55 m. Also, note that for this particular wave angle, the alignment of the WEC arrays is such that the wake zones extending from the 1st WEC array row are shadowing the lower placed second row array. The reader shall see this effect reflected in the values of the power output displayed in Tables 7.5 to 7.7. Notice that the shoaling effect such as that observed for the regular wave case in the small domain in Figs. 7.7 and 7.8, is dominated by the significant shadowing of the WEC farm. In this case a slight enhancement of $|\eta|$ due to this effect is only observed in the upper right side of the domain, where the influence of the WEC farm is minimized.

7.7.2 The 50-OSWEC farm η for a the site summer climate

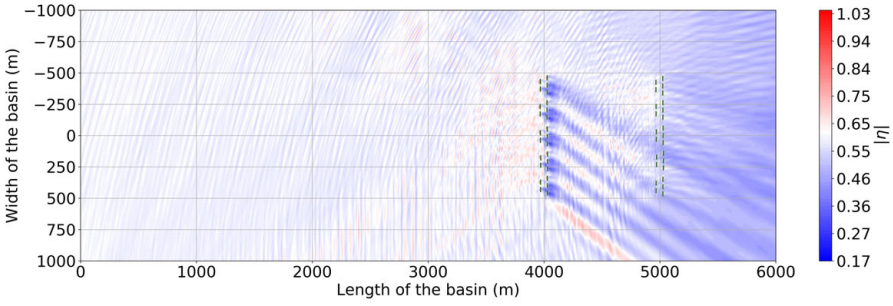

Figure 7.12: Coupled total $|\eta|$ for the mean summer wave H_{m0} = 1.20 m , T_p = 8.71 s, and β = -30 ° for a 50 WEC 10-Array farm

When we study the total coupled absolute wave amplitude $|\eta|$ for the summer climate in Fig. 7.12, it is striking to observe that nearly the entire domain is an

area of negative anomalies in η. Because the summer mean peak wave period T_p = 8.71 s, the shoaling effects of the decreasing water depth are minimal. Therefore the overriding effect on the shore side boundary is a decrease in η of 0.10 m to 0.15 m off the mean incident η of 0.6 m, which is approximately equal to a 15% to 20% reduction in the mean η. Interestingly, for the modelled wave incidence of β = -30°, in contrast with the scenario presented in Fig. 7.11, in Section 7.7.1, the back array is aligned with the positive regions of interference behind the front row. This indicates that for the particular wave incidence, the placing of the arrays in the WEC farm is advantageous from the point of view of WEC farm power output. Indeed, observe that the back row value of the power output for the summer climate case in Table 7.6 is 0.10 m higher than for the other two wave climates. Likewise, for the smaller wavelength modelled in this scenario, the interference patterns are nearly averaged out, in contrast to the more apparent one in Fig. 7.11 or in Fig. 7.13.

7.7.3 The 50-OSWEC farm η for a the autumn wave climate

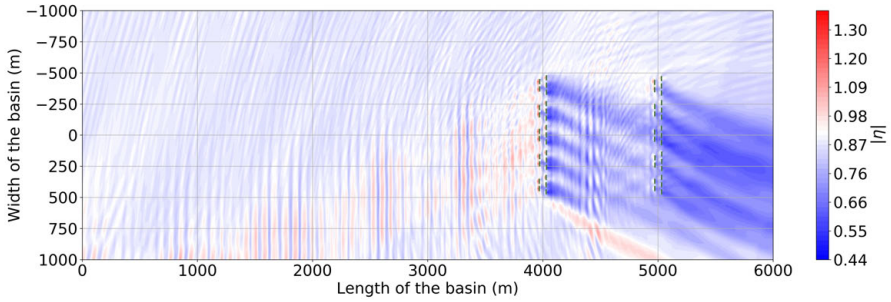

Figure 7.13: Coupled total $|\eta|$ for the mean autumn wave H_{m0} = 1.80 m , T_p = 10.54 s, and β = -22 ° for a 50 WEC 10-Array farm.

Finally, the contour plot of the mean η in Fig. 7.13 for the autumn mean wave climate, with H_{m0} = 1.71 m, T_p = 10.54 s, and a β = -22 °, presents a picture very similar to the results for the winter that was exhibited in Fig. 7.11 in Section 7.7.1. However, a close observation will highlight some discrepancies. Notably, the near-shore positive anomalies in η due to the shoaling effect are significant for the winter wave climate while for the autumn wave climate in Fig. 7.13 there is no appreciable positive anomaly in η in the same region. Observe also that the slight change in the incidence β of 2 ° from the winter case modifies the shoaling effect of the front WEC farm row on the back, but that the overall effect is still negative as observed in similar reduced values of the power output of the back OSWEC array row in Tables 7.5 and 7.7. Moreover, observe the reflected zone of mostly positive interference that is reflected of the front WEC array row at a β approximately equal to -120 °. While this reflection is not as large in magnitude as the one which is observed for the winter climate case in Fig. 7.11, it is still appreciable in contrast to its absence for the summer climate of Fig. 7.12. And finally, note the near absence

of the shoaling effect, indicating that for this wave incidence of $T_p = 10.54$ s, it is not significant enough to influence the 'wake zone' at the shore boundary.

7.7.4 The power output of a 10 Array 50 WEC farm for the seasonal wave climate

It was shown how the wave field is modified in the presence of the 10 WEC arrays in Figs. 7.11 and 7.13 and Section 7.7.2 for the three modelled scenarios of Table 7.3 in Section 7.7. Now we turn the attention to the how the changes in the wave field are reflected in the power absorption of a 50 WEC farm in a realistic operating environment. We calculate the power for each array consisting of 5 OSWECs for the three irregular sea states displayed in Tables 7.5 to 7.7, using Eq. (7.5). The results are displayed by back and front row.

The first thing we observe in all three tables is the asymmetry in power output due to the off-axis angle of incidence β for the modelled wave climates. Observe that in all three cases the power output from the front row is greater than that of the back row, yet the constant of proportionality in the difference is not the same across the three simulated cases. As was referred to in Section 7.7, this disparity is due to the interplay of the array row side to side separation and the wave incidence angle β for the three cases. Also observe that for the irregular wave cases studied, the location of the back array in shallower water does not compensate for the reduction due to the presence of the front row. That is the shoaling effect which increases the wave amplitude driving the power output cannot overcome the significant shadowing imparted by the front row array of OSWECs. In looking at the difference between adjacent rows of WEC arrays, that is along the y-axis, we can see a slight attenuation in the power output as we move from the outer arrays to the inner most ones, but observe that this decrease is not symmetrical. In the values of the individual WEC array power output, the two arrays down-angle from the wave incidence, that is WEC arrays *v* and *x* are the most shadowed, while for certain wave scenarios, the counterpart arrays *i* and *vi* are in fact producing power nearly equal or slightly above the mean.

Therefore, the power output values indicate that the WEC farm configuration where the front and back rows are separated by only 1 km are detrimental to the power performance, and an alternative configuration might be preferred. At the same time, the total WEC farm power output is quite high for all the three wave climates compared to the analogue maximum stated commercial OSWEC power rating (AW-Energy Oy, 2019) of 1000kW per WEC. This indicates a good match between the target OSWEC performance and the site wave climate. As is expected, the summer total is the lowest. This is expected of the highly variable North Atlantic wave climate, and it indicates the need to study seasonality in the WEC farm power output as opposed to using a mean annual value. Based on the somewhat limited parametrization presented in Tables 7.5 to 7.7, we can observe the complicated interplay between the wave climate and the various scales present in a large WEC farm.

7.7.5 The nominal power output of a 10 Array 50 OSWEC farm for the seasonal wave climate

The first thing one observes in all three tables, Tables 7.5 and 7.7, is the asymmetry in power output due to the off-axis angle of incidence β for the modelled wave climates. Notice that in all three cases the power output from the front row is greater than that of the back WEC array row, yet the constant of proportionality in the difference is not the same across the three simulated cases. As was referred to in Section 7.7, this disparity is due to the interplay of the WEC array row side-to-side separation and the wave incidence angle β for the three cases. Also observe that for the irregular wave cases studied, the location of the back array in shallower water does not compensate for the reduction due to the presence of the front WEC array row. That is the shoaling effect which increases the wave amplitude driving the power output cannot overcome the significant reduction in η imparted by the front row array of OSWECs. In looking at the difference between adjacent rows of WEC arrays, that is along the y-axis, one can see an attenuation in the power output as one moves from the outer arrays to the inner most ones for the winter and autumn cases in Tables 7.5 and 7.7. Yet this is a uniform decrease as one moves down the y-axis for the summer power output in Table 7.6. This disparity is chiefly due to the 10° higher wave incidence β for the summer climate.

Studying the values of the individual WEC array power output, the two arrays down-angle from the wave incidence, that is WEC arrays *ix* and *x* are the most shadowed, while for certain wave scenarios, the respective arrays on the positive y-axis side of the farm, *i* and *ii*, are in fact producing power nearly equal or slightly above the mean. In terms of the overall power output, one sees a slight reduction between the winter and the autumn values, but a significant reduction in the summer values compared to the winter power. This is expected of the highly variable North Atlantic wave climate, and it indicates the need to study seasonality in the WEC farm power output as opposed to using a mean annual value.

Table 7.5: Power output in kW for the 50 OSWEC farm for an irregular wave of H_{m0} = 2.55 m and T_p = 11.71 s. Wave incidence angle β = -20 °. Wave climate based on the 9-year site winter mean.

Array i **Array vi**	**Array ii** **Array vii**	**Array iii** **Array viii**	**Array iv** **Array ix**	**Array v** **Array x**	$\mathbf{P}_{farm}$ **per row [kW]**	$\mathbf{P}_{farm}$ **[kW]**
743.1	774.8	772.8	744.3	733.8	3769	
771.6	620.8	546.9	586.0	567.4	3093	6861
					CWR_{farm}	0.18

7.7.6 Relative Power Output of the 50-WEC Farm

In addition to looking at the absolute power values in Tables 7.5–7.7, it is also useful to look at the relative differences in the power output in terms of the CWR as defined by Eq. (3.79). Remark that in this chapter we are looking at the CWR of the WEC farm. Therefore, the W is taken as 1 km, which is the total width

Table 7.6: Power output in kW for the 50 OSWEC farm for an irregular wave of H_{m0} = 1.2 m and T_p = 8.71 s. Wave incidence angle β = -30 °. Wave climate based on the 9-year site summer mean.

Array i Array vi	Array ii Array vii	Array iii Array viii	Array iv Array ix	Array v Array x	$\mathbf{P}_{farm}$ per row [kW]	$\mathbf{P}_{farm}$ [kW]
300.7	309.5	306.7	313.5	302.5	1533	
241.3	244.4	243.8	296.7	296.9	1323	2856
					CWR_{farm}	0.46

Table 7.7: Power output in kW for the 50 WEC farm for an irregular wave of H_{m0} = 1.80 m and T_p = 10.54 s. Wave incidence angle β = -22 °. Wave climate based on the 9-year site autumn mean.

Array i Array vi	Array ii Array vii	Array iii Array viii	Array iv Array ix	Array v Array x	$\mathbf{P}_{farm}$ per row [kW]	$\mathbf{P}_{farm}$ [kW]
686.7	699.6	705.8	708.3	698.8	3499	
699.34	593	498.44	561.49	546.08	2898	6398
					CWR_{farm}	0.38

of the WEC farm relative to the coast as witnessed in Fig. 7.4. Naturally, this is different from the results presented in Section 6.5.4 where the CWR was for the array only and did not include the inter-array spacing. Consequently, one expects the CWR for the WEC farm to be lower than for the WEC array and that is indeed what is seen when the CWR in Tables 6.7 and 6.8 are compared to the CWR in Tables 7.5 to 7.7.

Notice that the highest CWR = 0.46 is for the summer wave climates, which is when the total power output is in fact the lowest, as seen in Section 7.7.5. The winter CWR is by contrast the lowest at 0.18. Despite the higher nominal power, the relative performance of the OSWEC farm is decreased for the higher wave height and period representative of this wave climate. The autumn value of 0.38 is closer to the summer value, indicating that despite the greater overall energy in the incident waves compared with the summer, the OSWEC is able to extract an appreciable amount of power from the incident waves. This is a good result from the standpoint of the WEC farm economics, as this would tend to slightly improve the performance in what are typically the lower power output periods of the year.

At the same time, one must take note of the fact that CWR is not an ideal measurement tool for the presented case. As pointed out in the previous paragraph, W includes empty space in between the WEC arrays that is not account in the CWR. Furthermore, the WEC farm consists of two parallel rows of WEC arrays, and the point at which the measurement of the wave power is taken has to be taken into consideration. In this chapter the total power is taken at the ocean side of the domain (l.h.s. in Fig. 7.4). As is discussed in Section 7.8

7.8 Discussion

From the contour plots of $|\eta|$ given in Figs. 7.11 to 7.13 and power output results in Tables 7.5 to 7.7 in Section 7.7.4 we can see the importance of looking at both the near-field and the far-field effects in analysing the WEC farm. The former are key in determining the WEC farm power output, as the power of each WEC array is determined by its constituent devices' motions that are in turn proportional to the perturbed wave field. We have seen that a slight change in the incoming incidence angle from $\beta = 0°$ to $\beta =$ -20 ° has an appreciable impact on the WEC farm performance such as the difference in the power output between Tables 7.5 and 7.7 and Table 7.6. In effect, this shift in the wave angle renders the present configuration more staggered which is of net benefit to the WEC farm performance because of decreased shadowing in the back row.

Looking at the shore side, the far-field effects that are necessary to assess the impact on the coastal zone down-wave of the modelled WEC farm, one sees a pronounced difference between the winter and summer climates, but a much lesser discrepancy between the winter and autumn. This difference is due to both the wave height and wave period of the winter and autumn waves, but also the difference of 10° in the wave incidence angle β plays a role by modulating the effect of the front row of OSWECs on the back row. Because of shoaling effects that impact the higher wave period components of the $H_{m0} = 2.5$ m, $T_p = 11.71$ s wave, the area and the magnitude of the 'wake zone' of the 50 WEC farm is slightly reduced compared with the smaller wave period autumn wave. The shoaling effect is completely absent with the summer waves of $H_{m0} = 1.20$ m and $T_p = 8.71$ s, where the reduction in the η is nearly uniform at 15-20% on the shoreward boundary of the modelled domain. There is no appreciable increase in $|\eta|$ as one moves into the shallower zone of the domain. This is a key result of the work that indicates that the near-shore impact area of a OSWEC farm is more dependent on the incidence wave angles than on the changing bathymetry. One would not intuitively arrive at this fact from a study that does not take changing incidence angle β and the bathymetry into account. In contrast, the total wave field up-wave of the WEC farm differs between the three incidence angles, yet the small magnitude of these effects and the lesser strategic importance of offshore zones for most coastal areas means that quantifying them is of less importance to the WEC farm developer.

Most economic studies conclude that a large number of WECs must be aggregated in a small area in order for them to be economical. Many investigations have been performed to date exploring the optimal configuration of WEC farms or arrays, for example (Child and Venugopal, 2010; de Andrés et al., 2014; Sharp and DuPont, 2016), yet most of them have focused on a WEC array of a few buoys. The few that did, such as (McNatt et al., 2015), did not investigate WEC farms over variable bathymetry. Furthermore, an analysis with a real wave climate such as performed in this investigation, has hitherto been performed only for the calculation of economic variables, such as by de Andrés et al. (2014), but not for the near-field effects. Conversely, investigations such as Rijnsdorp et al. (2017), calculate the near-field effects in a WEC array but do not have the coupling with a

motion solver which can accurately calculate the power output of the WEC array using a realistic PTO. Although an optimization scheme can be set up that takes a large number of individual WECs as inputs, such as the parametric optimization study (Ruiz et al., 2017b), for large numbers of WECs such a study is still numerically expensive, especially for WECs whose hydrodynamic parameters cannot be simplified analytically. Moreover, even if such an optimization is performed, these results are often hard to intuit because of the many variable inputs involved in the optimization of a WEC farm that are hard to connect to the outcome. Accordingly, the simplifying approach the investigation employ, not only reduces the time of calculation by *a priori* grouping WECs in clusters that the authors term arrays, but also provide an intuitive link between WEC farm layout and the power output. The link between the two is via the perturbed wave field. Because the most important constructive and destructive effects in the WEC farm are of the 1st order, the approach presented in this study can be utilized to make a rapid visual assessment of various WEC farm configurations.

7.8.1 A note on the computational time

Several remarks can be made about the computational time of the various components of the W2W wire model presented in this chapter, and more broadly in this thesis. All the simulations have been performed using 10 cores (Intel(R) Core(TM) i7-8700 CPU@3.2GHz).

It can be observed that in NEMOH, simulations with a single body are solved rapidly, within minutes. However when the number of bodies, $\mathcal{M}$, and frequency components, N is increased, the computational time increases rapidly. For the 5-OSWEC arrays simulated in this chapter, the computational time is 2 hours for $N = 20$.

The simulation times in WEC-Sim greatly depend on the PTO type modelled. For the linear PTO given in Chapter 6, each WEC takes approximately 5 minutes to simulate. For the hydraulic PTO the results is considerably longer, with a 20 minute simulation time. Since each frequency is coupled separately, as N increases the calculation time can become burdensome. For the hydraulic PTO simulation with $N = 20$, the total WEC-Sim simulation time is approximately 3 hours.

In the MILDwave domain, the number of bodies present does not affect the computational time, however, the simulation duration is directly to the grid resolution and the total domain size. Moreover, the computational time increase in MILDwave is not as significant as the increase observed in NEMOH when modelling multiple frequencies. In terms of computational effort therefore, NEMOH can become a limiting factor of the coupled model when large WEC arrays need to be studied. Hence the benefit of the multiple coupling zone approach introduced in Chapter 5 and fully developed in this chapter. With the grid resolution set to $\delta x = \delta y \equiv 5m$, and $N = 20$, for the small domain of 1 km by 2 km the MILDwave runtime is approximately 1 hour while for the large 6 km by 2 km domain shown the comparable time is 6 hours.

Considering the fine grid cell size resolution that has been used to perform the numerical validation, it is concluded that the MILDwave-NEMOH coupled model

is a cost-efficient numerical tool for the estimation of "far field" effects. The MILDwave-NEMOH coupled model will perform simulations at a higher computational time than phase-averaged wave propagation models in trade-off a better representation of the hydrodynamics and wave transformations around the WEC array. In relation with phase-resolving wave propagation models the MILDwave-NEMOH coupled model will provide high speed solution as MILDwave is an efficient tool providing accurate results in cases that non-linear effects are not important

Looking at the coupled model algorithm it can be seen that three different simulations are performed. Consequently, when studying possible WEC array deployment locations at a specific water depths at a coastal area, it is possible to perform one NEMOH simulation and one WEC-Sim run, one incident wave run in MILDwave, and several perturbed wave runs in MILDwave. If the modelled depth in NEMOH is the same for various coupling zones, as is the case in the simulations herein, then only one NEMOH and one WEC-Sim run is needed for the W2W model. This results in an additional decrease in the calculation time for a large array.

Moreover, the coupled model algorithm has been parallelized,which allows for the use of High Performance Clusters to perform high computational time simulations like irregular short-crested waves over coastal areas. This will result on even faster simulations using the MILDwave-NEMOH coupled model.

7.9 Conclusions

In this chapter we have calculated the perturbed wave fields and analysed the power output of a conceptual 50 OSWEC farm using W2W model with a coupling between a BEM solver, a PTO simulator, and a wave propagation model in a real wave climate and an actual depth profile off the west coast of Bretagne, France. In Section 7.6, in a small domain with a shallow sloping sea bottom ranging from 17.5 m to 5 m, we observed how the wave field of a 10 OSWEC farm is influenced by the change in the wave incidence angle β. In the small basin results was seen that the incident wave angle plays a very important role in determining the wave fields and that the shoaling effects are of negligible importance at the simulated depths for the incident wave height $H_{m0} = 1.2$ and $T_p = 8.71$ s. We have also demonstrated that significant wake effects can extend out to a more than 1 km or over 12 wavelengths behind the arrays, even for a small wave farm of only 10 OSWECs. Even though the effect of the simulated WEC farm configuration on the power output is mostly negative, as witnessed in the values of the power output in Tables 7.5 to 7.7, the relative placement of the WEC arrays is still of utmost importance as the difference in power output of the most shadowed arrays and the least shadowed is nearly 30%. Our analysis indicates that for the particular OSWEC technology simulated, with the restriction on deployment water depth, an aligned two WEC array row solution might not be the optimal solution. The rows are too close together to allow for the recovery of the wave incidence behind the front row to benefit the back row. An alternative might be to stagger the WEC arrays or even place them side-by-side in a line. Yet, this solution entails a much

greater use of sea space, which might not be feasible for the project developers given area lease restrictions. Ultimately, the optimal solution will emerge for an analysis of various operating scenarios given the site characteristics such as those in Sections 7.2.1 to 7.2.3 for the WATTMOR project site in Bretagne.

More generally, the results of this chapter demonstrate the need to simulate a changing sea bottom and a real wave climate in the modelling of the near-shore effects of a WEC farm. It has been chosen to place the WECs in relatively shallow water because of the restrictions of the OSWEC technology proposed for the site. The location bathymetry determined a very gradual slope of 0.005. Still, if one had determined to model WECs at different depths and with a steeper slope, the effect of a sloping bathymetry would have been significant in terms of both the power output and the near field interaction with the steep slope. The flexibility of the hybrid methodology of this thesis allows us to calculate such scenarios with, unlike those models which require that the bottom water depth is constant. The inclusion of a Wave Structure Interaction (WSI) and a PTO simulator allows us to map the economics of a WEC farm project on top of the expected environmental impacts. This further increases the usefulness of the herein introduced W2W model. Further investigation will focus on refining the methodology for a real bathymetry and for other types of WECs that will have a different impact on the near-shore zone then the OSWECs modelled in this investigation.

Chapter 8

Conclusions and Further Work

In this work, a coupled model suite has been introduced to model WEC arrays with realistic Power Take-off (PTO) systems. With the coupling methodology underlying the numerical models, the thesis addresses key knowledge gaps with regards to numerical modelling of arrays of Wave Energy Converters (WECs), namely the possibility of accurately modelling the economic and environmental impacts of a WEC array project in a timely and computationally cost-effective manner. The inclusion of a PTO system module in the coupled numerical model suite addresses a key source of uncertainty in present WEC array models by allowing the simulation of any PTO which can be in the Matlab Simulink® environment.

8.1 Contribution of Thesis

The main contributions made by this thesis are listed below in order of completion:

1. A novel coupling methodology combining a Boundary Element Method (BEM) wave structure interaction solver and a Mild-slope wave propagation model. The contribution of the present thesis consists of an expansion of the capabilities of the Mild-slope propagation model and the inclusion of multiple coupling zones in the outer domain model.

2. An application of the novel coupling methodology to resolve the WEC 'array effects' via an original iterative method.

3. An implementation of the above two items in the calculation of the power output of a WEC farm.

4. Integration of a time-domain Power Take-off (PTO) solver into the calculations in the above two items allowing the modelling of realistic PTO systems.

5. Definition of the notion of 'WEC array hydrodynamic independence' in a WEC farm, analogous to 'WEC hydrodynamic independence' in a WEC array. The 'independence' signifies that the magnitude of potential hydrodynamic interactions is below a 5% threshold allowing for a significant reduction in the calculation time of the WEC array power and wave field.

6. A wave-to-wire (W2W) coupled model suite including the wave structure interaction (WSI) solver, the PTO solver, and the mild-slope wave propagation model which allows for the efficient calculation of array effects in medium to large WEC farms with realistic PTO systems.

7. An application of the W2W model to a proposed WEC array project consisting of a WEC farm of 50 OSWECs. The W2W model is used to investigate the role of the interplay between the site wave climate, realistic bathymetry, and the WEC farm power output as well as examine impacts on the surrounding area via an analysis of the WEC farm wave field.

8. A robust and user-friendly script for running the W2W mode in the Python scientific computing platform.

8.2 Summary of Principal Findings

The principle findings of the thesis centre on the notion of a balance between the accuracy of the numerical calculation of the 'array effects' in a WEC array for the purposes of estimating the power output and by extension the economic profitability of a WEC array project, and the study of the environmental impacts of such an array on a wider coastal area. To date a majority of numerical models have been utilized with exclusively pursuing either the first or the second goal. Yet because the power economic and environmental impacts are linked through the wave field modification created by the presence of the hydrodynamically interacting WECs in a WEC array, the two objectives cannot be separated. In other words, an ideal model should be able to simultaneously resolve the two objectives, preferably in a time and computationally efficient manner.

Although the recent increases in computer power, specifically Graphical Processing Units (GPUs), have greatly increased the applicability of non-linear models to solving various classes of hydrodynamic problems, it is still the case that WEC array problem presents a formidable challenge in terms of processing capacity. Therefore the vast majority of WEC array models are linear, moreover, the models which accurately resolve the near-field effects cannot be reasonably run in large

domains that are needed to assess the far-field effects. They in turn constitute any potential environmental impacts of the WEC array on the surrounding sea and coastal area.

It was decided therefore, in the work of this thesis, to pursue a hybrid strategy of coupling a high definition numerical wave-structure interaction solver to resolve the near-field effects and a lower definition wave propagation model to simulate the far-field effects. In addition, the WSI solver was integrated with a time-domain module allowing for power calculation of WEC arrays with realistic PTO systems. The three modules were joined into a complete wave-to-wire model with the hybrid objective of assessing the calculation of both the economic and environmental impacts of a WEC array project.

Such a hybrid approach allows the user to produce modelling results that play on the strengths of both models while minimizing the weaknesses, namely, the inability of a wave-structure solver to model large domains in a reasonable time frame and computational costs, and the low capacity of wave propagation models to resolve near-field wave structure interaction which determines the power output of WECs in an array. Finally, the third piece of the coupled model suite, the time-domain PTO solver, addresses a key shortcoming of the other parts, namely its ability to model time-variant processes such as a non-linear PTO system. In this thesis an implementation of the PTO module was performed to simulate a hydraulic PTO, the most frequently encountered and commercially viable PTO system in the current generation of WECs and an example of system with a non-linear response.

Through the application of the different parts of the W2W model, various facets of the WEC array problem were explored:

1. In Chapter 4, the impact of varying the number of WECs in an array on the near-field η was investigated. It was found that the greatest modifications in the wave field K_d occurred for simulation periods close to the chosen WEC resonance, given a simplified PTO system.

2. In Chapter 5, the principles of WEC array hydrodynamic analysis were applied to WEC farms consisting of multiple WEC arrays. Using a similarity principle, the relative magnitude of WEC array effects between disparate WEC arrays in a WEC farm was studied. It was found that the influence of WEC array separation distance D_1 was the primary determinant in inter-array effects.

3. The notion of WEC array hydrodynamic independence was defined for WEC arrays in a WEC farm in Chapter 5. It was concluded that for the heaving cylindrical WEC investigated, in a majority of the wave conditions WEC separation distances D_1 the WEC arrays can be treated as hydrodynamically independent.

4. In Chapter 6, a time-domain PTO module developed in the Matlab Simulink ® environment was integrated into the coupled model suite.

5. The effect of a linear PTO versus a hydraulic PTO on the power output and WEC arrays near-field was explored using the coupled PTO module-WSI

solver. In regular waves, the effect of the hydraulic PTO was found to have a greater impact on the power output than on the near-field K_d.

6. The difference in the array effects between a heaving cylindrical WEC and an OSWEC operating in shallow water conditions was explored. The magnitude of the effects of the OSWECs on the wave field were found to be significance greater.

7. In Chapter 7, the effects of a real spectral wave climate on the power output and the near- and far-field $|\eta|$ were illustrated.

8. Wave directionality effects on a medium size near-shore WEC farm of OSWECs were investigated in Chapter 7. It was found that the while the power output of the OSWECs was not significantly diminished, the area of strongest wake effects was displaced away from the WEC farm area on the coast.

9. The interactions of a the array effects of a medium size WEC farm with real bathymetry were elucidated. It was found that for a gently sloping depth profile of .005, the shoaling effects were much less than the shadowing effects of the OSWEC arrays, for the studied wave cliamte.

10. Utilizing the developed W2W model, the economic and environmental implications of a real WEC array projects were explored in Chapter 7. While a connection between the power output of an OSWEC farm and the magnitude and extent of the near- and far-field effects exits, it was determined that the link is not linear, due to the interplay of radiation and diffraction effects.

8.3 Recommendations for Future Research

The wave-to-wire (W2W) model consisting of the coupling methodology developed in this thesis has greatly extended the possibilities for WEC array and WEC farm modelling, and has significantly reduced the necessary computational effort to perform accurate wave-structure interaction simulations. Yet the linear W2W model introduced herein is only a first step in the development of a robust and versatile WEC array modelling tool that can be used to assess the economic and environmental impacts of a WEC array project. Specifically five key developments would provide a quantum leap in the accuracy and applicability of the considered W2W model.

1. Update of the capabilities of the WSI solver.

   The W2W model currently runs the linear BEM solver NEMOH to resolve the hydrodynamics of individual WECs. While this is sufficient to ascertain array effects in operation conditions, the modelling of extreme conditions which violate the restrictions of Potential Flow Theory requires the capability to model non-linear hydrodynamics.

A possible first step is the modelling of non-linear Froude-Krylov forces and viscous effects in a so-called non-linear BEM, which is a partial non-linear extension of linear BEM (Penalba and Ringwood, 2019). Two possible candidates for non-linear expansion are Froude-Krylov forces that were found to be the primary source of non-linearities in the modelling of heaving cylindrical WEC, and the simulating of viscous effects which are primary sources of non-linearities in simulating OSWECs (Giorgi and Ringwood, 2018). As of the time of publication of this thesis, there is a plan in the open source community for an update to the WSI solver NEMOH with the aforementioned capabilities. If it comes to fruition, the W2W model in this thesis would benefit from availing of the expanded capabilities.

2. Substitution of the WSI solver for a non-linear model.

   An alternative to the proposition in the first item is to substitute the linear WSI solver with a fully non-linear one, such as a CFD NWT (Numerical Wave Tank) solver (Devolder et al., 2018a) or a particle following SPH solver (Crespo et al., 2015). The advantages of this alternate coupling approach would be in accurately modelling non-linear effects in WEC arrays, especially for large wave heights and wave periods associated with extreme wave conditions and with very closely spaced WECs. The disadvantage is a step increase in the simulation time and the limited capacity of the wave propagation model to assimilate strongly non-linear information and propagate it to the far-field domain. A possible step forward is the integration of the non-linear two-way coupling approach outlined in (Verbrugghe et al., 2017a) into the presented W2W framework.

3. Further development of the PTO module enabling the simulation of various PTO system architectures.

   At present, the PTO module developed in Chapter 6 is only applied to the cases of a hydraulic and linear PTO for two types of WECs, namely heaving cylindrical WECs and OSWECs. The capabilities of the W2W model would be greatly enhanced by the development of further PTO simulators, such as for the case of the Power Electronic Controlled Magnet Gear PTO *i.e.* currently developed by Ecosse Subsea Systems Ltd. (Wave Energy Scotland, 2019) or a rack and pin PTO system which is most adaptable to scaled wave basin experiments such as those planned as part of the WECANET collaboration.

4. The improvement of the coupling of the WSI solver to the wave propagation model for multi-frequency real sea states.

   Currently, each frequency component of a multi-frequency real sea state is coupled separately for each simulation frequency before the summing up of the total sea state. Likewise, the power calculations are performed at each

frequency and then normalized by the given spectral distribution. Although the W2W model is quite fast in computation, especially compared to existing numerical simulators of WEC arrays, a more integrated approach in dealing with multi-frequency sea states is warranted, especially in the case of simulating short-crested waves that require a significant increase in the number of modelled frequencies to accurately represent a given sea state.

5. Extension of the W2W model capabilities for modelling short-crested waves directional seas.

   At present, the NEMOH-MILDwave coupling allows for the simulation of multi-directional seas with directional spreading via a cos^{2s} spreading function. It is planned to extend this capability capability to the integration with WEC-Sim whereby the power output calculation of the WEC arrays will be performed with directional spreading taken into account.

6. Simulating multiple degrees of freedom of floating WECs and integration of a mooring simulator into the W2W model.

   Up to now, only floating and fixed WECs with one degree of freedom (DoF) have been modelled, *e.g.* heaving cylindrical WECs and OSWECs. Since both NEMOH and WEC-Sim allow full 6 DoF modelling, this could be easily implemented into the coupling methodology. Additionally, the mooring systems, a key driver of WEC array hydrodynamics, are not included in the version of the model presented in the thesis. A possible solution would be to implement the mooring system simulator MoorDyn (Hall and Goupee, 2015) into the W2W model suite.

7. Integration with an economic model for a full techno-economic optimization of a WEC array project.

   The chief goal of a WEC array project is profitability, *i.e.* the production of low-cost electricity from wave energy. In order to fully assess the economics of a WEC array project, it is necessary to include not just the WEC array power output such as that presented in this thesis, but also the CAPEX and OPEX (Operating Expenses) costs of a given WEC array. Often times, the costs can override the hydrodynamic considerations when designing such a project. If a rudimentary cost algorithm such as the LCOE (Levelised Cost of Energy) calculated for various WEC technologies in (Neary et al., 2014) were included in the W2W model, it could be used as an assessment tool by wave energy developers. Given the relatively low computational cost of the exhibited W2W model, it would be possible in theory for wave energy developers to use the tool to perform a first-order techno-economic analysis for a wide range of possible project sites.

8. Integration with environmental impact models

After profitability, the secondary objective of a WEC array project is the minimization of potential deleterious environmental effects, on both the natural environment and sea users and coastal residents and business interests. Therefore, an appraisal of the impact of the external effects of a WEC array project on the surrounding area needs to be made. The changes in the wave field brought on by the presence of the WEC arrays can alter the long-shore currents and the sediment transport on a stretch of coast, potentially impacting coastal residences and businesses. Therefore, the present W2W model can be linked with a sediment transport model such as XBeach (Abanades et al., 2014) or SNL-EFDC (Jones et al., 2014).

References

Abanades, J., Flor-Blanco, G., Flor, G., and Iglesias, G. (2018). Dual wave farms for energy production and coastal protection. *Ocean & Coastal Management*, 160:18 – 29.

Abanades, J., Greaves, D., and Iglesias, G. (2014). Coastal defence through wave farms. *Coastal Engineering*, 91:299 – 307.

Agamloh, E. B., Wallace, A. K., and von Jouanne, A. (2008). Application of fluid–structure interaction simulation of an ocean wave energy extraction device. *Renewable Energy*, 33:748–757.

Alexandre, A., Stallard, T., and Stansby, P. (2009). Transformation of wave spectra across a line of wave devices. In *Proceedings of the 8th European Wave and Title Energy Conference, Uppsala, Sweden*.

Alves, M. (2016). Wave energy converter modelling techniques based on linear hydrodynamic theory. In Folley, M., editor, *Numerical Modelling of Wave Energy Converters*, chapter 1, pages 11–65. Elsevier.

Angelelli, E. and Zanuttigh, B. (2012). A farm of wave activated bodies for coastal protection purposes. In *Proceedings of 33rd international conference on coastal engineering, vol. 1 (2012), Santander, Spain.*

Angelelli, E., Zanuttigh, B., and Kofoed, J. (2012). Numerical modelling of the hydrodynamics around the farm of wave activated bodies (wab). In *Proceedings of the 4th International Conference on Ocean Energy (ICOE), 17-19 Oct. 2012, Dublin, Ireland*.

Annuar, A., Macpherson, D., Forehand, D., and Mueller, M. (2012). Optimum power control for arrays of direct drive wave energy converters. In *6th IET International Conference on Power Electronics, Machines 1 Drives (PEMD 2012), Bristol, UK*.

ANSYS inc. (2019). Ansys aqwa. `https://www.ansys.com/products/structures/ansys-aqwa`.

Antonutti, R. and Hearn, G. E. (2011). Optimisation of point-absorber arrays. In *Proceedings of the 9th European Wave and Tidal Energy Conference, Southampton, UK*.

Astariz, S. and Iglesias, G. (2016a). Selecting optimum locations for co-located wave and wind energy farms. part i: The co-location feasibility index. *Energy Conversion and Management*, 122:589 – 598.

Astariz, S. and Iglesias, G. (2016b). Selecting optimum locations for co-located wave and wind energy farms. part ii: A case study. *Energy Conversion and Management*, 122:599 – 608.

Astariz, S., Perez-Collazo, C., Abanades, J., and Iglesias, G. (2015). Co-located wave-wind farms: Economic assessment as a function of layout. *Renewable Energy*, 83:837 – 849.

AW-Energy Oy (2019). Waveroller. `https://aw-energy.com/waveroller/#surge`.

Babarit, A. (2010). Impact of long separating distances on the energy production of two interacting wave-energy converters. *Ocean Engineering*, 37:718–729.

Babarit, A. (2013). On the park effect in arrays of oscillating wave energy converters. *Renewable Energy*, 58:68–78.

Babarit, A. (2015). A database of capture width ratio of wave energy converters. *Renewable Energy*, 80:610 – 628.

Babarit, A. (2017). *Ocean Wave Energy Conversion Resource, Technologies and Performance*. ISTE Press.

Babarit, A. and Delhommeau, G. (2015). Theoretical and numerical aspects of the open source BEM solver NEMOH. In *Proc. of the 11th European Wave and Tidal Energy Conference 6-11th Sept 2015, Nantes, France*.

Bacelli, G., Balitsky, P., and Ringwood, J. V. (2013). Coordinated control of arrays of wave energy devices — benefits over independent control. *IEEE Transactions on Sustainable Energy*, 4(4):1091–1099.

Bailey, H., Robertson, B. R., and Buckham, B. J. (2016). Wave-to-wire simulation of a floating oscillating water column wave energy converter. *Ocean Engineering*, 125:248 – 260.

Bailey, I., West, J., and Whitehead, I. (2011). Out of sight but not out of mind? public perceptions of wave energy. *Journal of Environmental Policy & Planning*, 13(2):139–157.

Balitsky, P., Bacelli, G., and Ringwood, J. (2014). Control-influenced layout optimization of arrays of wave energy converters. In *Proc. of the ASME 2014 33rd Int'l Conference on Ocean, Offshore and Arctic Engineering June 8-13, 2014 (OMAE2014), San Francisco, CA, USA*.

Balitsky, P., Quartier, N., Verao Fernandez, G., Stratigaki, V., and Troch, P. (2018a). Analyzing the near-field effects and the power production of an array of heaving cylindrical WECs and osWECs using a coupled hydrodynamic-PTO model. *Energies*, 11(12).

Balitsky, P., Verao Fernandez, G., Stratigaki, V., and Troch, P. (2017a). Assessing the impact on power production of WEC array separation distance in a wave farm using one-way coupling of a BEM solver and a wave propagation model. In *Proceedings of the 12th European Wave and Tidal Energy Conference (EWTEC2017),Cork, Ireland*, pages 1176–1186.

Balitsky, P., Verao Fernandez, G., Stratigaki, V., and Troch, P. (2017b). Coupling methodology for modelling the near-field and far-field effects of a wave energy converter. In *Proceedings of the ASME 36th International Conference on Ocean, Offshore and Arctic Engineering (OMAE 2017)*.

Balitsky, P., Verao Fernandez, G., Stratigaki, V., and Troch, P. (2018b). Assessment of the power output of a two-array clustered WEC farm using a BEM solver coupling and a wave-propagation model. *Energies*, 11(11).

Beels, C. (2009). *Optimization of the lay-out of a farm of wave energy converters in the North Sea: analysis of wave power resources, wake effects, production and cost*. PhD thesis, Ghent University.

Beels, C., Troch, P., Backer, G. D., Vantorre, M., and Rouck, J. D. (2010). Numerical implementation and sensitivity analysis of a wave energy converter in a time-dependent mild-slope equation model. *Coastal Engineering*, 57(5):471 – 492.

Beels, C., Troch, P., Kofoed, J. P., Frigaard, P., Kringelum, J. V., Kromann, P. C., Donovan, M. H., De Rouck, J., and De Backer, G. (2011). A methodology for production and cost assessment of a farm of wave energy converters. *Renewable Energy*, 36:3402–3416.

Bellew, S. and Stallard, T. (2010). Linear modelling of wave device arrays with comparison to experimental measurements 1 second order models. In *21st International Workshop on Water Waves 1 Floating Bodies (21st IWWWFB); Harbin, China. 2010.*

Bharath, A. (2018). *Numerical Analysis of Arrays of Wave Energy Converters*. PhD thesis, University of Tasmania.

Blavette, A., O'Sullivan, D., Egan, M., and Lewis, T. (2012). Grid impact assessment of a medium size wave farm connected to different test sites. In *Proceedings of the 4th International Conference on Ocean Energy (ICOE), 17-19 Oct. 2012, Dublin, Ireland*.

Blavette, A., O'Sullivan, D. L., Alcorn, R., Lewis, T. W., and Egan, M. G. (2014). Impact of a medium-size wave farm on grids of different strength levels. *IEEE Transactions on Power Systems*, 29(2):917–923.

Bonar, P. A., Bryden, I. G., and Borthwick, A. G. (2015). Social and ecological impacts of marine energy development. *Renewable and Sustainable Energy Reviews*, 47:486 – 495.

Booij, N. (1983). A note on the accuracy of the mild-slope equation. *Coastal Engineering*, 7(3):191 – 203.

Booij, N., Ris, R. C., and Holthuijsen, L. H. (1999). A third-generation wave model for coastal regions: 1. Model description and validation. *Journal of Geophysical Research*, 104:7649–7666.

Borgarino, B., Babarit, A., and Ferrant, P. (2011a). Extension of free-surface green's function multipole expansion for infinite water depth case. *International Journal of Offshore and Polar Engineering*, 21:161–168.

Borgarino, B., Babarit, A., and Ferrant, P. (2011b). Impact of the separating distance between interacting wave energy converters on the overall energy extraction of an array. In *Proceedings of the 9th European Wave and Tidal Energy Conference, Southampton, UK*.

Borgarino, B., Babarit, A., and Ferrant, P. (2012). Impact of wave interaction effects on energy absorbtion in large arrays of wave energy converters. *Ocean Engineering*, 41:79–88.

Bossuyt, S., Stratigaki, V., Holdorf, R., Troch, P., and Kortenhaus, A. (2017). A search group algorithm for wind and wave farm layout optimization. In *Proceedings of the 12th European Wave and Tidal Energy Conference (EWTEC2017),Cork, Ireland*, pages 972–982.

Brito, M., Canelas, R., Ferreira, R., García Feal, O., Domínguez, J., Crespo, A., and Neves, M. (2016). Coupling between dualsphysics and chrono-engine: towards large scale hpc multiphysics simulations. In *Proceedings of SPHERIC 2016, Munich, Germany*.

Brorsen, M. and Helm-Petersen, J. (1998). On the reflection of short-crested waves in numerical models. In *Proceedings of the 26th International Conference on Coastal Engineering, Copenhagen, pp. 394–407*.

Budal, K. (1977). Theory for absorbtion of wave power by a system of interacting bodies. *Journal of Ship Research*, 21:248–253.

Budal, K. and Falnes, J. (1975). A resonant point absorber of ocean-wave power. *Nature*, 256.

Budal, K., Falnes, J., Iversen, L., Lillebekken, Oltedal, P., Hals, G., Onshus, T., and Hoy, A. (1982). The norwegian wave-power buoy project. In *Proc. Second International Symposium on Wave Energy Utilization (H. Berge, ed)*.

Canelas, R., Brito, M., Feal, O., Domínguez, J., and Crespo, A. (2018). Extending dualsphysics with a differential variational inequality: modeling fluid-mechanism interaction. *Applied Ocean Research*, 76:88 – 97.

Carballo, R. and Iglesias, G. (2013). Wave farm impact based on realistic wave-WEC interaction. *Energy*, 51:216 – 229.

Carbon Trust (2011). Accelerating marine energy. Technical report, Carbon Trust.

Carengie Clean Energy (2018). Carnegie clean energy ceto. https://www.carnegiece.com/wave/what-is-ceto/.

Cargo, C. (2013). *Design and Control of Hydraulic Power Take-Offs for Wave Energy Converters*. PhD thesis, University of Bath.

Cargo, C., Hillis, A., and Plummer, A. (2014). Optimisation and control of a hydraulic power take-off unit for a wave energy converter in irregular waves. *Proceedings of the Institution of Mechanical Engineers, Part A: Journal of Power and Energy*, 228(4):462–479.

Cargo, C. J., Plummer, A. R., Hillis, A. J., and Schlotter, M. (2012). Determination of optimal parameters for a hydraulic power take-off unit of a wave energy converter in regular waves. *Proceedings of the Institution of Mechanical Engineers, Part A: Journal of Power and Energy*, 226(1):98–111.

CEREMA Eau, mer et fleuves - ER/MMH (2019). Centre d'archivage national de données de houle in situ. http://candhis.cetmef.developpement-durable.gouv.fr/.

Charrayre, F., Benoit, M., Peyrard, C., and Babarit, A. (2014a). Modélisation des interactions dans une ferme de systèmes houlomoteursavec prise en compte de la bathymétrie. In *14èmes Jounrées de l'Hydrodynamique 18-20 novembre 2014*.

Charrayre, F., Peyrard, C., Benoit, M., and Babarit, A. (2014b). A coupled methodology for wave-body interactions at the scale of a farm of wave energy converters including irregular bathymetry. In *Proc. of the ASME 2014 33rd Int'l Conference on Ocean, Offshore and Arctic Engineering June 8-13, 2014, San Francisco, CA, USA*.

Child, B., Cruz, J., and Livingstone, M. (2011). The development of a tool for optimising of arrays of wave energy converters. In *Proceedings of the 9th European Wave and Tidal Energy Conference, Southampton, UK*.

Child, B. and Venugopal, V. (2007). Interaction of waves with an array of floating wave energy devices. In *Proceedings of the 7th European Wave and Tidal Energy Conference, Porto, Portugal*.

Child, B. and Venugopal, V. (2008). Non-optimal tuning of wave energy device arrays. In *2nd International Conference on Ocean Energy (ICOE), 15th Brest, France*.

Child, B. and Venugopal, V. (2010). Optimal configurations of wave energy devices. *Ocean Engineering*, 37:1402–1417.

École Centrale de Nantes (2019). Nemoh-presentation - lheea. https://lheea.ec-nantes.fr/logiciels-et-brevets/nemoh-presentation-192863.kjsp.

Contardo, S., Hoeke, R., Hemer, M., Symonds, G., McInnes, K., and O'Grady, J. (2018). In situ observations and simulations of coastal wave field transformation by wave energy converters. *Coastal Engineering*, 140:175 – 188.

COST European Cooperation in Science & Technology (2019). WECanet. `https://www.cost.eu/actions/CA17105/#tabs|Name:overview`.

Crespo, A., Domínguez, J., Rogers, B., Gómez-Gesteira, M., Longshaw, S., Canelas, R., Vacondio, R., Barreiro, A., and García-Feal, O. (2015). Dualsphysics: Open-source parallel {CFD} solver based on smoothed particle hydrodynamics (sph). *Computer Physics Communications*, 187:204 – 216.

Crespo, A. J. C., Hall, M., Domínguez, J. M., Altomare, C., Wu, M., Verbrugghe, T., Stratigaki, V., Troch, P., and Gómez-Gesteira, M. (2018). Floating moored oscillating water column with meshless sph method. In *Proceedings of the ASME 37th International Conference on Ocean, Offshore and Arctic Engineering (OMAE 2018), Madrid, Spain.*, pages UNSP V11BT12A053:1–UNSP V11BT12A053:10. ASME.

Cruz, J. (2008). *Ocean Wave Energy*. Green Energy 1 Technology. Springer.

Cruz, J., Sykes, R., Siddorn, P., and Taylor, R. (2010). Estimating the loads an energy yield of arrays of wave energy converters under realistic seas. *IET Renewable Power Generation*, 4:488–497.

CSIRO (2012). Ocean renewable energy: 2015-2050 an analysis of ocean energy in australia. Technical report, Commonwealth Scientific 1 Industrial Research Organisation (CSIRO).

Cummins, W. (1962). The impulse response function and ship motions. *Schiffstechnik*, 9:101–109.

Davidson, J. and Ringwood, J. V. (2017). Mathematical modelling of mooring systems for wave energy converters—a review. *Energies*, 10(5).

de Andrés, A., Guanche, R., Meneses, L., Vidal, C., and Losada, I. (2014). Factors that influence array layout on wave energy farms. *Ocean Engineering*, 82:32 – 41.

De Backer, G., Vantorre, M., Beels, C., De Rouck, J., and Frigaard, P. (2010). Power absorption by closely spaced point absorbers in constrained conditions. *IET Renewable Power Generation*, 4:579–591.

de O. Falcão, A. F. (2008). Phase control through load control of oscillating-body wave energy converters with hydraulic PTO system. *Ocean Engineering*, 35:358–366.

Delhommeau, G. (1987). *Les problemes de diffraction-radiation et de resistance de vagues : etude theorique et resolution numerique par la methode des singularites*. PhD thesis, École Centrale de Nantes. Thèse de doctorat dirigée par Sulmont, Patrice Physique Nantes 1987.

Delhommeau, G. (1989). Amélioration des performances des codes de calcul de diffraction-radiation au premier ordre. In *Proceedings of the 2nd Journées de l'Hydrodynamique*.

Delhommeau, G. (1993). Seakeeping codes aquadyn and aquaplus. In *In 19th WEGMENT School, Numerical Simulation of Hydrodynamics : Ship and Offshore Structures*.

Devolder, B., Rauwoens, P., and Troch, P. (2016). Numerical simulation of a single floating point absorber wave energy converter using openfoam. In *2nd International Conference on Renewable energies Offshore*, pages 197–205.

Devolder, B., Rauwoens, P., and Troch, P. (2017). Numerical simulation of an array of heaving floating point absorber wave energy converters using openfoam. In *VII INTERNATIONAL CONFERENCE ON COMPUTATIONAL METHODS IN MARINEENGINEERING (MARINE2017)*, pages 777–788.

Devolder, B., Stratigaki, V., Troch, P., and Rauwoens, P. (2018a). Cfd simulations of floating point absorber wave energy converter arrays subjected to regular waves. *Energies*, 11(3):1–23.

Devolder, B., Troch, P., and Rauwoens, P. (2018b). Performance of a buoyancy-modified k-ω and k-ω sst turbulence model for simulating wave breaking under regular waves using openfoam ®. *Coastal Engineering*, 138:49–65.

DT Ocean Developers (2019). DTOcean Optimal Design Tools for Ocean Energy Arrays. `http://www.oceansatlas.org`.

Dynaflow, inc. (2019). 3dynafs-bem©. `http://www.dynaflow-inc.com/Products/Software/2_3DynaFS/Boundary-Element-3DynaFS.htm`.

EIB, The European Investment Bank (2016). Eu support for development of commercial wave energy technology in europe. `http://www.eib.org/en/infocentre/press/releases/all/2016/2016-165-eu-support-for-development-of-commercial-wave-energy-technology-htm`.

Electric Supply Board (ESB), Ireland (2019). ESB Westwave. `https://www.esb.ie/being-innovative/future-energy/ocean-energy`.

Enerdata (2018). Global energy statistical yearbook 2018. `https://yearbook.enerdata.net/electricity/electricity-domestic-consumption-data.html`.

Energy Technologies Institute (2019). Perawat. `https://www.eti.co.uk/programmes/marine/perawat`.

Engström, J., Eriksson, M., Göteman, M., Isberg, J., and Leijon, M. (2013). Performance of large arrays of point absorbing direct-driven wave energy converters. *Journal of Applied Physics*, 114(20):204502.

Eriksson, M., Isberg, J., and Leijon, M. (2005). Hydrodynamic modelling of a direct drive wave energy converter. *International Journal of Engineering Science*.

European Marine Energy Centre Ltd. (2019). European marine energy centre. `http://www.emec.org.uk/`.

European Wave and Tidal Energy Conference (2019). `http://www.ewtec.org/`.

Evans, D. (1979). Some theoretical aspects of three-dimensional wave-energy absorbers. In *Sympoisum on Ocean Wave Energy Utliziation*, Gothenburg, Sweden.

Evans, D. (1981). Maximum wave-power absorbtion under motion constraints. *Applied Ocean Research*, 3:200–203.

Evans, D. V. (1976). A theory for wave-power absorption by oscillating bodies. *Journal of Fluid Mechanics*, 77(1):1–25.

Falnes, J. (1980). Radiation impedance matrix and optimum power absorbtion for interacting oscillators in surface waves. *Applied Ocean Research*, 2:75–80.

Falnes, J. (1995). On non-causal impulse response functions related to propagating water waves. *Applied Ocean Research*, 17:379–389.

Falnes, J. (2001). Optimum control of oscillation of wave-energy converters. In *Proceedings of the Eleventh (2001) International Offshore 1 Polar Engineering Conference,Stavanger, Norway, June 17-22*.

Falnes, J. (2002). *Ocean waves and oscillating systems: linear interactions including wave-energy extraction*. Cambridge University Press.

Falnes, J. (2007). A review of wave-energy extraction. *Marine Structures*, 20:185–201.

Falnes, J. and Budal, K. (1982). Wave-power absorbtion by parallel rows of interacting oscillating bodies. *Applied Ocean Research*, 4(4):194–207.

Fitzgerald, C. and Thomas, G. P. (2007). A preliminary study of the optimal formation of an array of wave power devices. In *Proceedings of the 7th European Wave 1 Tidal Energy Conference,Porto, Portugal*.

Fitzgerald, J. and Bergdahl, L. (2008). Including moorings in the assessment of a generic offshore wave energy converter: A frequency domain approach. *Marine Structures*, 21:23–46.

Flavià, F. F., McNatt, C., Rongère, F., Babarit, A., and Clément, A. (2018). A numerical tool for the frequency domain simulation of large arrays of identical floating bodies in waves. *Ocean Engineering*, 148:299 – 311.

Folley, M. (2017). The wave energy resource. In *Handbook of Ocean Wave Energy*, chapter 3, pages 43–78.

Folley, M., Babarit, A., Child, B., Forehand, D., O'Boyle, L., Silverthorne, K., Spinneken, J., Stratigaki, V., and Troch, P. (2012). A review of numerical modelling of wave energy converter arrays. In *Proceedings of the ASME 2012 31st International Conference on Ocean, Offshore and Arctic Engineering (OMAE), Rio de Janeiro, Brazil*.

Folley, M. and Whittaker, T. (2009a). The control of wave energy converters using active bipolar damping. *Proceedings of the Institution of Mechanical Engineers, Part M: Journal of Engineering for the Maritime Environment*, 223(4):479–487.

Folley, M. and Whittaker, T. (2009b). The effect of sub-optimal control and the spectral wave climate on the performance of wave energy converter arrays. *Applied Ocean Research*, 31(4):260–266.

Folley, M. and Whittaker, T. (2010). Spectral modelling of wave energy converters. *Coastal Engineering*, 57:892–897.

Folley, M. and Whittaker, T. (2013). Preliminary cross-validation of wave energy converter array interactions. In *Proceedings of ASME International Conference on Offshore Mechanics and Arctic Engineering (OMAE2013) , Nantes, France.*, volume 8.

Food and Agriculture Organization (FAO) of the United Nations (2012). Un atlas of the oceans. `http://www.oceansatlas.org`.

Gao, Z. and Moan, T. (2009). Mooring system analysis of multiple wave energy converters in a farm configuration. In *Proceedings of the 8th European Wave and Title Energy Conference, Uppsala, Sweden*.

Garcia Rosa, P. B., Bacelli, G., and Ringwood, J. (2015). Control-informed optimal layout for wave farms. *IEEE Transactions on Sustainable Energy*, 6:575–582.

Garrison, T. (2015). *Oceanography: An Invitation to Marine Science*. Brooks Cole, Belmont, USA.

Ghent University (2019). Flansea. `http://www.flansea.ugent.be/`.

Giassi, M. and Göteman, M. (2018). Layout design of wave energy parks by a genetic algorithm. *Ocean Engineering*, 154:252 – 261.

Gilloteaux, J.-C. and Ringwood, J. (2010). Control-informed geometric optimisation of wave energy converters. In *Proc. IFAC Conf. on Control Applications in Marine Systems (CAMS), Rostock*.

Giorgi, G. and Ringwood, J. V. (2018). Comparing nonlinear hydrodynamic forces in heaving point absorbers and oscillating wave surge converters. *Journal of Ocean Engineering and Marine Energy*, 4(1):25–35.

Goda, Y. (2000). *Random Seas and Design of Maritime Structures*. World Scientific, 3rd edition.

Göteman, M., Engström, J., Eriksson, M., and Isberg, J. (2015). Optimizing wave energy parks with over 1000 interacting point-absorbers using an approximate analytical method. *International Journal of Marine Energy*, 10:113 – 126.

Greaves, D., Collazo, C. P., Magagna, D., Conley, D., Bailey, I., Simas, T., rian Holmes, O'Hagan, A. M., Torre-Enciso, J. O. Y., Marina, D., Olivares, C. H., Le-Crom, I., Saulnier, J.-B., Sundberg, J., Embling, C., Witt, M., Godley, B., and Leitão, J. C. (2013). Enabling wave power: Streamlining processes for progress. Technical report, Plymouth University.

Greaves, D. and Iglesias, G. (2019). *Wave and Tidal Energy*. Chicester: Wiley.

Greenwood, C., Christie, D., Venugopal, V., Morrison, J., and Vogler, A. (2016). Modelling performance of a small array of wave energy converters: Comparison of spectral and boussinesq models. *Energy*, 113:258 – 266.

Göteman, M., McNatt, C., Giassi, M., Engström, J., and Isberg, J. (2018). Arrays of point-absorbing wave energy converters in short-crested irregular waves. *Energies*, 11(4).

Gunn, K. and Stock-Williams, C. (2012). Quantifying the potential global market for wave power. *Renewable Energy*, 44:296–304.

Hall, M. and Goupee, A. (2015). Validation of a lumped-mass mooring line model with deepcwind semisubmersible model test data. *Ocean Engineering*, 104:590 – 603.

Hasselmann, K. and Olbers, D. (1973). Measurements of wind-wave growth and swell decay during the joint north sea wave project (jonswap). *Ergänzung zur Deut. Hydrogr. Z., Reihe A (8)*, 12:1–95.

Henry, A., Folley, M., and Whittaker, T. (2018). A conceptual model of the hydrodynamics of an oscillating wave surge converter. *Renewable Energy*, 118:965–972.

Johanning, L., Smith, G. H., and Wolfram, J. (2004). Mooring systems for wave energy converters: a review of design issues and choices. In *Proceedings of the 3rd International Conference on Marine Renewable Energy (MAREC). Blyth, UK, 2004.*

Johanning, L., Smith, G. H., and Wolfram, J. (2005). Towards design standards for WEC moorings. In *Proceedings of the 6th European Wave and Tidal Energy Conference, (EWTEC05),Glasgow, UK, 2005.*

Jones, C., Magalen, J., and Roberts, J. (2014). Wave energy converter (WEC) array effects on wave, current, and sediment circulation: Monterey bay, ca. Technical report, Sandia National Laboratories.

Kagemoto, H. and Yue, D. (1993). Hydrodynamic interaction analyses of very large floating structures. *Journal of Marine Structures*, Vol.6:295–322.

Kagemoto, H. and Yue, D. K. P. (1986). Interactions among multiple three-dimensional bodies in water waves: an exact algebraic method. *Journal of Fluid Mechanics*, 166:189–209.

Kasanen, E. (2015). Aw-energy – positive experiences of the waveroller in portugal and france. In *WavEC Annual Seminar and International B2B Meetings, Lisbon, Portugal. Nov. 15-17 2015.*

Kempener, R. and Neumann, F. (2014). Wave energy technology brief. Technical report, International Renewable Energy Agency (IRENA).

Kiprakis, A. E., Nambiar, A. J., Forehand, D. I. M., and Wallace, A. R. (2009). Modelling arrays of wave energy converters connected to weak rural electricity networks. In *2009 International Conference on Sustainable Power Generation and Supply*, pages 1–7.

Konispoliatis, D. and Mavrakos, S. (2014). Hydrodynamics and power absorption characteristics of free floating and moored arrays of owc's devices. In *Proc. of the ASME 2014 33rd Int'l Conference on Ocean, Offshore and Arctic Engineering June 8-13, 2014 (OMAE2014), San Francisco, CA, USA*.

Larsen, J. and Dancy, H. (1983). Open boundaries in short wave simulations – a new approach. *Coastal Engineering*, pages 285–297.

Lazard (2018). Lazard levelized cost of energy analysis,12th edition. Technical report.

Lee, C. and Suh, K. D. (1998). Internal generation of waves for time-dependent mild-slope equations. *Coastal Engineering*, 34(1):35 – 57.

Lee, C.-H. and Newman, J. N. (2005). Computation of wave effects using the panel method. In Chakrabarti, S. K., editor, *Numerical Models in Fluid-Structure Interaction*, volume 18 of *Advances in Fluid Mechanics*. WIT Press, Southampton.

LeMehaute (1976). *An introduction to hydrodynamics and water waves*. Springer, New York.

Lewis, A., Estefen, S., Huckerby, J., Musial, W., Pontes, T., and Torres-Martinez, J. (2011). Ocean energy. In *IPCC Special Report on Renewable Energy Sources and Climate Change Mitigation*.

Li, G. and Belmont, M. (2014). Model predictive control of sea wave energy converters - part ii: The case of an array of devices. *Renewable Energy*, 68:540–549.

Magagna, D. and Uihlein, A. (2015). Ocean energy development in europe: Current status and future perspectives. *International Journal of Marine Energy*, 11:84 – 104.

Mavrakos, S. (1991). Hydrodynamic coefficients for groups of interacting vertical axisymmetric bodies. *Ocean Engineering*, 18:485–515.

Mavrakos, S. and Koumoutsakos, P. (1987). Hydrodynamic interaction among vertical axisymmetric bodies restrained in waves. *Applied Ocean Research*, 9:128–140.

Mavrakos, S. and McIver, P. (1997). Comparison of methods for computing hydrodynamic characteristics of arrays of wave power devices. *Applied Ocean Research*, 19:283–291.

McCallum, P. D. (2017). *Numerical methods for modelling the viscous effects on the interactions between multiple wave energy converters*. PhD thesis.

McIver, P. (1994). Some hydrodynamic aspects of arrays of wave energy devices. *Applied Ocean Research*, 16:61–69.

McIver, P. and Evans, D. (1984). Approximation of wave forces on cylinder arrays. *Applied Ocean Research*, 6:101–107.

McIver, P., Mavrakos, S., and Singh, G. (1996). Wave-power absorption by arrays of devices. In *Proceedings of the 2nf European Wave Power Conference, Lisbon, Portugal*.

McNatt, C., Venugopal, V., and Forehand, D. (2013). The cylindrical wave field of wave energy converters. *Int'l Journal of Marine Energy*, 3:26–39.

McNatt, J. C., Venugopal, V., and Forehand, D. (2015). A novel method for deriving the diffraction transfer matrix and its application to multi-body interactions in water waves. *Ocean Engineering*, 94:173 – 185.

Mei, C. C. (1976). Power extraction from water waves. *Journal of Ship Research*, 20:63–66.

Mei, C. C., Stiassnie, M., and Yue, D. K.-P. (2005). *Theory and Application of Ocean Surface Waves Part 1: Linear Aspects*. World Scientific Publishing Co. Pte. Ltd.

Mendoza, E., Silva, R., Zanuttigh, B., Angelelli, E., Andersen, T. L., Martinelli, L., Nørgaard, J. Q. H., and Ruol, P. (2014). Beach response to wave energy converter farms acting as coastal defence. *Coastal Engineering*, 87:97 – 111. Coasts@Risks: THESEUS, a new wave in coastal protection.

Merigaud, A., Gilloteaux, J.-C., and Ringwood, J. (2012). A nonlinear extension for linear boundary element methods in wave energy device modelling. In *Proceedings of the ASME 2012 31st International Conference on Ocean, Offshore 1 Arctic Engineering (OMAE2012), Rio de Janeiro, Brazil*.

Michele, S., Sammarco, P., d'Errico, M., Renzi, E., Abdolali, A., Bellotti, G., and Dias, F. (2015). Flap gate farm: From venice lagoon defense to resonating wave energy production. part 2: Synchronous response to incident waves in open sea. *Applied Ocean Research*, 52:43 – 61.

Millar, D., Smith, H., and Reeve, D. (2007). Modelling analysis of the sensitivity of shoreline change to a wave farm. *Ocean Engineering*, 34(5–6):884 – 901.

Mitsuyasu, H., Tasai, F., Suhara, T., Mizuno, S., Ohkusu, M., Honda, T., and Rikiishi, K. (1975). Observation of the directional spectrum of ocean waves using a clover-leaf buoy. *Journal of Physical Oceanography*, 5.

Molinas, M., O.Skjervheim, Sorby, B., Andreasen, P., Lundberg, S., and Undeland, T. (2007). Power smoothing by aggregation of wave energy converters for minimizing electrical energy storage requirements. In *Proceedings of the 7th European Wave 1 Tidal Energy Conference, Porto, Portugal.*

Mork, G., Barstow, S., Kabuth, A., and Teresa Pontes, M. (2010). Assessing the global wave energy potential. In *Proceedings of OMAE2010 29th International Conference on Ocean, Offshore Mechanics and Arctic Engineering June 6-11, 2010, Shanghai, China.*, volume 3.

Munk, W. (1950). Origin and generation of waves. *Coastal Engineering Proceedings*, 1(1):1.

National Renewable Energy Laboratory (2017). Marine and hydrokinetic technology database. `http://en.openei.org/wiki/Marine_and_Hydrokinetic_Technology_Database`.

Neary, V. S., Previsic, M., Jepsen, R. A., Lawson, M. J., Yu, Y.-H., Copping, A. E., Fontaine, A. A., Hallett, K. C., and Murray, D. K. (2014). Methodology for design and economic analysis of marine energy conversion (mec) technologies. Technical report, Sandia National Laboratories.

Newman, J. (1977). *Marine Hydrodynamics*. MIT Press.

Newman, J. N. (2001). Wave effects on multiple bodies. In *Hydrodynamics in Ship and Ocean Engineering*, pages 1–24.

O'Boyle, L., Elsäßer, B., and Whittaker, T. (2017). Experimental measurement of wave field variations around wave energy converter arrays. *Sustainability*, 9(1).

Ocean Energy Systems (2018). Spotlight on ocean energy. Technical report, WaveEC-Offshore Renewables.

O'Dea, A., Haller, M. C., and Özkan Haller, H. T. (2018). The impact of wave energy converter arrays on wave-induced forcing in the surf zone. *Ocean Engineering*, 161:322 – 336.

Okhusu, M. (1974). Hydrodynamic forces on multiple cylinders in waves. In Institute of Mechanical Engineers, editor, *Proceedings of the International Symposium on Dynamics of Marine Vehicles 1 Structures in Waves, London, U.K*, pages 107–112.

Oskamp, J. A. and Ozkan-Haller, H. T. (2010). Wave predicitons at the site of a wave energy conversion array. In *Proceedings of 32nd Conference on Coastal Engineering, Shanghai, China, 2010*.

O'Sullivan, A. and Lightbody, G. (2015). Wave to wire power maximisation from a wave energy o sullivan, a.c.; lightbody,. In *Proceedings of the 11th European Wave and Tidal Energy Conference, Nantes, France,6–11 September 2015*.

O'Sullivan, A. C. M., Sheng, W., and Lightbody, G. (2018). An analysis of the potential benefits of centralised predictive control for optimal electrical power generation from wave energy arrays. *IEEE Transactions on Sustainable Energy*, 9(4):1761–1771.

O'Sullivan, D. and Dalton, G. (2009). Challenges in the grid connection of wave energy devices. In *Proceedings of the 8th European Wave and Title Energy Conference (EWTEC2009), Uppsala, Sweden*.

Palha, A., Mendes, L., Fortes, C. J., Brito-Melo, A., and Sarmento, A. (2010). The impact of wave energy farms in the shoreline wave climate: Portuguese pilot zone case study using pelamis energy wave devices. *Renewable Energy*, 35(1):62 – 77.

Paredes, G. M., Eskilsson, C., Palm, J., Bergdahl, L., Leite, L. M., and Taveira-Pinto, F. (2013). Experimental and numerical modelling of a moored, generic floating wave energy converter. In *Proceedings of the 10th European Wave and Tidal Energy Conference, Aalborg, DK*.

Parkinson, S. C., Dragoon, K., Reikard, G., García-Medina, G., Özkan Haller, H. T., and Brekken, T. K. (2015). Integrating ocean wave energy at large-scales: A study of the us Pacific Northwest. *Renewable Energy*, 76:551 – 559.

Pastor, J. and Liu, Y. (2014). Frequency and time domain modeling and power output for a heaving point absorber wave energy converter. *International Journal of Energy and Environmental Engineering*, 5(2):101.

Peñalba Retes, M., Merigaud, A., Gilloteaux, J.-C., and Ringwood, J. (2015). Nonlinear Froude-Krylov force modelling for two heaving wave energy point absorbers. In *Proceedings of the 11th European Wave and Tidal Energy Conference 6-11th Sept 2015, Nantes, France*.

Pecher, A. and Kofoed, J. P. e. (2016). *Handbook of Ocean Wave Energy*, volume 7. Springer Open.

Penalba, M., Davidson, J., Windt, C., and Ringwood, J. V. (2018). A high-fidelity wave-to-wire simulation platform for wave energy converters: Coupled numerical wave tank and power take-off models. *Applied Energy*, 226:655–669.

Penalba, M. and Ringwood, J. (2018a). The impact of a high-fidelity wave-to-wire model in control parameter optimisation and power production assessment. In *Proceedings of the 37th International Conference on Ocean, Offshore and Artic Engineering, Madrid, Spain*.

Penalba, M. and Ringwood, J. V. (2018b). A reduced wave-to-wire model for controller design and power assessment of wave energy converters. In *Proceedings of the 2018 RENEW conference, Lisbon, Portugal, Oct 8-10, 2018*.

Penalba, M. and Ringwood, J. V. (2019). Linearisation-based nonlinearity measures for wave-to-wire models in wave energy. *Ocean Engineering*, 171:496 – 504.

Penalba, M., Sell, N., A.J., H., and Ringwood, J. V. (2017a). Validating a wave-to-wire model for a wave energy converter – part i: The hydraulic transmission system. *Energies*, 10(7):977–998.

Penalba, M., Touzón, I., Lopez-Mendia, J., and Nava, V. (2017b). A numerical study on the hydrodynamic impact of device slenderness and array size in wave energy farms in realistic wave climates. *Ocean Engineering*, 142(Supplement C):224 – 232.

Perez Collazo, C., Astariz, S., Abanades, J., Greaves, D., and Iglesias, G. (2014). Co-located wave and offshore wind farms - a preliminary case study of an hybrid array. In *Proceedings of the International Conference in Coastal Engineering (ICCE) Seoul, South Korea*.

Pierson, W. J. and Moskowitz, L. (1964). A proposed spectral form for fully developed wind seas based on the similarity theory of s. a. kitaigorodskii. *Journal of Geophysical Research*, 69:32.

Pizer, D. (1993). Maximum wave-power abosrbtion of point absorbers under motion constraints. *Applied Ocean Research*, 15:227–234.

Radder, A. and Dingemans, M. (1985). Canonical equations for almost periodic, weakly nonlinear gravity waves. *Wave Motion*, 7(5):473 – 485.

Ransley, E. J., Greaves, D. M. R., Raby, A. C., Simmonds, D. I., and Hann, M. (2017). Survivability of wave energy converters using cfd. *Renewable Energy*, 109.

Renzi, E. and Dias, F. (2012). Resonant behaviour of an oscillating wave energy converter in a channel. *Journal of Fluid Mechanics*, 701:482–510.

Renzi, E. and Dias, F. (2013). Relations for a periodic array of flap-type wave energy converters. *Applied Ocean Research*, 39:31.

Région Bretagne (2019). Energies marines, la bretagne à pleine puissance. `http://energies-marines.bretagne.bzh/`.

Ricci, P., Alves, M., ao, A. F., and Sarmento, A. (2006). Optimisation of the geometry of wave energy converters. In *Proceedings of the Int.Conf. on Ocean Energy, Bremerhaven, Germany*.

Ricci, P., Saulnier, J.-B., and de O. Falcão, A. F. (2007). Point-absorber arrays: a configuration study off the portuguese west coast. In *Proceedings of the 7th European Wave 1 Tidal Energy Conference, Porto, Portugal*.

Rijnsdorp, D., Hansen, J., and Lowe, R. (2017). Predicting coastal impacts of wave farms using a wave-resolving model. In Lewis, A., editor, *Proceedings of the 12th European Wave and Tidal Energy Conference (EWTEC2017),Cork, Ireland*, University College Cork, Ireland. EWTEC. ISSN: 2309-1983.

Rijnsdorp, D. P., Hansen, J. E., and Lowe, R. J. (2018). Simulating the wave-induced response of a submerged wave-energy converter using a non-hydrostatic wave-flow model. *Coastal Engineering*, 140:189 – 204.

Ringsberg, J., Jansson, H., Örgård, M., Yang, S.-H., and Johnson, E. (2018). Comparison of mooring solutions and array systems for point absorbing wave energy devices. In *Proceedings of the 37th International Conference on Ocean, Offshore and Artic Engineering, Madrid, Spain*.

Ringwood, J. V., Bacelli, G., and Fusco, F. (2014). Energy-maximizing control of wave-energy converters: The development of control system technology to optimize their operation. *IEEE Control Systems*, 34(5):30–55.

Rodriguez-Delgado, C., Bergillos, R. J., Ortega-Sánchez, M., and Iglesias, G. (2018). Protection of gravel-dominated coasts through wave farms: Layout and shoreline evolution. *Science of The Total Environment*, 636:1541 – 1552.

Rogelj, J., Shindell, D., Jiang, K., Fifita, S., Forster, P., Ginzburg, V., Handa, C., Kheshgi, H., Kobayashi, S., Kriegler, E., Mundaca, L., Séférian, R., and Vilariño, M. V. (2018). Global warming of 1.5°C. an ipcc special report on the impacts of global warming of 1.5 °C above pre-industrial levels and related global greenhouse gas emission pathways, in the context of strengthening the global response to the threat of climate change, sustainable development, and efforts to eradicate poverty. Technical report, Intergovernmental Panel on Climate Change (IPCC).

Rouck, J. D. and Meirschaert, V. (2009). SEEWEC - Sustainable Economically Efficient Wave Energy Converter. Technical report, Ghent University.

RPS and REMTec Consulting (2018). Offshore renewable energy development plan (oredp) interim review. Technical report, The Department of Communications, Climate Action and Environment of the Government of Ireland.

Ruano-Chamorro, C., Castilla, J. C., and Gelcich, S. (2018). Human dimensions of marine hydrokinetic energies: Current knowledge and research gaps. *Renewable and Sustainable Energy Reviews*, 82:1979 – 1989.

Ruehl, K., Porter, A., Posner, A., and Roberts, J. (2013). Development of snl-swan, a validated wave energy converter array modeling tool. In *Proceedings of the 10th European Wave and Tidal Energy Conference, Denmark, 2013.*

Ruiz, P. M., Ferri, F., and Kofoed, J. P. (2017a). Experimental validation of a wave energy converter array hydrodynamics tool. *Sustainability*, 9:115.

Ruiz, P. M., Nava, V., Topper, M. B. R., Minguela, P. R., Ferri, F., and Kofoed, J. P. (2017b). Layout optimisation of wave energy converter arrays. *Energies*, 10(9).

Salter, S. (1974). Wave power. *Nature*, 249.

Sammarco, P., Michele, S., and d'Errico, M. (2013). Flap gate farm: From venice lagoon defense to resonating wave energy production. part 1: Natural modes. *Applied Ocean Research*, 43:206 – 213.

Saulnier, J.-B., Clement, A., Falcao, A. F. D. O., Pontes, T., Prevosto, M., and Ricci, P. (2011). Wave groupiness and spectral bandwidth as relevant parameters for the performance assessment of wave energy converters. *Ocean Engineering*, 38(1):130–147.

Schmitt, P., Asmuth, H., and Elsäßer, B. (2016). Optimising power take-off of an oscillating wave surge converter using high fidelity numerical simulations. *International Journal of Marine Energy*, 16:196 – 208.

Schmitt, P. and Elsaesser, B. (2015). On the use of openfoam to model oscillating wave surge converters. *Ocean Engineering*, 108:98 – 104.

Scottish Renewables (2019). Uk marine energy 2019: A new industry. Technical report, Scottish Renewables.

Sell, N., Plummer, A., Hillis, A., and Chandel, D. (2017). Modelling and calibration of a direct drive hydraulic PTO. In Lewis, A., editor, *Proceedings of the 12th European Wave and Tidal Energy Conference (EWTEC2017) ,Cork, Ireland*, University College Cork, Ireland. EWTEC. ISSN: 2309-1983.

Shadman, M., Estefen, S. F., Rodriguez, C. A., and Nogueira, I. C. (2018). A geometrical optimization method applied to a heaving point absorber wave energy converter. *Renewable Energy*, 115:533 – 546.

Sharkey, F., Bannon, E., Conlon, M., and Gaughan, K. (2011). Dynamic electrical ratings and the economics of capacity factor for wave energy converter arrays. In *Proceedings of the 9th European Wave and Tidal Energy Conference, Southampton, UK*.

Sharp, C. and DuPont, B. (2018). Wave energy converter array optimization: A genetic algorithm approach and minimum separation distance study. *Ocean Engineering*, 163:148 – 156.

Sharp, C. and DuPont, B. A. (2016). Multi-objective real-coded genetic algorithm method for wave energy converter array optimization. In *ASME. International Conference on Offshore Mechanics and Arctic Engineering, Volume 6*.

Sharp, C. and DuPont, B. L. (2015). Wave energy converter array design: A preliminary study on the effect of minimum separation distance between converters. In *Proc, of 3rd Marine Energy Technology Symposium, 2015*.

Simon, M. J. (1982). Multiple scattering in arrays of axisymmetric wave-energy devices. Part 1. A matrix method using a plane-wave approximation. *Journal of Fluid Mechanics*, 120:1–25.

Singh, J. and Babarit, A. (2013). Hydrodynamic interactions in multiple body array: A simple and fast approach coupling boundary element method and plane wave approximation. In *Proceedings of the 32nd International Conference on Ocean, Offshore and Arctic Engineering OMAE2013, Nantes, France.*

SINN Power GmbH (2018). Sinn power achieves breakthrough in energy supply by ocean waves. `https://www.sinnpower.com/single-post/2018/07/05/SINN-Power-achieves-breakthrough-in-energy-supply-by-ocean-wavesg`.

Sjökvist, L., Göteman, M., Rahm, M., Waters, R., Svensson, O., Strömstedt, E., and Leijon, M. (2017). Calculating buoy response for a wave energy converter—a comparison of two computational methods and experimental results. *Theoretical and Applied Mechanics Letters*, 7(3):164 – 168.

Sjolte, J., Tjensvoll, G., and Molinas, M. (2013). Power collection from wave energy farms. *Applied Sciences*, 3(2):420–436.

Smith, H., DL, M., and DE., R. (2007). Generalisation of wave farm impact assessment on inshore wave climate. In *Proc. of 7th European Wave and Tidal Energy Conference, Porto, 11th - 14th Sep 2007.*

Smith, H., Pearce, C., and Millar, D. (2012). Further analysis of change in nearshore wave climate due to an offshore wave farm: An enhanced case study for the wave hub site. *Renewable Energy*, 40(1):51–64.

So, R., Casey, S., Kanner, S., Simmons, A., and Brekken, T. K. A. (2015). PTO-sim: Development of a power take off modeling tool for ocean wave energy conversion. In *2015 IEEE Power Energy Society General Meeting*, pages 1–5.

Stansby, P., Moreno, E. C., and Stallard, T. (2015). Capture width of the three-float multi-mode multi-resonance broadband wave energy line absorber m4 from laboratory studies with irregular waves of different spectral shape and directional spread. *Journal of Ocean Engineering and Marine Energy*, 1(3):287–298.

Stokes, C., Beaumont, E., Russell, P., and Greaves, D. (2014). Anticipated coastal impacts: What water-users think of marine renewables and why. *Ocean & Coastal Management*, 99:63 – 71. Science in support of governance of wave and tidal energy developments.

Stokes, C. and Conley, D. C. (2018). Modelling offshore wave farms for coastal process impact assessment: Waves, beach morphology, and water users. *Energies*, 11(10).

Stratigaki, V. (2014). *Experimental study and numerical modelling of intra-array interactions and extra-array effects of wave energy converter arrays*. phdthesis, Ghent University.

Stratigaki, V. (2019). WECanet: The first open pan-european network for marine renewable energy with a focus on wave energy-cost action ca17105. *Water*, 11(6).

Stratigaki, V., Troch, P., Baelus, L., and Keppens, Y. (2011). Introducing wave regeneration by wind in a mild-slope wave propagation model mildwave to investigate the wake effects in the lee of a farm of wave energy converters. In *ASME International Conference on Offshore Mechanics and Arctic Engineering, Volume 5: Ocean Space Utilization; Ocean Renewable Energy*, pages 429–436.

Stratigaki, V., Troch, P., and Forehand, D. (2019). A fundamental coupling methodology for modeling near-field and far-field wave effects of floating structures and wave energy devices. *Renewable Energy*.

Stratigaki, V., Troch, P., Stallard, T., Forehand, D., Folley, M., Kofoed, J., Benoit, M., Babarit, A., Vantorre, M., and Kirkegaard, J. (2015). Sea-state modification and heaving float interaction factors from physical modelling of arrays of wave energy converters. *Journal of Renewable and Sustainable Energy*, 7(7).

Stratigaki, V., Troch, P., Stallard, T., Forehand, D., Folley, M., Vantorre, M., Kofoed, J. P., Babarit, A., and Benoit, M. (2013). Development of a point absorber wave energy converter for investigation of array wake effect in large scale experiments. In Troch, P., Stratigaki, V., and De Roo, S., editors, *Proceedings of the International conference of the application of physical modeling to port and coastal protection*, pages 787–796. ACCO.

Stratigaki, V., Troch, P., Stallard, T., Forehand, D.and Kofoed, J., Folley, M. a., Benoit, M., Babarit, A., and Kirkegaard, J. (2014). Wave basin experiments with large wave energy converter arrays to study interactions between the converters and effects on other users. *Energies*, 7:701–734.

Taghipour, R., Arswendy, A., Devergez, M., and Moan, T. (2008). Efficient frequencydomain analysis of dynamic response for the multi-body wave energy converter in multi-directional waves. In *18th International Offshore 1 Polar Engineering Conference*.

Tay, Z. Y. and Venugopal, V. (2017). Hydrodynamic interactions of oscillating wave surge converters in an array under random sea state. *Ocean Engineering*, 145:382 – 394.

Tedeschi, E., Ricci, M. S. P., Molinas, M., and J.L.Villate (2011). Control strategies for the grid integration of wave energy converters at the biscay marine energy platform. In *Proceedings of the 9th European Wave and Tidal Energy Conference, Southampton, UK. Septermber 1-7, 2011.*

Thomas, G. P. and Evans, D. (1981). Arrays of three-dimensional wave-energy absorbers. *Journal of Fluid Mechanics*, 108:67–88.

Thorpe, T. (1999). A brief review of wave energy. Technical report, The UK Department of Trade 1 Industry.

Tissandier, J., Babarit, A., and Clément, A. H. (2008). Study of the smoothing effect on the power production in an array of searev wave energy converters. In *Proc. of The Eighteenth International Offshore and Polar Engineering Conference, 6-11 July, Vancouver, Canada*.

Tomey-Bozo, N., Babarit, A., Murphy, J., Stratigaki, V., Troch, P., Lewis, T., and Thomas, G. (2019). Wake effect assessment of a flap type wave energy converter farm under realistic environmental conditions by using a numerical coupling methodology. *Coastal Engineering*, 143:96 – 112.

Tomey-Bozo, N., Murphy, J., Lewis, T., Troch, P., and Thomas, G. (2016). Flap type wave energy converter modelling into a time-dependent mild-slope equation model. In *Proc. of the 2nd Int'l Conference on Offshore Renewable Energies*, pages 277–284.

Troch, P. (1998). Mildwave—a numerical model for propagation and transformation of linear water waves. Technical report, Department of Civil Engineering, Ghent University,Ghent. Internal Report.

Troch, P. and Stratigaki, V. (2016). Phase-resolving wave propagation array models. In Folley, M., editor, *Numerical Modelling of Wave Energy Converters*, chapter 10, pages 191–216. Elsevier.

Troch, P., Stratigaki, V., Devriese, P., Kortenhaus, A., De Maeyer, J., Monbaliu, J., Toorman, E., Rauwoens, P., Vanneste, D., Suzuki, T., and Verwaest, T. (2018). Design features of the upcoming coastal and ocean basin in ostend, belgium, for coastal and offshore applications. In *Proceedings of the 7th International Conference on the Application of Physical Modelling in Coastal and Port Engineering and Science (Coastlab18) Santander, Spain, May 22-26, 2018*, pages 1–9.

Varing, A., Filipot, J.-F., Roeber, V., Leckler, F., Duarte, R., Michard, B., and Delpey, M. (2017). Phase-resolving wave modeling for the wave characterization of coastal and nearshore marine renewable energy sites. In *Proceedings of the 12th European Wave and Tidal Energy Conference (EWTEC2017),Cork, Ireland*.

Vasarmidis, P., Stratigaki, V., and Troch, P. (2019). Accurate and fast generation of irregular short crested waves by using periodic boundaries in a mild-slope wave model. *Energies*, 12(5).

Venugopal, V. and Smith, G. (2007). Wave climate investigation for an array of wave power devices. In *Proceedings of the 7th European Wave and Tidal Energy Conference, Porto, Portugal.*, page 10, Porto, Portugal.

Verao Fernandez, G., Balitsky, P., Stratigaki, V., and Troch, P. (2018). Coupling methodology for studying the far field effects of wave energy converter arrays over a varying bathymetry. *Energies*, 11(11).

Verao Fernandez, G., Balitsky, P., Tomey Bozo, N., Stratigaki, V., and Troch, P. (2017). Far-field effects by arrays of oscillating wave surge converters and heaving point absorbers : a comparative study. In *Proceedings of the 12th European Wave and Tidal Energy Conference (EWTEC2017),Cork, Ireland*, pages 1030–1039.

Verbrugghe, T., Devolder, B., Dominguez, J., Kortenhaus, A., and Troch, P. (2017a). Feasibility study of applying sph in a coupled simulation tool for wave energy converter arrays. In *Proceedings of the 12th European Wave and Tidal Energy Conference (EWTEC2017),Cork, Ireland*, pages 679–689.

Verbrugghe, T., Domínguez, J. M., Crespo, A. J., Altomare, C., Stratigaki, V., Troch, P., and Kortenhaus, A. (2018). Coupling methodology for smoothed particle hydrodynamics modelling of non-linear wave-structure interactions. *Coastal Engineering*, 138:184–198.

Verbrugghe, T., Kortenhaus, A., and De Rouck, J. (2015). Numerical modelling of control strategies and accumulator effect of a hydraulic power take-off system. In *OCEANS 2015 - Genova*, pages 1–9.

Verbrugghe, T., Stratigaki, V., Troch, P., Rabussier, R., and Kortenhaus, A. (2017b). A comparison study of a generic coupling methodology for modeling wake effects of wave energy converter arrays. *Energies*, 10.

Verbrugghe, T., Troch, P., Kortenhaus, A., Stratigaki, V., and A.P., E.-K. (2016). Development of a numerical modelling tool for combined near field and far field wave transformations using a coupling of potential flow solvers. In *Proceedings of the 2nd International Conference on Renewable Energies Offshore 24 - 26 October 2016, Lisbon, Portugal*.

Vervaet, T., Herpelinck, M., Stratigaki, V., Troch, P., Stockman, K., and Quartier, N. (2019). Experimental study of wave energy converter arrays: Development of a single device for the WECfarm project. In *Seanergy 2019, Dunkerque, France, 30-31 May, 2019.*

Vicente, P. C., de O. Falcão, A. F., and Justino, P. A. (2009). Dynamics of arrays of floating point-absorber wave energy converters with inter-body and bottom slack-mooring connections. *Applied Ocean Research*, 31:267–281.

Vicente, P. C., de O. Falcão, A. F., and Justino, P. A. (2010). A time domain analysis of arrays of floating point-absorber wave energy converters including the effect of nonlinear mooring forces. In *3rd International Conference on Ocean Energy, 6 October, Bilbao*.

Vicinanza, D., Contestabile, P., and Ferrante, V. (2013). Wave energy potential in the north-west of sardinia (italy). *Renewable Energy*, 50:506 – 521.

Vidal, C., Fernando, M., J., Díaz, G., and Legaz, R. (2007). Impact of santoña WEC installation on the littoral processes. In *Proceedings of the 7th European Wave and Tidal Energy Conference, Porto, Portugal.*

WAMIT inc. (2019). `https://www.wamit.com/`.

Wang, L. and Isberg, J. (2015). Nonlinear passive control of a wave energy converter subject to constraints in irregular waves. *Energies*, 8(7):6528–6542.

Wave Energy Scotland (2019). Wave energy scotland power take-off projects. http://www.oceansatlas.org.

Weller, S., T.J., S., and Stansby, P. (2010). Experimental measurements of irregular wave interaction factors in closely spaced arrays. *IET Renewable Power Generation*, 4:628–637.

West, J., Bailey, I., and Whithead, I. (2009). Stakeholder perceptions of the wave hub development in cornwall, uk. In *Proceedings of the*.

Windt, C., Davidson, J., and Ringwood, J. V. (2018). High-fidelity numerical modelling of ocean wave energy systems: A review of computational fluid dynamics-based numerical wave tanks. *Renewable and Sustainable Energy Reviews*, 93:610 – 630.

Wolgamot, H., Eatock Taylor, R., Taylor, P., and Fitzgerald, C. (2011). The interaction factor for wave power in arrays. In *Proceedings of the 26th International Workshop on Water Waves 1 Floating Bodies, Athens, Greece*.

Wolgamot, H., Taylor, P., and Eatock Taylor, R. (2012). The interaction factor and directionality in wave energy arrays. *Ocean Engineering*, 47:65–73.

Wolgamot, H., Taylor, R. E., and Taylor, P. (2016). Effects of second-order hydrodynamics on the efficiency of a wave energy array. *International Journal of Marine Energy*, 229.

Yang, S.-H., Ringsberg, J. W., Johnson, E., Hu, Z., Bergdahl, L., and Duan, F. (2018). Experimental and numerical investigation of a taut-moored wave energy converter: A validation of simulated buoy motions. *Proceedings of the Institution of Mechanical Engineers, Part M: Journal of Engineering for the Maritime Environment*, 232(1):97–115.

Yilmaz, O. and Incecik, A. (1998). Analytical solutions of the diffraction problem of a group of truncated vertical cylinders. *Ocean Engineering*, 25:385–394.

Yu, Y., Lawson, M., Ruehl, K., and Michelen, C. (2014a). Development and demonstration of the WEC-sim wave energy converter simulation tool. In *Proceedings of the 2nd Marine Energy Technology Symposium, METS 2014, Seattle, WA, 2014.*

Yu, Y.-H. and Jenne, D. (2018). Numerical modeling and dynamic analysis of a wave-powered reverse-osmosis system. *Journal of Marine Science and Engineering*, 6(4).

Yu, Y. H., Li, Y., Hallett, K., and Hotimsky, C. (2014b). Design and analysis for a floating oscillating surge wave energy converter. *Proc. of the ASME 2014 33rd Int'l Conference on Ocean, Offshore and Arctic Engineering June 8-13, 2014 (OMAE2014), San Francisco, CA, USA*.

Yu, Z. and Falnes, J. (1995). State-space modelling of a vertical cylinder in heave. *Applied Ocean Research*, 17(5):265 – 275.

Zhao, H.-t., Sun, Z.-l., Hao, C.-l., and Shen, J.-f. (2013). Numerical modeling on hydrodynamic performance of a bottom-hinged flap wave energy converter. *China Ocean Engineering*, 27(1):73–86.